Development and application of analytical methods for trace analysis of organic marker species in climate archives using liquid chromatography and high-resolution mass spectrometry

Dissertation

zur Erlangung des Grades

„Doktor der Naturwissenschaften”

im Promotionsfach Chemie

am Fachbereich Chemie, Pharmazie, Geographie und Geowissenschaften der Johannes Gutenberg-Universität Mainz

vorgelegt von

Anja Christina Beschnitt

Geboren in Bad Schwalbach

Mainz, März 2022

Dekanin

1. Gutachter

2. Gutachter

Tag der mündlichen Prüfung 08.07.2022

D77 Dissertation der Johannes Gutenberg-Universität Mainz

The good thing about science is that it’s true, whether you believe it or not.

Neil deGrasse Tyson, Astrophysicist

Zusammenfassung

Klimaarchive wie Eisbohrkerne, Sedimente oder Speläotheme sind wertvolle Instrumente zur Untersuchung des Klimas in der Vergangenheit und werden zur verlässlicheren Vorhersage des Klimas in der Zukunft genutzt. Eisbohrkerne konservieren abgelagerte atmosphärische Aerosole, deren chemisches Profil, und enthalten somit Informationen über die ökologischen Bedingungen der Vergangenheit und den Einfluss anthropogener Emissionen. Im Gegensatz dazu enthalten Speläotheme Informationen über die Vegetation oberhalb einer Höhle, die sich in Abhängigkeit zu den klimatischen Bedingungen verändert. Eisbohrkerne und Speläotheme können mit unterschiedlichen Methoden wie dem Zählen einzelner Schichten oder dem radioaktiven Zerfall von Isotopen jeweils bis zu 800.000 bzw. 640.000 Jahre zurück genau datiert werden. Das Ziel der hier beschriebenen Arbeit war die Entwicklung spurenanalytischer Methoden für charakteristische „Proxies“ in den jeweiligen Klimaarchiven und die Anwendung auf Realproben zur Analyse zeitlicher Profile und Interpretation veränderter klimatischer Bedingungen.

Im ersten Teil der Arbeit wurde eine Methode zur simultanen Analyse von Lignin und Levoglucosan in Speläothemen entwickelt. Lignin ist ein hoch abundantes Biopolymer das ausschließlich von Gefäßpflanzen produziert wird. Die Monomerzusammensetzung variiert in Abhängigkeit der Vegetationsart. Daher ist die Analyse von Lignin in Speläothemen nicht nur geeignet, um die Abundanz der Vegetation oberhalb einer Höhle zu bestimmen, sondern gleichzeitig um zwischen Gymnospermen und Angiospermen, sowie verholzter und unverholzter Vegetation zu unterscheiden. Um diese Informationen zu erhalten, muss das polymere Lignin, dass aus dem Tropfwasser in den Speläothem gelangt, in seine monomeren Untereinheiten gespalten werden. Bisher wurde dazu eine katalysierte alkalische Oxidation durchgeführt, bei der festes Kupferoxid als Katalysator verwendet wurde. Dabei wird das Polymer abgebaut und die Abbauprodukte werden zu den Ligninoxidationsprodukten umgesetzt. Das Verhältnis der Oxidationsprodukte ist repräsentativ für die monomere Zusammensetzung. In dieser Arbeit wurde das Kupferoxid durch lösliches Kupfersulfat ersetzt und der gesamte Ansatz stark miniaturisiert, um den Lösemittelverbrauch zu verringern und einen höheren Probendurchsatz per Batch zu erhalten. Der Vergleich beider Methoden zeigte gleiche Leistung und der Kupfersulfat-Ansatz wurde weiter hinsichtlich Temperatur und Dauer der Oxidation optimiert. Zusätzlich wurde eine Festphasenextraktion mit graphitiertem Kohlenstoff zur Anreicherung von Levoglucosan, einem spezifischen Verbrennungsprodukt von Zellulose, durchgeführt. Als „proof-of-principle“ wurden beide „Proxies“ in Tropfsteinen aus zwei unterschiedlichen Höhlen in Neuseeland analysiert, die jeweils die Zeit des Holozäns abbilden: „Daves Cave“ und „Waipuna Cave“. Obwohl sich die Vegetation oberhalb beider Höhlen in der heutigen Zeit stark unterscheidet, zeigten beide Höhlen vergleichbare Lignin Konzentrationen in der Vergangenheit. Korrelationen mit Ionen wie Mg, Sr und Ba zeigten, dass der Transport von Lignin unter Anderem von der Niederschlagsmenge abhängt.

Die Konzentration von Levoglucosan korrelierte mit unverholzter Vegetation, was mit der höheren Entflammbarkeit von Gräsern im Vergleich zu phenolreichen verholzten Spezies übereinstimmte. Weiterhin war anhand der Levoglucosan Konzentration während des Holozäns eine höhere Frequenz an Bränden auf der Südinsel Neuseelands, oberhalb von „Daves Cave“, zu beobachten.

Der zweite Teil dieser Arbeit behandelte den möglichen Eintrag organischer Verbindungen in Speläotheme über Aerosole. Dazu wurden in „Waipuna Cave“ an verschiedenen Stellen in der Höhle, wie dem Eingang oder tief in der Höhle, Proben auf unterschiedlichen Oberflächen, wie Glas- und Plastikpetrischalen, Wasser oder Filtern gesammelt. Nach der Extraktion der organischen Verbindungen mit einem Methanol-Wasser Gemisch wurde ein „non-target screening“ und ein „suspect-target screening“ durchgeführt, um die Effizienz der verschiedenen Oberflächen zur Probenahme und die chemische Zusammensetzung der Aerosole zu untersuchen. Die Probenahme auf Filtern zeigte die höchste Effizient und die Analyse der chemischen Zusammensetzung resultierte in einer Klassifizierung von Aerosolen in „Eingetragen aus der externen Atmosphäre“, „Menschlich eingetragen“ und „Innerhalb der Höhle entstanden“. Die Experimente demonstrierten das Auftreten einer Vielzahl von Aerosolen in der Höhlenatmosphäre, sowie deren nötige Berücksichtigung als Quelle organischer Verbindungen in Speläothemen.

Im dritten Teil der Arbeit wurde eine Methode zur simultanen Bestimmung von organischen Aerosol-Markern und intaktem polymeren Lignin in Eisbohrkernen entwickelt. Dafür wurde die chromatographische Trennung optimiert, sowie verschiedene Extraktionsmethoden in Hinblick auf das Festphasenmaterial und die Lösungsmittel, um organische Verbindungen anzureichern und vom polymeren Lignin zu trennen. Die finale Methode bestand aus zwei aufeinanderfolgenden Festphasenextraktionen, welche zunächst mit schwachem Anionentauscher Material zur Anreicherung von Aerosol Bestandteilen wie Mono-, Di-, und Tricarbonsäuren, und im Anschluss mit „hydrophilic-lipophilic balanced“ Material zur Anreicherung von Lignin durchgeführt wurde. Die Lignin Degradation wurde von den Speläothem auf die Eisbohrkern Proben übertragen. Kleine, polare Verbindungen wie Levoglucosan, Mannit, Xylit und Erythritol wurden angereichert, indem die wässrige Matrix mittels Zentrifugalverdampfung entfernt wurde. Die Methode wurde auf Proben aus der Zeit von 1844-1995 vom Alpinen Gletscher Colle Gnifetti in der Schweiz angewendet. Die Korrelation von Monoterpen Oxidationsmarkern mit Markern für anthropogene Emissionen deutete einen starken Einfluss anthropogener Schadstoffe auf Aerosol Alterung an. Die Levoglucosan Konzentrationen waren mit Aufzeichnungen von Waldbränden übereinstimmend und demonstrierten die Nützlichkeit von Levoglucosan als Verbrennungsmarker in Eisbohrkernen. Erste Daten von polymerem Lignin in Eisbohrkernen zeigten eine steigende Abundanz der Vegetation, die mit veränderter Landnutzung wegen verringerter landwirtschaftlicher Nutzung übereinstimmte. Weiterhin bestätigte der zeitliche Verlauf der Ligninoxidationsprodukte die Daten über die Waldentwicklung in den südlichen Schweizer Alpen.

Im letzten Teil wurde eine zweidimensionale Flüssigchromatographie für ein „comprehensive non-target screening“ organischer Verbindungen in Eisbohrkernen entwickelt. Das chemische Profil der Proben von Colle Gnifetti war in Übereinstimmung mit Temperaturdaten, Daten über Rußemission und Daten der Emission von kohlehaltigen Partikeln. Darüber hinaus zeigten Verbindungen mit der elementaren Zusammensetzung CHOS Korrelationen mit Monoterpen Oxidationsmarkern, womit die Verbindung zwischen anthropogenen Emissionen und Aerosol Alterung gestützt wurde. Hierarchisches Clustering zeigte zwei unterschiedliche Arten anthropogener Emissionen, einerseits postuliert als landwirtschaftliche Emissionen, die hauptsächlich repräsentiert von der elementaren Zusammensetzung CHON, andererseits postuliert als fossile Brennstoffnutzung, repräsentiert von der elementaren Zusammensetzung CHOS.

Abstract

Climate archives like ice cores, sediments, or speleothems are valuable tools to study the climate of the past and more reliably predict climate change in the future. Ice cores preserve deposited atmospheric aerosols, whose chemical profiles reveal information on environmental conditions of the past and the influence of anthropogenic emissions. In contrast, speleothems preserve information on the vegetation above a cave that changes in dependence to climate conditions. Ice cores and speleothems can be accurately dated back to 800,000 years and 640,000 years, respectively, using different methods like layer counting or radioactive isotope decay. The aim of this work was to develop suitable trace analysis methods for characteristic environmental proxies of the respective climate archives and to apply them to real samples to evaluate the timely progress and draw conclusions on changed environmental conditions.

In the first part of this work a method for the simultaneous analysis of lignin and levoglucosan in speleothems was developed. Lignin is a highly abundant biopolymer, that is exclusively produced in vascular plants. The monomeric composition of lignin varies depending on the type of vegetation. Therefore, lignin analysis in speleothems is suitable to determine the vegetation abundance, and to distinguish between angiosperm and gymnosperm vegetation, as well as wooden and non-wooden species in the past. To access this information, the polymeric lignin, that is included into the speleothem from drip water, has to be degraded into its monomeric subunits. To date, a catalyzed alkaline oxidation approach was used, using solid CuO as catalyst, where the polymer is degraded, and degradation products are further oxidized to the lignin oxidation products (LOPs). The ratio of LOPs is representative for the monomeric composition. In this work, the CuO was replaced by soluble $CuSO_4$, and the entire approach was strongly miniaturized reducing solvent use and enabling a higher throughput of samples per batch. The comparison of both methods showed similar performance and the $CuSO_4$ approach was further optimized by the duration and temperature of the degradation procedure. In addition, a solid-phase extraction with graphitized carbon black material was introduced for enrichment of levoglucosan, a specific product of cellulose burning. Both proxies were analyzed as proof-of-principle in samples from two caves from New Zealand, Daves Cave and Waipuna Cave, covering the Holocene. Despite today, the vegetation above both caves strongly differs in type and abundance, both caves showed similar LOP concentrations in the past. Correlation with ions like Mg, Sr, or Ba revealed that the transport processes of lignin through the soil change depending on the amount of precipitation. The levoglucosan concentration was correlating with non-wooden vegetation, which was conclusive since the flammability of grasses is higher than the flammability of phenolic-rich wooden species. Levoglucosan also showed that during the Holocene, Daves Cave on the Southern Island of New Zealand was exposed to wildfires more frequently than Waipuna Cave on the Northern Island.

The second part of this work focused on the evaluation of aerosols as a source of organic compounds in speleothems. Samples were collected in Waipuna Cave at different locations, like the cave entrance and a site deep in the cave, and on different surrogate surfaces like glass and plastic petri dishes, water, or filters. After extraction of organic compounds with methanol/water mixtures, non-target and suspect target screening was conducted to evaluate the sampling efficiency on different surfaces and the chemical composition of aerosols at different sites in the cave. Sampling on filters proved most efficient and by the chemical composition aerosols were classified as introduced from the external atmosphere, anthropogenically introduced, and cave-internally produced. The experiments demonstrated the presence of a variety of aerosols in the cave atmosphere and their necessary consideration as an entry source of organic compounds in speleothems.

In the third part of this work the simultaneous trace analysis of organic aerosol marker compounds and analysis of intact polymeric lignin in ice cores was aimed. For that, chromatographic separation was optimized, and different extraction methods were evaluated considering the type of solid phase material and solvents to sufficiently enrich and separate the organic compounds from the lignin. The final method consisted of two consecutive solid-phase extractions using weak anion-exchange material for enrichment of aerosol constituents like mono-, di-, and tricarboxylic acids, and hydrophilic-lipophilic balanced material for the enrichment of lignin. The lignin degradation approach was transferred from speleothem to ice core samples. Small, polar compounds like levoglucosan, mannitol, xylitol, and erythritol were enriched from the flow-through of both extractions by centrifugal evaporation of the aqueous matrix. The method was applied to samples from the Alpine Colle Gnifetti glacier in Switzerland covering the time from 1844 to 1995. The correlation of monoterpene oxidation markers and markers for anthropogenic emissions indicated a strong influence of anthropogenic pollutants on aerosol aging and the levoglucosan concentrations were consistent with fire records, demonstrating its utility as a biomass burning marker. First data of polymeric lignin in ice cores showed increasing abundance of vegetation, consistent with changes land use due to decreasing agricultural activity and the progress of LOPs was confirming with data on forest development in the Southern Swiss Alps.

Finally, a two-dimensional liquid chromatography method was developed for comprehensive non-target screening of organic compounds in ice cores. The chemical profile in samples from Colle Gnifetti was consistent with the literature concerning temperature, black carbon emission, and carbonaceous particle emission. Furthermore, the compounds detected with the general elemental composition CHOS were correlating with monoterpene oxidation markers from target analysis, consolidating the connection between anthropogenic emission and aerosol aging. Hierarchical clustering revealed two different anthropogenic emission sources, proposed as agricultural, which was mainly represented by compounds with the elemental composition CHON, and fossil fuel burning, mainly represented by the elemental composition CHOS.

Table of Contents

Introduction and theory

1. Ice cores as climate archives

Dealing with climate change is the major challenge of the twenty-first century. Climate models predict different scenarios with a surface temperature increase between 0.3-4.8°C until the year 2100 (Stocker et al. 2013). Feeding these models with recovered data on the climate of the past from archives like ice cores, sediments or speleothems is crucial to improve their reliability and accuracy.

Even remote Arctic and Antarctic regions are already affected by anthropogenic emissions, but they still provide the cleanest atmospheric conditions in their respective hemisphere and the unique meteorological conditions in polar regions enable a preservation of deposited atmospheric aerosols for several thousand years. A well-marked seasonal cycle facilitates the dating of ice cores, and the long polar night with very cold temperatures, dry air, and quasi-absence of photochemistry in the winter months strongly decrease the chemical reactivity of the atmosphere (Legrand and Mayewski 1997). At Dome C in Antarctica, the "European Project of Ice Coring in Antarctica" drilled a 3.3 km long core, which was dated back to 800,000 years and to date is the oldest continuous ice core ever retrieved (Augustin et al. 2004). While polar ice cores are used to study global climate and environmental changes on a long-time scale, ice cores from mid- and low-latitude glaciers are valuable to study regional anthropogenic air pollution on a time scale between decades to centuries.

1.1 Dating of ice cores

Correct interpretation of organic proxies relies on precise dating of the ice core sections. For that, different approaches are available. The accuracy of annual layer counting depends on factors like significantly seasonally fluctuating signals, regular distribution of precipitation, high snow accumulation rates, and minimal post-depositional snow erosion from the ice sheet surface. In addition, dating of ice cores by annual layer counting is not suitable for the older, deeper parts of the ice cores because there the strong plastic deformation results in significant but uneven layer thinning and a non-linear age-depth relationship (Jenk et al. 2009; Uglietti et al. 2016; Nardin et al. 2021).

A marker with pronounced seasonality is the stable isotope ratio of δ^2H and $\delta^{18}O$ in water, because the fractionation of stable oxygen isotopes is temperature dependent (Dansgaard 1964; Eichler et al. 2000). Trace concentrations of ammonium ions, methanesulfonic acid, nitrate, non-marine related sulfate ions, and black carbon also show seasonal variability due to the temperature dependent atmospheric convection (Uglietti et al. 2016; Nardin et al. 2021). Furthermore, annual layer counting is influenced by two independent time-depth relationships from the ice-phase related proxies (water isotopes) and the gas-phase related proxies (for example CO_2 and CH_4). While the air is isolated approximately 50-120 m under the sheet surface, the firn is progressively migrating into the deeper parts of the ice sheet (Veres et al. 2013). The firn densification model and the $\delta^{15}N$ isotope from the N_2 in ice-entrapped air are used

to assess the resulting age difference and minimize the interference to the age models. Recent studies showed more accurate results using the $\delta^{15}N$ isotope (Schwander et al. 1997; Goujon et al. 2003; Dreyfus et al. 2007; Parrenin et al. 2012).

To overcome the non-linear age-depth relationship, the decay of radioactive isotopes is analyzed. The ^{210}Pb isotope is formed in the troposphere by decay of ^{222}Rn and transported by adsorption to aerosols before dry or wet deposition. It has a half-life of 22.3 years, which is suitable for dating of time-scales up to 100 years (Tinner et al. 1998). For a long time, radiocarbon dating was strongly restricted by the limited amount and uneven distribution of organic matter from plants or insects in ice cores. However, more recent research analyzed the ^{14}C content from extracted water-insoluble organic carbon and from dissolved organic carbon, which has a 2-8 times higher abundance compared to the water-insoluble fraction and reduced the required ice mass to approximately 250 g with a dating accuracy of ±200 years (Jenk et al. 2009; Uglietti et al. 2016; Fang et al. 2021).

The analysis of stratigraphic marker compounds provides traces of events with an absolute date, so-called "reference horizons". Volcanic eruptions result in the formation of tephra and high atmospheric sulfate loading, which is recoverable from peaking sulfate concentrations in ice cores (Dunbar 2003; Davies et al. 2010; Coulter et al. 2012; Abbott et al. 2021). Radioactive fallouts from thermonuclear weapon tests in the 1960s resulted in peaking tritium abundance and the nuclear accidents in Chernobyl 1986 and Fukushima Daiichi 2011 are recoverable by ^{137}Cs peaks in climate archives worldwide (Maggi et al. 1998; Wang et al. 2020a). Another example for a "reference horizon" are depositions from Saharan dust events (Schwikowski et al. 1995).

The appropriate method for the dating of ice cores is chosen based on the expected time-scale and the desired accuracy, however to obtain a dating as precise as possible, a combination of dating methods should be forced (Maggi et al. 1998; Eichler et al. 2000).

1.2 Ice core study site

The Colle Gnifetti glacier is located in the Swiss-Italian Alps (45°55´50´´N, 7°52´33´´E, 4455 m above sea level (a.s.l.)) and is part of the Monte Rosa massif. As the uppermost part of the accumulation area of *Grenzgletscher* it forms a saddle between *Zumsteinspitze* and Punta Gnifetti of Monte Rosa. It is the highest glacier saddle in the Alps which is suitable for ice core studies. Wind erosion preferably removes the winter snow, which is why the snow accumulation rates on Colle Gnifetti are rather low (0.2-1.1 m per year) resulting in very strong spatial and temporal variations. This enables the recovery long time series, which is highly advantageous for ice core research (Barbante et al. 2004; Jenk et al. 2009). Intense solar radiation and elevated temperatures can produce meltwater, which refreezes at a depth of a few centimeters, however the ice temperatures measured in these depths did not exceed a range between - 14°C to -9°C (Haeberli and Funk 1991; Lüthi and Funk 2001). The location of Colle Gnifetti glacier in the center of the European continent is useful to study the atmospheric impact vegetation, agriculture,

industrial emissions, and fires of the last millennium especially the changing dynamics between the pre-industrial and industrial era. Microfossil and oxygen isotope records from Colle Gnifetti revealed an adaptation of the European societies to the Little Ice Age cold period by changing of the crop cultivation species (Brugger et al. 2021). In addition, a record of heavy metals showed significantly increasing concentrations between the 17th and 18th century compared to the second half of the 20th century related to the strongly elevated amount of metal emissions since the industrial revolution (Barbante et al. 2004).

Pollen data from Colle Gnifetti revealed high portions of Mediterranean pollen and occasional input of pollen from wild grass from the dry areas of Northern Africa and southernmost Europe correlating with orange dust layers indicating aerosol transport from more distant areas. Furthermore, pollen data showed alternating progress of forest species with agricultural grassland and crop species. Especially before 1750 CE forest species rapidly replaced crop species when population decreased due to social crisis or epidemics like the Black Death (More et al. 2017; Rey et al. 2019; Brugger et al. 2021).

2. Speleothems as climate archives

Besides ice cores, speleothems constitute another valuable climate archive. They are formed by precipitation of dissolved carbonate from cave drip water and thereby include and preserve different organic and inorganic proxies, which provide information on climate conditions of the past represented by changing vegetation and soil conditions above a cave (Fairchild et al. 2006; Blyth et al. 2008; Yang et al. 2011; Blyth et al. 2016; Heidke et al. 2019). They are advantageous over ice cores in their continuous growth for several thousand years without decreasing timely resolution, more accurate dating methods back to 640,000 years using U-series methods (Scholz and Hoffmann 2008; Cheng et al. 2016), and preservative character given by the atmospheric conditions in the cave, where the absence of light suppresses photochemistry and temperature fluctuations are moderate. Furthermore, speleothems are available on all continents except Antarctica and therefore speleothem research is not limited to certain climate conditions or vegetation zones (Fairchild et al. 2006; Fairchild and Baker 2012).

2.1 Speleothem formation

The formation of speleothems is based on different processes in and above the cave environment in karstified carbonate bedrock. The extensive cavity development in karstic host rock leads to the drainage of surface water into deeper zones below the soil. The epikarst or subcutaneous zone below the soil feeds the fissures and pores with surface water and constitutes the pathways of drip water locations in the cave. In a suchlike porous, water-permeable host rock an aquifer below the epikarst is formed. The soil, upper epikarst and aquifer are characterized as the dissolution region, where carbonate is dissolved in water with a high partial CO_2 pressure. The required CO_2 is a product from microorganisms in the soil and plant respiration. In contact with surface water, carbonic acid is formed (Equation 1). While seeping through the soil and bedrock, the weakly acidic solution dissolves the carbonate resulting in a saturation of the solution (Equation 2). In the precipitation region in the cave, the supersaturation and

$p(CO_2)$ difference between the soil and the cave ($p(CO_2)_{cave} << p(CO_2)_{soil}$) results in degassing of CO_2, shifting the reaction equilibrium to the right and enhancing precipitation of $CaCO_3$ (Equation 3) which is responsible for formation and growth of speleothems (Fairchild et al. 2006).

$$\text{soil: } CO_2 + H_2O \rightleftharpoons H_2CO_3 + H_2O \rightleftharpoons HCO_3^- + H_3O^+$$

Equation 1

$$\text{bedrock: } CaCO_{3\,(s)} + H_2CO_3 \rightleftharpoons Ca^{2+} + 2\,HCO_3^-$$

Equation 2

$$\text{cave: } Ca^{2+} + 2HCO_3^- \rightleftharpoons CaCO_{3(s)} + H_2O + CO_2$$

Equation 3

The three most common types of speleothems are stalagmites, stalactites, and flowstones. Flowstones are formed from sheets of flowing water on the cave surfaces, which derive from larger fissures in the aquifer rather than small and distinct drip sites. Flowstones are primarily sampled by coring but due to the non-uniform growth-rates of the flowstone and flow-behavior of the water a representative analysis requires repeated sampling and complicates the dating of the layers (Hellstrom et al. 1998; Richards and Dorale 2003; Fairchild et al. 2006). Stalactites grow in cylindrical shape from the cave ceilings and are very vulnerable, which is why they tend to naturally break and drop from the ceiling and only preserve information from a few decades (Huang et al. 2001). Stalagmites are the counterparts of stalactites growing upwards from the cave floor. Their shape and the diameter of the comparably flat surface depends on the flowrate of the water, resulting in a smaller diameter with lower flowrates, the saturation of the drip water, because a higher saturation results in more irregular precipitation, and the distance between the ceiling the stalagmite surface, since a larger distance results in a larger diameter (Fairchild et al. 2006). Stalagmites are often subjected to growth hiatus, which can be visible as a dust layer, and result from changing climate conditions or randomly changing drip locations in the cave, which are two difficultly distinguishable parameters (Kaufmann and Dreybrodt 2004). The growth rate of stalagmites is predicted by comparing the calcium content of cave drip water with theoretical speleothem growth models and expected to range between 70-100 µm per year at 6°C and up to 800 µm per year at 13°C. However, in practice a stalagmite grows between 10-100 µm per year in cold regions and 300-500 µm per year in subtropical, warm regions with high drip rates (Genty et al. 2001a; Fairchild et al. 2006).

2.2 Dating of speleothems

The most indispensable requirement for a climate archive like a speleothem is the precise dating. Similar to ice cores, speleothems can be dated by layer counting. For that, pronounced visible layers and continuous speleothem growing without hiatus are required. In contrast to ice cores, radiocarbon dating using the ^{14}C isotope is not possible due to the mixture of dead carbon from the host rock and atmospheric carbon introduced by the overlying vegetation and the soil (Fairbanks et al. 2005; Hua 2009). However, an absolute and precise dating method is available for speleothems using the ^{230}Th-U

method, which enables dating back to 640,00 years. The high difference in the half-life of the mother nuclide ^{234}U ($T_{1/2}$ = 2.453 x 10^5 years) and daughter nuclide ^{230}Th ($T_{1/2}$ = 7.569 x 10^4 years) results in a secular activity equilibrium within several million years in naturally occurring and undisturbed materials and a constant quantity of ^{230}Th (Scholz and Hoffmann 2008; Fairchild and Baker 2012; Cheng et al. 2016). The key to the appliance of this equilibrium for speleothem dating are natural disturbances for example by elemental fractionation of U from Th. Uranium is naturally occurring in two oxidation states, predominantly in the water-soluble state U^{+VI} for example in the uranyl ion UO_2^{2+}, and to a lesser extent in the insoluble and less mobile state U^{+IV}. In contrast, Th mainly occurs in the oxidation state Th^{+IV}, which is insoluble in water and therefore only transported by minerals or adsorption to particles in the soil (Ivanovich and Harmon 1992; Scholz and Hoffmann 2008). These different geochemical behaviors result in a disruption of the equilibrium during the transport from the karst rock to the drip water where no Th is solved so the initial $^{230}Th/^{234}U$ ratio is zero. In consequence, only U is included into the growing speleothem. Additional important requirements for speleothem dating by ^{230}Th-U are the absence of initial Th in the speleothem and a closed system where no U or Th can enter or leach from the speleothem after inclusion. The initial presence of Th in the speleothem is determined by measuring detrital ^{232}Th which is accompanied by ^{230}Th. However, a generally valid isotope ratio cannot be predicted and different correction procedures are used to minimize the error (Scholz and Hoffmann 2008 and references therein). If all conditions are fulfilled, the degree of the U decay in a closed system is determined by the $^{230}Th/^{234}U$ ratio in the speleothem calcite layers and used to calculate to the age.

The isotope concentration can be analyzed by determination of the isotope specific energy from α-particles released by radioactive isotope decay with an α-spectrometer. α-spectrometry requires several days for one measurement, a sample size of more than 1 µg of U, and only provides a precision in the percent range and dating back to 300,000 years (Scholz and Hoffmann 2008). Therefore, mass spectrometric techniques are favored like thermal ionization mass spectrometry (MS) and multi-collector inductively coupled plasma (ICP) MS. The thermal ionization MS requires a few hours for one measurement, a sample size of 10-100 ng of U and provides a precision in the parts per million (ppm) range (Edwards et al. 1987) while multi-collector ICP-MS only requires 10-20 minutes, 5-10 ng of U with a comparable precision (Halliday et al. 1998; Goldstein and Stirling 2003; Hoffmann et al. 2007) and is therefore considered as the state-of-the art technique.

Since only selected samples along the growth axis of a speleothem are measured, a mathematical description of the consecutive relation between age and distance of a dating point to the top or bottom of the speleothem is necessary to calculate an age model. The reliability of the ageing procedures is roughly evaluated by the stratigraphic order of calculated ages (Scholz and Hoffmann 2011) however most age-modelling approaches show severe drawbacks in comparability and age uncertainty determination. Linear interpolation does not sufficiently consider errors (McDermott et al. 1999; Wang et al. 2005b), while a least-squares polynomial fit and splines lack in comparability due to the high variety of approximations (Spötl and Mangini 2002; Spötl et al. 2006; Vollweiler et al. 2006; Hodge et

al. 2008). More sophisticated methods use Bayesian statistics and take into account the general speleothem growth mechanisms (Spötl et al. 2008). More recently, algorithms were developed like "StalAge" (Scholz and Hoffmann 2011) and "Constructing Proxy Records from Age Models" (COPRA) (Breitenbach et al. 2012) specifically designed to calculate speleothem age models with respect to age uncertainties, hiatus, outliers, and age reversals, strongly improving comparability of different climate archives and allowing more spatio-temporal analysis and quantitative reconstructions.

2.3 Lignin as a vegetation proxy in speleothems

Lignin is the second most abundant biopolymer after cellulose, almost exclusively found in terrestrial vascular plants, and constituting approximately 30% of all organic carbon in the biosphere (Brown 1969; Hedges and Mann 1979). As part of the secondary cell walls, it strongly contributes to plant stability and due to its hydrophobic character it is involved in the transport of water, while simultaneously protecting the cells from pathogens and microbial degradation (Vanholme et al. 2010). Lignin is composed of three monomers: *p*-coumaryl alcohol, coniferyl alcohol, and sinapyl alcohol (Figure 1), which are linked by oxidative radical coupling mechanisms (Boerjan et al. 2003; Ralph et al. 2004; Vanholme et al. 2010). Other monomers incorporated to a lesser extent are for example 5-hydroxyconiferyl alcohol, hydroxycinnamate esters, or hydroxybenzaldehydes (Ralph et al. 2004).

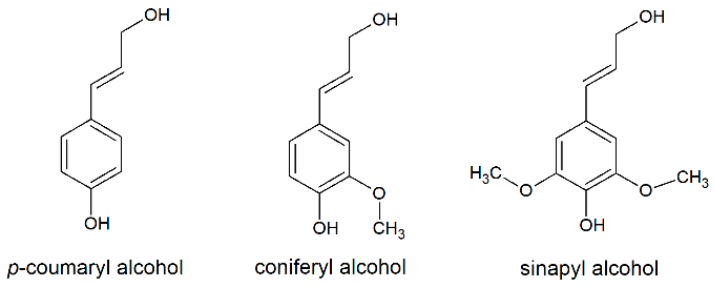

Figure 1: Molecular structures of the monomeric alcohols, the three predominant constituents of polymeric lignin.

The monomers are incorporated into the polymer as *p*-hydroxyphenyl-, guaiacyl-, and syringyl-phenylpropanoid subunits, which are linked by the formation of stable C-C and C-O bonds. The monomeric radicals are formed by dehydrogenation of the 4-hydroxy-position by peroxidase or laccasse enzymes, and the radical position in the delocalized electron system is either located at the 1-,3-, or 5-position of the aromatic ring or at one of the carbon atoms involved in the double-bond of the side chain (α or β). By recoupling of coniferyl alcohol moieties [β-5]-linked dimers, [β-O-4]-linked ethers, [β-β]-linked dimers, and to a lesser extent [5-5]-linked biphenyls and [5-O-4] linked biphenyl ethers are formed. Due to the occupied 5-position of the aromatic ring in the sinapyl alcohol, here radical coupling only results in the formation of [β-O-4]-linked ethers and [β-β]-linked dimers, which is why lignin with a high sinapyl alcohol content is less branched (Figure 2). Although the dimerization of two monomeric radicals is the thermodynamically favored reaction, their limited availability prevents a radical chain reaction growth of the lignin polymer. Instead, oligomeric radicals are recombined consecutively to a chain length of for example 13-20 units in the vegetation species poplar (Vanholme et al. 2010). The [β-

O-4]-ether is the most frequently occurring linkage in the polymeric lignin and the only chemically cleavable bond (Boerjan et al. 2003; Ralph et al. 2004). The strong C-O and C-C ether bonds and the complex three-dimensional structure contribute to a high resistance of lignin towards microbial degradation. Only white-rot fungi are able to completely disintegrate and mineralize lignin to CO_2, while brown-rot fungi only induce minor structural changes (Kögel-Knabner 2002). Due to the high stability, high environmental abundance, and vegetation specific monomeric composition lignin is a valuable proxy to reconstruct vegetation of the past in climate archives like soils or speleothems.

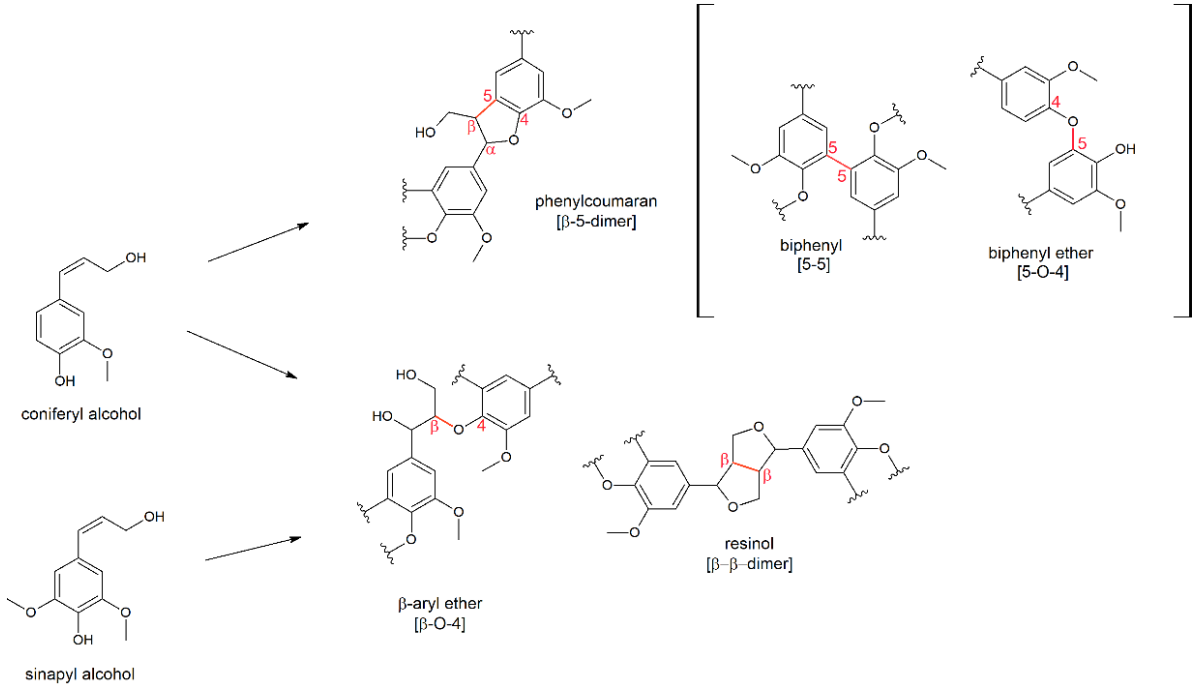

Figure 2: Main linkages of coniferyl alcohol and sinapyl alcohol in the lignin polymer.

Lignin from gymnosperm plants primarily consist of guaiacyl phenylpropanoid units from coniferyl alcohol, while lignin from angiosperm plants consists of guaiacyl and syringyl phenylpropanoids from coniferyl and sinapyl alcohol. A higher proportion of *p*-hydroxyphenyl units from *p*-coumaryl alcohol is found in lignin from grasses (Hedges and Mann 1979; Boerjan et al. 2003; Jex et al. 2014). To assess the monomeric composition of lignin, the polymeric structure has to be disintegrated either chemically by thermal degradation, acid/base catalyzed hydrolysis, catalytic oxidation, or electrochemical conversion (among others), or enzymatically (Brebu and Vasile 2010; Zakzeski et al. 2010; Pandey and Kim 2011; Xu et al. 2014; Li et al. 2016; Zirbes et al. 2019). While most of these degradation methods focus on the production of oxidized monomeric compounds on a preferably industrial scale, an analytical degradation approach aiming for information on the composition and structure must force as little alteration of the initial structure as possible. For analytical degradation of lignin, initially a Cu(II)O catalyzed alkaline oxidation was developed (Hedges and Erte 1982; Goñi and Montgomery 2000; Yan and Kaiser 2018a), which was more recently replaced by $CuSO_4$ as catalyst (Yan and Kaiser 2018b). The complete mechanism of alkaline lignin oxidation remains elusive, however different mechanisms are proposed of which sequential single-electron oxidations followed by retro-aldol cleavage for the

formation of aldehyde derivatives from the lignin phenols is to date the most conclusive (Figure 3). The mechanism starts by deprotonation of the hydroxy group in the alkaline medium and further electron detachment. Afterwards a *p*-quinonemethide is formed either by disproportionation of two phenoxy radicals or by further deprotonation and oxidation (Figure 3a). Afterwards, the *p*-quinonmethide is deprotonated, followed by a nucleophilic addition of a hydroxy-group and retro-aldol cleavage (Figure 3b). If the carbonyl group is formed at the γ- instead of the α-position after the nucleophilic addition, the retro-aldol reaction results in the formation of a ketone derivative of the lignin phenol. According to this mechanism acidic derivatives are only formed from initially present carbonyl groups at the α-position, resulting from microbial or geochemical alteration, but if the atmosphere in the reaction vessel is not inert, over-oxidation reactions of the oxidized lignin phenols is observable (Tarabanko et al. 2004; Tarabanko and Tarabanko 2017).

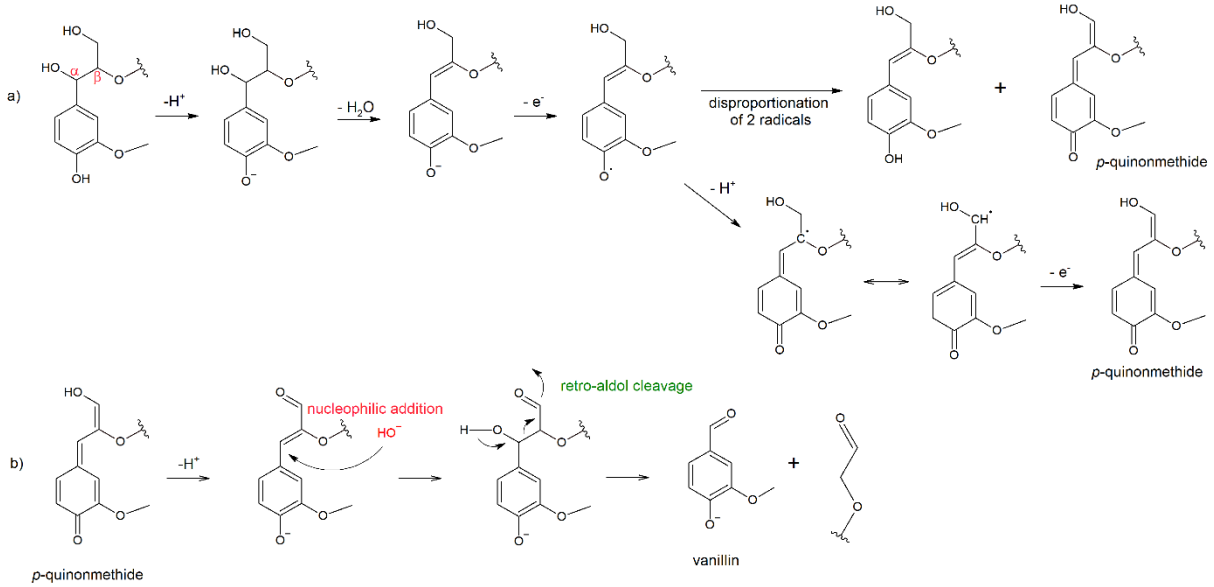

Figure 3: Proposed reaction pathway of the alkaline lignin oxidation forming aldehyde derivates of the lignin phenols. a) Formation of *p*-quinonmethide by deprotonation and sequential electron detachment followed by either disproportionation or deprotonation. b) Nucleophilic addition of a hydroxide ion to the *p*-quinonmethide followed by a retro-aldol cleavage resulting in the formation of vanillin.

The products from alkaline lignin oxidation are referred to as lignin oxidation products (LOPs), which are further classified into three groups, according to their monomeric precursors. Products from the coniferyl-alcohol (guaiacyl phenylpropanoid subunit) are assigned to the vanillyl-group (V-group) consisting of vanillin, vanillic acid, and acetovanillone, while products from sinapyl-alcohol (syringyl phenylpropanoid subunit) include syringaldehyde, syringic acid, and acetosyringone, and are assigned to the syringyl-group (S-group). Lastly, the products from *p*-coumaryl alcohol (*p*-hydroxyphenyl subunit) are assigned to the cinnamyl-group (C-group) and contain *p*-coumaric acid and *trans*-ferulic acid (Figure 4).

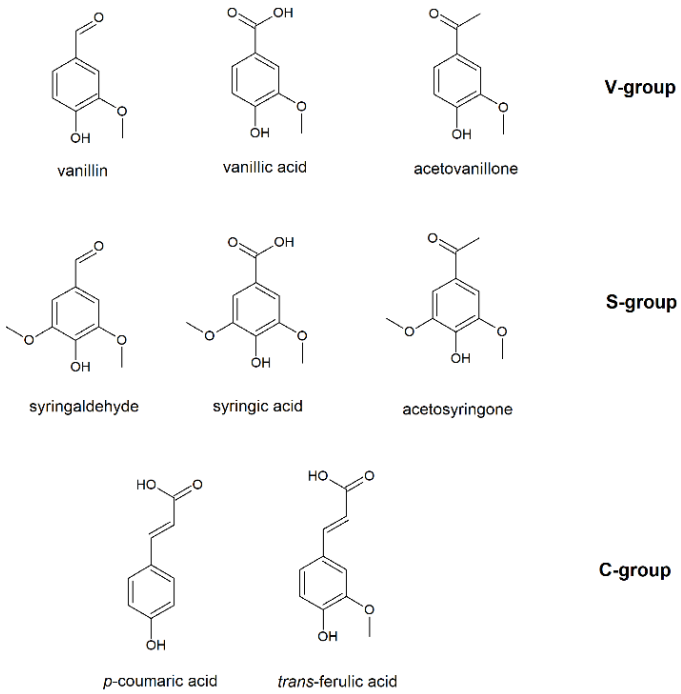

Figure 4: Molecular structures of lignin oxidation products from alkaline lignin oxidation and classification into the V-group, S-group, and C-group based on their monomeric precursors.

A fourth group, the *p*-hydroxyl group (P-group or H-group) consists of *p*-hydroxybenzoic acid, *p*-hydroxybenzaldehyde, and *p*-hydroxyacetophenone, which are also microbiologically produced by bacteria and are naturally occurring as oxidation products of the amino acid tyrosine, which is why compounds of the P-group are no unequivocal products of lignin degradation and not used for vegetation reconstruction. Lignin from gymnosperm vegetation primarily consists of compounds from the V-group, while angiosperm vegetation contains a mixture from the S- and V-group. In contrast, compounds from the C-group are only found in non-woody tissues like grasses, which is why the parameters S/V and C/V were introduced to distinguish between angiosperm (A), gymnosperm (G), wooden (w), and non-wooden (nw) vegetation (Figure 5) (Hedges and Mann 1979; Jex et al. 2014).

Lignin provides information on the abundance and the type of vegetation and is a valuable tool to reconstruct the vegetation and climate induced changes of vegetation in the past, which is why it is analyzed in a variety of climate archives like soil (Thevenot et al. 2010; Hernes et al. 2013; Heidke et al. 2021), peat (Comont et al. 2006), marine cores (Pancost and Boot 2004; Sun et al. 2011; Arndt et al. 2013), sediments (Hedges and Parker 1976; Hartog et al. 2004), or speleothems (Jex et al. 2014; Blyth et al. 2016; Heidke et al. 2019, 2021) where they complement to other less specific vegetation proxies like fatty acids (Blyth et al. 2006; Bosle et al. 2014) or n-alkanes from plant leaf waxes (Blyth et al. 2007, 2011).

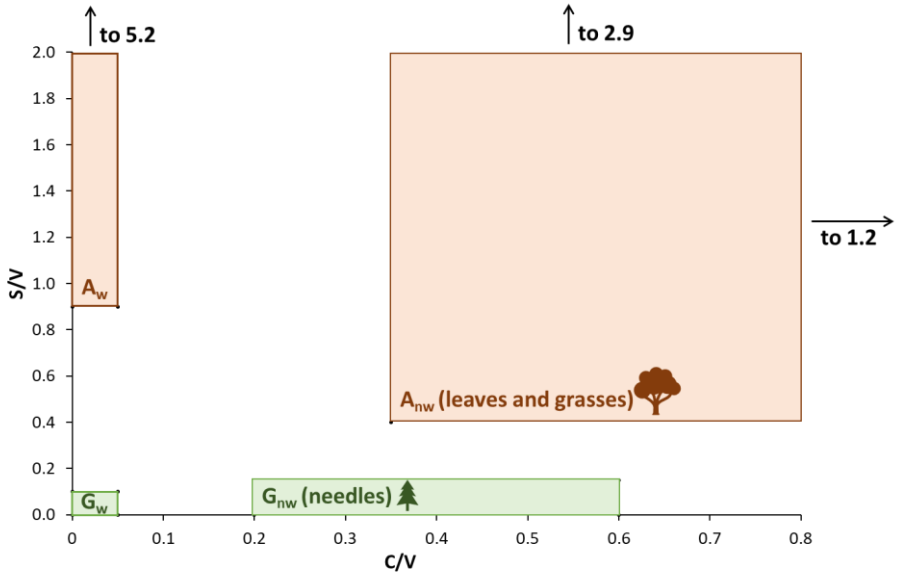

Figure 5: Scatterplot of the parameters S/V and C/V, introduced for assignment of lignin to different vegetation species like gymnosperms (G) and angiosperms (A), as well as wooden (w) and non-wooden (nw) parts of the plants. The assigned areas were determined by studies of lignin composition in twenty-three different vascular and non-vascular plant tissues (Hedges and Mann 1979; Jex et al. 2014).

Although the fate of lignin in soil, interaction with minerals, and transport through the karst system and aquifer before entering a cave remains elusive, first studies showed that a fractionation in the soil is occurring by different degrees of leaching and sorption to the mineral surface of soil particles (Hernes et al. 2007, 2013). Different abundance of lignin in soil, drip water and speleothems was observed, but since the relative vegetation signal was preserved, a comparability of samples from the same type (speleothem samples, soil samples, and water samples) was demonstrated (Heidke et al. 2021). No data on intact polymeric lignin in ice cores is available and this work also aims to elucidate the presence of lignin in ice core samples and consequently the possibility of intact polymeric lignin transport by aerosols. Correlation with other atmospheric marker compounds is expected to provide information on the emission source.

3. Atmospheric aerosols

Aerosols are defined as a suspension of liquid or solid particles in the gas phase with sizes between nanometers to micrometers. Primarily, solid particles are atmospherically relevant as they are ubiquitous and influence the radiative budget of the earth's atmosphere and consequently the climate (Pöschl 2005; Seinfeld and Pandis 2006). Atmospherically relevant fine air particulate matter (PM) ranges from aerodynamic diameters ≤ 1 µm (PM1) to ≤ 2.5 µm (PM2.5) and can be sampled using filters of the respective pore diameters (Raes et al. 2000; Van Dingenen et al. 2004). The emission of fine air PM into the atmosphere has rapidly increased since the preindustrial age due to the immense burning of fossil fuels and biomass in the industry and domestic households (Bond et al. 2004a; Tsigaridis et al. 2006;

Lamarque et al. 2010; Takemura 2012). Although the direct and indirect effects of aerosols on radiation and clouds are generally characterized, the response of the climate system is highly uncertain.

Direct effects of aerosols in the atmosphere are scattering of light or absorption of solar radiation, while indirect effects influence the formation and lifetime of clouds, which in turn determine their radiative properties (Houghton J.T., Ding, Y., Griggs, D.J., Noguer, M., van der Linden, P.J., Dai, X., Maskell, K., Johnson 2001; Pöschl 2005; Bauer and Menon 2012). Aerosols with a size between 50-100 nm primarily act as cloud condensation nuclei (CCN) initiating different indirect effects. One indirect effect describes that a higher number of aerosol particles in the atmosphere results in a higher number of CCN and consequently enhanced cloud formation and albedo (cloud albedo effect or Twomey effect). Another indirect effect (cloud lifetime effect) indicates that a higher number of CCN reduces cloud droplet size resulting in less precipitation and longer lifetime of the clouds (Lohmann and Feichter 2005). Thereby the light scattering capabilities of the clouds are enhanced, and consequently radiative forcing is expected to be reduced, resulting in a cooling effect ("Whitehouse effect"). In contrast, an increased radiative forcing by absorption of solar radiation results in a warming effect ("Greenhouse effect"), which is observed by greenhouse gases or particles containing black carbon. All these effects influence the global radiative balance, hydrological cycle, temperature, circulation of the oceans, and circulation of the atmosphere (Ramanathan et al. 2001; Andreae et al. 2005). Moreover, extreme weather events can occur at increasing degree (Andreae et al. 2004). Finally, aerosols have a considerable effect on human health because they can enter the respiratory and cardiovascular system, causing severe inflammation and allergic reactions (Bernstein et al. 2004; Kim et al. 2015; Thompson 2018).

Directly emitted particles like dust, pollen, combustion particles, volcanic ashes or sea salt are classified as primary aerosols, while secondary organic aerosols (SOA) are formed in the atmosphere by oxidation of volatile organic compounds (VOC) into less volatile species that undergo gas-to-particle conversion, forming new particles by nucleation or condensation on existing particles (Pöschl 2005; Seinfeld and Pandis 2006; Kroll and Seinfeld 2008; Hallquist et al. 2009). The size of aerosols strongly determines their atmospheric lifetime and accumulative behavior. Primarily emitted coarse particles with a diameter larger than 1 µm constitute a large portion of the aerosol mass and have a short atmospheric lifetime because they are strongly subjected to gravitational deposition. The removal of particles with a diameter smaller than 1 µm from the atmosphere is mainly controlled by wet deposition and they are subdivided into three categories: accumulation mode (0.1-1 µm), Aitken mode (0.1-0.01 µm), and nucleation mode (<0.01 µm). Aerosols of the accumulation mode category have the longest atmospheric lifetime from days to weeks, while aerosols from the categories of nucleation mode and Aitken mode have lifetimes between minutes to hours. Another driving force of the atmospheric lifetime of aerosols is their atmospheric altitude (Williams et al. 2002; Pöschl 2005; Seinfeld and Pandis 2006).

Global radiative forcing is controlled by different emissions and drivers. The share of the individual precursors and resulting atmospheric drivers is elucidated to different levels of confidence. While the

direct effect of aerosols or the influence of anthropogenic greenhouse gases like CO_2, CH_4, or N_2O are now elucidated with high or very high level of confidence, the indirect effect of aerosols on cloud formation and lifetime remains the largest uncertainty (Houghton J.T., Ding, Y., Griggs, D.J., Noguer, M., van der Linden, P.J., Dai, X., Maskell, K., Johnson 2001). It is generally assumed that the anthropogenic impact on clouds by aerosols results in a cooling effect, however first studies observed a reversed Twomey effect by anthropogenic emission on cirrus clouds and clouds over the northern Indian Ocean (Jose et al. 2020; Zhu and Penner 2020). Therefore, the need to analyze the high spatial and temporal variability of aerosol concentration, size, structure, and chemical composition in the atmosphere is more urgent than ever to fully understand the mechanisms of aerosol cloud interactions and reliably predict the impact on radiative forcing in the future.

3.1 Secondary organic aerosol formation and reactions

The formation of SOA is a result of lowered volatility of VOCs by oxidation in the gas phase. VOCs are distinguished as biogenic VOCs and anthropogenic VOCs. Among the most important biogenic VOCs are isoprene, monoterpenes, or sesquiterpenes, which are naturally and continuously released in forested regions like the Amazon rainforest or the boreal forest. The global biogenic VOC emission is approximately ten times higher than anthropogenic VOC emission, but anthropogenic emissions have more significant local and regional effects (Tsigaridis and Kanakidou 2003; Jenkin 2004; Pöschl 2005). Due to the chemical complexity of the VOC oxidation products the mechanisms of the volatility reduction are hardly elucidated. SOA formation is initiated by the oxidation of VOCs by reactions with OH radicals, NO_3 radicals, ozone, or photolysis (Kroll and Seinfeld 2008; Hallquist et al. 2009; Jimenez et al. 2009). The reaction introduces more polar, oxygenated groups forming for example (poly)-alcohols, carboxylic acids, or aldehydes, with lower vapor pressure than the educts. The addition of a carbon atom to a molecule results in a vapor pressure decrease to 0.35, while the introduction of a hydroxy group results in a reduction to 5.7×10^{-3}, and the addition of a carboxy group to 3.1×10^{-4} (Pankow and Asher 2008). By further oxidation to “second-generation products” volatility is continuously decreased and water solubility increased until ultimately CO_2 would be formed, if sufficient reaction time was given. However, the introduction of polar functional groups also increased reactivity and forces the fragmentation of compounds to highly oxygenated compounds of lower molecular weight (MW) (Hallquist et al. 2009). The aerosol particles are formed in the atmosphere by different mechanisms. New particles can be formed by the reaction of VOCs in the gas phase to semivolatile organic compounds which then participate in the nucleation. Furthermore, semivolatile organic compounds can adsorb to existing particles or aerosols, resulting in the growth of these particles. Non-volatile or low-volatile compounds can be formed at the surface of an aerosol or in an aerosol by heterogeneous or multiphase reactions. Afterwards, the formation of a particle from the gas phase by gas-to-particle transfer is controlled by the nucleation of molecular clusters in the nanometer size, which are growing by coagulation and condensation of more low-volatile OCs. The dominating precursor for atmospheric nucleation is sulfuric acid, but model simulations and field measurements propose a

combination of sulfuric acid with water, ammonia, and small organic compounds (Kulmala et al. 2004; Benson et al. 2011; Bianchi et al. 2016). First experiments observed nucleation events in the absence of sulfuric acid, indicating ion induced or neutral nucleation by organic vapor (Rissanen et al. 2016). Hydroxy radicals are formed in the atmosphere by dissociative recombination of H_3O^+ with water (Harju et al. 2000) and the OH initiated degradation of VOC is the most thoroughly studied reaction pathway besides ozone induced and nitrate induced oxidation (Figure 6).

$$H_3O^+ + e^- \rightarrow OH\cdot + H_2$$

The distribution of products created by the hydroxy pathway is controlled by the alkyl peroxy (RO_2^*) and alkoxy (RO^*) radicals, whose reactions in the atmosphere are influenced by the atmospheric NO_x concentration, the temperature, relative humidity, and the structure of the original VOC. In an atmosphere with high NO_x concentration, the RO_2^* radical is rapidly converted into the RO^* radical, or reacts with NO_2, forming peroxynitrates, or reacts terminative with NO to organic nitrates (Atkinson 2007; Hallquist et al. 2009).

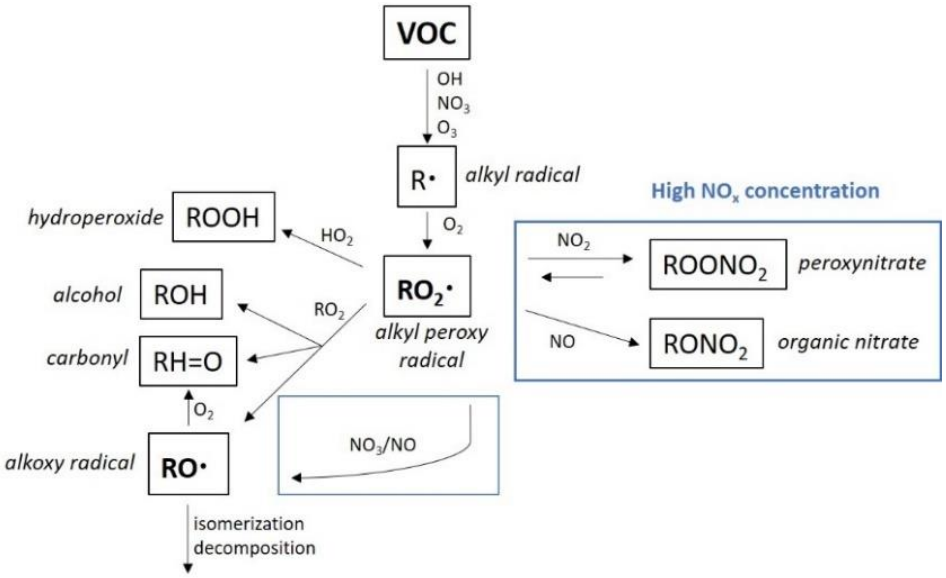

Figure 6: Simplified reaction scheme of the atmospheric oxidation of VOCs initiated by the oxidants OH, NO_3 or O_3. Pathways of the reactions favored by high atmospheric NO_x concentrations are marked in blue.

The RO^* radical in turn reacts with O_2 to carbonyl and HO_2, decomposes by cleavage of a C-C bond, or forms an isomer by the shift of an H-atom to a hydroxycarbonyl (Figure 7). In general, high atmospheric NO_x concentration favors the formation of carbonyls, organic nitrates, peroxynitrates, and hydroxycarbonyls. The atmospheric NO_x concentration is governing not only the dominating reaction pathway for SOA formation, but also the SOA yield. A substantially lower SOA yield was observed for the oxidation of small hydrocarbons ($<C_{10}$), including monoterpenes (Ng et al. 2007a), isoprene (Kroll et al. 2006), and simple aromatics (Ng et al. 2007b), with increasing NO_x-level, while a reversed effect was observable for larger hydrocarbons like sesquiterpenes and alkanes with more than twelve carbon atoms (Lim and Ziemann 2005). Low atmospheric NO_x concentration leads to a competitive reaction of

the RO_2^* radical with HO_2 and the re-combination with other RO_2^* radicals. The reaction with HO_2 is terminating in the formation of hydroxyperoxides, while the combination with other RO_2^* radicals results in the formation of carbonyls, hydroxycarbonyls, and alcohols. Beside the proposed reaction mechanisms, the atmospheric OH radicals can react with many initially present polar functional groups of the VOC, resulting in a highly complex, hardly predictable molecular composition of the final SOA (Hallquist et al. 2009).

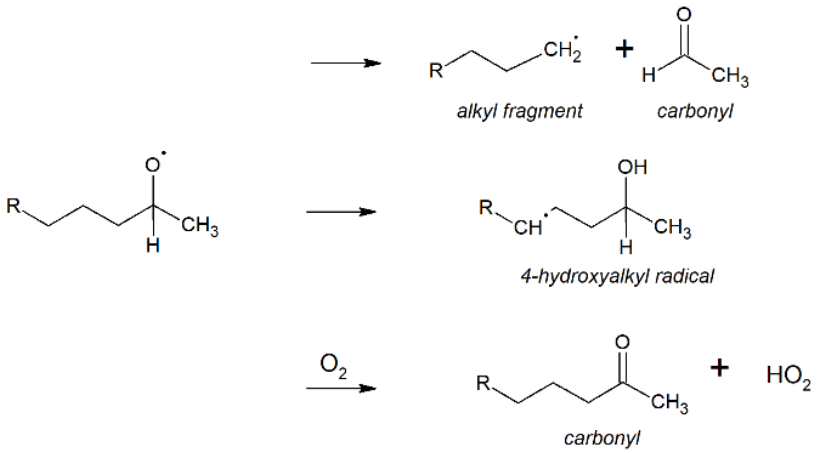

Figure 7: Exemplary atmospheric reactions of the alkoxy radical including decomposition (upper reaction), isomerization (middle), and reaction with O_2 to carbonyl and HO_2 (lower reaction).

The reactions initiated by oxidation of the VOC with NO_3 radicals, ozone, or photolysis tend to follow similar pathways as the OH initiated reactions, since the main reaction products, the RO_2^* radical and the RO^* radical, remain similar. The abundance of OH radicals is much higher during daytime, which is why OH initiated oxidation and ozonolysis of α-pinene was primarily observed during daytime, while NO_3 initiated oxidation was observed under dark conditions (Kristensen et al. 2014). The reaction of unsaturated compounds with ozone follows a different reaction pathway and is proposed to control the atmospheric fate of highly relevant compounds classes like monoterpenes or sesquiterpenes (Atkinson and Arey 2003). The reaction of alkenes with ozone leads to the formation of Criegee intermediates, which in turn react in two different ways (Figure 8). The excited Criegee intermediate in the hydroxyperoxide pathway reacts to OH and an RO^* radical, which in turn follows the proposed OH initiated reaction pathway (Figure 7). A stabilized Criegee intermediate (SCI) can react with water or oxygenated organic species to either a α-hydroxy-hydroperoxide or a secondary ozonide (Johnson and Marston 2008). The rate of the two reactions is strongly controlled by the presence of NO_x (Donahue et al. 2005), the presence of water (Bonn et al. 2002; Jonsson et al. 2006), and the molecular structure of the precursor. The formation of the α-hydroxy-hydroperoxide from linear alkenes is an important SOA constituent (Tobias and Ziemann 2000), while the SCI pathway of cyclic alkenes results in unstable α-hydroxy-hydroperoxides which are rapidly decomposed to compounds of lower volatility (Ziemann 2002). An atmospherically relevant example is the ozonolysis of α- and β-pinene. The initial cleavage of the C-C bond of the cyclic *exo*-alkene structure of β-pinene results in a decrease of the carbon number and a smaller carbon backbone, which outweighs the addition of functional groups in terms of volatility.

For α-pinene, a cyclic *endo*-alkene, the cleavage of the C-C bond allows the addition of multiple functional groups without a smaller carbon number. Therefore, the atmospheric oxidation of α-pinene is dominated by ozonolysis, while more SOA of β-pinene is formed by OH initiated oxidation (Griffin et al. 1999; Bonn and Moortgat 2002; Jenkin 2004).

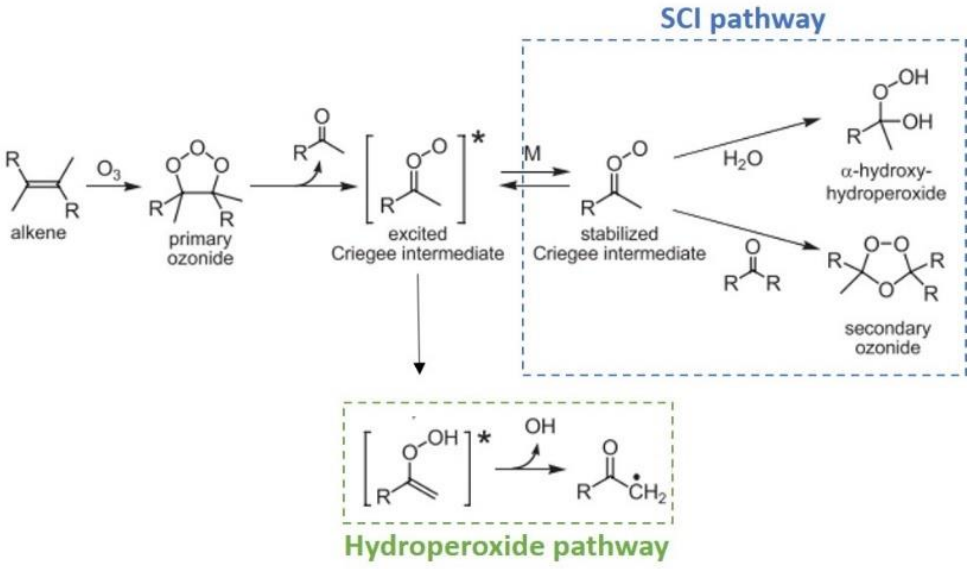

Figure 8: Reaction mechanism of the ozonolysis of alkenes by formation of excited Criegee intermediates which are further stabilized and react by the SCI pathway or react in the hydroperoxide pathway to an alkoxy radical.

Once the volatility of the compounds is decreased, particles are formed by gas-to-particle conversion either by nucleation or by condensation of the compounds on existing particles. However, the formation of a particle does not inhibit further heterogeneous or multiphase reactions of compounds partitioning between the particle and the gas phase. The partitioning equilibrium of each particle is defined by equilibrium partitioning coefficient $K_{p,i}$ ($m^3 \mu g^{-1}$), or the inverse saturation vapor concentration C_i^* ($\mu g\ m^{-3}$), where C_i^p is the mass concentration per unit volume of air in the particulate phase, C_i^g is the mass concentration per unit volume of air in the gas phase, and C_{OA} is the mass concentration per unit volume of air in the total absorbing particle phase (all in µg m^{-3}) (Equation 4) (Pankow 1994; Odum et al. 1996; Donahue et al. 2006).

$$\frac{C_i^p}{C_i^g} = K_{p,i} C_{OA} = \frac{C_{OA}}{C_i^*}$$

Equation 4

Particle phase reactions include oxidative and non-oxidative reactions, depending on the initial and final oxidation state of the carbon atoms. Non-oxidative reactions do not change the carbon oxidation state and are dominated by dimerization and oligomerization, hence growth or "accretion" reactions (Barsanti and Pankow 2004). Thereby, the vapor pressure of a compound is decreased by one order of magnitude with addition of two carbon atoms (Donahue et al. 2006; Pankow and Asher 2008; Kroll and Seinfeld 2008). Oxidative reactions in the particle-phase are initiated similarly to the gas-phase (although the

branching ratios are different) by the oxidants OH, NO_3 or ozone and are referred to as "aerosol ageing", strongly influencing the vapor pressure of the oxidation products and physical properties of the aerosols like hygroscopicity (Rudich et al. 2007). Particle phase reactions and the partitioning equilibrium between particulate and gas phase are strongly influenced by temperature, particle size, surface tension of the particles, and the atmospheric concentration of oxidants like NO_x (Donahue et al. 2006; Müller et al. 2012; Zhao et al. 2019).

Aqueous phase oxidation of organic compounds is proposed as a different formation mechanism of SOA, which occurs in rain, clouds, fogs, or other aqueous aerosols. The oxidation is initiated by the OH radical which was detected in atmospheric water (Anastasio and McGregor 2001; Arakaki et al. 2006) and the formation was proposed by different mechanisms (Equation 5 a-d). The reaction of nitrite with water is dominant in the atmospheric boundary layer which is strongly influenced by anthropogenic emission of nitrous acid (Equation 5a), (Anastasio and McGregor 2001). In the troposphere, OH radicals in the aqueous phase are formed by the reaction of nitrate with water (Equation 5b), (Arakaki et al. 2006), the photo-Fenton reaction (Equation 5c), (Arakaki and Faust 1998), and the photolysis of hydrogen peroxide (Equation 5d). (Arakaki and Faust 1998; Parazols et al. 2007). The reaction products of the OH initiated oxidation of organic compounds in the aqueous phase were dominated by carboxylic acids, although oligomerization was observed as well. After evaporation of the aqueous matrix, the products of the photochemical reactions can react similarly to lower volatile compounds in the gas phase (Hallquist et al. 2009).

$$a)\ NO_2^- + H_2O \xrightarrow{h\nu\ (\lambda<400\ nm)} OH + NO + OH^-$$

$$b)\ NO_3^- + H_2O \xrightarrow{h\nu\ (\lambda<355\ nm)} OH + NO_2 + OH^-$$

$$c)\ FeOH^{2+} \xrightarrow{h\nu\ (\lambda<370\ nm)} OH + Fe^{2+}$$

$$Fe^{2+} + H_2O_2 \rightarrow OH + FeOH^{2+}$$

$$d)\ H_2O_2 \xrightarrow{h\nu\ (\lambda<320\ nm)} 2OH$$

Equation 5

3.2 Chemical composition and important SOA markers

The most abundant precursors for SOA formation in the atmosphere are isoprene and monoterpenes (Seinfeld and Pandis 1998; Atkinson and Arey 2003), which are naturally permanently emitted by vegetation and contribute to the global biogenic VOC (BVOC) budget, which is approximately ten times higher than global anthropogenic VOC emission (Guenther 1995). On regional scales, the anthropogenic emissions exceed the BVOC by up to 50% (Zemankova and Brechler 2010). Large amounts of BVOC in the atmosphere are found in forested regions, like the Amazonian rainforest and the boreal forest. Here the high SOA concentration results in a prominent phenomenon, the "blue haze" in the summertime which is a result of wavelength dependent Rayleigh scattering of light by the SOA particles (Went 1960; Zhang et al. 2009).

The oxidation products of the precursors isoprene and monoterpenes constitute a major fraction of the chemical composition of SOA. The molecular structure of the oxidation products is influenced by various factors like the formation and transformation mechanisms, oxidants (OH radicals, NO_3 radicals, O_3), the atmospheric NO_x concentration, or other atmospheric conditions like humidity or acidity. Therefore, the chemical composition of SOA is highly complex consisting of several hundred individual compounds, solely from biogenic precursors (Schauer et al. 1996; Kroll and Seinfeld 2008; Hallquist et al. 2009).

The photooxidation of isoprene results in a variety of first-generation VOCs. Under high NO_x concentrations, hydroxynitrate derivatives of isoprene are formed, while low NO_x concentrations result in the formation of hydroxy hydroperoxide derivates (Surratt et al. 2006). Further oxidation results in stepwise formation of C_5 alkene triols, methyltetrols, methylglyceric acid, or glyoxal among others (Claeys et al. 2004; Surratt et al. 2006; Carlton et al. 2009). The formation of 2-methyltetrols is described by the formation of epoxydiol intermediates, which are further hydrolyzed under acidic conditions (Figure 9). Glyoxal and methylglyoxal were detected in aerosols (Fu et al. 2008) and ice cores (Müller-Tautges et al. 2016; Pokhrel et al. 2020), while 2-methyltetrols were detected in aerosols from the Amazonian rainforest (Wang et al. 2005a; González et al. 2011, 2014) and proposed as a marker for isoprene oxidation under low NO_x conditions (Surratt et al. 2006). Erythritol as a different reaction product from the ring-opening reaction of the epoxydiol intermediate was analyzed as a potential biomass burning marker in aerosols, but solely contributed to the natural aerosol background, which is why it is used as a surrogate compound for methyltetrols as markers for isoprene photooxidation (Graham et al. 2002; Barbaro et al. 2015).

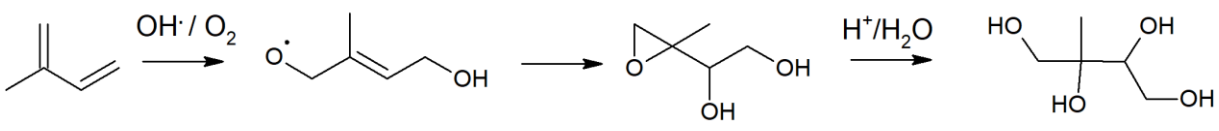

Figure 9: Proposed reaction pathway of the formation of 2.-methyltetrols from OH-radical initiated oxidation of isoprene (Surratt et al. 2006)

The most abundant monoterpenes in the atmosphere are α- and β-pinene. During oxidation induced by OH-radicals or ozone, a series of oxidation products are formd including pinonic acid, pinonaldehyde, formaldehyde, hydroxypinonic acid, pinic acid, or norpinonic acid (Glasius et al. 2000; Jenkin et al. 2000; Larsen et al. 2001). Pinic and pinonic acid are the most abundant carboxylic acids resulting from α- and β-pinene oxidation and were analyzed in aerosols (Zhang et al. 2010; Cheng et al. 2011; Hyder et al. 2012; Leppla et al. 2021; Feltracco et al. 2021) and ice cores (Müller-Tautges et al. 2016; Pokhrel et al. 2020). While the oxidation of the endocyclic α-pinene results in the formation of pinic and pinonic acid the exocylic β-pinene only forms pinic acid (Figure 10). Therefore, pinonic acid can be used to distinguish between α- and β-pinene emissions (Jenkin et al. 2000; Ma et al. 2007; Salvador et al. 2020). These results were similar for OH initiated oxidation and ozonolysis of α- and β-pinene (Glasius et al. 2000; Larsen et al. 2001).

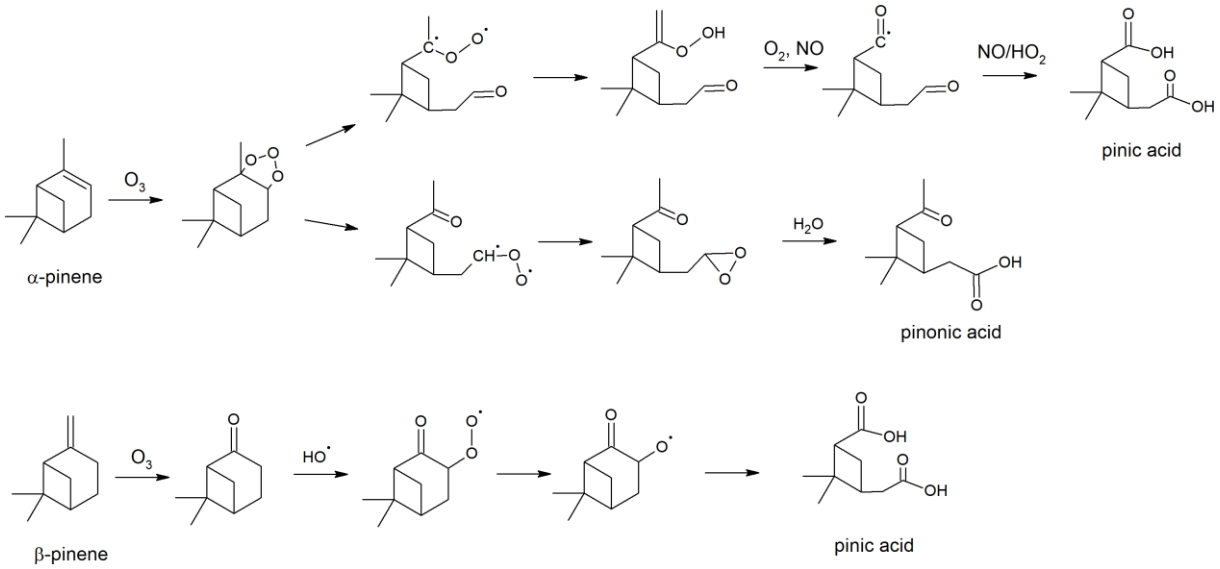

Figure 10: Proposed formation mechanisms of pinic and pinonic acid after ozonolysis of α- and β-pinene (Jenkin et al. 2000; Ma et al. 2007)

Other α- and β-pinene oxidation markers are lactone containing terpenoic acids like terpenylic acid or terebic acid, which is a further processed derivative of terpenylic acid. Both were detected in chamber experiments of pinene oxidation, as well as atmospheric aerosols, and a correlation of terpenylic acid from β-pinene to the atmospheric OH-radical concentration was observed (Kahnt et al. 2014; Sato et al. 2016; Kołodziejczyk et al. 2020; Thomsen et al. 2021). Terpenylic acid is formed after OH-radical initiated oxidation of α-pinene and further oxidation results in the formation of a highly oxidated lactone ring containing structure (Claeys et al. 2009)

Sesquiterpenes ($C_{15}H_{24}$) constitute up to approximately 40% of biogenic monoterpene emission (Tarvainen et al. 2005) and among the sesquiterpenes β-caryophyllene is the most abundant, constituting approximately 60% of the total emissions (Helmig et al. 2006). Due to their high reactivity the atmospheric lifetime of sesquiterpenes is very short and varies between a few minutes to hours (Kesselmeier et al. 2000; Fu et al. 2013). Consequently, their low volatile oxidation products strongly

participate in SOA formation. Models estimate a contribution of β-caryophyllene to the total biogenic VOC emission of 2% but a 12% contribution to the total SOA formation (Andersson-Sköld and Simpson 2001; Vestenius et al. 2014). Chamber experiments of the photooxidation of β-caryophyllene in the presence of NO_x resulted in the formation of β-caryophyllinic acid (Figure 11) and other oxidation products which were detected in pristine and urban atmospheric aerosols (Jaoui et al. 2007; Hu et al. 2008; Parshintsev et al. 2010; Fu et al. 2013; Yee et al. 2018). Aerosol analysis revealed a strong temperature dependence of sesquiterpene emission and a higher abundance of β-caryophyllinic acid at night (Jaoui et al. 2007; Hellén et al. 2018; Yee et al. 2018). Since the availability of analytical standards of sesquiterpene oxidation products is limited, studies synthesized their analytical standards (Parshintsev et al. 2010; van Eijck et al. 2013) or used ketopinic acid as a surrogate compound (Kleindienst et al. 2007), which was also detected in ice core samples (King et al. 2019a).

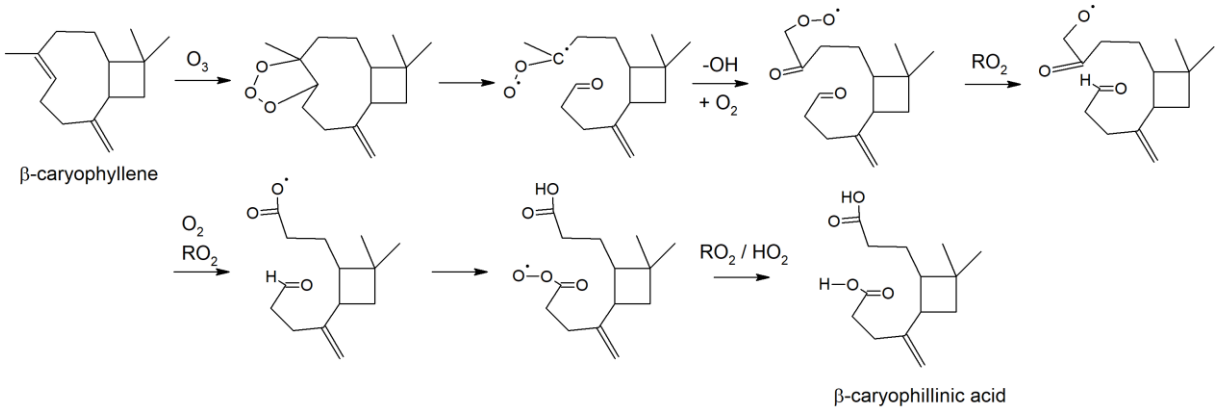

Figure 11: Proposed formation mechanism of β-caryophyllinic acid from β-caryophyllene photooxidation in presence of NO_x (Jaoui et al. 2007)

Oxidative aging alters the chemical composition of SOA and consequently their volatility, CCN properties, and hygroscopicity (Rudich et al. 2007; Shilling et al. 2007; George et al. 2009). Aging occurs on timescales of 5-12 days corresponding to the average atmospheric lifetime of aerosols and is distinguished between three different processes (Robinson et al. 2007; Rudich et al. 2007). Fragmentation would theoretically ultimately lead to the formation of CO_2, while oligomerization results in the formation of high MW compounds (chapter 1.3.2.2), and functionalization introduces additional oxygen containing functional groups to the molecules (Szmigielski et al. 2007; Reinnig et al. 2009). By OH-radical oxidation of pinonic acid, one of the first-generation products of pinene oxidation, 3-methyl-1,2,3-butanetricarboxylic acid (MBTCA) is formed in the gas phase which has a lifetime of approximately ten days (Szmigielski et al. 2007; Müller et al. 2012; Nozière et al. 2015). The degree of oxidative aging is correlated to the atmospheric OH concentration and the temperature (Müller et al. 2012; Sato et al. 2016). MBTCA is a tracer for atmospheric aging of biogenic SOA and was detected in urban (Kourtchev et al. 2014), marine (Fu et al. 2013), and ambient aerosols (Kristensen and Glasius 2011), as well as in ice cores (Fu et al. 2016; Pokhrel et al. 2016; Giorio et al. 2018; King et al. 2019a).

Other SOA sources beside vegetation derived precursors are marine aerosols (Fu et al. 2013), and fungal spores (Bauer et al. 2008; Elbert et al. 2010). Marine aerosols are emitted as primary organic aerosols by mechanical interaction of wind with the sea surface, commonly referred to as sea spray. A marker compound for sea spray in the atmosphere is methanesulfonic acid, as the oxidation product of dimethyl sulfide, which is the main biogenically produced precursor for primary marine aerosols in the ocean (Rinaldi et al. 2010). In addition, VOCs emitted from the oceans also contribute to SOA formation, for example isoprene emitted from phytoplankton or unsaturated fatty acids emitted from marine algae (Meskhidze and Nenes 2006; O'Dowd and de Leeuw 2007; Claeys et al. 2010). Fungi release their spores with liquids into the air and in the Amazonian rainforest these spores constitute a large proportion of the atmospheric particulate matter. Sugar alcohols like mannitol and xylitol are used as marker compounds for fungal contribution to the chemical composition of atmospheric aerosols (Simoneit et al. 2004; Bauer et al. 2008; Elbert et al. 2010).

Finally, the aerosol source whose atmospheric impact increased most significantly during the last decades are anthropogenic emissions. Already in the mid of the 20th century, anthropogenic air pollution was responsible for over a third of the variations of the global-mean annual-mean surface temperature and the effects on the global climate are expected to aggravate due to the influence on the jet streams or monsoons (Wilcox et al. 2013; Das et al. 2020; Wang et al. 2020b; Zhang et al. 2021). Anthropogenic SOA precursors are primarily emitted by biomass burning and fossil fuel combustion, including aromatics and alkenes, which are oxidized in the atmosphere to aromatic or aliphatic carboxylic and dicarboxylic acids (Kawamura and Yasui 2005; Ho et al. 2006; Kundu et al. 2010). Analysis of dicarboxylic acids in aerosols (Kawamura and Yasui 2005; van Pinxteren and Herrmann 2007; Hu et al. 2008; Zhang et al. 2010; Hyder et al. 2012; Fu et al. 2013) and ice cores (Kawamura et al. 2001; Müller-Tautges et al. 2016) revealed a stronger abundance in winter than in summer, associated with increased anthropogenic heating activities, and poor correlation with biogenic SOA markers like pinic and pinonic acid (Zhang et al. 2010; Hyder et al. 2012). Phthalic acid is a product of biomass burning, fossil fuel combustion, photooxidation of polycyclic aromatic hydrocarbons (PAH), and aging of plastics, where industrially used plasticizers like phthalate and phthalate esters are hydrolyzed (Thurén and Larsson 1990; Shiraiwa et al. 2009).

3.2.1 Biomass burning markers

Biomass burning records are an important tool to assess the impact of burning events on the ecology on a regional and global scale. They change the primary productivity of the vegetation, reduce biodiversity (Power et al. 2008) and release atmospheric aerosols, which in turn have direct and indirect effects in the atmosphere (chapter 1.3). Biomass burning was responsible for approximately 65% of the variability in enhanced carbon dioxide emissions between 1997 and 2001 and produces up to 50% more carbon dioxide than fossil fuel burning (Bowman et al. 2009). Besides greenhouse gases like carbon dioxide,

VOCs are emitted, as well as particulate matter comprising black carbon and brown carbon (Van Der Werf et al. 2010; Bhattarai et al. 2019).

Wooden material is primarily involved in biomass burning and the main constituents of wood are cellulose and lignin (approximately 30%) with a moisture between 20-30% (Core et al. 1984; Simoneit 2002). During combustion, primary aerosol particles are released with adsorbed organic compounds which are further altered and transformed in the atmosphere. The initial chemical composition of burning-derived SOA precursors and adsorbed compounds on primary aerosol depends on the burned material, the heat intensity, the aeration, and the duration of the fire event. Because of that, the analysis of the chemical composition of aerosols associated with biomass burning provides a chemical fingerprint on the burning event which can be reconstructed from climate archives like ice cores (Simoneit 2002; Bhattarai et al. 2019).

An unequivocal tracer for cellulose combustion at degrees higher than 300°C is levoglucosan (1,6-anhydro-β-glucopyranose, Lev), which has been studied as a biomass burning marker in aerosols (Gao et al. 2003; Barbaro et al. 2015; Zangrando et al. 2016; Schreuder et al. 2018), sediments (Elias et al. 2001; Simoneit et al. 2004; Kirchgeorg et al. 2014), and ice cores (Legrand et al. 2007; Kawamura et al. 2012; Kehrwald et al. 2012; Yao et al. 2013; Pokhrel et al. 2020). It is recognized as the most suitable biomass burning marker due to its long atmospheric lifetime, stability, and high abundance (Simoneit 2002; Hoffmann et al. 2010; Bhattarai et al. 2019). While the connection between atmospheric Lev and biomass burning of cellulose is well known, the detailed degradation mechanism of cellulose remains elusive. Studies suggested four possible mechanisms, including glucose intermediate mechanism (Figure 12a), free-radical mechanism (Figure 12b), ionic mechanism (Figure 12c), and Lev chain-end mechanism (Figure 12c). The calculation of the activation energy, Gibbs free energy, and enthalpy of every reaction mechanism indicated the Lev chain-end mechanism as thermodynamically favored and in best agreement with experimental data (Scheirs et al. 2001; Choi et al. 2011; Zhang et al. 2013). This reaction consists of two transglycosylation steps. During the first transglycosylation, the cellulose chain is depolymerized into an intermediate with a terminal Lev moiety and a short cellulose residue. In the second transglycosylation, the terminal Lev is detached from the cellulose chain, and another Lev-end intermediate is formed (Zhang et al. 2013).

Besides the distinct association of Lev to cellulose pyrolysis, another advantage of Lev as a biomass burning marker is the determination of smoke sources by the relation of Lev to galactosan (1,6-anhydro-β-galactopyranose, Gal) and mannosan (1,6-anhydro-β-mannopyranose, Man). Gal and Man are formed by the combustion of hemicellulose, which is a biopolymer of variable composition, constituting approximately 20-30% of the dry weight of wood (Pettersen 1984). The variable hemicellulose composition is represented by emission factors of Lev to Man (L/M) and Lev to the sum of Man and Gal (L/M+G), which were experimentally determined for different species of wood, lignite, or grasses, allowing association of the biomass burning markers to a biomass burning event (Fabbri et al. 2009).

Lignin consists of three aromatic alcohols with varying proportions in different plant classes: *p*-coumaryl alcohol, coniferyl alcohol, and sinapyl alcohol. During combustion, oxidized degradation products of the monomers are formed (ketones, aldehydes, carboxylic acids), which have been analyzed in aerosols (Simoneit et al. 1993) and ice cores (Kawamura et al. 2012; Pokhrel et al. 2020). Coniferyl-type lignin is highly abundant in softwood species (gymnosperms), while sinapyl-type lignin is more abundant in hardwood and flowering plant species (Simoneit et al. 1993; Jex et al. 2014). Therefore, the lignin burning products constitute a more vegetation specific biomass burning marker than Lev when their relative proportions are analyzed. After the biomass burning markers are emitted into the atmosphere, they are transported with the aerosols through atmospheric convection and deposited by wet or dry deposition on snow and ice sheets where they are preserved without much further degradation (Kehrwald et al. 2012; Zennaro et al. 2014).

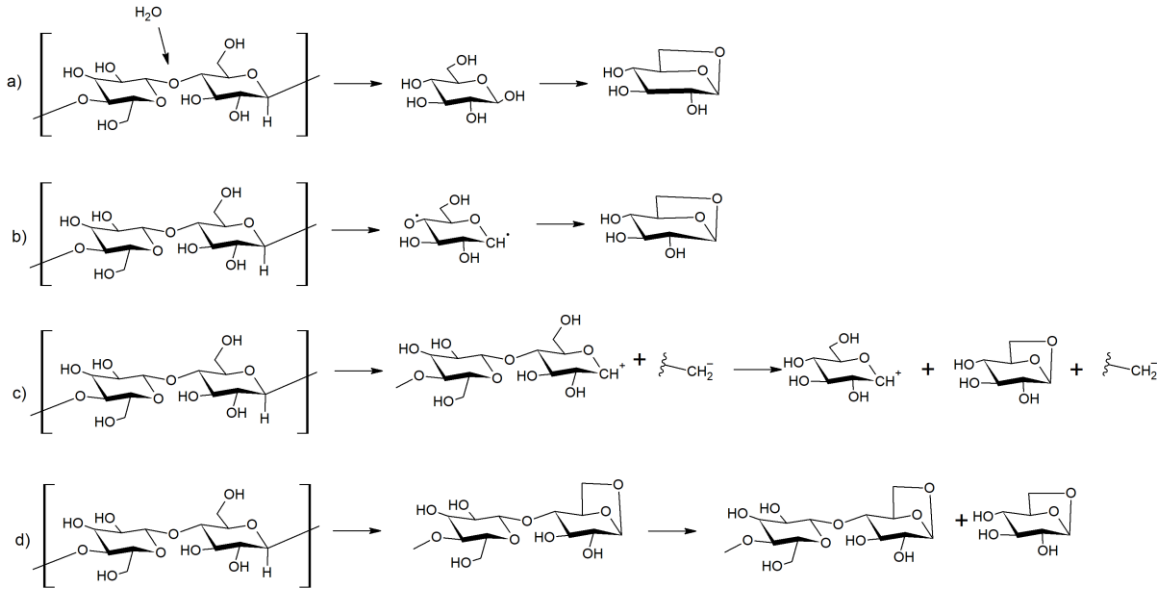

Figure 12: Proposed mechanisms for cellulose degradation during combustion at temperatures >300°C. a) Glucose intermediate mechanism, b) free-radical mechanism, c) ionic mechanism, d) levoglucosan chain-end mechanism (Zhang et al. 2013)

3.2.2 Dimers

The oligomerization of the oxidized VOCs is an important part of aerosol formation and aerosol growth. High MW compounds constitute approximately 50% of the non-volatile SOA mass (Hall IV and Johnston 2011) and are therefore thoroughly investigated. The formation of non-covalently and covalently bound dimers is described by different mechanisms with different monomeric precursors, resulting in high chemical complexity and an unpredictable nature of the oligomeric SOA content. Proposed reactions in the particle phase are the combination of hydroperoxides with aldehydes to peroxyhemiacetals (Tobias and Ziemann 2000), alcohols with aldehydes to hemiacetals (Zhao et al. 2006), aldol addition of two carbonyls (Garland et al. 2006; Casale et al. 2007), esterification of a carboxylic acid with an alcohol (Yasmeen et al. 2010), sulfuric acid with an alcohol to organosulfates

(Iinuma et al. 2007b), or the combination of a SCI with an alcohol to a SCI adduct (Zahardis and Petrucci 2007).

The first product associated with dimerization was detected in SOA produced from α-pinene oxidation with O_3 with a MW of 358, which was tentatively assigned to a non-covalent adduct of *cis*-pinic acid and *cis*-pinonic acid (Hoffmann et al. 1998). A non-covalent bond did not explain the stability of this product in an analysis by LC-MS and therefore further studies described the MW 358 dimer as a product a dehydration reaction between the gem-diols of two norpinonic acid molecules (Gao et al. 2004), the product of esterification of *cis*-pinic acid and hydroxyl-containing terpenoic acid (Müller et al. 2008), or the product of *cis*-pinic acid with a hydroperoxyhemiacetal (Müller, L.; Reinnig, M.; Hayen, H.; Hoffman 2009). Dimerization is one of the non-oxidative reactions in the condensed phase of the aerosols and the resulting MW 358 dimer was assigned to later-generation products from esterification of terpenylic acid or diaterpenylic acid with *cis*-pinic acid, hence generally referred to as a pinyl-diaterpenyl dimer. It was detected in chamber experiments as well as field studies (Yasmeen et al. 2010; Kristensen et al. 2013, 2016). Different chemical structures were proposed containing different number of carboxylic acid and peroxide moieties (Müller, L.; Reinnig, M.; Hayen, H.; Hoffman 2009; Yasmeen et al. 2010). Derivatization of the carboxylic acids followed by detailed molecular elucidation with MS^n-experiments confirmed a structure with three carboxylic acid functionalities (Figure 13) (Yasmeen et al. 2010; Beck and Hoffmann 2016).

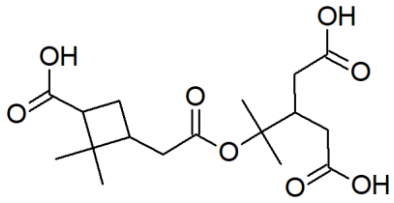

Figure 13: Proposed molecular structure of the pinyl-diaterpenyl dimer (MW 358) from α-pinene oxidation (Yasmeen et al. 2010; Beck and Hoffmann 2016)

The formation of dimer esters as late-generation products in the condensed phase contradicted with chamber experiments where dimer formation was observed simultaneously to their monomeric precursors at both high and low temperatures (Kristensen et al. 2013), and with kinetic studies indicating a thermodynamically unfavored esterification in the particle phase (Heaton et al. 2007; Depalma et al. 2013). Therefore, another formation mechanism was proposed based on gas-phase reactions of SCI from α-pinene ozonolysis rather than esterification in the particle phase (Kristensen et al. 2014). This was supported by chamber experiments, where dimers were only observed in SOA produced by α-pinene ozonolysis in the absence of NO_x, and not in SOA produced by OH initiated oxidation. The formation of dimers in the gas-phase as a result of α-pinene ozonolysis also provides a straightforward explanation for diurnal variations of dimer concentration in field and chamber studies (Yasmeen et al. 2010; Kristensen et al. 2013, 2020; Bell et al. 2021). Because the concentration of OH radicals is much lower during night-time, an O_3 initiated oxidation of α-pinene is favored.

Although the pinyl-diaterpenyl dimer is the most thoroughly studied compound, the chemical composition of dimers is highly complex due to the complexity of the first-generation products from VOC oxidation and the different proposed formation mechanisms. Thirty individual dimers with different O/C ratios were detected in chamber experiments from α-pinene ozonolysis, which is the most abundant, but by far not the only atmospheric precursor for dimerization. A temperature dependency of the degree of oxidation of the dimers was observed, with less highly oxygenated dimers at lower temperature. This indicated a formation of dimers in the gas-phase, as highly oxygenated carboxylic acids are readily removed from the gas phase due to their low volatility (Kristensen et al. 2020). First studies confirmed a heterogeneous oxidative dimer formation, dominated by esters, peroxides, and ethers, on the gas-particle interface. Here, the reactive OH radicals are proposed to be accumulated on the particle surface and initiate oxidative reactions in the particles to form peroxy and alkoxy radicals, which in turn undergo cross combination reactions. This process was primarily observed during aerosol ageing, as the reaction was favored by the presence of many highly oxygenated carboxylic acids (Zhao et al. 2019). In addition, oligomerization of small α-dicarbonyl compounds in the aerosol particle phase was observed also contributing to the highly complex dynamics of dimer formation in SOA.

The influence of dimers on the physical properties and lifetime of SOA are elusive and the unknown reversibility of dimerization is an unidentified factor influencing the prediction of SOA budget, as irreversible dimerization would result in a much higher SOA load than expected (Tsigaridis and Kanakidou 2003). First studies on the fate of dimers showed that after condensation in the particle phase approximately 60-70% undergo further oxidation, 10-20% undergo fragmentation, and only 10-15% decay into monomers (Bell et al. 2021), which is why suspect-target screening (STS) of dimer mass traces in ice cores will be valuable to further study the chemical composition of dimers and their atmospheric lifetime.

3.2.3 Organosulfates

Organosulfates are products of aerosol ageing from isoprene and monoterpene SOA compounds, like α- and β-pinene, which are highly abundant atmospheric VOC emitted by terrestrial vegetation (Hallquist et al. 2009). Sulfur-containing products of VOC oxidation in the atmosphere are ubiquitously found in SOA particles and these organosulfates constitute approximately 5-30% of the total aerosol mass (Surratt et al. 2008; Brüggemann et al. 2020). They are formed in the condensed phase of acidic sulfate seed aerosols after photooxidation of the precursors initiated by OH radicals in the presence of atmospheric NO_x (Surratt et al. 2008), or after NO_3 initiated oxidation in dark conditions (Iinuma et al. 2007a; Surratt et al. 2007; Ng et al. 2008). One formation pathway is esterification of sulfuric acid with hydroxyl groups or keto groups after gem-diol formation of the oxidated precursors (Liggio and Li 2006; Iinuma et al. 2007a; Surratt et al. 2007). Sulfuric acids in the atmosphere are a result of anthropogenic emissions and because of that organosulfates originate from a mixture of biogenic and anthropogenic emissions (Zhang et al. 2009). While monoterpene derived organosulfates have an amphiphilic, surface-

active character, the high polarity of isoprene derived organosulfates is proposed to enhance the CCN properties of aerosols by lowering surface tension (Hallquist et al. 2009; Hansen et al. 2015). Other possible formation mechanisms are the direct reaction of unsaturated hydrocarbons with SO_2 in the gas phase (Shang et al. 2016), perhydrolysis of organic hydroperoxides in the gas phase with subsequent reaction with sulfate ions (Riva et al. 2016), and radical reactions by photochemical formation of sulfate radicals in wet aerosols, which is the only reaction that does not require the presence of acidic seed aerosols (Nozière et al. 2010; Schindelka et al. 2013). The esterification of alcohols and sulfates is not feasible under atmospheric conditions (Minerath et al. 2008), which is why recent research suggests a reactive uptake of epoxides and organic nitrates from the gas phase to the acidic aerosol particle phase (Iinuma et al. 2007b; Darer et al. 2011; Kristensen and Glasius 2011; Brüggemann et al. 2017). The exemplary conversion of isoprene to organosulfates starts in the gas phase by nitration of isoprene at high NO_x levels, or tertiary epoxide formation at low NO_x levels. After uptake into the particle phase, the organonitrates can be hydrolyzed to polyols, or substituted by nucleophilic sulfate ions to an organosulfate. Similarly, the epoxides either undergo a ring-opening reaction with water to form polyols, or with sulfate ions to form organosulfates (Darer et al. 2011; Brüggemann et al. 2020). The acid catalyzed ring-opening reaction in the particle phase is feasible under atmospheric conditions (Minerath and Elrod 2009; Cole-Filipiak et al. 2010) and was observed in α-pinene and isoprene derived SOA in the presence of sulfate seed aerosol at different NO_x concentrations in chamber experiments and ambient aerosols (Surratt et al. 2008; Kristensen and Glasius 2011; Brüggemann et al. 2017). Field studies revealed high complexity of organosulfates in aerosols and the difficulties of quantitative determination, due to the lack of analytical standards. Camphorsulfonic acid was used as a surrogate for semi-quantitative analysis of organosulfates (Iinuma et al. 2007b; Kristensen and Glasius 2011). Thorough chamber experiments were conducted to elucidate the chemical structure of isoprene- and monoterpene derived organosulfates under different simulated atmospheric conditions (NO_x concentration, aerosol acidity, oxidant concentration and relative humidity) and resulted in a variety of products which were retroactively screened in filter samples of ambient aerosols. Several molecular structures were proposed based on the fragmentation behavior of the compounds in MS^n studies (Surratt et al. 2008) and demonstrated the high variability due to the chemical complexity of first-generation oxidation products of the isoprene and monoterpene precursors (Table 1).

Table 1: Precursor compounds and respectively one proposed organosulfate structure with the experimental reaction conditions.

Precursor compound	**Proposed isomeric organosulfate structure**	**Reaction conditions**
α-/β-pinene 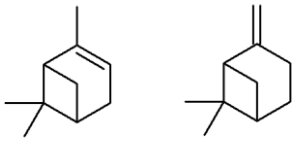	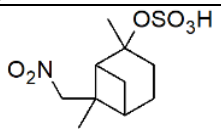 MW 295	- Photooxidation in presence of NO_x - NO_3 initiated nighttime oxidation
	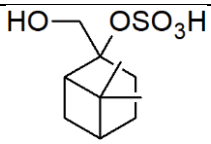 MW 250	OH-initiated oxidation
10-hydroxypinonic acid (Larsen et al. 2001) 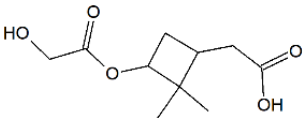	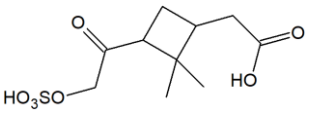 MW 280	OH-initiated α-pinene oxidation
2-hydroxyglutaric acid (Claeys et al. 2007) 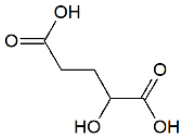	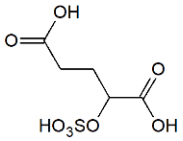 MW 228	Photooxidation of α-pinene in presence of NO_x
2-methyltetrol 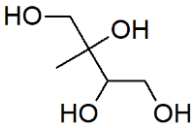	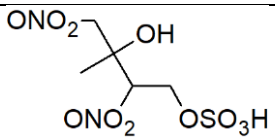 MW 306	- Photooxidation of isoprene in presence of NO_x - NO_3 initiated nighttime oxidation
2-methyl-1,2,3-butanetriol 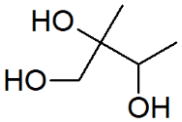	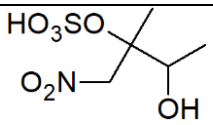 MW 245	Photooxidation of isoprene in presence of NO_x
Limonene 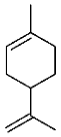	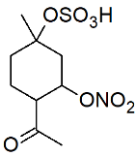 MW 297	Photooxidation in presence of NO_x

4. Analytical methods

The analytical workflow of this thesis consists of several sample preparation steps, including solid-phase extraction (SPE) and centrifugal evaporation. Afterwards, the samples are measured by an ultra-high pressure liquid chromatography (UHPLC) instrument coupled to a high-resolution mass spectrometer (HR-MS). Data evaluation was conducted as either targeted analysis, suspect target screening (STS), or non-target screening (NTS).

4.1 Sample preparation

Trace analysis of organic compounds requires analytical sample preparation methods with sufficient sample recovery and repeatability. As both ice core samples and speleothem samples are transferred to liquid form, either by melting or dissolving, SPE and centrifugal evaporation are used as the main sample preparation methods.

4.1.1 Solid-phase extraction

SPE is a widely used sample preparation method for trace analysis. A polypropylene or glass cartridge is densely packed with a sorbent between two frits. The three main aims of SPE are sample enrichment, sample clean up (or rather removal of matrix compounds), or medium exchange, for example from an aqueous matrix to an organic solvent. The solid phase is silica- or polymer based. Silica based solid phases offer either polar or non-polar surfaces with functionalized silanol groups, mostly with non-polar alkyl chains like octyl- or octadecyl- chains. To prevent unwanted ion exchange mechanisms, free silanol groups can be endcapped. A disadvantage of silica-based sorbents is the risk of dried out sorbent and therefore unrecoverable sample (Poole 2003). Other sorbents are based on porous polymers, mostly co-polymers of styrene and divinylbenzene. These sorbents offer larger surface areas and better retention. A special case is the macroporous poly(divinylbenzene-co-N-vinylpyrrolidone) polymer, also referred to as hydrophilic-lipophilic-balanced (HLB). This material offers larger, fully wettable surface of 800 m^2/g, and full sample recovery even if the sorbent runs dry (Camel 2003; Poole 2003).

A typical SPE workflow consists of at least two steps: loading the cartridge with the sample solution and eluting the analytes of interest with the right solvent (Figure 14). Depending on the sorbent material, a conditioning step is included to activate the functional groups, like straightening C_{18}-alkyl chains or ionizing a basic or acidic functional group. The flow of the sample solution can be supported by applying a vacuum manifold, yet the drip rate should remain slow and constant to ensure sufficient interaction of the analytes with the functional groups on the surface of the solid phase. If the sample is constituted of a complex matrix, an additional washing step is included to remove retained matrix compounds from the solid phase. Thereby the washing solution should not elute the analytes of interest. Analytes are eluted using a proper solvent. Either the solubility of analytes in the solvent is stronger than the affinity to the solid phase which is the common case for HLB or C_{18} material, or the ions from the solvent have

a higher affinity to the solid phase than the analytes, replacing the analytes at the active sites of the solid material, which applies for ion-exchange materials. The elution solvent should be applied in many small portions, to ensure complete coverage of the sorbent. Yet, the volume of the elution solvent is much lower than the initial sample volume, resulting in strong sample enrichment (Camel 2003; Poole 2003).

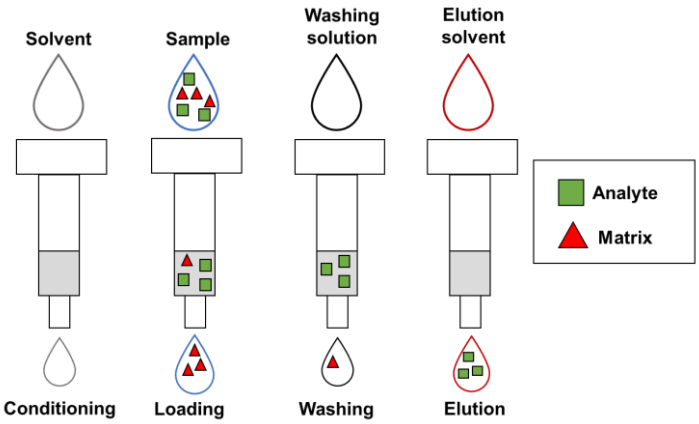

Figure 14: General SPE workflow including conditioning of the cartridge, loading of the sample, a washing step and elution of analytes.

Many different materials of solid phases are known and thoroughly reviewed (Camel 2003; Poole 2003), therefore only a short overview on the materials used in this work, HLB and weak anion-exchange (WAX) material (Figure 15) is provided.

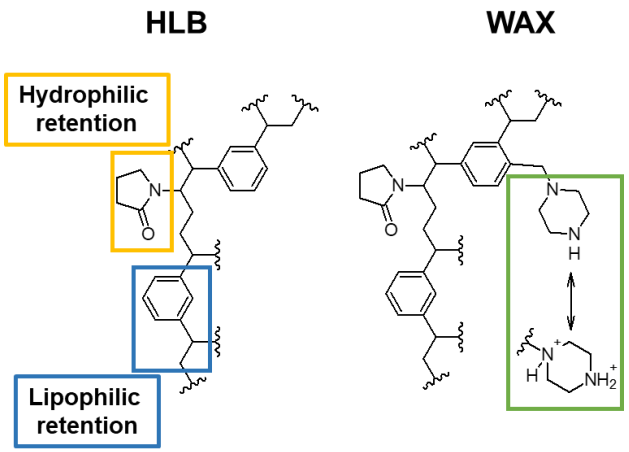

Figure 15: Chemical structures of HLB and WAX material, the parts for hydrophilic (yellow) and lipophilic (blue) retention in HLB are marked, as well as the ionizable group (green) in the WAX material (adapted from Waters GmbH)

Both materials, HLB and WAX are used for enrichment of analytes from a polar (aqueous) matrix. HLB material offers retention for a broad range of non-polar to moderately polar analytes by providing hydrophilic and lipophilic moieties and is therefore a material of low specificity. On the other hand, WAX material is class specific for acids and anions. Retention is based on interaction with the negatively charged functional groups of the analytes and the positively charged functionality of the solid phase. In

contrast to strong anion exchange material (SAX), the positive charge is not permanent but set by the pH-value of the solvent during the conditioning step. Due to that, it is crucial to set a proper pH-value to the sample solution to ensure a constant positive charge on the solid phase. Elution is provided by a slightly alkaline solution, deprotonating the functional groups, and thereby disrupting the ionic interactions.

With these methods the extraction of two different classes of analytes from an aqueous solution is covered: non-polar to moderately polar compounds, and ionic or ionizable compounds. Yet, the extraction of neutral, highly polar compounds is hardly accessible by SPE. Novel materials like graphitized carbon black (GCB) (Hennion 2000) or hydrophilic interaction liquid chromatography (HILIC) (Murakami et al. 2020) materials aim sufficient sample recovery. Another possible method for enrichment of highly polar compounds is evaporation of the aqueous matrix by centrifugal evaporation.

4.1.2 Centrifugal evaporation

When sufficient sample recovery cannot be obtained by extraction via SPE or liquid-liquid extraction (LLE), other approaches intend the elimination of the solvent rather than the extraction of analytes (Toth et al. 2018). For that, nitrogen blowdown or rotary evaporation are used. Nitrogen blowdown is very labor-intensive, prone to cross-contamination, and, due to the manual operation, repeatability is insufficient for large sample volumes, especially working with aqueous samples. Rotary evaporation is limited by the number of simultaneously prepared samples and the recovery from the flask. Another approach is evaporation of solvent with a centrifugal evaporator, invented in the 1960s by Savant Inc of USA as the SpeedVac brand.

Samples are dried in a centrifugal evaporator by converting a liquid into vapor using centrifugal force, heat, and vacuum. The transfer of liquid to vapor depends on the boiling point, which is defined as the point where vapor pressure equals atmospheric pressure, and which in turn depends on temperature and pressure (Figure 16).

To be evaporated from a solution, a water molecule must overcome intermolecular interactions in the solution, as well as surface tension and the pressure above the surface. With smaller atmospheric pressure, the barrier between liquid and gaseous phase is lower and evaporation is enhanced. As shown in the phase diagram, lower pressure at constant temperature shifts the phase equilibrium towards the gaseous phase. Consequently, evaporation of an aqueous sample is enabled at moderate temperatures with no harm of thermally degrading the samples.

Simply applying a vacuum to an aqueous solution can result in boiling retardation of the sample and hence cross contamination in the vacuum chamber. Therefore, evaporation is conducted in a centrifuge, consisting of a vacuum pump, centrifuge chamber, rotor, and a cold trap (or solvent condenser). An object revolving in a circle is objected to a force away from the center, the centrifugal force, which depends on the angular velocity, the radius of the circle, and the mass of an object. The rotational speed

is defined as revolutions per minute and the resulting force on the particles as relative centrifugal force in multiple of gravitational force (x g). In a liquid sample, denser particles are moved outwards of the radial direction, while substances with lower density are moved towards the center of rotation. Thereby a pressure gradient is built and the vacuum initiates boiling of the sample from the top to the bottom of the sample tube, preventing boiling retardation of the sample (Graham and Rickwood 2002; Gutiérrez et al. 2010).

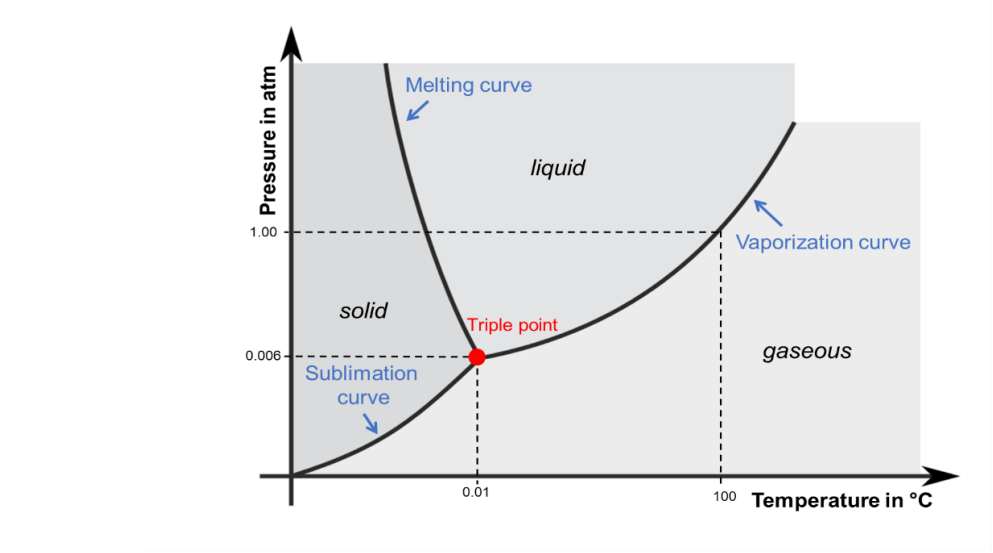

Figure 16: Phase diagram of water (adapted from Lide, 2011).

4.2 High pressure liquid chromatography

Chromatography is a separation method used for analytical or preparative purposes. The separation mechanism is based on interactions of compounds with a stationary (liquid or solid) and a mobile phase (liquid or gaseous). In liquid chromatography (LC), the solid stationary phase is mounted on spherical, porous microparticles densely packed into a column and the liquid mobile phase is passed through the column with high pressure. In gas chromatography (GC) the stationary phase is coated on the outer wall of the column either solid or as a thin film, and the mobile phase is gaseous. An HPLC setup generally consists of two solvent reservoirs, a degasser, a pump with an eluent mixing chamber, a pressure gauge, an injector, a column oven containing the column, and is coupled to suitable detector (Figure 17).

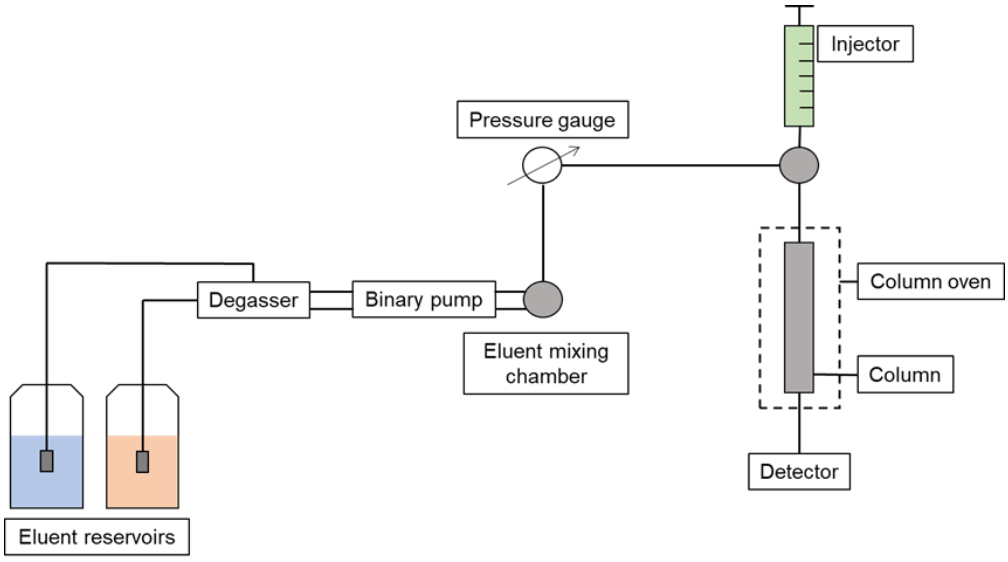

Figure 17: Schematic setup of an HPLC system including eluent reservoirs of two different eluents, a degasser, the binary pump, mixing chamber and pressure gauge. Sample solution is introduced to the system by the injector and carried through the column in the column oven to the detector (mostly UV/Vis or MS).

Usually, a mass spectrometer or an UV-detector is coupled to an HPLC-system and provides detection of ions or absorbed light to obtain a chromatogram with ideally one signal per analyte at an analyte specific retention time. The distance between two signals, or peaks, of analyte A and B in a chromatogram is defined as chromatographic resolution (R) and considered baseline separated at R>1 (Equation 6).

$$R = \frac{t_R(B) - t_R(A)}{\frac{1}{2}(w_{base}(B) + w_{base}(A))}$$

R = resolution

t_R(B) = retention time analyte B

t_R(A) = retention time analyte A

w_{base}(B) = baseline width analyte B

w_{base}(A) = baseline width analyte A

Equation 6

The effectivity of a chromatographic system is defined by the height equivalent to a theoretical plate (HETP), theoretically dividing a column in plates that each equal one interaction of an analyte between mobile and stationary phase. With increasing numbers of equilibriums (and consequently smaller HETP on a defined length), the retention time increases and becomes more analyte specific, so the resolving power of the chromatographic system is enhanced. Since an equilibrium is disrupted by the constant flow rate, efficiency of the system depends on an optimum of flow rate and HETP, defined by the van Deemter equation (Equation 7) (Synder and Kirkland 1979).

$$HETP = A + \frac{B}{v} + C \cdot v$$

HETP = height equivalent to a theoretical plate

A = Eddy-diffusion

B = longitudinal diffusion

C = mass transfer

v = linear velocity (mm/s)

Equation 7

Eddy diffusion (Term A) describes the influence of different pathways of analytes passing the microparticles in the packed column on signal broadening. The longitudinal diffusion in term B describes the diffusion of analytes along and against the flow direction. Term C describes the mass transfer, which is disturbed by the flow of the mobile phase. The combination of the three terms results in an optimal flow rate where HETP is at its minimum (Synder and Kirkland 1979). This optimum is very narrow for large particle sizes and increases with decreasing particle sizes (Figure 18). Therefore, newer HPLC columns are packed with smaller particles and can be operated at higher flow rates, reducing time of analysis. Thereby also the back pressure in the column is strongly increased and HPLC systems employed with these columns must resist pressures up to 1000 bar therefore being referred to as ultra-high pressure liquid chromatography (UHPLC) (Swartz 2005; Nováková et al. 2006).

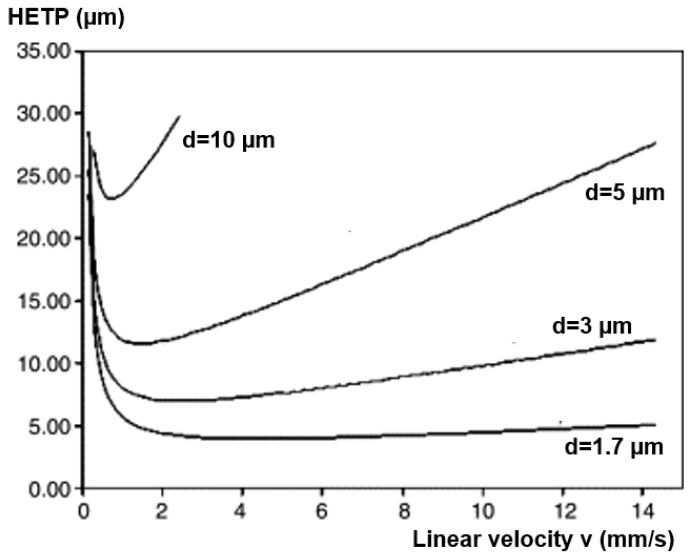

Figure 18: Development of the HETP as a function of linear velocity (mm/s) of the flow for different particle diameters (d) (adapted from Nováková et al., 2006)

Based on the chemical properties of the stationary phase and the mobile phase, HPLC is generally subdivided in three different categories: reversed-phase (RP), normal-phase (NP), and HILIC. The RP stationary phases consist of chemically modified silica gel, where free hydroxyl-groups on the surface are modified with non-polar alkyl-chains to provide interaction with non-polar compounds. The most common phases are n-octyl (C8), or n-octadecyl (C18) phases. In this work, a pentafluorophenyl (PFP) column was used, where additional phenylic moieties provide more selective retention for aromatic compounds due to π-π-interactions. Solvents used in RP-LC are inversely polar to the stationary phase, like water, methanol (MeOH), or acetonitrile (ACN) with increasing elution power from water to ACN. The stationary phase in NP-LC consists of raw silica gel with a hydrophilic surface, while the mobile phase is a non-polar solvent like hexane or dichloromethane (DCM). Due to the polar stationary phase, NP-LC is used for the separation of polar analytes, but the non-polar aprotic solvents disable the coupling of NP-LC to an electrospray ionization (ESI)-MS system (see chapter 4.3.1), hence strongly limiting the usage of this method (Figure 19) (Meyer 2010).

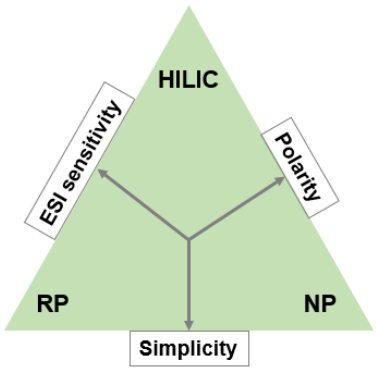

Figure 19: Schematic overview of characteristics and advantages of the three chromatographic methods RP-, NP- and HILIC chromatography

4.2.1 Hydrophilic interaction liquid chromatography

A novel approach for the separation of small polar analytes is HILIC. In contrast to ion chromatography, HILIC can be used for charged and uncharged polar species and combines the properties of the stationary phase from NP-LC and the mobile phase from RP-LC, consequently providing separation of polar analytes and coupling to ESI-MS. A large variety of stationary phases is available, all based on underivatized or aminopropyl-bonded silica. The chemical modifications range from diol-bonded or cyano-bonded phases over mixed-mode and polymeric structures to zwitterionic (Figure 20) and ionic phases. Thorough reviews on the stationary phases are available in the literature (Hemström and Irgum 2006; Buszewski and Noga 2012). The mobile phase consists of a water-miscible polar organic solvent (mostly acetonitrile) and a small portion of water, resulting in the formation of a thin water layer on the surface of the silica particles and a bulk organic layer (Figure 20).

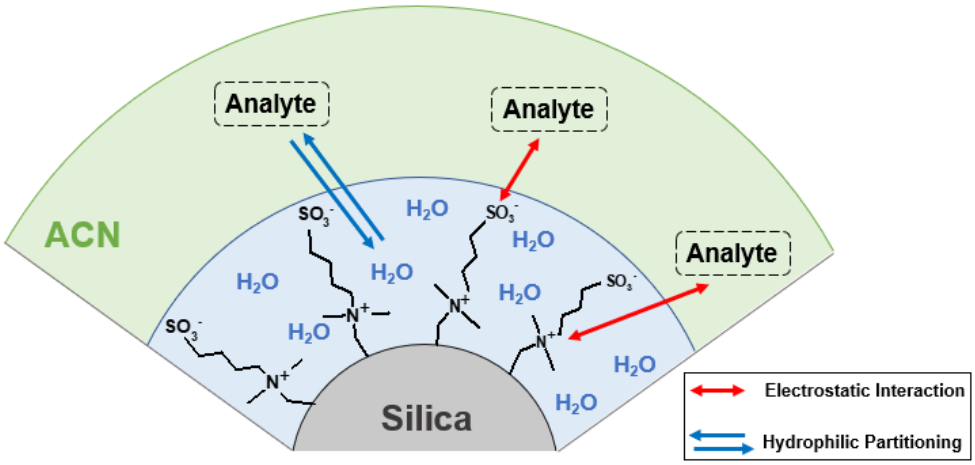

Figure 20: Simplified overview of HILIC retention mechanisms on a zwitterionic stationary phase (adapted from Jiang et al., 2011)

Proper formation of the water layer is essential for separation and strongly depends on the proportion of water and ACN. At least 3% (v/v) of water are necessary, while the proportion of water should not exceed 20% (v/v), as this constitutes the maximum excess adsorption of water to the surface of the modified silica particles (McCalley and Neue 2008). In general, water adsorption is higher with decreasing water content in the mobile phase. Increasing the water content in the mobile phase decreases retention of polar analytes and changing the pH-value of the mobile phase with a buffer or adding mobile phase additives, like ammonium acetate or ammonium bicarbonate, influences the separation in HILIC in three different possible ways. The first mechanism is analyte partitioning between the mobile organic phase and the immobilized aqueous stationary phase, which is based on the partitioning equilibrium and in turn on the hydrophilicity of each analyte. According to this, analytes are generally separated by their polarity. The equilibrium can be influenced by the buffer pH-value of the mobile phase as it has an impact on the charge state of analytes and consequently the hydrophilicity and affinity towards the aqueous phase (Alpert 1990; Hao et al. 2008; Karatapanis et al. 2010). The second mechanism is adsorption of the analyte onto the surface of the adsorbent on the silica particles. Thereby, also electrostatic interactions play a role, if the stationary phase is modified with a permanently charged or chargeable functional group. This process is influenced by the pH-value of the mobile phase as it changes the charge state of either the analyte or the stationary phase. Mobile phase additives modify the ionic strength of the mobile phase or influence the charge states similar to the pH-values (McCalley 2010; Dinh et al. 2011). The third mechanism describes adsorption of an organic phase modifier followed by partitioning of the analyte into the modified aqueous layer (Knox and Pryde 1975). Additional mechanisms which are part of the HILIC separation are hydrogen-donor or dipole-dipole interactions, electrostatic interactions with uncovered silanol groups, and temperature (Hao et al. 2008; Škeříková and Jandera 2010; Buszewski and Noga 2012). Overall, the complexity of the HILIC separation mechanism and the many influencing factors impede the calculation of retention models and reliable predictions of proper chromatographic conditions for certain analytes.

4.2.2 Two-dimensional liquid chromatography

HPLC, although highly versatile and prevalent, has its limitations. The separation of compounds cannot always be achieved by one certain stationary phase and samples become more and more complex. An emerging approach to address these issues is two-dimensional liquid chromatography (2D-LC), thoroughly reviewed in the literature (Iguiniz and Heinisch 2017; Pirok et al. 2019).

Three different implementations are known: (multiple)-heartcut 2D-LC (mLC-LC), comprehensive 2D-LC (LCxLC), and selected comprehensive 2D-LC (sLCxLC). LC-LC is used for resolving analyte pairs or groups with different functionalities, that cannot be separated on a one-dimensional LC, or to investigate the purity of a peak (Stoll and Carr 2017). Thereby single fractions of the first dimension are collected and transferred to the second dimension to analyze a small number of compounds in a highly complex mixture, for example enantiomers on a chiral column in the second dimension (Woiwode et al. 2018) or phospholipids on a HILIC column in the second dimension (Helmer et al. 2020). LC-LC strongly increases the resolving power and selectivity of a targeted method but is limited to a few target compounds, which can be multiplied using multiple heartcut 2D-LC, where more fractions are captured (Stoll and Carr 2017; Pirok et al. 2019).

In LCxLC, the entire first chromatographic dimension is sequentially injected to the second dimension. This method is used to gain as much information as possible from one sample, to perform sample profiling, like in metabolomics or proteomics. LCxLC offers high peak capacities and peak production rates with reasonable times of analysis, multiple options of retention mechanisms, and improved selectivity, especially when using orthogonal methods (like RP and HILIC). The highly increased peak production results in large amounts of data which have to be processed by adequate data-analysis software, so data interpretation is not as straightforward as in one-dimensional LC. Overall complexity of the method is increased, complicating method development, as well as compatibility of the two chromatographic methods. sLCxLC works according to the sample principle as LCxLC, yet only segments of the first dimension are comprehensively transferred to the second dimension (Pirok et al. 2019).

The issue of compatibility in 2D-LC is especially challenging when orthogonal methods are developed. In extreme cases the solvents of the two chromatographic methods are immiscible, like when using RP and NP chromatography. In addition, applying a sample to the second dimension in a solvent with high eluting power leads to peak deformation or peak splitting on the second dimension (Mayfield et al. 2005). Different approaches of modulation were developed, like active solvent modulation, stationary-phase-assisted modulation, or vacuum-evaporation modulation (Tian et al. 2008; Vonk et al. 2015; Stoll and Carr 2017; Pirok et al. 2019).

The approach developed in this work uses an existing instrumental setup of LC-LC to perform a mixture of LC-LC and sLCxLC. A six-port valve with a sample loop is used to collect the dead-volume of HILIC in the first dimension, store it in the sample loop throughout the HILIC run, and then transfer it to a RP column in the second dimension. While the RP is running, the HILIC in the first dimension is re-equilibrated. Thereby the entire information of the separation in the first dimension is maintained and complemented by the information of the dead-volume, which is analyzed on the second dimension.

4.3 Mass spectrometry

MS is a versatile analytical technique which can be used for quantification, determination of elemental composition, or structural elucidation. Mass spectrometric analysis relies on the creation of ions in the ion source, which are separated in an electric or magnetic field based on their mass-to-charge ratio (*m/z*) in the mass analyzer. Depending on the ion source and the detector, MS is used for inorganic compounds, organic molecules, biological samples, or polymers. For this thesis, an ESI source was used coupled to an Orbitrap mass spectrometer, and only these parts will be described in detail in chapters 4.3.1 and 4.3.2.

4.3.1 Electrospray ionization

ESI is the mainly used ion source to couple HPLC to a mass spectrometer. ESI provides transfer of ions from solution into the gas phase at atmospheric pressure similar to atmospheric pressure chemical ionization and atmospheric pressure photoionization. It is considered a “soft ionization” technique, as little to no fragmentation occurs in the ion source.

The ESI source is operated in positive or negative mode, depending on the desired charge of the analyte molecules. The three main steps of ESI exemplary in positive ionization mode are the formation of highly charged droplets, the shrinking of droplets and the formation of desolvated ions (Figure 21). The solution is pumped through a spray needle, to which a high voltage of approximately 2-5 kV is applied. In combination with the opposing counter electrode, an electric field is created. The charges in the solution are separated, thereby anions are oxidized on the inner wall of the capillary, while cations are attracted towards the counter electrode resulting in the formation of a cone, the so-called “Taylor cone”, at the tip of the needle. Once surface tension is overcome by electrostatic repulsion, the “Rayleigh limit” is reached and the cone starts ejecting a fine jet of liquid droplets with high charge density. The positive excess charges on the surface repel each other, so a fine spray is formed, hence the term “electrospray” (Cech and Enke 2001; Gross 2017). The shrinking of large ESI droplets by solvent evaporation is described by two different models, the charge residue model (Dole et al. 1968) and the ion evaporation model (Iribarne and Thomson 1976).

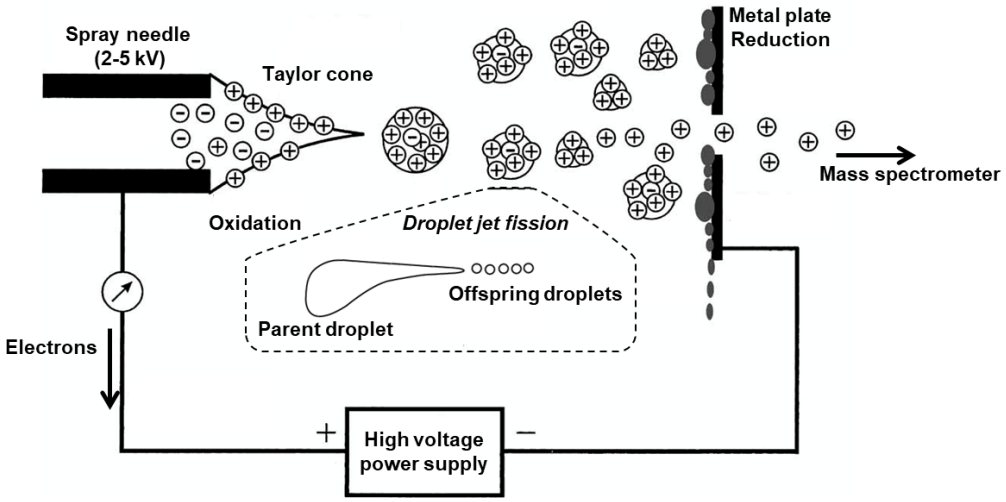

Figure 21: Schematic illustration of the ESI process starting with the formation of a Taylor Cone, shrinking of the droplets due to solvent evaporation and the principle of droplet jet fission, resulting in the formation of desolvated microdroplets prior to transfer to the mass spectrometer (adapted from Cech and Enke, 2001 and Gross, 2017).

The ion evaporation model is representative for small ions, assuming ejection of single ions from the surface of highly charged droplets. The charge residue model describes several "Coulomb explosions", like at the tip of the Taylor Cone. Solvent evaporation leads to decreased droplet size with constant amounts of charges and continuously increasing charge density. Once electrostatic repulsion in the droplet exceeds surface tension the droplet is divided into smaller droplets repeatedly until small desolvated microdroplets or, ideally, desolvated ions are formed. The principle of "Coulomb explosion" was extended to the "droplet jet fission" model, describing droplets of non-spherical shape with elongated ends, that emit droplets of smaller size containing only 1-2% of the mass, but 10-18% of the charge of the parent droplets due to inhomogeneous distribution of charges on the surface of the parent droplet, with charge concentration at the tip (Kebarle and Tang 1993).

The ions are transferred from the atmospheric pressure ion source into the vacuum of the mass spectrometer by an interface employing differential pumping stages. The sequential chambers of decreasing pressure are separated by orifices guiding the ions. Neutral species are driven away from the mass spectrometer entrance by a curtain gas (dry nitrogen gas), while ions are attracted by the field gradient and pass through the curtain gas. The evaporation of the solvent can be supported by heating of the capillary, also referred to as heated electrospray ionization (HESI).

Despite the term "ionization", ESI does not entirely provide the formation of ions, but rather the transfer of ions from the liquid into the gas phase. Charging of analytes is obtained by different mechanisms. Analytes that are already charged in solution are separated in the transfer capillary. This is applicable for molecules with acidic or basic functional groups, proteins, or inorganic species. The resulting protonated or deprotonated species are detected as $[M-H]^-$ or $[M+H]^+$ (M=molecule). Analytes with no ionizable functional groups can be charged by the formation of adducts with e.g. sodium or ammonium, resulting in $[M+Na]^+$ or $[M+NH_4]^+$ species. Adduct formation occurs in the solution prior to introduction

to the ESI source. Once the analytes are released from solution into the gas phase they can be charged by proton transfer in the gas-phase under the assumption that electrochemical reactions have to result in a closed electric circuit (Cech and Enke 2001). The crucial factor is a switch of proton affinity of an analyte from solution to the gas-phase. In solution, the pK_a-value is the determining factor for proton affinity, while in the gas-phase, the gas-phase basicity, or rather gas-phase proton affinity, is decisive. These terms are not related to each other, as a molecule with a low pK_a-value in solution can have a high proton affinity in the gas-phase (Amad et al. 2000).

Beside the efficiency of ionization of an analyte, also surface activity plays an important role in determining the ESI response. Two analytes of similar liquid concentration can differ tremendously in signal intensity in a mass spectrum when one analyte has higher surface activity than the other. Therefore, it is important to thoroughly evaluate analyte characteristics and matrix effects, as ion suppression and enhancement have large impacts on the results of an ESI-MS measurement.

4.3.2 High-resolution mass spectrometry

HR-MS is a versatile tool in the field of analytical chemistry. Different instrumentations are known and routinely used such as Fourier-transform ion cyclotrone resonance (FT-ICR), time-of-flight, or Orbitrap instruments. The idea of an electrostatic orbital trap of charged species goes back to the year 1923 (Kingdon 1923). Using the principle of periodic movement of ions along a central electrode (Makarov 2000) the first commercial Orbitrap instrument was released in 2005 by Thermo Electron (now Thermo Fisher Scientific).

Current Orbitrap instruments provide resolution up to 500,000 (at *m/z* 200) and mass accuracies between <1 ppm for internal and <3 ppm for external calibration. Mass accuracy describes the difference between the calculated exact mass and the measured mass. Mass resolution is defined as the smallest *m/z* difference that can be separated at a certain *m/z* value (Equation 8), (Murray et al. 2013; Gross 2017).

$$R = \frac{m}{\Delta m} = \frac{m/z}{\Delta m/z}$$

R = resolution
m = mass
z = charge

Equation 8

In this thesis a Q-Exactive Hybrid Quadrupole Orbitrap instrument from Thermo Fisher Scientific was used (Figure 22). Gas-phase ions emerge from the ESI ion source, pass through an ion guidance system into the C-trap. From the C-trap ions can either be transferred into the higher-energy collisional dissociation (HCD) cell in linear direction or the Orbitrap mass analyzer in orthogonal direction.

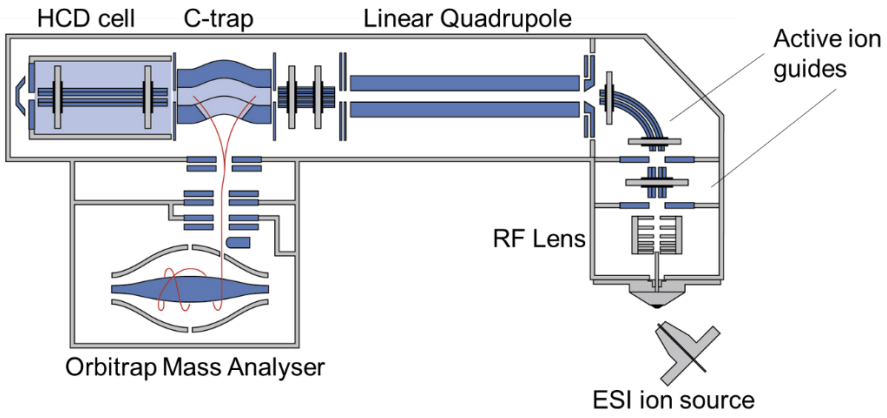

Figure 22: Schematic setup of the Q-Exactive Hybrid Quadrupole Mass Spectrometer from Thermo Fisher Scientific showing the ESI ion source followed by an RF lens and ion guidance multipoles. Ions are passing a linear quadrupole before reaching the C-trap followed by either the Orbitrap mass analyzer in orthogonal direction or the HCD cell in linear direction (Makarov and Scigelova 2010).

The C-trap is a crucial part of the instrument to provide fast and uniform extraction of large ion populations into the Orbitrap. It consists of rods with hyperbolic surfaces and is enclosed by the gate and the trap electrode, with respective apertures for the ions. The C-trap is filled with low-pressure nitrogen as a bath gas, which provides good collisional damping and low gas carryover to the Orbitrap. Due to the low pressure of the nitrogen, ions are cooled down by mild collisions without fragmentation. Approximately 200 V are applied to each electrode to compress the ions prior to a voltage pulse which forces the ions through a slot into the Orbitrap in orthogonal direction. Injection occurs at a slight offset to the center of the Orbitrap to introduce the ions into the electric field gradient without need for further excitation. This principle is referred to as excitation by injection (Makarov and Scigelova 2010; Gross 2017).

The Orbitrap itself consists of a spindle-like inner and a barrel-like outer electrode, with a ceramic ring in the center. After injection from the C-trap, the electrostatic field in the Orbitrap induces harmonic oscillations along the horizontal axis. The high kinetic energy of the ions results in rotational motion around the inner electrode. The combination of axial and rotational motion leads to the formation of thin rings, oscillating along the electrode. The axial motion is depending on the mass and charge of the respective ions resulting in different frequencies of the ion packets (Equation 9).

$$\omega_z = \sqrt{(\frac{z}{m})k}$$

ω_z = harmonic oscillation frequency (rad/s)

m = mass

z = charge

k = field curvature

Equation 9

In the two separate domains of the Orbitrap, separated by the central ring, the oscillating ion packets induce opposite currents on both halves of the outer electrode resulting in a time-dependent image current which is re-calculated to the frequency and fast Fourier-transformed into a mass spectrum (Makarov 2000; Perry, R.H.; Cooks, R.G.; Noll 2008; Zubarev and Makarov 2013; Gross 2017).

The high resolving power of the instrument is inversely proportional to the time of measurement. Ions have to oscillate along the electrode for certain number of times to reliably detect the mirror currents and calculate by Fourier-transformation, which is why ion trajectories have to be stable for about 0.1-1.5 s. Two possible disturbances of the stability are discharge on the electrodes and collision with other particles. The discharging on the electrodes is prevented by the voltage pulse from the C-trap into the Orbitrap providing the ions with sufficient kinetic energy to force them into orbital movement around the electrode. Collision with other gas phase components is prevented by the high vacuum (10^{-10} mbar), which in turn enhances vulnerability of the instrument to pressure inconsistencies (Perry, R.H.; Cooks, R.G.; Noll 2008; Gross 2017).

The used Q-Exactive instrument can perform tandem measurements (limited to MS^2) with the HCD-cell installed directly after the C-trap. For fragmentation, ions are transferred from the C-trap into the HCD-cell rather than directly into the Orbitrap. In this nitrogen-filled multipole ions are fragmented by high-energy collisions with nitrogen molecules. Thereby the initial kinetic energy is converted to internal energy resulting in the breaking of bonds. In contrast to resonant excitation, collision induced dissociation results in first- and higher order product ions. After fragmentation, fragment ions are transferred back to the C-trap and further into the Orbitrap for high-resolution measurements (Olsen et al. 2007; Bateman et al. 2009; Gross 2017). HR-MS is beneficial for target analysis in complex sample mixtures, the separation of isobaric ions, determination of the charge state, and the determination of a sum formula which is especially useful for non-target analysis.

4.4 Non-target analysis

The progress in HR-MS provides the users with large datasets of highly accurate masses. This led to a novel advancing analytical approach, the NTS, where untargeted data acquisition is used to obtain an overview over all components of a sample. It is commonly used in water analysis, aerosol analysis, or metabolomics.

Target analysis aims for quantification of known substances using reference standards, where exact mass, retention time, and fragmentation behavior are known. NTS starts with untargeted acquisition by an instrument providing high mass resolution (e.g. Orbitrap or FT-ICR). Different software is available for processing of the resulting large datasets, either directly from the manufacturers like Compound Discoverer (Thermo Fisher Scientific) or open-source software like MZmine. These softwares use several processing steps for peak detection, creation of extracted ion chromatograms (XIC), and finally

predicting elemental sum formulas. For evaluation of the chemical conclusiveness of the calculated sum formular the “seven golden rules” were defined (Kind and Fiehn 2007):

1) Restrictions for number of elements, starting with the six most common elements carbon, hydrogen, oxygen, nitrogen, sulfur, phosphorous and silicon
2) LEWIS and SENIOR check
    a. LEWIS: all atoms must have completely filled s- and p-valence shells
    b. SENIOR: sum of valences with odd valences must be even, sum of valences must be ≥ twice the maximum valence, sum of valences must be ≥ twice the number of atoms minus one
3) Isotopic pattern filter
4) H/C ratio check (2 > H/C > 0.5)
5) NOPS ratio check of element ratios of N, O, P, and S to carbon
6) HNOPS probability check of multiple unlikely high element counts (e.g. $C_{26}H_{28}N_{17}OP_3S_8$)
7) TMS check, only for GC-MS if silylation is involved

A mixed approach between target and non-target analysis is STS. Thereby a list of suspects is compiled prior to the mass spectrometric analysis with known molecular structures or at least sum formulas and corresponding exact masses, of which no analytical reference standards are available. The processed datasets are matched with the suspect target list to obtain a list of present suspects in a sample (Figure 23). For rough quantification, so-called surrogate compounds can be used which are expected to behave similarly in the ESI source.

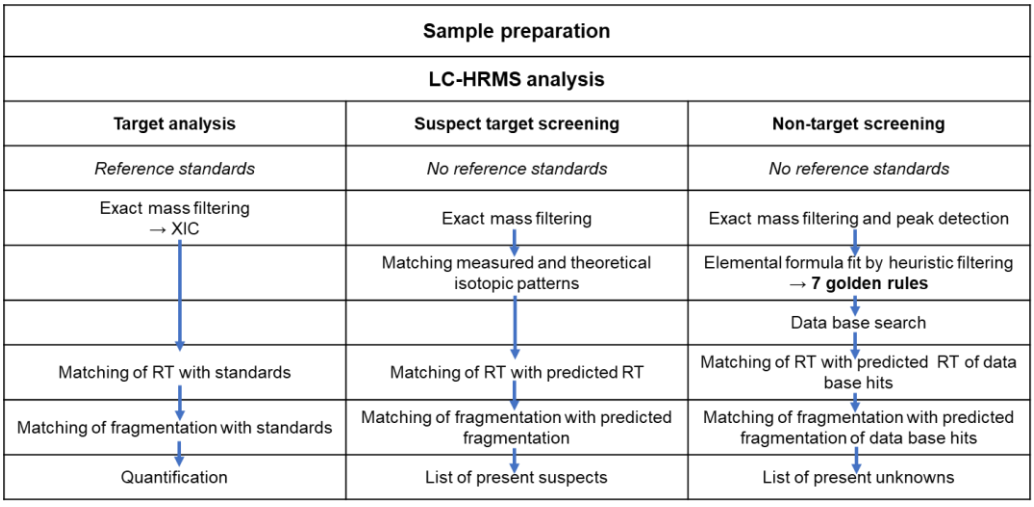

Figure 23: Schematic workflows of target analysis, suspect target screening and non-target screening (adapted from Krauss et al., 2010).

NTS aims for two different goals, either searching the data for potential novel target compounds or observing the entirety of signals in its overall chemical composition. Searching non-target data for potential target compounds is based on levels of identification (Schymanski et al. 2015). NTS starts at level 5, where the only part of identification is detection of a mass. With the elucidation of an

unequivocal molecular formula by the accurate mass, level 4 of identification is reached. A substructure or compound class must be known to refer to a compound as a tentative candidate, like in STS starting at level 3. Confirming a probable structure by a database search results in level 2 identification. Both NTS and STS can offer confidence up to level 2 solely based on experimental information (exact mass, isotope pattern, retention time, fragmentation), yet level 1 identification is only reached by confirming a structure with a reference standard, as in target analysis (Figure 24).

Possible level of identification ↑		HRMS-data		
		Target list	Suspect list	Peak picking
		Peak picking/XICs		
		Target screening	**Suspect target screening**	**Non-target screening**
Level 1	Confirmed structure → reference standard	**Start**		
Level 2	Probable structure → database hit		↑	↑
Level 3	Tentative candidate		**Start**	
Level 4	Unequivocal molecular formula			
Level 5	Mass of interest → detection			**Start**

Figure 24: Levels of identification in target, suspect target, and non-target screening (adapted from Schymanski et al., 2015)

To reduce a complex HR-MS dataset to the most relevant information, different (visual) approaches are available. One approach is the Kendrick mass scale used to find homologue series in complex mixtures. The Kendrick mass scale is based on the definition of $M(CH_2) = 14.000000$ and the normalization to the exact IUPAC mass of a CH_2-unit (M=14.0156050). The Kendrick Mass (KM_{CH2}) and Kendrick Mass Defect (KMD) are calculated according to Equation 10 and Equation 11. As molecular homologue series have the same KMD, a plot of KMD to the nominal mass visualized homologue series on horizontal lines (Hughey et al. 2001; Gross 2017).

$$\mathrm{KM_{CH2}} = \text{experimental observed mass} \cdot \frac{14.000000}{14.0156050}$$

Equation 10

$$\mathrm{KMD} = \text{nominal mass} - \mathrm{KM_{CH2}}$$

Equation 11

Plotting of the atomic H/C ratio to the atomic O/C ratio in a van Krevelen plot shows relations between products by similar reactions like decarboxylation, dehydration or oxidation, which are displayed along straight lines (Kim et al. 2003; Gross 2017). Additionally, compound classes like proteins, lipids, or hydrocarbons are located in distinct areas in a van Krevelen plot (Figure 25) (Kim et al. 2003; Sleighter and Hatcher 2007; Wozniak et al. 2008).

The ring and double bond equivalent (RDBE) represent the number of rings and double bonds in a molecule and therefore is utilized as an index for hydrogen deficiency. Molecules with many heteroatoms have to be considered carefully, as they can have multiple valences (for example sulfur). According to the notation $C_XH_YN_ZO_O$, the RDBE value is calculated by Equation 12. Other monovalent elements are counted as hydrogen (for example halogens), trivalent elements as nitrogen (for example silicon), and tetravalent elements as carbon (Nozière et al. 2015). The RDBE is used to reduce datasets by eliminating sum formulas with unreasonably high RDBE values, as well as to elucidate molecular composition of a sample.

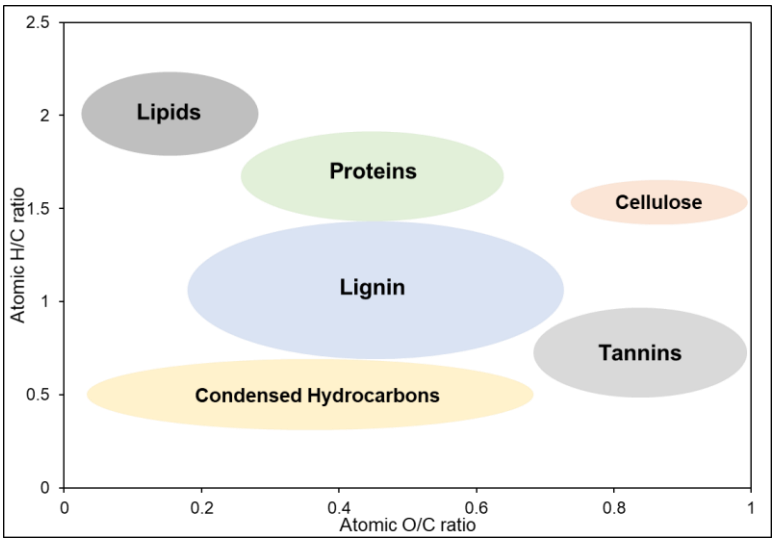

Figure 25: Examples of distinct areas of compound classes in a van Krevelen diagram plotting the atomic H/C ratio to the atomic O/C ratio (adapted from Wozniak et al., 2008).

One example are aromatic hydrocarbons and their oxidized derivatives, which are representative for anthropogenic emission and show characteristic RDBE values larger than five (Wozniak et al. 2008; Kourtchev et al. 2014).

$$\mathrm{RDBE} = 1 + \mathrm{X} - 0.5\mathrm{Y} + 0.5\mathrm{Z}$$

Equation 12

The degree of oxidation of organic species in the atmosphere is described by the average oxidation state (OSc), which increases upon oxidation processes and can be calculated straightforwardly with the data provided by NTS (Kroll et al. 2011; Nozière et al. 2015). It is defined as the average charge carbon atoms in an organic molecule would take, if they were to lose all electrons of bonds with atoms of higher electronegativity and to gain all electrons of bonds with less electronegative atoms. While the oxidation state of individual carbon atoms of a molecule might decrease during oxidation, the overall state is always increasing. The scale of OSc starts at -IV (CH_4) and ends at +IV (CO_2). There are two equations to calculate the OSc. Equation X sums up over all non-carbon atoms, associated to the element *i* and the molar ratio n_i/n_c of that element to carbon. Since organic species in the atmosphere are mainly composed of carbon, hydrogen, and oxygen, Equation 13 can be simplified to Equation 14 (Kroll et al. 2011).

$$\overline{OS}_c = -\sum_i OS_i \frac{n_i}{n_c}$$

Equation 13

$$\overline{OS}_c = 2 \cdot O/C - H/C$$

Equation 14

Plotting the OSc to the number of carbon atoms reveals three key classes of reactions of organic species in the atmosphere in the respective samples: oligomerization, functionalization, and fragmentation, all of which result in a change of OSc and number of carbons and are therefore read off a suchlike plot.

Thesis objective and outline

Information on the climate of the past is necessary to improve climate models and make predictions on climate change in the future more reliable. Such information is recovered from climate archives like ice cores, speleothems, or sediments. Each climate archive has its characteristic advantages and preserves a variety of individual organic and inorganic compounds. Speleothems grow continuously and can be accurately dated up to 640,000 years back with the ^{230}Th-U method. They provide chemically closed systems for long-time preservation of compounds and are available on all continents so they are not limited to certain regions or climate conditions. While speleothems primarily represent the conditions directly above a cave, ice cores can be used to reconstruct climate variations on a global scale. Atmospheric organic aerosols are preserved in the ice and their chemical composition can be recovered by analyzing certain organic marker compounds or by non-targeted analysis of the entire chemical profile. Thereby information on the aerosol source is obtained and led back to anthropogenic, biogenic, or marine origin.

The first part of the thesis aimed the optimization of a lignin oxidation approach and its application to speleothem samples (chapter 5). Lignin is the second most abundant biopolymer, exclusively found in vascular terrestrial vegetation. The monomeric composition provides information on the type of vegetation and is accessible by oxidative degradation of lignin and analysis of the LOPs. For that, an existing alkaline oxidation procedure was replaced by a more sensitive approach following the principles of Green Chemistry using $CuSO_4$ as a catalyst instead of CuO. In addition, an SPE was developed to enrich Lev and its isomers Gal and Man with GCB. Lev is an important biomass burning marker formed exclusively by the combustion of cellulose at temperatures higher than 300°C. Although it was already analyzed in ice cores or sediments, no data on Lev in speleothems is available. For the analysis of the small and highly polar organic compound, a HILIC method was developed for separation of the three isomers. Thereby different columns, buffers and pH values were compared. Finally, a post-column flow (PCF) of a methanolic ammonium hydroxide solution was evaluated to enhance the ionization of Lev in the ESI source and improve the sensitivity of the method. The ratio of the isomers was used to distinguish between different burned materials like softwood or hardwood. The lignin oxidation procedure and Lev analysis were combined and applied to flowstones from two caves in New Zealand with significantly different surrounding conditions. The behavior of lignin and Lev was examined for correlation with trace elements like barium, strontium, or magnesium.

In addition, cave aerosols were evaluated as an entry source for organic compounds into speleothems (chapter 6). Here, a study in Waipuna Cave was conducted, sampling aerosols on different surrogate surfaces, evaluating their sampling efficiency and the influence of the location in the cave on the aerosol load. Wet and dry deposition of aerosols on filters were compared as well as water as a surrogate surface of growing speleothems. Both methods were used to evaluate externally introduced aerosols and

aerosols related to human activity as relevant sources of organic compounds and examine a variety of environmentally relevant contaminants by STS.

The second part of this thesis dealt with ice cores as climate archives (chapter 7). Because ice core samples are valuable and rare, highly sensitive methods have to be developed covering a broad range of compounds with different functionalities. HR-MS was suitable since the high-resolution provides an unequivocal assignment of a signal to a sum formula. Ice core samples represent the chemical profile of atmospheric aerosols which are preserved in the glacier after snow deposition. Consequently, ice core samples contain a high number of different compounds in very low concentrations. Therefore, highly efficient enrichment methods were developed using WAX-SPE, HLB-SPE, and centrifugal evaporation. Biogenic SOA markers, lignin biomass burning markers, and markers for anthropogenic emission were enriched by anion-exchange SPE, while small and polar compounds like Lev, a cellulose burning marker were not enriched traditionally, but rather the aqueous matrix was removed by centrifugal evaporation. In addition to the known atmospheric markers, a method for the analysis of intact polymeric lignin in ice cores was developed. For that, the polymeric lignin was separated from the initially present lignin burning markers by a combination of anion-exchange and HLB-SPE. The alkaline oxidation method from the first part of the thesis was successfully adapted to ice core samples and the monomeric composition of lignin offered deeper insights into the type of vegetation. The novel elaborate workflow was applied to ice core samples from Colle Gnifetti glacier, which is located in the Swiss-Italian Alps and a part of the Monte Rosa massif. Samples covered the time range from 1844 to 1995 and were chosen to evaluate changing environmental conditions in the pre- and post-industrial era, which are represented by changing vegetation, fire dynamics, and anthropogenic emissions from agricultural and industrial activities.

Finally, STS and NTS were aimed to detect novel marker compounds and to reconstruct the chemical profile of the ice core samples over time (chapter 8). A strong limitation of one-dimensional chromatographic methods was demonstrated and a therefore a 2D-LC chromatography method was developed. For that, the instrumental setup of heart-cut two-dimensional LC was used for quasi-comprehensive analysis of the ice core samples. The void volume of the HILIC in the first dimension was transferred to an additional sample loop and transferred to the second dimension, consisting of a PFP column with a RP functionality, that was running during the HILIC re-equilibration time. Thereby, polar compounds were detected on the HILIC in the first dimension, while non-polar compounds eluting in the HILIC void volume were accessible with the RP column in the second dimension, strongly enhancing the comprehensiveness of the NTS. The method is presented as first-author publication in Journal of Chromatography A and was applied to samples from Colle Gnifetti for NTS and STS.

Speleothem analysis

5. Development of a novel analytical method for lignin and levoglucosan as proxies for past vegetation and fire dynamics, and their application to speleothem samples from New Zealand

5.1 Introduction

Speleothems are secondary carbonate mineral (calcite or aragonite) deposits in caves, formed by degassing of excess carbon dioxide from cave drip water. Continuous growth over several 10,000 years and accurate dating methods up to 640,000 years into the past by the ^{230}Th/U methods (Scholz and Hoffmann 2008; Cheng et al. 2016) make these carbonates highly beneficial climate and environmental archives. The stable climate conditions (temperature, humidity, UV-radiation) in cave systems protect the speleothems from most external influences (Fairchild et al. 2006; Blyth et al. 2016)

During the deposition of $CaCO_3$, organic matter as well as inorganic trace elements and their isotopes are included and preserved in or between the crystals. Since the early beginnings of speleothem research, stable isotopes were routinely analyzed, like $\delta^{18}O$ to reconstruct temperature (McDermott 2004; Treble et al. 2005), moist history like the moisture source, or seasonal precipitation (Breitenbach et al. 2010; Wong and Breecker 2015). $\delta^{13}C$ is analyzed to determine soil and vegetation dynamics (Genty et al. 2003) and more recently as a proxy for local droughts (Lechleitner et al. 2017; Fohlmeister et al. 2020; Baldini et al. 2021). Subsequently trace elements, like Mg, Ca, or Sr, were analyzed for example as markers for local precipitation (Hellstrom and McCulloch 2000; Treble et al. 2003; Fairchild and Treble 2009). While traditional geochemical proxies inform on (pan-)regional moisture history, local vegetation, or soil and infiltration changes, there is a need for novel, quantitative proxies, that inform more directly on the type of vegetation, and wildfire activity. Recent research thus focused on the organic matter in speleothems, beginning with the total organic content (Blyth et al. 2008), followed by low MW fatty acids (Bosle et al. 2014) or lipid biomarker n-alkanes (Blyth et al. 2007) as indicator of the vegetation above a cave. Another proposed vegetation proxy were lignin phenols because they could be unambiguously linked to vascular plants (Blyth and Watson 2009).

Lignin is the second most abundant biopolymer after cellulose. It occurs exclusively in terrestrial vascular plants, (Hedges and Mann 1979) is not produced by microorganisms, and stable against microbial degradation enabling transport through the soil into speleothems without major modification of the composition (Kögel-Knabner 2002; Jex et al. 2014). Lignin consists of three monomers: *p*-coumaryl-, sinapyl-, and coniferyl alcohol, thus making lignin the only presently known and accessible vegetation marker which offers information on the abundance and type of vegetation. The initial coniferyl alcohol is integrated into the polymeric lignin as guaiacyl phenylpropanoid, the sinapyl alcohol as syringyl phenylpropanoid and the *p*-coumaryl alcohol as *p*-hydroxyphenyl phenylpropanoid. The

ratios of the different subunits vary depending on gymnosperms and angiosperm vegetation, as well as wooden and non-wooden types of vegetation (Boerjan et al. 2003).

To analyze the composition of lignin, the polymeric structure is disintegrated, and the low MW phenolic monomer units are analyzed straightforwardly by LC and MS. To alter the structure as little as possible, catalyzed alkaline oxidation methods were developed by Hedges and Parker(1976), producing LOPs. These LOPs include acid, aldehyde, or methyl ketone derivates of the initial lignin phenols and are classified by the oxidation products of the original monomeric unit into the S-group, consisting of syringaldehyde, acetosyringone, and syringic acid, the V-group consists of vanillin, acetovanillone and vanillic acid, and the C-group consisting of coumaric acid and ferulic acid. The respective S/V and C/V ratios provide more detailed information on the type of vegetation, as the S/V ratio corresponds to angiosperm and gymnosperm vegetation, while the C/V ratio differentiates between wooden and non-wooden vegetation (Jex et al. 2014).

The alkaline oxidation method of (Hedges and Parker 1976) used Cu(II)O as a catalyst and subsequent enrichment of the resulting LOPs by LLE and quantification by GC coupled to a flame ionization detector. However, the long duration of the reaction and limited number of samples per batch set significant drawbacks to this method. Goñi and Montgomery (2000) improved the procedure by performing the oxidation reaction microwave-assisted and modifying the LLE. They applied their approach on sediment samples, as well as wooden, and non-wooden plant tissues. (Benner and Kaiser 2012) developed a method for lignin analysis in soil by replacing the LLE procedure by SPE and the flame ionization detector by MS. The first LC-MS methods were used for lignin analysis in aqueous samples using triple-quadrupole MS instrumentation (Yan and Kaiser 2018a), and for lignin analysis in speleothems using HR-MS (Heidke et al. 2018). It took until 2018, that the hazardous copper oxide was replaced as a catalyst by soluble copper sulfate ($CuSO_4$) and a new degradation method using ultralow sample volumes of 200 µL (Yan and Kaiser 2018b). This setup significantly reduced solvent consumption and solid waste of CuO. The method was applied to river and ocean water samples. In this work, the $CuSO_4$ oxidation method is applied to speleothem samples with a preceding enrichment of polymeric lignin from dissolved speleothem samples, and subsequent enrichment of LOPs, by HLB-SPE.

The second organic proxy analyzed in this work is Lev (1,6-Anhydro-beta-glucopyranose). Lev is formed by pyrolysis of cellulose above 300°C (Nolte et al. 2001; Elias et al. 2001; Simoneit 2002). The isomers of Lev, Gal and Man are formed by likewise by pyrolysis of hemicellulose (Nolte et al. 2001). The detailed formation mechanism is yet to be elucidated, but different mechanisms are proposed including radical cleavage, ionic cleavage, or glucose intermediate reactions (Zhang et al. 2013). By determination of the ratios of Lev to Gal and Man, the emission source of the burning event can be enclosed for example as hardwoods, softwoods, grasses or lignites (Fabbri et al. 2009).

Fire events affect the regional and global biogeochemical cycle, temperature, vegetation, and climate (Bond and Keeley 2005; Shakesby and Doerr 2006; Bowman et al. 2009). Thorough investigation of suchlike biomass burning events is urgently required to complement information on wildfire recurrence under warming climates. Paleoclimatic reconstruction can greatly elucidate on regional vulnerability against wildfires. Multiple global charcoal records were reviewed to reconstruct Holocene paleofire events and highlighted the importance of these events on climatological and biological processes (Marlon et al. 2013). Lev is analyzed as a biomass burning marker in organic aerosols, ice cores, and sediments. Significant correlation of Lev to charcoal and other temperature proxies in sediments was proved, supporting its suitability for paleofire reconstruction (Elias et al. 2001). However, atmospheric stability of Lev is strongly affected by the concentration of -OH radicals in the atmosphere, temperature, and pressure (Hennigan et al. 2010; Hoffmann et al. 2010). First studies determined a lifetime of Lev between 1-10 days, comparable to other atmospherically relevant compounds (Donahue et al. 2013). Many chamber experiments evaluating different atmospheric conditions showed decreasing lifetime of Lev with increasing -OH concentration (Hennigan et al. 2010). The high emission factor and high concentration of Lev in aerosols still enable long-range atmospheric transport (Hoffmann et al. 2010) and inclusion into climate archives, which is why Lev is thoroughly analyzed in aerosols (Puxbaum et al. 2007; Kourtchev et al. 2011; Barbaro et al. 2015; Zangrando et al. 2016), ice cores (Gambaro et al. 2008; Yao et al. 2013; Zennaro et al. 2014; Pokhrel et al. 2020), and sediments (Elias et al. 2001; Oros et al. 2002).

Here, a first approach to analyze Lev in speleothems using a GCB-SPE method followed by HILIC coupled to a high-resolution Orbitrap MS is presented. The developed method allowed quantification of Lev and its isomers Gal and Man in speleothems in combination with the initial lignin analysis method and without interference on the lignin results. The main goal of this novel method was to determine the abundance of Lev, test the interaction and correlation to other proxies and thus draw conclusions on the transport of Lev into speleothems, and to obtain information on the source of Lev by determining the emission factor Lev/Gal+Man (LMG).

5.2 Methods and samples

5.2.1 Speleothem samples

Speleothem samples were collected by the University of Waikato (Hamilton, New Zealand). The sampling sites were selected to represent different altitudes and as little human influence as possible. In this work flowstone samples from Daves Cave (DC) and Waipuna Cave (WP) were analyzed. The age-depth modelling of both flowstones was conducted using the COPRA algorithm (Breitenbach et al. 2012) in MATLAB. COPRA was used to generate 2000 Monte-Carlo simulations of each age-model, whilst Piecewise cubic Hermite interpolation (PCHIP) was applied to interpolate the ages and produce median proxy values with 95 % confidence intervals. One half of the respective flowstones was used for dating and analysis of trace elements, while the other half was embedded in polymeric resin and cut evenly using a sire saw with a 0.3 mm diameter diamond-coated wire.

DC (45°S) is located in the Fiordland national park at the foothills of Mount Luxmore (ca. 1450 m a.s.l) in the southwestern Southern Island of New Zealand. The vegetation up to the tree line is dominated by temperate rainforest with mostly silver- and mountain beech, podocarps, shrubs, and ferns. The ground surface is covered in mosses and liverworts. The vegetation is supported by high rainfalls in this area, yet the flora stands on a thin soil layer heavily subjected to tree and scree avalanches. The area between the tree line and snow line is dominated by snow grasses like daisies and buttercups (Figure 26). The Mount Luxmore caves reside above the tree line under a thick ground cover of tussock and other native alpine plants. Cold and wet conditions promote water-logging and peaty organic rich soils have developed over the years. Up to 6000 mm rainfall are recorded in this region per year. Soils were found to have light brown A horizons beginning at around 20 cm with characteristic iron staining indicating iron reduction and oxidation within the soil profile.

WP (38°S) is located in the central Northern Island of New Zealand in a karst landscape (ca. 395 m a.s.l). Belonging to the Waipuna scenic reserve in the Waitomo district, the cave is covered by a lush podocarp forest with a dense undergrowth of shrubs, ferns, and tree-ferns. Soils in the locality are deep (> 1m) typic orthic allophanic being developed on extensive North Island rhyolitic volcanic ash deposits. These soils are exceptionally well drained and water typically reaches the cave on timescales of days to a few weeks following rainfall events (Nava-Fernandez et al. 2020).

The flowstone DC15 was 200 mm long and cut into 18 pieces (Figure 26). The WP flowstone sample was 460 mm long with a gap between 270 and 310 mm. Flowstone WP15-1.1 was evenly cut into 17 pieces starting at 20 mm, while flowstone WP15-2.1 was cut into 7 pieces of 10 mm, respectively, with gaps between 340-380 mm, and 390-430 mm (Figure 26).

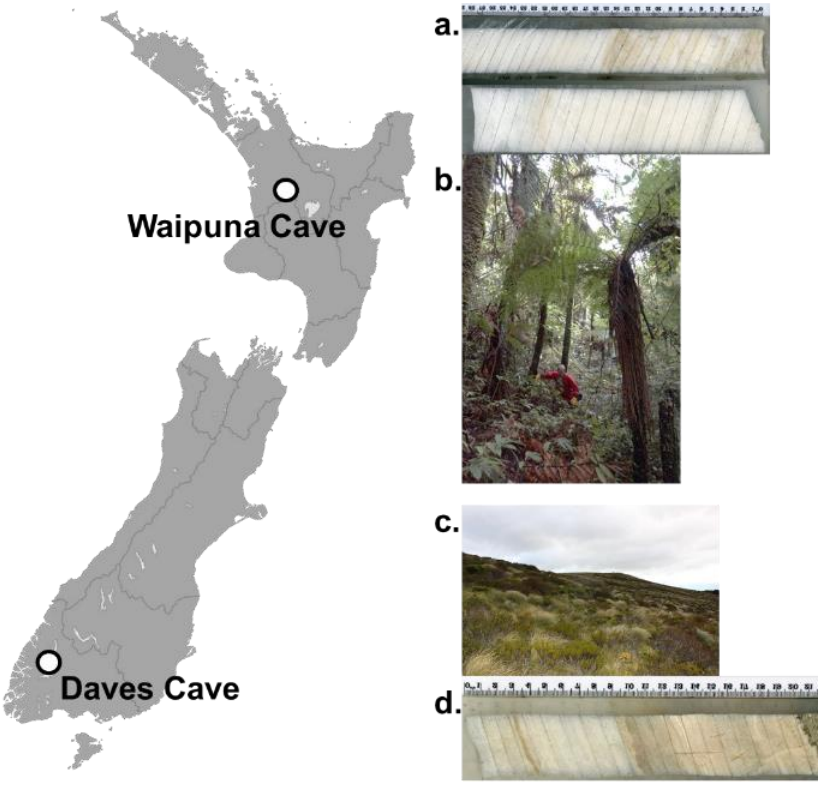

Figure 26: Location of sampling sites Waipuna Cave (38°S) and Daves Cave (45°S) on the Northern and Southern Island of New Zealand. a) cross-section of flowstone WP15-2.1 with sampling lines, b) vegetation overlaying Waipuna Cave, c) vegetation above Daves Cave, d) cross-section of flowstone DC-15 with sampling lines

5.2.2 Methods

Flowstone samples were rinsed with Milli-Q water prior to being covered with MeOH/CH_2Cl_2 (1:9, v/v) and sonicated for 10 minutes at 35°C. This procedure was repeated and afterwards contaminations on the outer layer were removed by covering the samples with hydrochloric acid (HCl)-solution (0.6%) for 5 minutes. After rinsing with Milli-Q water and drying, the sample was dissolved in concentrated hydrochloric acid (30%). The acidic sample solutions were diluted 1:1 (v/v) with Milli-Q water. Differential weighing of the sample before dissolving and the remaining polymeric resin after dissolving provided the actual weight of the samples (Table S 1 and Table S 2).

5.2.2.1 $CuSO_4$ oxidation

Polymeric lignin was extracted from the dissolved flowstone samples by SPE using HLB cartridges (200 mg, 6 mL) from Waters (Milford, USA). The sorbent was conditioned with 6 mL of MeOH and 6 mL of HCl-solution (0.6%). The samples were filtered and applied to the cartridges using 20 mL reservoirs, the flow-through was captured for subsequent analysis of Lev. After washing the sorbent with 6 mL of HCl-solution (0.6%) twice, the cartridges were dried for 20 minutes by sucking air through the cartridges using vacuum manifold. Samples were eluted with 10 times 500 µL of MeOH and evaporated to dryness at 30°C under a gentle stream of nitrogen prior to re-constitution in 200 µL of MeOH. The solutions

were sonicated for 10 minutes at 45°C and transferred to 500 µL Teflon reaction vials, purchased from Savillex Corporation (Eden Prairie, MN). Vials were rinsed with additional 100 µL of MeOH, sonicated for another 10 minutes at 45°C and the methanolic solution was added to the reaction vials. The solution was evaporated to dryness in the reaction vials and samples were re-constituted in 200 µL of nitrogen-sparged NaOH (1 mol/L). For oxidation, samples were spiked with 10 µL of $CuSO_4$-solution (10 mmol/L) and 10 µL of ascorbic acid (0.2 mol/L). To create an inert atmosphere, the air in the vials was purged with nitrogen. Reaction vials were placed into microwave vessels, which were filled with NaOH (1 mol/L) to half the height of the reaction vials (in our case 7 mL) for pressure compensation. The temperature program in the GC oven started at 25°C with a subsequent ramping of 31°C/min to a final temperature of 155°C, which was held for 90 minutes.

After cooling of the samples to room temperature, 30 µL of HCl (30%) were added for neutralization, as well as 1.5 µL of ethylvanillin (1 µg/mL in ACN) as an internal standard for monitoring instrument fluctuations. The LOPs were extracted by SPE using HLB cartridges (30 mg, 1 mL) from Waters (Milford, USA). Cartridges were conditioned twice with 1 mL of MeOH, and twice with 1 mL of 0.6% HCl solution. The sorbent was washed three times with 500 µL of 0.6% HCl solution and dried for 20 minutes by sucking air through the cartridges using vacuum manifold. Samples were eluted with 8 times 125 µL of 2% NH_3 in ACN. Afterwards the solutions were evaporated to dryness at 30°C under a gentle stream of nitrogen and re-constituted in 200 µL of H_2O/ACN (9:1, v/v). Samples were sonicated for 10 minutes at 45°C and filtered through Micropur polyamide filters with a pore size of 0.20 µm from Altmann Analytik (Munich, Germany) into vials with inlets prior to liquid chromatography (LC)-MS analysis.

5.2.2.2 Cu(II)O oxidation

The Cu(II)O oxidation is described in detail elsewhere (Heidke et al. 2018). The first HLB-SPE procedure was conducted similarly to the $CuSO_4$ oxidation. The dried residue was re-constituted in 1.5 mL of NaOH (2 mol/L) and sonicated for 10 minutes at 45°C. After transfer of the solution to a microwave vessel, the vial was flushed with additional 1.5 mL of NaOH (2 mol/L), which were added to the respective microwave vessels. Additionally 250 mg of Cu(II)O, 50 mg of $(NH_4)_2Fe(SO_4)_2$ x 6 H_2O, and 8mL of NaOH (2 mol/L) were added and the vessels were purged with argon gas to create an inert atmosphere in the vessels. The microwave temperature was increased to 155°C within 5 minutes and held for 90 minutes. After cooling, the solutions were transferred to centrifuge tubes and the vessels were flushed with 3 mL of NaOH (2 mol/L) twice. The supernatants of the solutions after twofold centrifugation (10 minutes at 3000 rpm) were transferred to glass vessels, acidified with HCl (30%) and prepared by a second HLB-SPE.

5.2.2.3 Levoglucosan extraction

The flow-through of the first HLB-SPE was further processed using a GCB-SPE method. The Supelclean™ ENVI-Carb™ cartridges (250 mg, 3mL) were purchased from Sigma-Aldrich (Schnelldorf, Germany). The sorbent was conditioned using 3 mL MeOH and 3 mL of 0.6% HCl solution. Samples were applied to the cartridges using 20 mL reservoirs. The sorbent was washed twice with 3 mL of the 0.6% HCl solution. After drying 20 minutes by sucking air through the cartridges using vacuum manifold elution was conducted using four times 250 µL of MeOH/CH_2Cl_2 (1:3, v/v) and two times 250 µL of MeOH/CH_2Cl_2 (8:2, v/v). Samples were evaporated to dryness under a gentle stream of nitrogen at 30°C and re-constituted in 200 µL of ACN/H_2O (95:5, v/v). Prior to LC-MS analysis, samples were sonicated for 10 minutes at 45°C and filtered through Micropur PTFE filters with a pore size of 0.20 µm from Altmann Analytik (Munich, Germany) into vials with inlets.

5.2.2.4 UHPLC-HR-MS analysis

All methods were conducted using a Dionex UltiMate 3000 ultrahigh-performance LC system coupled to a heated ESI source and a Q Exactive Orbitrap HR-MS (all Thermo Fisher Scientific).

Lignin analysis

Chromatographic separation of LOPs was conducted using an ACQUITY UPLC Fluoro-Phenyl column (2.1x100 mm, 1.7 µm particle size) from Waters (Milford, USA). Eluent A consisted of H_2O/ACN (98:2) with 400 µL/L of formic acid, while eluent B consisted of H_2O/ACN (2:98). The gradient started with 95% of eluent A, which was decreased to 90% within 0.5 minutes and held for another 4.5 minutes. Within one minute, the percentage was decreased to 85% and within another minute to 70%. From minute 7 to 7.5, the percentage was decreased from 70 to 50%, and then to 1% for 2 minutes. At 9.5 minutes, the percentage of eluent A was set back to 5% and held for 1.5 minutes until a total run time of 11 minutes. The injection volume was 15 µL, the flowrate was set to 0.5 mL/min and the column was heated to 40°C.

Levoglucosan analysis

Chromatographic separation of Lev and its isomers was obtained using an iHILIC-Fusion column (2.1x100 mm, 1.8 µm particle size) from HILICON (Umeå, Sweden). Eluent A was a buffer solution, set to pH 6, containing 5 mM of NH_4HCO_2, while eluent B consisted of 100% ACN. The flowrate was set to 0.4 mL/min, and an additional PCF containing 50 mM of NH_4OH in MeOH was introduced between the column and the MS with a flowrate of 0.1 mL/min. An isocratic method was used with 97% of eluent B for 5 minutes. To clean and re-equilibrate the column afterwards, the percentage of ACN was reduced to 80% within 0.5 minutes and held to 15 minutes. Within another 0.5 minutes, the percentage was set back to 97% for 10 minutes. The injection volume was 15 µL and the column was heated to 30°C.

Settings of the Orbitrap MS were similar for both analyses. The HESI source was operated in negative ionization mode with spray voltage set to -3.5 kV, capillary temperature to 320°C, sheath gas to 60 psi and aux gas to 20 psi. The HESI probe was heated to 150°C to enhance solvent evaporation. Full-MS spectra were recorded in the range of *m/z* 80-550 with a resolution of 70,000. MS^2 spectra were acquired in the respective retention time windows of the analytes by HCD with a normalized collision energy of 35%.

5.3 Results and Discussion

5.3.1 Comparison of oxidation catalysts Cu(II)O and $CuSO_4$

The two methods were compared and evaluated by fivefold determination of LOP concentrations after the respective oxidations. For that, a large flowstone sample from *Herbstlabyrinth* cave (Heidke et al. 2019) was dissolved in hydrochloric acid. The solution was thoroughly mixed and afterwards ten times 10 mL were collected into individual glass containers for method comparison. This prepared surrogate standard solution was also used for subsequent method optimization presented in chapter 4. Ten milliliters of HCl (30%)/Milli-Q water (1:1) were used as blank samples, respectively. No significant concentration differences of individual LOPs between the two oxidation methods were observable (Figure 27). Acetovanillone and ferulic acid showed the highest concentration deviation, yet only acetovanillone showed a larger variation in the $CuSO_4$ oxidation method. All other compounds showed similar concentrations and deviations, with maximum one significant outlier. The summed concentrations of all LOP groups showed slightly lower, yet comparable concentrations in the $CuSO_4$ oxidation method. The maximum difference in the share of a group to the total LOP concentration was observable for the S-group with a difference of 3.2% (Figure 27, lower right). All percentage differences between the two oxidation methods were below five percent. Overall, reviewing the LOP concentrations, as well as proportions of the LOP groups, the $CuSO_4$ oxidation method showed comparable results with reasonable standard deviations and was therefore considered equally applicable for lignin analysis in speleothems.

Furthermore, smaller sample sizes, lower consumption of hazardous chemicals and solvents, and a larger batch size (hence lower batch-to-batch variation), made the $CuSO_4$ oxidation more efficient compared to the CuO oxidation method. Additionally, less artifacts and lower blank signals, *ergo* lower detection and quantification limits were expected. The total ion chromatograms (TIC) of the blanks prepared by both, the CuO and the $CuSO_4$ oxidation methods, showed lower peak intensities and a lower noise between 0-8.5 minutes for the $CuSO_4$ blank (Figure 28).

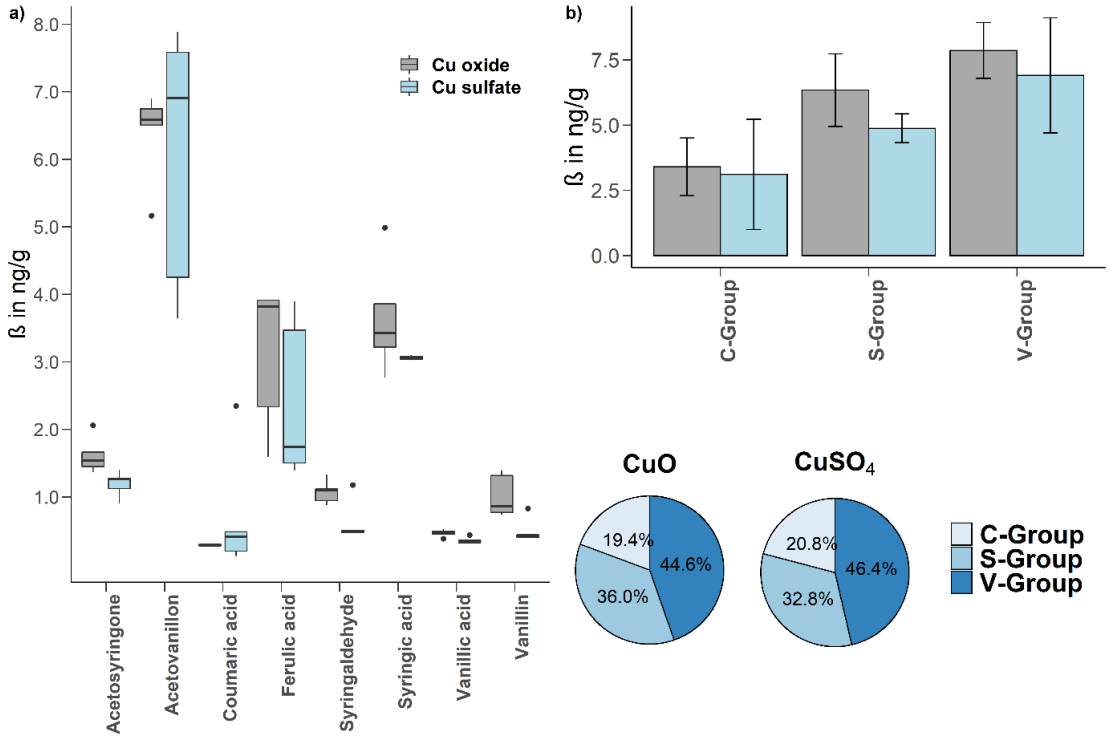

Figure 27: Boxplot diagram of LOP mass-concentrations (ng/g) after oxidation with CuO and $CuSO_4$ in fivefold determination (a). Bar diagram of summed up mass concentrations (ng/g) of the LOP groups (b) and pie charts of the composition of lignin of C-, S-, and V-group in percent.

The evaluation of the quantitative performances and the blank chromatograms allowed the comparability of both oxidation methods, with the final assessment of $CuSO_4$ oxidation method as being more efficient, environmentally friendly, and sensitive approach for lignin analysis in speleothems.

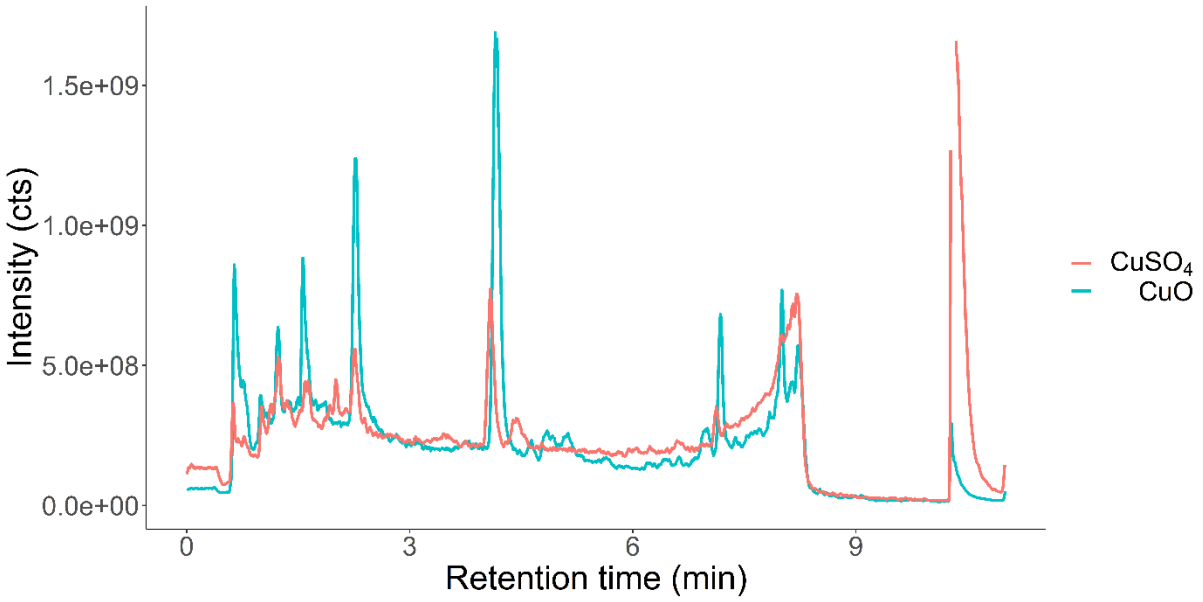

Figure 28: Overlayed TICs of blank samples prepared by CuO oxidation (blue) and $CuSO_4$ oxidation (red).

5.3.2 Method optimization $CuSO_4$ oxidation

To ensure comparability, CuO and $CuSO_4$ oxidations were conducted using the same temperature programs, where 155°C were held for 90 minutes. The CuO oxidation was microwave-assisted resulting in a maximum number of 10 samples per run, while the $CuSO_4$ oxidation method was conducted in a GC oven, resulting in a maximum possible number of 50 samples in one batch. After the $CuSO_4$ oxidation was selected as more efficient, further method optimization was conducted using different temperature programs in the GC oven. The temperature of 155°C was tested for 30, 60, and 90 minutes, and a higher temperature of 175°C for 30 minutes was evaluated. The compounds of the S- and V-group showed comparable concentrations with reasonable standard deviations in all tested temperature programs. The only significant difference in LOP concentration was observable for coumaric acid and ferulic acid. In the 90 minute program, coumaric acid was significantly lower than in the other three approaches, while ferulic acid behaved contrary with a significantly higher concentration. As both compounds rank among the C-group, this observation did not affect the overall concentration. Regarding the LOP groups, only the 30 minute approach with 155°C showed substantially lower concentrations, hence this temperature program was too short to obtain sufficient degradation of the polymeric lignin and because of that was ruled out as the optimal method (Figure 29).

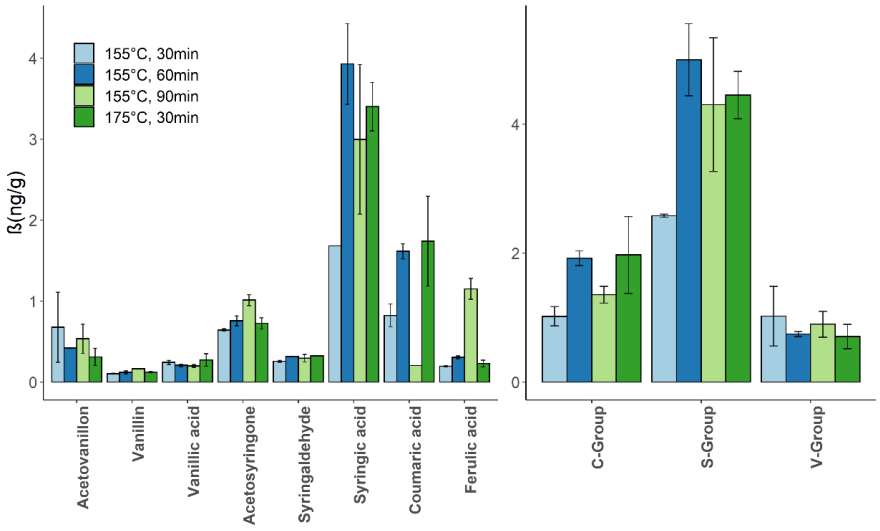

Figure 29: Bar diagrams of mass concentrations (ng/g) of LOPs (left) and bar diagram of summed up mass concentrations of LOP groups (right) resulting from different temperature programs with $CuSO_4$ oxidation. Errors were determined by the standard deviations of respectively threefold determinations.

5.3.2.1 Evaluation of side reactions

As the three remaining temperature programs showed comparable results, another approach to evaluate the quality of the different temperature programs, was the impact of possible side reactions. One of those, which is only relevant for the C- and V-group is a ring-opening reaction, whereby the aromatic system of the compounds is disturbed and a diacid is formed (Figure 30).

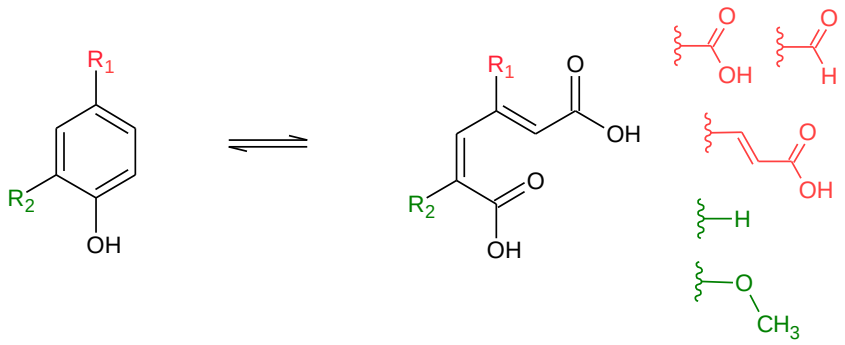

Figure 30: Possible ring-opening reaction of compounds of the C- and V-group

To qualitatively evaluate the ring-opening reaction, the sum formulas, *m/z* values, and retention times shown in Table 2 were used.

Table 2: Sum formula, *m/z*, and retention time (t_R) of LOPs and the postulated products of the ring-opening reaction

Compound	**Formula**	***m/z***	**t_R (min)**	**Ring-opened formula**	**Ring-opened *m/z***	**Ring-opened t_R (min)**
Acetovanillon	$C_9H_{10}O_3$	165.0557	4.7	$C_9H_{10}O_6$	213.0405	3.7
Vanillin	$C_8H_8O_3$	151.0400	3.0	$C_8H_8O_6$	211.0248	2.2
Vanillic acid	$C_8H_8O_4$	167.0350	2.6	$C_8H_8O_7$	241.0354	1.9
Coumaric acid	$C_9H_8O_3$	163.0400	4.2	$C_9H_8O_6$	211.0248	4.1
Ferulic acid	$C_{10}H_{10}O_4$	193.0506	5.8	$C_{10}H_{10}O_7$	241.0354	5.7

Acetovanillon and coumaric acid showed very low ratios, hence the ring-opening reaction is negligible for all temperature programs concerning these compounds. Ferulic acid showed similar ratios in all temperature programs, while vanillic acid and vanillin were most prone to the ring-opening reaction, especially at a higher temperature of 175°C. The lowest impacts of the ring-opening reaction were observed for the temperature programs of 155°C for 30 and 90 minutes (Figure 31).

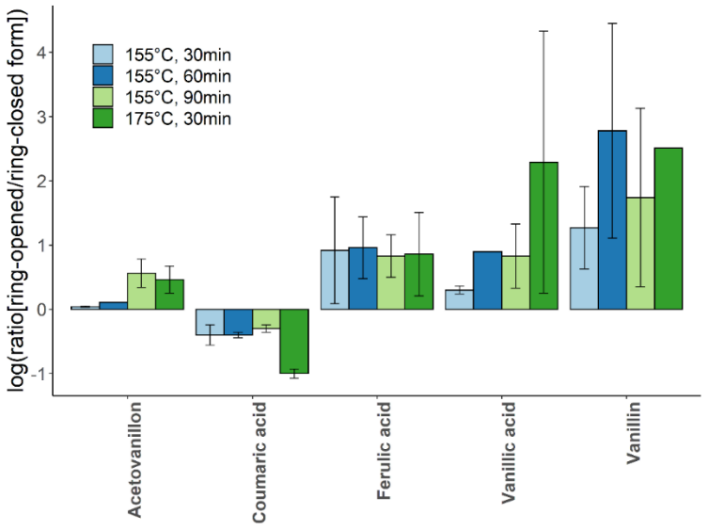

Figure 31: Common logarithm of ratio of peak areas of ring-opened and closed structures at different temperature programs using the $CuSO_4$ oxidation. Peak areas were calculated from the XIC's of the respective *m/z* values but not confirmed by reference standards.

A more relevant issue concerning lignin degradation was over-oxidation. Thereby, the aldehydes of the LOPs are oxidized to the respective acids, and the acids are further oxidized to compounds like caffeic acid or dihydroxybenzoic acid (DHBA), which are not accounted to the LOP groups and therefore decrease the quality of the analysis. The aldehydes of the S- and V-group (syringaldehyde and vanillin) were prone to over-oxidation when highly oxidative conditions were utilized. To evaluate the impact of over-oxidation on the LOP concentrations, the respective aldehyde and acid ratios of the S- and V-group were calculated for the different temperature programs. The share of vanillic acid varied between 63-70% for the 30 minutes and 60 minutes approach using 155°C and decreased in the 90 minutes approach. A possible explanation for this observation would be the establishment of an equilibrium of the oxidation reaction which requires a certain amount of time. The high amount of vanillic acid in the 175°C program was explained by the high temperature favoring the unwanted side-reaction. Using the 155°C approach for 90 minutes showed the most balanced ratio between vanillin and vanillic acid, while the compounds of the S-group did not show significant dependencies on temperature and time (Figure 32).

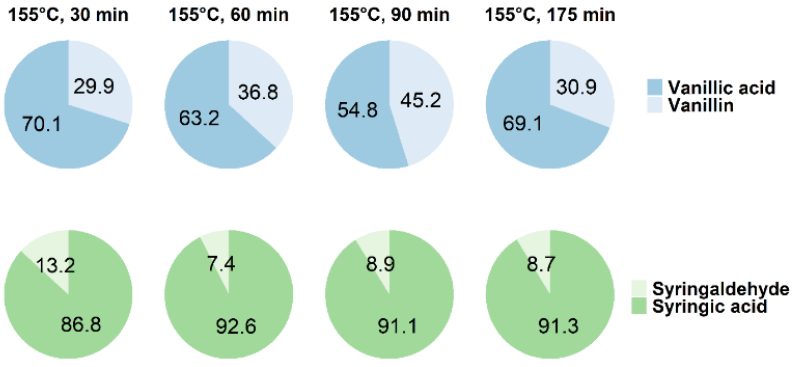

Figure 32: Pie charts of the ratios of acids and aldehydes from the S-group (green) and V-group (blue) using different temperature programs.

Not only the aldehydes of the LOP groups, but also the acids were affected by oxidation. Vanillic acid can be oxidized to DHBA, while coumaric and ferulic acid can be oxidized to caffeic acid (Figure 33).

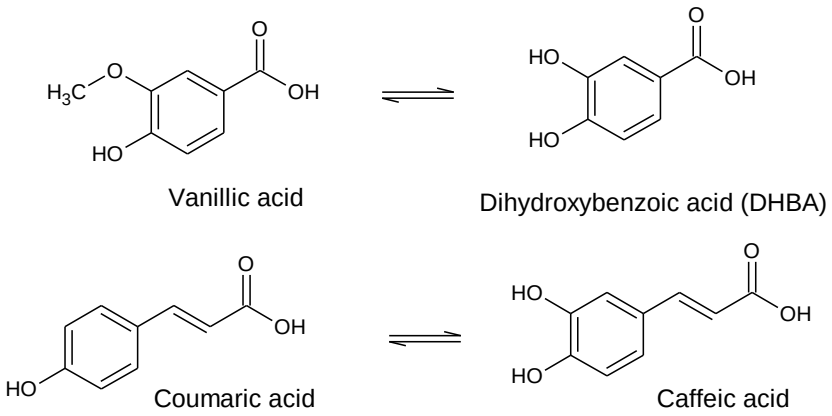

Figure 33: Over-oxidation reaction of vanillic acid to dihydroxybenzoic acid and coumaric acid to caffeic acid.

The XIC of the respective *m/z* values of caffeic acid and DHBA were evaluated for peaks at reasonable retention times (DHBA=1.5 min, caffeic acid=7.0 min) and compared to the peak areas of vanillic acid, coumaric acid, and ferulic acid (Figure 34).

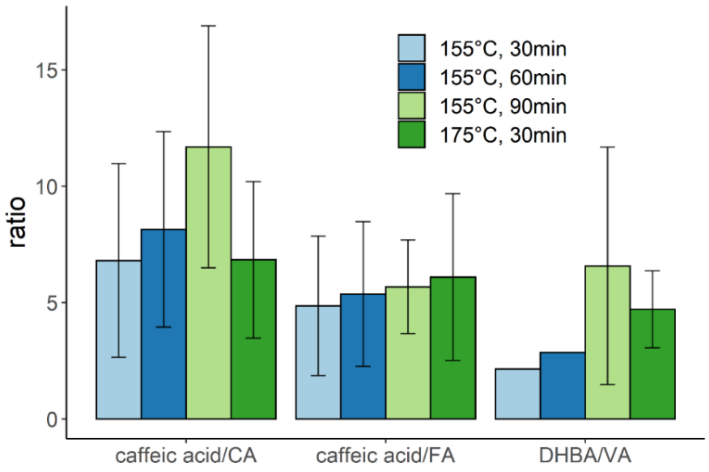

Figure 34: Ratio of peak areas of the *m/z* values of caffeic acid to coumaric acid (CA) and ferulic acid (FA), as well as the ratio of the *m/z* value of DHBA to vanillic acid (VA).

The ratio of caffeic acid to ferulic acid, and hence the over-oxidation of ferulic acid, was similar in all used temperature programs. Coumaric acid showed the highest vulnerability to over-oxidation in the 155°C, 90 minutes approach. Vanillic acid was the least prone to over-oxidation, especially in the 30 minutes and 60 minutes approach at 155°C. Considering all presented observations, no temperature program showed significant improvement compared to the initial approach using 155°C for 90 minutes. Thus, this approach was selected for further measurements and method validation.

5.3.3 Method validation $CuSO_4$ method

The validation of the lignin degradation method proved difficult, as no analytical lignin standards with known lignin compositions are commercially available. Therefore, repeatability was evaluated with the standard speleothem solution (Figure 27). Not taking into account the presented outliers, the standard deviations were between 1.23% for syringaldehyde and 49.75% for coumaric acid. Since the used speleothem standard solution was not entirely homogeneous, these standard deviations were not interpreted as low repeatability, but rather representing large differences in the distribution of lignin in the solution (homogeneity) and the overall lignin composition.

The subsequent SPE was evaluated with analytical standards of LOPs by the method limit of detection (mLOD), method limit of quantification (mLOQ), linearity, recovery, and matrix effects, as it was a novel approach using a total sample volume of only 250 µL. After the $CuSO_4$ oxidation, a second SPE was conducted to extract the LOPs and replace the alkaline solution by an organic solvent. This second HLB-SPE was evaluated for the mLOD, mLOQ (Table 3) and linearity of the individual LOPs by enrichment of standards of linearly increasing concentrations (1 ng/mL, 5 ng/mL, 10 ng/mL, 25 ng/mL, 50 ng/mL, 75 ng/mL, 100 ng/mL, 250 ng/mL, 500 ng/mL). Eight blank samples containing only the matrix (NaOH and HCl) were similarly enriched, to calculate the mLOD and mLOQ according to Equation 15 and Equation 16.

$$mLOD = \frac{3 \cdot SD(blank)}{m}$$

Equation 15

$$mLOQ = \frac{10 \cdot SD(blank)}{m}$$

SD = standard deviation

m = slope of calibration curve

Equation 16

All mLOQ values were in comparable ranges between 1.28 ng/mL and 15.66 ng/mL. Coumaric and ferulic acid showed the lowest mLOQ values, as they contain the largest π-electron systems, they are strongly enriched by the HLB phase and are well ionized in the ESI, due to their acidic functionality. Acetovanillon, syringaldehyde and vanillic acid showed the highest mLOQ values, most probably due to their low ESI response.

Table 3: mLOD and mLOQ of individual LOPs for the second solid-phase extraction and subsequent measurement.

Compound	mLOD (ng/mL)	mLOQ (ng/mL)
Acetovanillon	4.70	15.66
Vanillin	1.33	4.43
Vanillic acid	3.61	12.03
Acetosyringone	2.83	9.44
Syringaldehyde	3.01	10.02
Coumaric acid	0.38	1.28
Ferulic acid	0.99	3.30

The linearity of the SPE method was evaluated by plotting the ratio of peak area and concentration (I/c) to the logarithm of the concentration (c). By this calculation, the ratio (I/c) is equal for all concentrations and hence each standard that ranged within a 5% deviation of the mean value of all ratios was considered in linear range (Figure 35).

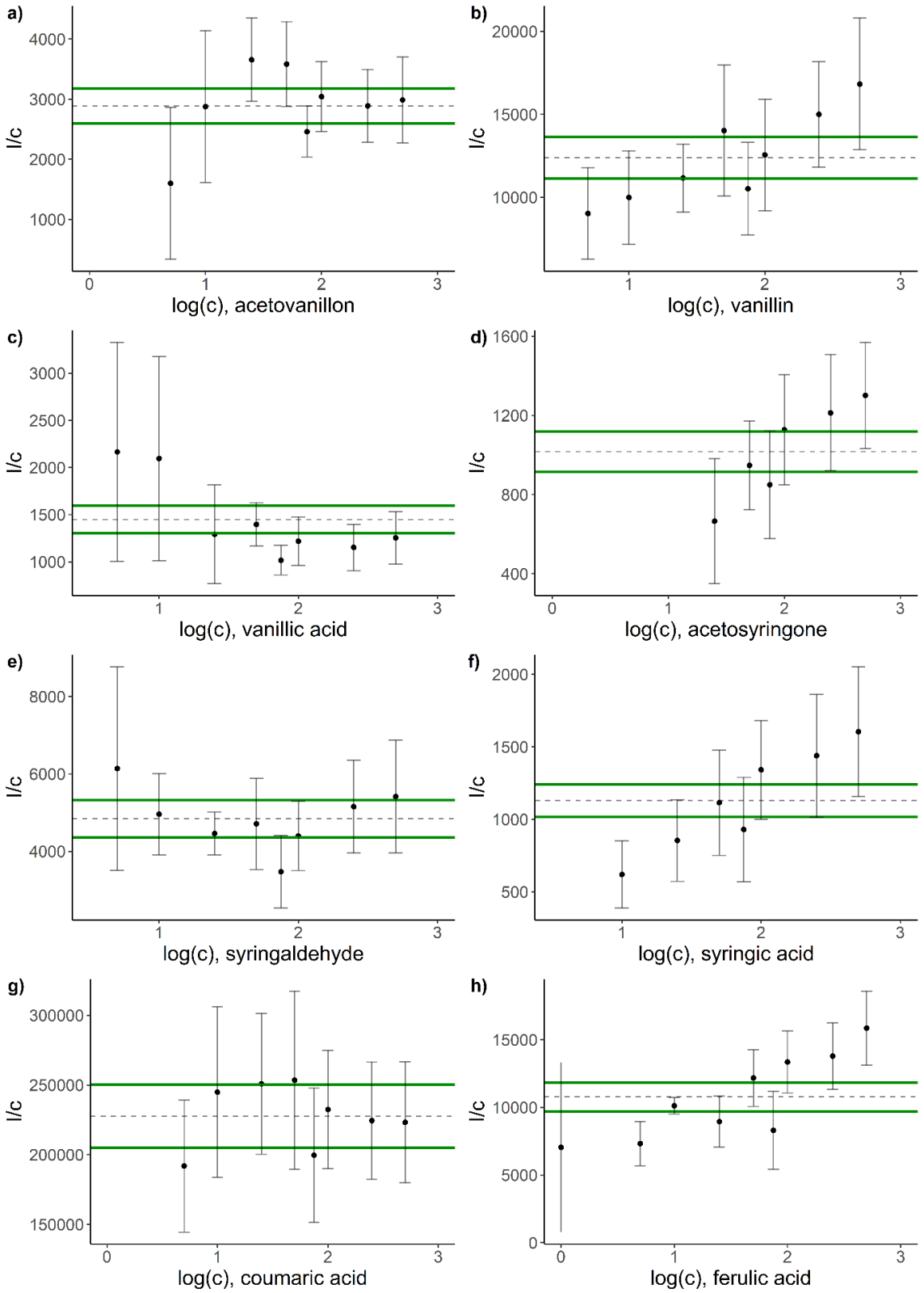

Figure 35: Visualization of the linearity of the HLB-SPE and LC-MS measurement for each individual LOP (a=acetovanillon, b=vanillin, c=vanillic acid, d=acetosyringone, e=syringaldehyde, f=syringic acid, g=coumaric acid, h=ferulic acid) by plotting the peak areas (I) divided by the concentration to the logarithm of the concentration. The mean value of all concentrations is shown, as well as the five percent limits, which are used to classify a value as in linear range. Error bars were calculated by the standard deviation of threefold measurements.

With the known mLOQ values and linearity estimation, the recovery and matrix effects of the $CuSO_4$ oxidation on individual LOPs was experimentally investigated. For that, three different standard solutions containing 100 ng/mL (final concentration) were prepared (Figure 36).

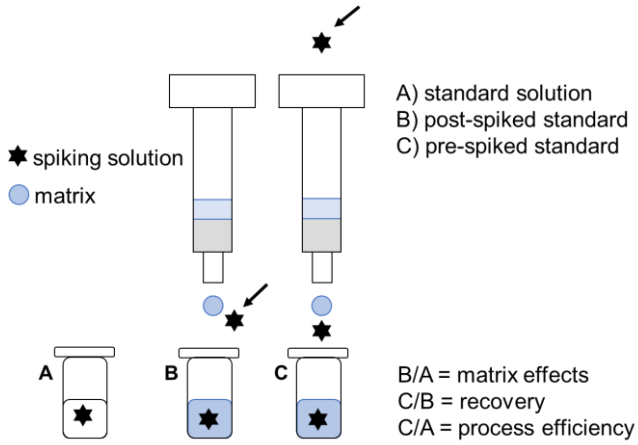

Figure 36: Experimental design of the determination of recovery, matrix effects and process efficiency by examination of a standard solution (A), post-spiked standard (B), and pre-spiked standard (C).

Each standard solution was prepared three times to calculate recovery and matrix effects, as well as respective standard deviations (Figure 37). The recovery of a compound was considered sufficient in a range between 80-120%, which is marked by a green square. Acetosyringone, syringic acid, vanillic acid and vanillin showed recoveries in this range, while all other compounds had lower recoveries. Recovery represented the retention behavior of the respective compounds on the HLB cartridge. Coumaric acid, syringaldehyde, ferulic acid, and acetovanillone showed low recovery around 50%, hence they were not quantitatively retained (coumaric and ferulic acid due to their acid functionalities) or eluted (syringaldehyde and acetovanillone due to their strong affinity to the solid phase) from the HLB material. Additionally, the low sample volume of 250 µL complicated the SPE, as sufficient wetting of the entire solid phase with the sample proved difficult. The matrix effects represented the behavior of compounds in comparison to matrix components in the ESI source and were distinguished between ion enhancement (green) and ion suppression (red). Ion suppression led to lower signal intensities of the LOPs due to co-eluting matrix compounds with higher ESI responses, while ion enhancement resulted in an opposite effect of higher signal intensities. Both effects can result in either over- or underestimation of a compound. No LOP showed matrix effects entirely higher than 50%. All compounds of the V-group were affected by ion suppression, while the S-group compounds were affected by ion enhancement. The C-group was hardly influenced by matrix compounds, which is why coumaric acid was not displayed.

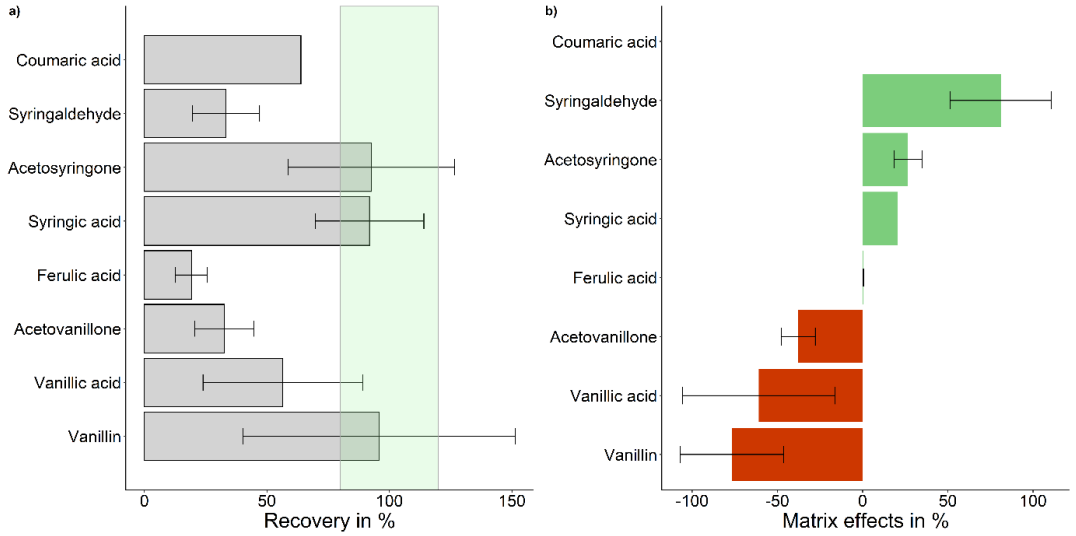

Figure 37: Recovery (a) and matrix effects (b) of LOPs enriched by HLB-SPE after the $CuSO_4$ oxidation. Sufficient recovery of 80-120% is marked in green. Matrix effects are distinguished between ion enhancement (green) and ion suppression (red). Error bars result from the standard deviation of threefold determinations.

5.3.4 Method development levoglucosan HILIC

Lev and its isomers Gal and Man are small, polar compounds, which were not accessible by standard RP-LC methods, as they were not retained by the non-polar stationary phases and eluted in the void volume. Thus, a novel chromatographic approach was evaluated using HILIC columns with two different functionalities: the iHILIC-Fusion and the iHILIC-Fusion(+). Both columns are silica-based with hydroxyethyl amide chains, modulated with trimethyl-ammonium groups for positive charging and sulphate groups for negative charging. The Fusion(+) column contains a higher amount of positively charged moieties to enhance retention of negatively charged compounds like carboxylic acids or phenolic compounds. Both columns were tested using ammonium formate as a buffer and ACN as organic solvent at a proportion of 3:97 (buffer/ACN). The buffer concentration, buffered pH-value, as well as temperature were modified to obtain proper separation of Lev and the adjacent Man (Figure 38). Some conditions, marked by a green connection, like higher temperatures that strongly influenced the separation on the iHILIC-Fusion column did not have an effect on the retention time on the iHILIC-Fusion(+) column. In general, higher temperature led to lower retention time and likewise lower separation. The clearest separation was achieved using a buffer concentration of 10 mM, at a pH value of 6.0 and a temperature of 30°C (Figure 38, red). The chromatographic results did not only depend on the separation of the individual compounds, but also on the signal-to-noise ratios. These were significantly higher using a buffer concentration of 5 mM at a pH value of 6, compared to all other conditions. As the separation was also sufficient using these conditions (Figure 38, blue), the final method was set up of a buffer concentration of 5 mM ammonium formate at a pH value of 6, and a temperature of 30°C.

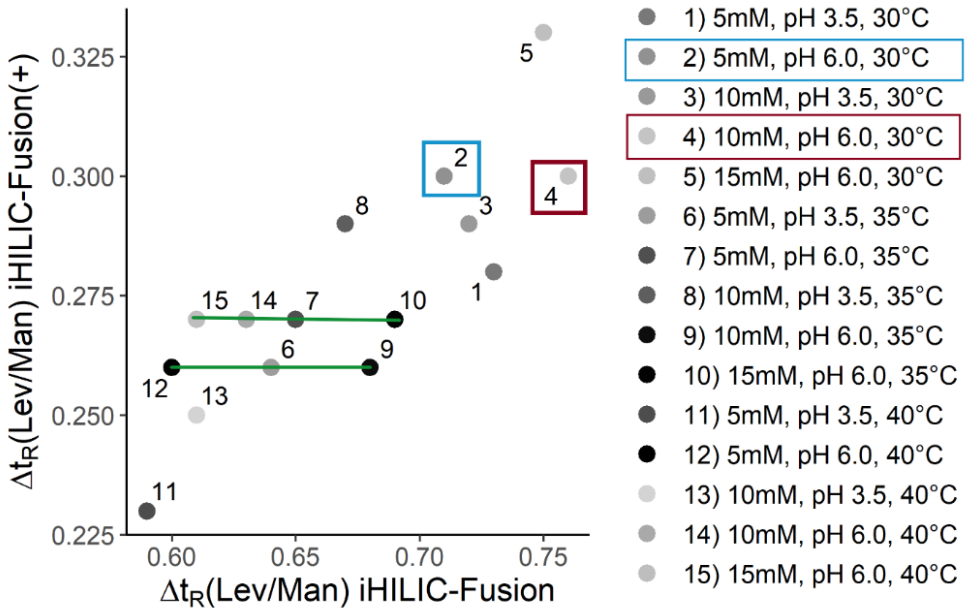

Figure 38: Retention time differences of levoglucosan and mannosan on the iHILIC-Fusion, and iHILIC-Fusion(+) column using different concentrations of ammonium formate buffer (5mM, 10 mM, 15mM) at different temperatures (30°C, 35°C, 40°C) and different pH values (3.5 and 6.0). Optimum conditions which were used hereafter are marked in red. Conditions which influenced retention on the iHILIC-Fusion column but not on the iHILIC-Fusion(+) column are marked with a green connection.

Another issue concerning Lev and its isomers was ionization in the ESI source. Although it is a very polar compound, ionization of Lev is challenging, as the pK_a values range from 12.21 to 14.74 and the used HILIC column did not provide pH stability above a pH value of 10. An alkaline PCF was used to support deprotonation of Lev after the HILIC column. A solution of 50 mM ammonium hydroxide in different solvents (ACN, MeOH, and water) was tested and peak intensities were compared to the results with no PCF (Figure 39, left). The peak intensities were enhanced strongest with a methanolic solution of ammonium hydroxide, while ACN and water showed only minor positive influence compared to the results with no PCF. The methanolic solution of ammonium hydroxide was further evaluated by different flow rates of the PCF from 50 µL/min to 200 µL/min (Figure 39, right). Here, peak intensities were lowest when using a flowrate of 200 µL/min and 150 µL/min due to heavy dilution. A PCF of 50 µL/min and 100 µL/min resulted in comparable peak intensities, with predominantly better results using 100 µL/min. The final method consisted of a flowrate of 400 µL/min through the column and additional 100 µL/min of PCF with 50 mM ammonium hydroxide in MeOH.

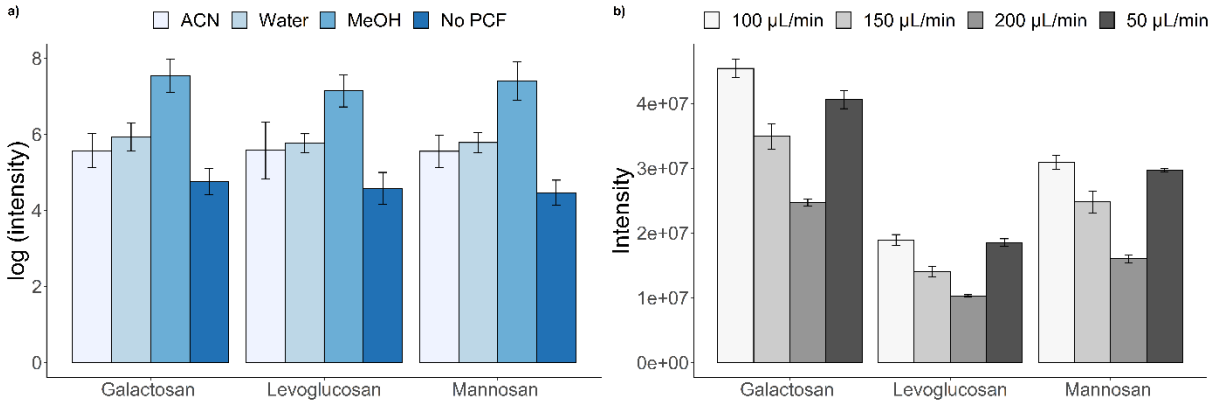

Figure 39: Influence of different post-column flow conditions on the peak intensities of galactosan, levoglucosan, and mannosan. 50 mM of ammonium hydroxide were tested in different solvents (a). The best results were observed in methanol, so methanol was further investigated as a solvent with different flow rates (b) from 50-200 µL/min.

5.3.5 Application of the novel lignin extraction approach

The novel lignin degradation approach was applied to two flowstone samples from DC and WP from New Zealand. Lev was analyzed using the methods described in 2.3 and 2.4. Data on trace elements were provided by Adam Hartland and Andrew Pearson from the University of Waikato (Hamilton, New Zealand) and can be found in detail elsewhere (Pearson, 2020). The development of the Mg/Ca ratio, the mass concentration of Lev, the sum of LOPs, as well as the C/V and S/V ratios in DC and WP were analyzed between 14,000 years before present (yrs BP) to the present day (Figure 40). Four stages were defined from 14,000-12,000 yrs BP (1), 11,500-9000 yrs BP (2), 9,000-6,000 yrs BP (3), and 4,000 yrs BP to the present day (4). Stage 1 is referred to as “Lateglacial warming”, stage 2 as the “Holocene Climatic Optimum” (HCO), stage 3 as “Mid Holocene cooling”, and stage 4 as “Late Holocene Cooling”.

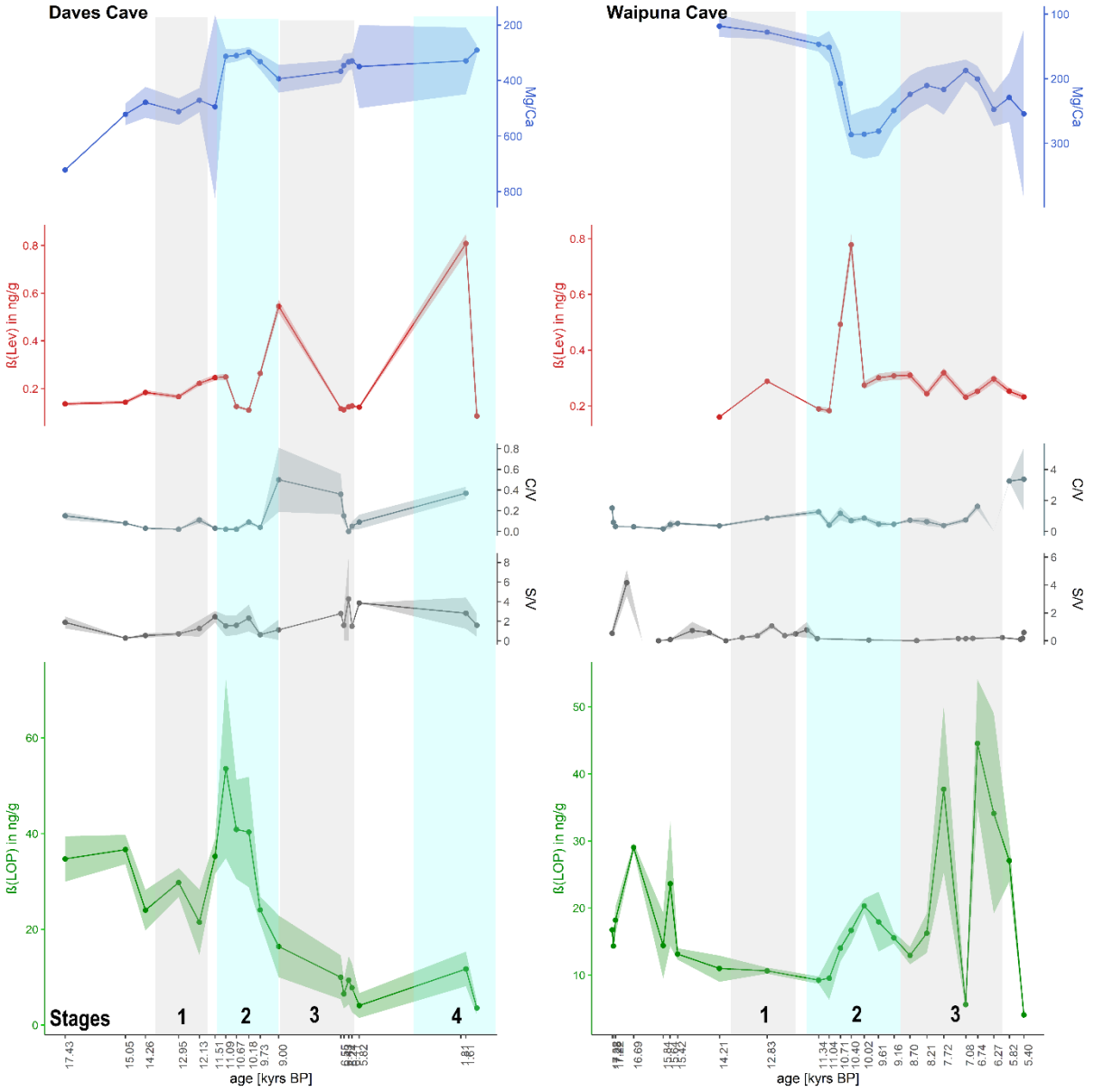

Figure 40: Temporal course of Mg/Ca ratio (blue), mass concentration of levoglucosan in ng/g (red), C/V ratio (lightgrey), S/V ratio (darkgrey), and summed mass concentration of LOPs in ng/g (green) in Daves Cave (left) and Waipuna Cave (right). Four stages are marked assigned to certain time periods in the Holocene. Deviations were calculated by the standard deviations of multiple measurements (n=3), or rather the standard deviations of multiple trace element measurements on one sample used for lignin and levoglucosan analysis.

5.3.5.1 Daves Cave

The analysis of the DC samples showed two distinct concentration plateaus of LOP and Mg/Ca. From 10,000 yrs BP to ca. 1,000 yrs BP Mg/Ca and LOP mass concentration were rather low while rising in the second half from ca. 17,500 yrs BP to 10,500 yrs BP. Higher Mg/Ca ratio are associated to drier conditions, while lower Mg/Ca ratio represent higher precipitation (Immenhauser et al. 2010; Riechelmann et al. 2012).

The time range covered by the flowstone covered different stages of climate conditions, including the lateglacial warming, HCO, and Mid Holocene cooling phase, stages 1-3, respectively. The lateglacial warming was characterized by lower temperature, lower treeline, and hence lower organic productivity above the cave compared to modern times. In the DC flowstone, this was reflected by higher Mg/Ca ratios, medium LOP concentrations, and low C/V and S/V ratios.

Stage 1 showed a positive correlation of Mg/Ca to LOP (r=1), a strong anticorrelation of Mg/Ca to Lev (r=-0.8), and an anticorrelation of Lev to LOP (r=-0.8). The positive correlation of LOP to the Mg/Ca ratio revealed that during dry phases, lignin was not exclusively transported by water, as this would result in an anti-correlation between the proxies (Figure 41). Adsorption of lignin to particulate matter in drip water was described in the literature (Heidke et al. 2021), which was supported by the Mg/Ca correlation to the V-group concentration because V-group lignin is less water soluble. The transport of lignin adsorbed to particulate matter through the soil depends on soil productivity (Hellstrom and McCulloch 2000), the leaching and sorption equilibrium of lignin to particles (Hernes et al. 2007), and microbial resistance of lignin during transport as described by the soil-continuum model (Lehmann and Kleber 2015). In stage 1, Lev was strongly correlated to the C-group concentration (r=1) and C/V ratio (r=1), such that more Lev corresponded to dominantly non-woody vegetation species, e.g. native tussock grasses which are highly flammable representatives of the group of Myrtaceae (Bond et al. 2004b), found at the surface of DC. Due to the anti-correlation of Lev to LOP, a direct entry of Lev from the overlying vegetation by cellulose degradation was ruled out, and the anti-correlation of Lev to Mg/Ca indicated aqueous transport of Lev through the soil.

Stage 2, the HCO, was characterized by expanding forest communities, higher temperature, and precipitation, reflected in the shifting Mg/Ca ratio and LOP concentration plateaus. LOP concentration was strongly elevated in this phase, and the S/V ratio showed a tendency towards gymnosperm vegetation. The influence of Mg/Ca on LOP and Lev changed, as observable in the shift of the correlation between Mg/Ca to LOP to R=-0.4. Here, generally wetter conditions resulted in predominantly aqueous transport of lignin through the soil. The positive correlation of Lev to the C-group concentration (r=0.8), C/V ratio (r=0.9) and slight correlation to the Mg/Ca ratio (r=0.4) indicated that during the HCO increased flammability of non-wooden vegetation was observed during drier conditions.

Stage 3, the late Holocene cooling, was characterized by lowering temperature, yet with no significant impact on the tree line. The lower Mg/Ca ratio indicated higher amounts of precipitation and generally wetter conditions. The lignin concentration decreased drastically, to even lower levels than during the lateglacial warming. A maximum Lev concentration was found to correspond with strongly increased C/V ratios. Here, both proxies, LOP and Lev showed a strong positive correlation to the Mg/Ca ratio (r=0.9 and r=0.8, respectively), and consequently LOP and Lev were also positively correlated to each other (r=0.9). While the correlation of Lev to the C-group was constantly observed (r=1), the relationship to the V-group changed from strong negative correlation in stage 1 (r=-1) to strong positive correlation (r=1) in stage 3.

Summarizing, in stage 1, the proxy correlations indicated dominantly aqueous transport of Lev, and contrary behavior of LOPs, for which a transport through the soil by adsorption to particles was postulated. In stage 2, the correlations of both proxies changed. During the warmer and wetter conditions, neither Lev, nor the LOP concentration reflected precipitation. However, LOPs shifted towards aqueous transport, rather than adsorption. During stage 3, Lev and LOPs behaved similarly in a positive correlation to decreasing precipitation. Here, no straightforward explanation was available, but the increased C/V ratios, as well as peaking Lev concentrations indicated the influence of biomass burning events on LOP and Lev concentration in the DC flowstone.

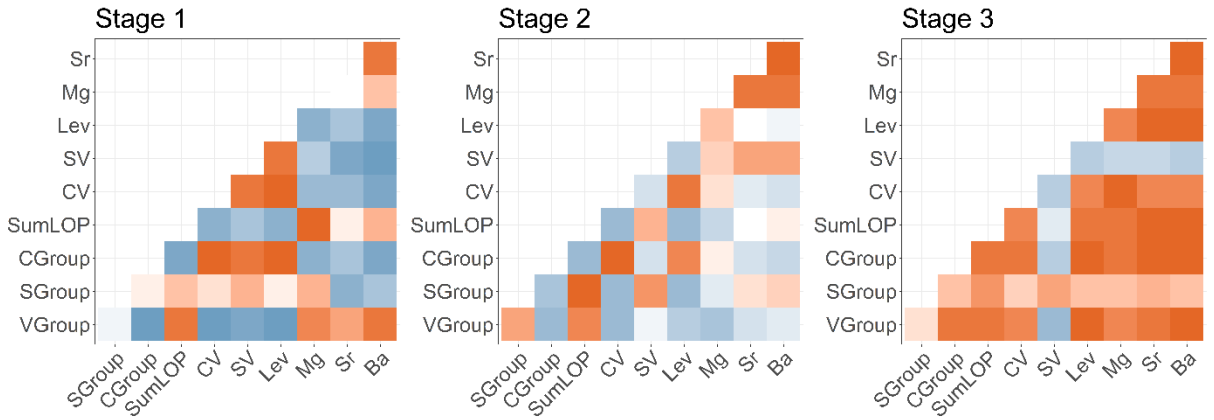

Figure 41: Correlograms of LOP proxies, trace elements and levoglucosan in stages 1-3 of Daves Cave.

5.3.5.2 Waipuna Cave

WP, located in the Northern Island of New Zealand, is covered by dense vegetation, and currently, the amount of rainfall is much higher than at DC, so drip rates inside the cave are also higher (Hartland and White 2019). Lignin concentration was not expected to be influenced by shifts of the tree line in response to varying temperature, due to the comparably low altitude of 395 m above sea line. All these external observations led to the assumption that lignin concentrations should be much higher in WP than in DC, yet mass concentrations were comparable (Figure 40).

Stage 2 showed high Mg/Ca ratios and LOP concentrations similar to those observed in DC. Lev showed a concentration peak and a positive correlation to the C-group (r=0.6) and C/V ratio (r=0.7), accordingly to DC indicating a linkage between abundance of non-wooden vegetation and flammability (Figure 42). LOP concentration was a strongly positively correlated to the Ba/Ca (r=0.9) and Sr/Ca (r=0.8) ratio, while a weak anti-correlation to the Mg/Ca ratio (r=-0.4) was found. Thus, transport of lignin through the soil was proposed to be more influenced by aqueous transport depending on the amount precipitation. Even though the HCO was characterized by higher temperature and precipitation, the Mg/Ca ratios in the flowstone sample decreased. During a three-year drip water monitoring study in WP, increasing prior calcite precipitation (PCP) in WP especially during dry phases was observed (Nava-Fernandez et al. 2020) suppressing the inclusion of Mg into the speleothem crystal. The correlation of Mg/Ca and Sr/Ca in speleothems is a proxy for enhanced PCP (Fairchild and Treble 2009; Mischel et al. 2017), but was not observed in the WP flowstone sample (r=0). Another explanation for incoherent LOP concentrations were the high drip rates in WP, which disturbed proper inclusion of proxies into the speleothem due to dilution (van Beynen et al. 2008).

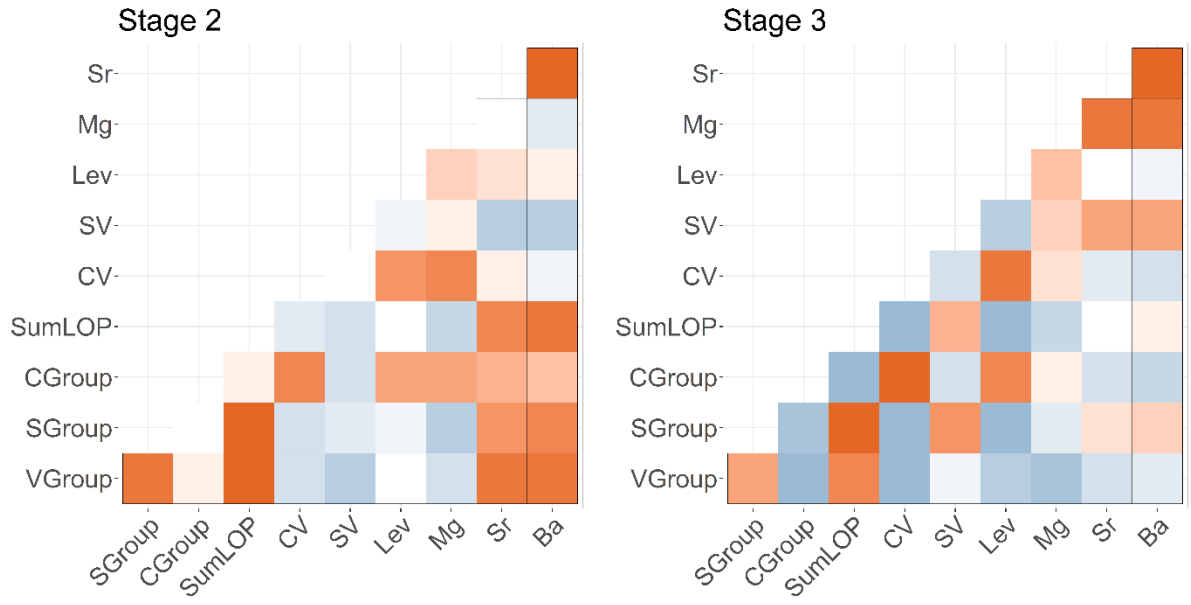

Figure 42: Correlograms of LOP proxies, trace elements, and levoglucosan in the stages 2 and 3 of Waipuna Cave.

Stage 3 showed high variations in LOP concentrations, with two peaks at 7,720 yrs BP and 6,270 yrs BP. The Mg/Ca ratio showed a shift back to lower values. Although the amount of precipitation was increasing, as indicated by decreasing Mg/Ca ratio, the associated correlation to the LOP concentration remained at r=0.4. Lev maintained a strong correlation to the C/V ratio (r=0.9) and C-group concentration (r=0.8). In stage 2, high Mg/Ca ratios in a period of elevated precipitation were observable indicating strong PCP effects, but the supportive Mg/Ca to Sr/Ca correlation was missing. In stage 3, these counterintuitive observations continued, as a decreasing Mg/Ca ratio indicated less PCP but a strong correlation to Sr/Ca (r=0.9) was found. The inclusion of Lev and lignin into the speleothem could also be disturbed by PCP in this stage, however the available data did not allow drawing reasonable

conclusions on that. Artificial cave setups could be used to study the inclusion mechanism of lignin and Lev into speleothems under different conditions like temperature, drip rates, or pCO_2 (Wiedner et al. 2008; Polag et al. 2010; Hansen et al. 2017).

5.3.5.3 Comparison of Daves Cave and Waipuna Cave

In the comparison of the proxy records in both caves (Figure 43) DC showed stronger positive correlations between LOP proxies, Lev, and trace elements Ba, Sr, and the Mg/Ca ratios, while the developments in WP were more independent from each other. The Mg/Ca ratio as a proxy of precipitation did not show strong correlations along the entire records, but proxy interactions were influenced by the predominant conditions in the defined stages 1-4.

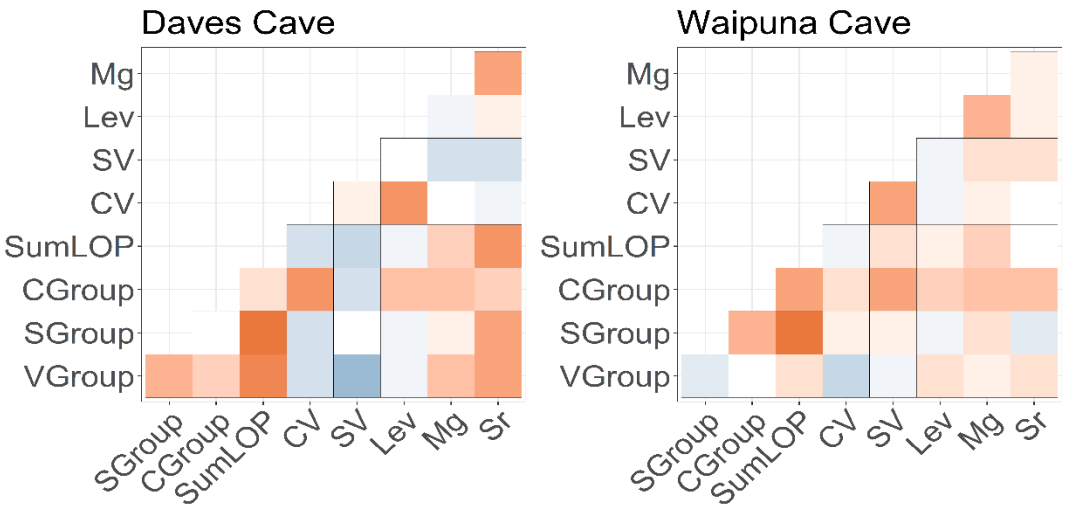

Figure 43: Correlograms of LOP proxies, trace elements, and levoglucosan in all samples from the flowstone of Daves cave (left) and Waipuna cave (right).

When the Mg/Ca ratio was lower during phases of elevated precipitation clear positive correlations of Lev to the Mg/Ca ratios were observed in both caves. Here, the correlation was associated to increased flammability of the vegetation during drier conditions, rather than the transport mechanism of Lev through the soil. The Sr/Ca to Mg/Ca correlation was proposed to evaluate the impact of PCP, so a strong positive correlation hinted to high PCP impact and vice versa. In DC, the Lev to Mg/Ca correlation changed from dry to wet conditions from a negative to a positive correlation, as well as the Lev/LOP correlation, while in WP these values remained constantly in a medium range independently from external conditions. The Lev input to DC appeared to be strongly influenced by external conditions like precipitation and vegetation. In the drier phase, this supported the theory of biomass burning related entry of Lev into the flowstone, since Lev showed negative correlation to LOP, so a direct entry from the vegetation above the cave was ruled out. In addition, decreasing vegetation cover, represented by lower LOP concentration, resulted in higher Lev concentrations, indicating burning events, limiting the vegetation above the cave. A long-term feedback effect of the soil CO_2 concentration in karst environments showed an influence of wildfires on speleothem growth (Coleborn et al. 2016). The lack

of CO_2 reduced the amount of dissolved carbonate in the soil and epikarst, which then led to lower dissolved carbon concentration in drip water and thus lower speleothem growth rates (Genty et al. 2001b). This was supported by the fact that Lev only showed higher concentrations during the dry phase, where burning events, or rather ignition by lightnings are more likely than in wetter periods, and the correlation of Lev to the C/V ratio, which corresponded to higher amounts of grasses than fire-intolerant forests (Bond et al. 2004b).

To improve the understanding of the influence of external influences on proxy concentrations, a principal component analysis (PCA) was conducted (Figure 44). In DC 42.49% of the variance was explained by principal component (PC) 1. The LOP concentration (0.44), Sr/Ca (0.43), and the V-group had the highest weightings on PC1, while the C/V ratio (0.59), C-group (0.59), and Lev concentration (0.50) had the highest weightings on PC2, which explained 22.85% of the total variance in DC. PC1 was summarized as vegetation abundance and composition and was mainly responsible for the distinction of the two concentration levels (Figure 40). PC2 was summarized as biomass burning and showed a strong effect on the sample from 9,000 yrs BP. This again supported the assumption of enhanced fire probability based on the type of vegetation defined by the C/V ratio. Here, Lev showed a peaking concentration, and the LMG ratio was 1.84 (Figure 45).

In WP, PC1 explained 28.23% of the total variance and PC2 explained 21.53%. PC1 was weighted by the C-group (0.54), the LOP concentration (0.48) and the S-group (0.42), while PC2 was weighted by Ba (0.53), the C/V ratio (0.45), and Sr (0.43). Neither PC1 nor PC2 were significantly influenced by Lev, so biomass burning had a less severe effect on vegetation above WP than DC. Samples which were influenced by PC2, showed a rather low Mg/Ca ratio, so in drier periods the transport processes of Lev and lignin in WP appeared similar to DC in terms of a shift from transfer through the aquifer towards transport by adsorption to particles through the soil. Some samples in the PCA of WP were strongly influenced by the LOP concentration and in general the LOP concentration in WP was in comparable ranges to DC. This observation contradicted with the expectations of much higher LOP concentrations in WP due to the lower altitude, higher extents of rainfall, and denser vegetation Due to high precipitation and resulting high drip rates in the cave, Lev was expected to be readily transported into the speleothem due to its high water-solubility. In turn, the inclusion of lignin into the speleothem was proposed to be disturbed by the high drip rates. Here, a drip water study of Lev and lignin would provide a clearer insight into the inclusion mechanisms of both proxies into the speleothem at the respective sites. Only one clear Lev concentration maximum was observed between 10,710 yrs BP and 10,400 yrs BP. The corresponding LMG ratios were assigned to atmospheric aerosols, grasses, or average hardwood as emission sources (Fabbri et al. 2009). No decrease in LOP concentration was observable following the elevated Lev concentration. Therefore, aerosol deposition from a remote fire event concluded more likely than a local fire event eliminating vegetation above the cave. In general, fire events on this part of the North Island during the Holocene were unlikely, due to the high rainfall and lack of severe drought phases. Lightning strikes were the only natural course in pre-settlement times to

ignite a wildfire event but in comparison to the western part of the southern island, (where DC is located), fewer thunderstorms and lightning strikes were observed (Bond et al. 2004b).

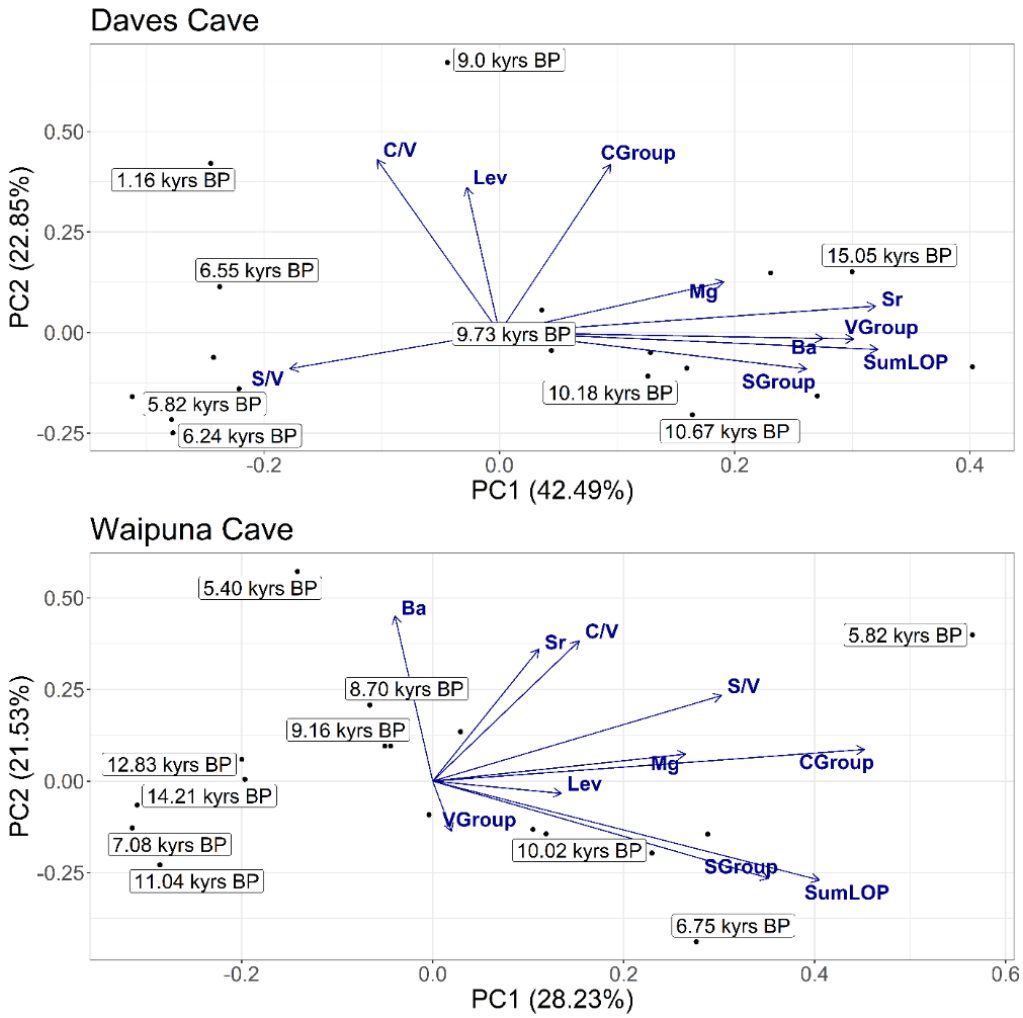

Figure 44: Principal component analysis of LOP proxies, levoglucosan, and trace elements in the flowstone samples from Daves cave (top plot) and Waipuna cave (bottom plot).

The LMG ratio of 1.84 in DC was assigned to an emission source of hardwood, softwood, or grasses, yet not to atmospheric aerosols (Fabbri et al. 2009), indicating a local fire event which reduced the vegetation, and resulted in larger relative amounts of non-wooden vegetation. Charcoal and pollen records from the eastern southern island of New Zealand indicated three phases of wildfire activity during the Holocene from 10,000-2,600 yrs BP (infrequent, patchy fires), 2,600-1,000 yrs BP (slightly increased fire frequency), and 800-500 yrs BP (strongly increased frequency) (Rogers et al. 2007). Increased wildfire frequency after 2,600 yrs BP is presumed to result from intensified El Niño activity and related droughts. Several fire events on the Southern Island were observed between ~9,000 yrs BP and ~7,500 yrs BP (Porters Pass, Canterbury, 8,900 yrs BP, Mackenzie Basin, 7,996 yrs BP, Manorburn, Central Otage, 7,667 yrs BP). The flammability of vegetation was defined by ignitibility and combustibility. Both depend on droughts and type of vegetation. Low-phenolic hardwood species and shrubs were rather low-flammable, while phenolic-rich woody species and grasses were highly prone to

ignition. This supported the observation of the sample from 9,000 yrs BP, where predominantly non-wooden, flammable species (according to the C/V ratio and the LMG ratio), and a peak in Lev concentration were observed. The equally high Lev concentration at 1,160 yrs BP fell into the time of increasing amount of fire events with a LMG ratio of 4.84 (similar to 11,090 yrs BP), which was not assigned to a certain emission source as it included softwood, hardwood, and grasses. (Fabbri et al. 2009)

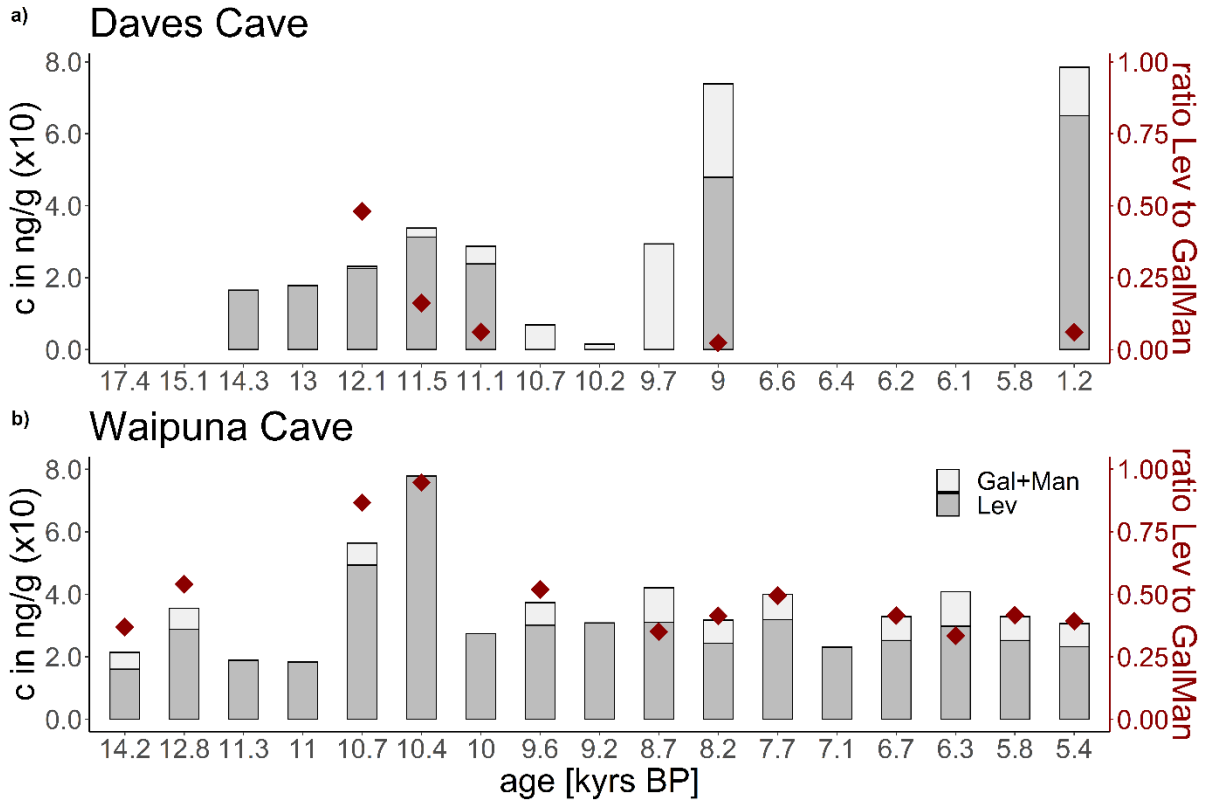

Figure 45: Levglucosan, mannosan and galactosan mass concentrations in ng/g in flowstone DC15 from Daves cave (a) and WP15 from Waipuna cave (b). The total concentration is divided into the isomer levoglucosan and the summed concentration of galactosan and mannosan in each sample. The ratio of levoglucosan to the isomers (Lev/Gal+Man) is shown by red squares.

5.4 Conclusion and Outlook

Lignin is a the second most abundant biopolymer after cellulose and exclusively linked to terrestrial vegetation. The amount and monomeric composition of lignin is analyzed to study paleo-vegetation. The polymeric structure is degraded, to access the monomeric subunits. For that, a catalyzed alkaline oxidation was used, with Cu(II)O as catalyst. However, these oxidation methods consumed large amounts of organic solvents and produced hazardous solid CuO waste. Here, a novel degradation approach using soluble $CuSO_4$ as catalyst was adapted from the analysis of river and ocean samples to speleothem samples. A thorough comparison of the two oxidation methods using CuO and $CuSO_4$ demonstrated comparable performance for both methods. Different reaction conditions for the $CuSO_4$ oxidation were evaluated for possible side reactions and consistent representation of the monomeric composition. The optimized method was validated by linearity, LOD, LOQ, recovery, and matrix effects.

Another environmental proxy analyzed in this work was Lev. To separate Lev from its isomers Gal and Man, a novel HILIC-HR-MS method was developed. Lev from the dissolved speleothem solution was straightforwardly enriched by addition of a second SPE using GCB material. The enrichment of Lev from the speleothem requires further optimization for example using LLE, other SPE materials, or liquid extraction from the solid speleothem samples before dissolving. Also, the HILIC method can be optimized regarding long-term performance or other columns can be used for the separation for example with chiral stationary phases.

Both methods were applied to two different flowstone samples from cave sites in New Zealand as proof-of-principle and to evaluate the behavior of Lev and lignin compared to trace elements like Mg, Ba, and Sr. This comparison revealed, that the LOP concentration strongly depends on the transport mechanisms through the soil. Especially in DC, during drier phases, lignin was not exclusively transported by water, but also by adsorption to particles. However, in phases with increased rainfall, and hence higher drip rates, the dominant transport mechanism proposedly shifted towards aqueous transport.

Additionally, Lev shows strong affinity to lignin from non-wooden vegetation, in accordance with the higher flammability of grasses in comparison to phenolic-rich wooden species. In DC, the overall impact of Lev and the non-wooden vegetation markers was significant, thus DC seemed to be exposed to local fire events more frequently and more intense than WP during the Holocene. The moderate correlations of Lev to the Mg/Ca ratio (positive and negative) did not reveal a dominant transport mechanism.

In the time after the HCO (stage 3), Lev and LOP concentration showed trends, which were not explainable by the available data. Further experiments should be conducted analyzing drip water in both caves at regular intervals and additional speleothem samples with higher temporal resolution. Special focus should be given to the inclusion mechanism of both proxies into speleothem carbonate. A study of the inclusion mechanism is possible using artificial cave setups.

6. Cave aerosols as important source for organic compounds in speleothems – a case study from Waipuna Cave, New Zealand

6.1 Introduction

The impact of aerosols on cave environments and therein growing speleothems is of growing interest (Zhao and Hopke 2006; Dredge et al. 2013; Smith et al. 2013; Faimon et al. 2019). Partial CO_2 pressure in the cave is regulated by the air exchange between surface and has an influence on speleothem growth, (Spötl et al. 2005). The consequences of increasing anthropogenic CO_2 emissions in the atmosphere and their influence on cave air are not yet fully elucidated (Faimon et al. 2006). The presence of aerosols in caves is also driven by cave ventilation and the sources include externally introduced aerosols and internally produced aerosols (Dredge et al. 2013; Grgić et al. 2014)

In the cave, aerosols are accumulated either by dry or wet deposition and removed from the cave with air and water flux. Dry deposition results from interception of the air pathway, thereby aerosols collide with obstacles, by sedimentation, or by statistical particle collision due to Brownian diffusion (Wesely and Hicks 2000; Petroff et al. 2008). Wet deposition is induced by drip water, cloud formation in the cave (Badino 2004), or condensation from cave moisture (Dreybrodt et al. 2005). Aerosol abundance is associated with the source activity, transport, and distribution mechanisms, while the inorganic chemistry reveals information on the aerosol source, transport, impact on speleothems, interaction with the water film during speleothem growth, and deposition. In addition, the organic chemistry provides information on microbial activity in the cave (Dredge et al. 2013). Transport and distribution of aerosols is studied by their size and morphology (Faimon et al. 2019). Finer particles (PM 2.5, <2.5 µm) are associated to anthropogenic emission, while coarse particles (>10 µm) are emitted naturally (Kertész et al. 1999; Pöschl 2005).

The Sr isotope ratio in aerosols provides information on the source region of terrestrial dust and has been analyzed in cave aerosols to assign their source more precisely (Yang et al. 2009; Masson et al. 2010). Internally produced aerosols result from cave visitors (humans or animals), drip water, or host-rock disintegration (weathering). Human cave visitors and cave wind also re-suspend particles from the ground and cave walls (Smith et al. 2013) and carry externally sourced aerosols into the cave. The rate of sedimentation within a 20 meter radius of one person multiplied tenfold during a study conducted in Caves of the Cupp-Coutunn System (Dredge et al. 2013). When drip water droplets hit the floor or stalagmite surface, the turbulent water surface releases aerosols similar to sea spray generation (Maltsev 1997; Schmitt-Kopplin et al. 2012). Weathering leads to host-rock alteration and corrosion resulting in the emission of carbonate particles, another in-cave aerosol source (Zupan Hajna 2003). The most extensively studied aerosol type in cave environments are pollen (Caseldine et al. 2008). Airborne, waterborne, and insect-borne transport of pollen into the cave has been described and comparative deposition studies proposed that the behavior of pollen aerosols can be extrapolated to other pollen-

unrelated aerosols of similar size and morphology (Coles et al. 1989; Burney and Burney 1993; McGarry and Caseldine 2004).

The distribution of aerosols in the cave is controlled by cave ventilation, which itself depends on cave morphology, surface-to-cave air pressure and temperature gradients, and the number of entrances. In general, the aerosol load is reduced towards the cave interior (Navarro et al. 2001) because the required energy for particle transport is not maintained with decreasing cave ventilation (Navarro Camacho et al. 2000), which is particularly relevant for larger, coarse particles (Faimon and Lang 2013; Faimon et al. 2019). The cave morphology has a strong influence on aerosol distribution, because the pathway of the cave air is not undisturbed and surface irregularities cause turbulent air increasing the probability of particle collision, collision of particles with cave walls, and collision of particles with (growing) speleothems.

The aerosol contribution to growing speleothems was studied at the Alpine Obir Cave in Austria, and was found to depend on speleothem growth rate, deposition flux, and aerosol incorporation, factors, which remain insufficiently understood. Gravitational deposition had a stronger influence on stalagmites than stalactites and stalagmites were particularly exposed to aerosols during hiatus events because deposited aerosols were not washed away by drip water flowing over the speleothem surface (Dredge et al. 2013). However, the entry of trace elements to speleothems by aerosols was significantly lower than by drip water, and a drip rate reduction by more than 99.99% would be necessary for similar trace element supply by aerosols and drip water (Fairchild et al. 2010). Beside trace elements, atmospheric aerosols also contain a variety of organic compounds, and their impact on the organic content of speleothems has not been targeted yet. The many factors influencing the aerosol load, distribution, and deposition, which differ between caves, due to their morphology, ventilation, location, and frequency of human presence require an individual evaluation of the relevance of atmospheric aerosols for each cave. The present study aimed to do so for WP, a thoroughly monitored cave on the North Island of New Zealand (Nava-Fernandez et al. 2020).

6.2 Samples and Methods

6.2.1 Sample collection

WP is located in the North Island of New Zealand (38°18’41.3’’-S, 175°1’14.3’’-E) ca. 395 m a.s.l and 27 km from the coast. It is a fluvial developed cave, where an underground stream connects several cave chambers in a narrow passage, limiting air flow in the cave at several constrictions. Passive sampling was conducted on filters consisting of borosilicate glass microfibers bonded with PTFE (Pallflex Emfab, 37 mm diameter) from VWR (Darmstadt, Germany), glass petri dishes filled with water, empty glass petri dishes, and plastic petri dishes (transparent polystyrene, 90 mm diameter) from VWR (Darmstadt, Germany). Duration of sampling was increased from 7 days (11/28/2017 to 12/05/201), to 14 days (28/11/2017 to 12/12/2017), and 44 days (28/11/2017 to 11/01/2018). Each surface at each sampling

site was sampled in duplicates over the respective time intervals. The cave-external atmosphere was passively sampled using filters and water surfaces at a weather monitoring station few hundred meters from the cave entrance. The cave atmosphere was sampled at a site close to the entrance, where several drip sites were monitored, thus human presence was necessary at monthly intervals. Here, water, filter, plastic, and glass surfaces were sampled. In addition, a sampling site deeper in the cave was chosen to analyze a more undisturbed cave environment, where aerosols were passively sampled on water surface and filters (Figure 46).

Active sampling on filters was conducted in the surface atmosphere, at the monitoring site, and in the cave at the entrance. For active sampling, filters were attached to a pump, actively sucking air through the filters to collect particles. Sampling in the external atmosphere was conducted on 11/28/2017 for 4 hours and 14 minutes with an air-flowrate of 3995 cm^3/min (1016 L in total). The site close to the cave entrance was sampled on 12/12/2017 for 4 hours with a flowrate of 3995 cm^3/min (966 L in total), and the monitoring site in the cave was sampled on 12/05/2017 for 4 hours and 28 minutes with a flowrate of 3995 cm^3/min (1074 L in total).

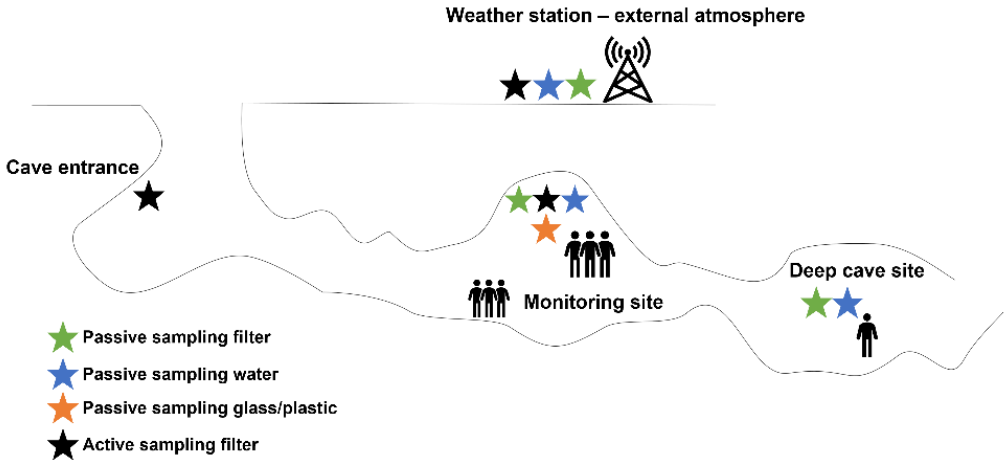

Figure 46: Conceptual cave profile marked at the sampling sites with the respective sampling methods.

6.2.2 Sample preparation

Filters were stored in a 5% HNO_3-bath, and petri dishes (glass and plastic) in a 10% HNO_3-bath. Two days before sampling in the cave the filters were transferred into double-deionized water and rinsed again before being set up in the cave. Blanks were prepared and measured similarly to the samples.

After sampling in the cave, water samples were further prepared by SPE using LiChrolut® RP-18 cartridges (40-63 µm, 200 mg, 3 mL) from Merck (Darmstadt, Germany). The cartridges were conditioned using 3 mL MeOH and 3 mL of ultrapure water. After addition of 1.5 mL of water to the cartridge, samples were applied using a 20 mL reservoir. The cartridges were rinsed with 1 mL of water prior to elution with three times 1 mL of MeOH. After evaporation to dryness under a gentle stream of nitrogen at 30°C, samples were re-constituted in 200 µL H_2O/ACN (9:1, v/v) and sonicated for 10 minutes at room temperature.

Samples collected on plastic petri dishes were prepared by covering the surface of the petri dish with 2 mL of MeOH/H_2O (9:1, v/v) and gently shaking for 30 minutes. The solution was transferred into a vial, and the procedure was repeated using 1.5 mL and 1 mL of MeOH/H_2O. After evaporation of the entire solution to dryness, the sample was re-constituted in 200 µL H_2O/ACN (9:1, v/v) and sonicated for 10 minutes at room temperature. Samples collected on glass petri dishes were prepared similarly to the plastic petri dishes, yet due to the larger surface, more solution was used (3 mL, 2 mL, and 2 mL).

All filter samples (passively and actively sampled) were prepared by cutting the filter into small pieces and covering the pieces with MeOH/H_2O (9:1. v/v). Passively sampled filters were extracted with 3 mL twice, while actively sampled filters were extracted with 1.5 mL twice (due to the different filter sizes). Each extraction step was conducted under gentle shaking on a vortex shaker for 30 minutes. The entire solution was evaporated to dryness under a gentle stream of nitrogen at 30°C and the samples were re-constituted in 200 µL H_2O/ACN (9:1, v/v) and sonicated for 10 minutes at room temperature.

To monitor the stability of the instrument and the retention times, standard solutions for positive and negative mode were prepared and measured repeatedly. The standard solution for the positive mode contained caffeine, reserpine, and acetovanillone in a concentration of 50 ng/mL, respectively, while the standard solution for the negative mode contained p-hydroxybenzoic acid, vanillic acid, and lauric acid. Both standard solutions were prepared in 500 µL H_2O/ACN (9:1, v/v).

6.2.3 Chromatography and mass spectrometry

Mass spectrometric analysis was conducted using a Dionex UltiMate 3000 ultrahigh-performance liquid chromatography system with an HPG-3400 RS pump (Thermo Fisher Scientific) coupled to a Q Exactive Orbitrap high resolution MS (Thermo Fisher Scientific). Chromatographic separation was achieved using an ACQUITY UPLC CSH Fluoro-Phenyl column (2.1x100 mm, 1.7 µm particle size) from Waters (Milford, USA). The injection volume was 10 µL and the column was heated to 30°C. Eluent A consisted of H_2O/ACN (98:2, v/v) with 400 µL/L of formic acid, while eluent B consisted of H_2O/ACN (2:98). The gradient started with 95 % of eluent A which was decreased to 20% within 20 minutes at a flowrate of 0.4 mL/min. This was held for three minutes before going back to 95% of eluent A within 30 seconds. Afterwards the column was re-equilibrated with 95% of eluent A for 90 seconds. The mass spectrometer was operated in full-MS mode in an *m/z* range of 50-750. Resolution was set to 140,000, capillary temperature to 300°C, sheath gas to 50 psi, and aux gas to 10 psi. In negative ionization mode the spray voltage was set to -3.2 kV and the HESI probe was heated to 150°C. XCalibur 4.3 and the integrated SII control plugin for the chromatography system was used for instrument control and for NTS the open-source software MZmine 2 (version 2.53) was used for peak detection and sum formula prediction. Settings were adapted (Brüggemann et al. 2017) and further optimized for the cave aerosol samples. Blank subtraction was conducted using an in-house Matlab script, so only signals of significant difference from blank samples (H_2O/ACN, 9:1) were further analyzed. The script set a

signal/blank ratio of >3, removed signals which were only detected in one of the threefold measurements, and signals with an intensity <1.0E4.

6.3 Results and Discussion

Aerosol sampling in WP was conducted in three different time intervals (7 days, 14 days, and 44 days) on different surrogate surfaces at different sites. Samples were taken at a weather monitoring station outside of the cave (here and in following referred to as "external atmosphere"), in the cave on a plateau where several drip points and speleothems are routinely monitored (here and in following referred to as "monitoring site"), and at a location deeper in the cave, less disturbed by human activity from the monitoring site (here and in following referred to as "deep cave site"). To study the efficiency of different surrogate surfaces on aerosol sampling, and concluding the influence of aerosols on growing speleothems, sampling on different surfaces (plastic, glass, filter, water) was conducted at the monitoring site.

6.3.1 Comparison of sampling methods

To compare the different sampling methods, all compounds detected by NTS of interval 3 (44 days) from the monitoring site on the different surrogate surfaces after blank subtraction were plotted in van Krevelen diagrams (Figure 47). The chemical composition and overall polarity of compounds was evaluated by plotting the H/C to the O/C ratios. Although wet surfaces of growing speleothems are assumed to retain more aerosols and particles than dry surfaces in a cave (Dredge et al. 2013), here the aqueous surface showed the lowest number of compounds, as well as least compounds exclusively sampled in water (Figure 47a). Contrarily, the filter sampling showed a strongly enhanced number of compounds especially in the ranges of H/C 0-1 and O/C 0-1, which is assigned to condensed and unsaturated hydrocarbons (Kim et al. 2003; Rivas-Ubach et al. 2018). Also, a significant number of compounds exclusively detected on the filter samples was observed in this area of the plot. Sampling on glass and plastic petri dishes resulted in a comparable number of compounds, but the plastic surface collected more compounds located in the hydrocarbon area of the van Krevelen diagram. Compounds collected on more than one surrogate surface ranged along the entire O/C and H/C ratios, with an aggregation in the range of H/C 1.5-2.5 and O/C 0.5-1, where assigned to the location of peptides, lignin, tannins, and carbohydrates in the diagram.

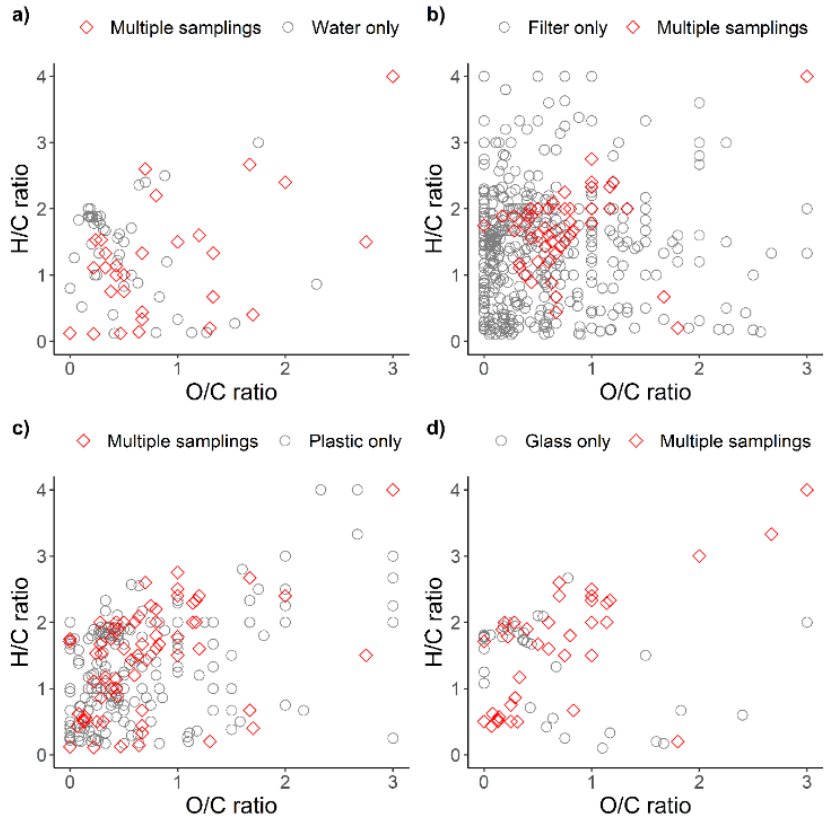

Figure 47: Van Krevelen diagrams of compounds from aerosol sampling on an aqueous surface (a), a filter (b), plastic petri dish (c), and glass petri dish (d) in Waipuna Cave in a 44-day period

Beside the amount and chemical composition of the compounds collected on different surfaces, also the intensities were evaluated with respect to the three different time intervals (Figure 48a). The box-whisker plot shows that medium signal intensity on the filter samples increased from interval 1 to interval 2, and then stagnated to interval 3. The variance along the medium intensity was comparable in all three intervals on the filter samples. The glass surface showed similar medium intensities to the filter surface in interval 1, while in interval 2, the intensities and the variance decreased, and in interval 3 particularly the variance of the intensities was strongly increasing. In interval 1, signal intensities on the plastic and water surface were significantly lower than on filter and glass surface, before aligning in interval 2. Compounds on the water surface showed the lowest overall intensities and variances.

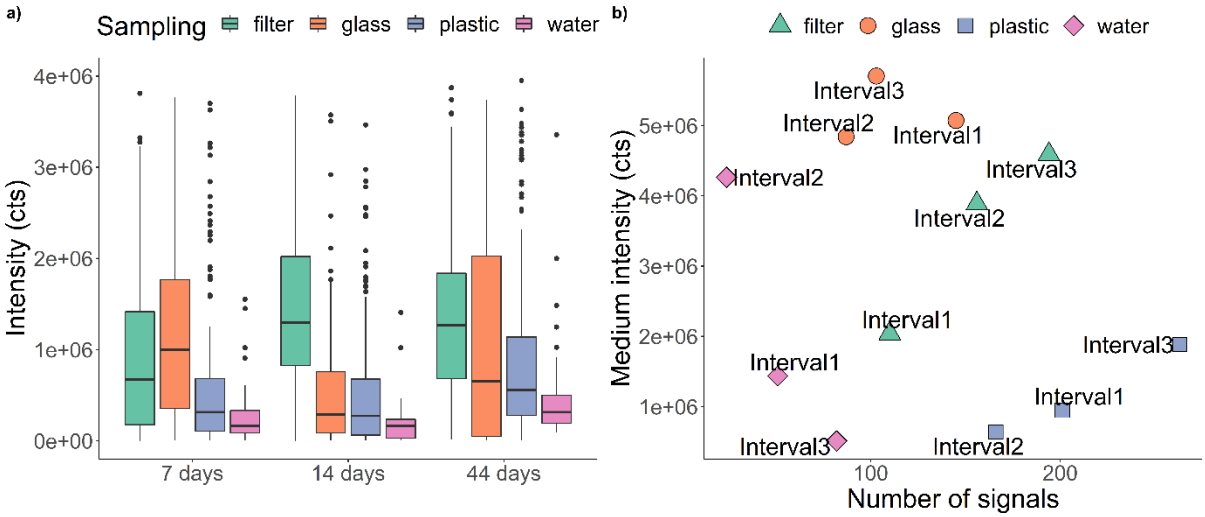

Figure 48: Boxplot of signal intensities (cts) detected on the filter, water, plastic, and glass samples in three different time intervals (a). Scatterplot of medium intensity to number of compounds detected on the respective surrogate surfaces (filter, glass, plastic, and water) in the three time intervals (b).

To examine the efficiency of the sampling methods, the medium signal intensities were compared to the number of compounds (Figure 48b). Water sampling showed a decreasing number of compounds with increasing medium signal intensity from interval 1 to interval 2, and a strongly opposed trend from interval 2 to interval 3. Overall, water sampling showed the lowest number of compounds, and no consistent behavior in the three intervals. Comparing the glass and plastic sampling, glass showed higher signal intensities than the plastic sampling, but a lower total number. Neither method showed a consistent trend of increasing number and intensity of signals. Sampling on the filters showed a linear increase of number and intensity of signals along the three intervals and was considered the most efficient surrogate surface for accumulative aerosol sampling in WP.

To explain the observed differences in the three intervals, cave ventilation was evaluated as potential driver. The external temperature outside the cave and the internal cave temperature were monitored from 01/06/17 to 16/05/18 in 30-minute intervals (Figure 49), and the geometry of WP allowed a conceptual connection between the temperature difference in and outside the cave and the ventilation. When the temperature in the cave was lower than the external temperature, the pressure difference and air density in the cave created a stagnant cold air sink that suppresses air exchange and air movement. This was observable from autumn to early spring (06/2017 to 10/2017) and is reflected as positive ΔT values. Higher cave temperatures resulted in a pressure gradient supporting the flow of warm air into the cave and thus enhancing cave ventilation (Nava-Fernandez et al. 2020). The three sampling intervals were timed in periods of generally strong ventilation but including significant fluctuations along the ΔT axis (Figure 49). These high fluctuations indicated temporarily limited entry of aerosols into the cave and thus strong deviations between number and intensity of signals in the respective intervals.

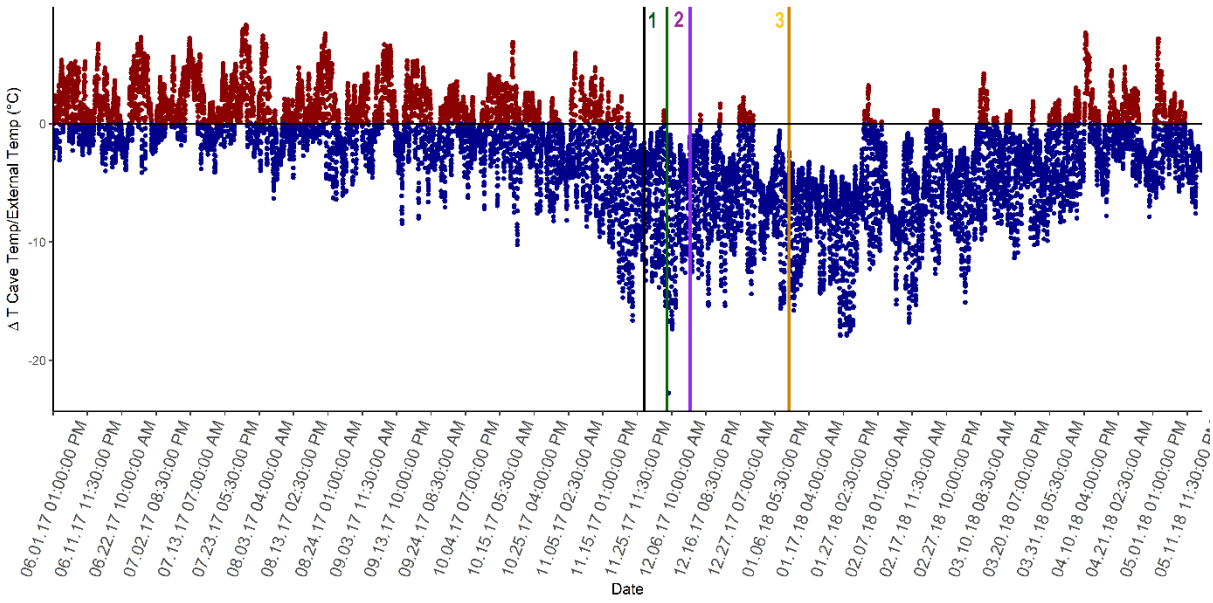

Figure 49: Temperature difference between external temperature outside of the cave and internal cave temperature (ΔT in °C) monitored between 06/01/17 to 05/16/18 in 30-minute intervals. The three aerosol sampling intervals are marked in green (interval 1), purple (interval 2), and orange (interval 3). A positive temperature difference refers to higher temperature in the cave (red) and a negative temperature difference to lower temperature in the cave (blue).

6.3.2 Passive filter and water sampling over time

Aerosol sampling on different surfaces demonstrated filter sampling as most efficient, while water sampling showed a significantly lower number of compounds. However, since the water sampling was intended to represent the water-film on the surface of growing speleothems, both, filter, and water sampling, were evaluated at three different sites in and outside of the cave over the respective time intervals.

The filter sampling site outside the cave (external atmosphere) showed similar medium intensities and variances in intervals 1 and 3. Interval 2 showed the highest medium intensity with a comparable variance, but a slope towards lower intensities. The increased aerosol load of the atmosphere during interval 2 was also observable in the peaking signal intensities at the monitoring site. However, the sampling site deeper in the cave (deep cave site) was not affected, as here the signal intensities in interval 2 were lowest. During interval 2, the temperature outside of the cave was much higher than in the cave, resulting in suppressed cave ventilation. In general, the duration of sampling at the different sites did not result in significant differences in signal intensities, yet a trend of decreasing intensities from external atmosphere to the sampling site deep in the cave was observable. In addition, the deep cave site showed a trend of accumulating intensities from interval 2 to 3 (Figure 50a).

Water sampling at the three sites showed different results. Here, sampling in the external atmosphere showed slightly, but linearly increasing signal intensities from interval 1 to 3. In contrast, the monitoring site did not show increasing signal intensities and behaved conversely to the filter sampling with interval 2 showing the lowest signal intensities at the monitoring site. No compounds were detected at the deep cave site in interval 2, and interval 3 showed significantly higher intensities than interval 1. (Figure 50b). The filter and water sampling results suggest that the deep cave was less influenced by external aerosol input and more exposed to internally produced aerosols, which accumulated over the three intervals. Aerosols showed different affinities to deposit on the respective surrogate surfaces hence the influence of aerosols on the organic content in speleothems varies whether they are growing or in a hiatus. Because the water sampling showed significantly lower number of compounds and lower intensities, the chemical composition was only evaluated in greater detail on the filter samples.

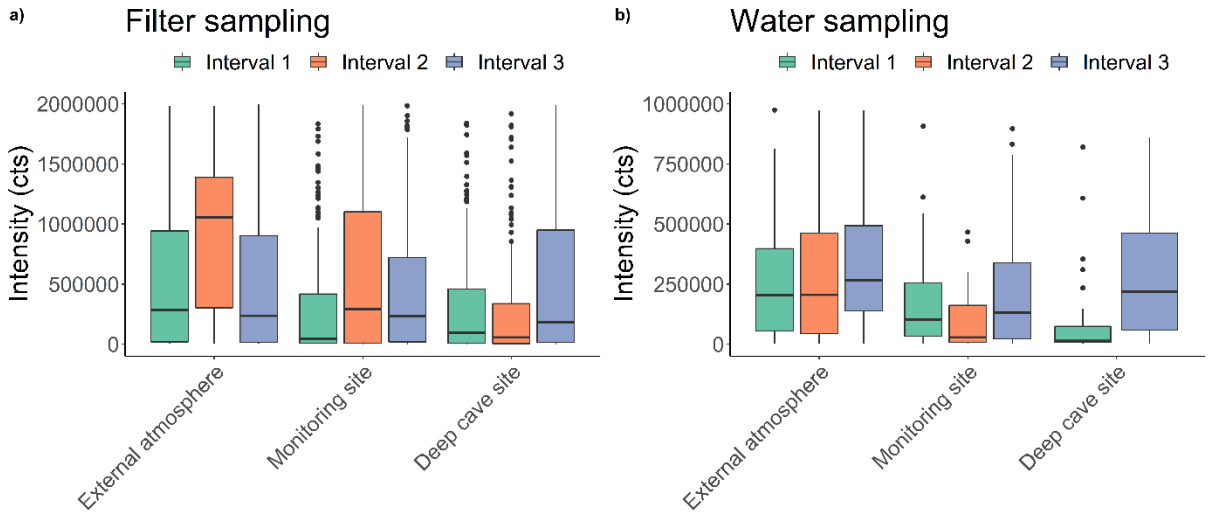

Figure 50: Boxplots of signal intensities (cts) detected on filter samples (a) and water samples (b) at three different sites in and outside of the cave in three different time intervals (interval 1 = 7 days, interval 2 = 14 days, interval 3 = 44 days).

The chemical composition of samples passively collected on filters at the different sampling sites was evaluated using van Krevelen diagrams (Figure 51). Most compounds were detected at all three sampling sites with generally higher intensities at the monitoring and deep cave sites. Compounds only detected in the atmosphere had low intensities and accumulated in H/C values of 0-2 and O/C values of 0-0.5, suggesting unsaturated and condensed hydrocarbons, lipids, peptides, and lignins.

Compounds detected at the cave surface and monitoring site revealed higher intensities in the external atmosphere, hence these compounds were poorly transported by the ventilation in contrast to the compounds, found at all three sites (Figure 51a). Compounds only detected at the monitoring site showed intermediate intensities. Three of those compounds were ranging at H/C ratios of circa 1.9 and O/C ratios of 0.25-0.5, which in the diagram is assigned to peptides. Two of the three samples correspond to molecular formulas ($C_7H_{13}NO_3$ and $C_{15}H_{28}N_2O_4$) with adequate elemental ratios for amide

bonds (Figure 51b). In addition, two highly oxidated compounds were found with O/C ratios of 1.5 and 2.0. One was assigned to the molecular formula $C_2H_2O_3$ corresponding to glyoxylic acid, an oxidation product of glyoxal or pyruvic acid, and a well-known SOA marker (Carlton et al. 2007; Hallquist et al. 2009; Müller-Tautges et al. 2014). Against our expectations, this relevant SOA-marker was not detected in the filter samples collected in the external atmosphere but a molecular formular corresponding to the precursor compound pyruvic acid ($C_3H_4O_3$) was detected, indicating SOA ageing during transport from the external atmosphere into the cave. Compounds detected at the monitoring site and in the deep cave site showed similar intensities. Only two compounds were detected exclusively in the deep cave, contrasting the theory that deep cave compounds were hardly influenced by externally introduced aerosols.

The graphical evaluation of the compounds from interval 3 revealed only minor differences in the composition of compounds at the different sampling sites. This indicates that cave ventilation did not efficiently transport all aerosols equally through the cave. Since air motion through the cave is partly obstructed, deposition on the walls of the cave and on speleothems is likely, so that number and intensity of compounds decrease with the distance to the entrance, such that both were lowest at the deep cave site. The negative correlation between air-borne load and distance from the entrance (Navarro Camacho et al. 2000; McGarry and Caseldine 2004) was confirmed by the passive filter sampling results and should be carefully considered when analyzing stalagmites from different locations in a cave. In addition, stalagmites formed near cave entrances have fundamentally different mechanisms of formation compared to those in deep cave environments (James et al. 1994).Thus the aerosol load on the organic content is subject to a number of variables, which complicates comparability of stalagmites from the same cave.

One distinct marker for atmospheric entry of atmospheric aerosols and particles by cave ventilation are pollen. Pollen are analyzed in sediment cores to reconstruct paleo-vegetation (Jara et al. 2015) and the potential of speleothem palynology for paleo-environmental studies is still underexploited (Navarro Camacho et al. 2000; McGarry and Caseldine 2004; Sniderman et al. 2016; Matley et al. 2020). Important components of the extracellular pollen matrix are lipids (Bashir et al. 2013), which were representatively analyzed in the van Krevelen diagrams of the aerosol samples in the ratio ranges of H/C 1.8-2.2 and O/C 0-0.2 (Kim et al. 2003). An entry source of lipids via pollen in the drip water could be examined by drip water monitoring studies at the respective sites. The highest intensities were observed at the monitoring site, though here the anthropogenic introduction of lipid contamination is important. Fatty acids, the building blocks of lipids, are ubiquitous contaminants, and can easily be dissolved from the human skin (Carta et al. 2017). In addition, the clinging of material to clothes and release inside the cave poses a potential entry mechanism and source for lipids and pollen (McGarry and Caseldine 2004).

In conclusion, the analysis of the chemical composition of compounds detected on passively sampled filters revealed only minor differences in the H/C-, O/C-ratios, and signal intensity. The entry of atmospheric aerosols into the cave was confirmed as a significant source for organic compounds into the deeper cave, and anthropogenic introduction of particles and aerosols was observed. The results demonstrate the urgent need of careful interpretation of data obtained from different stalagmites from the same cave.

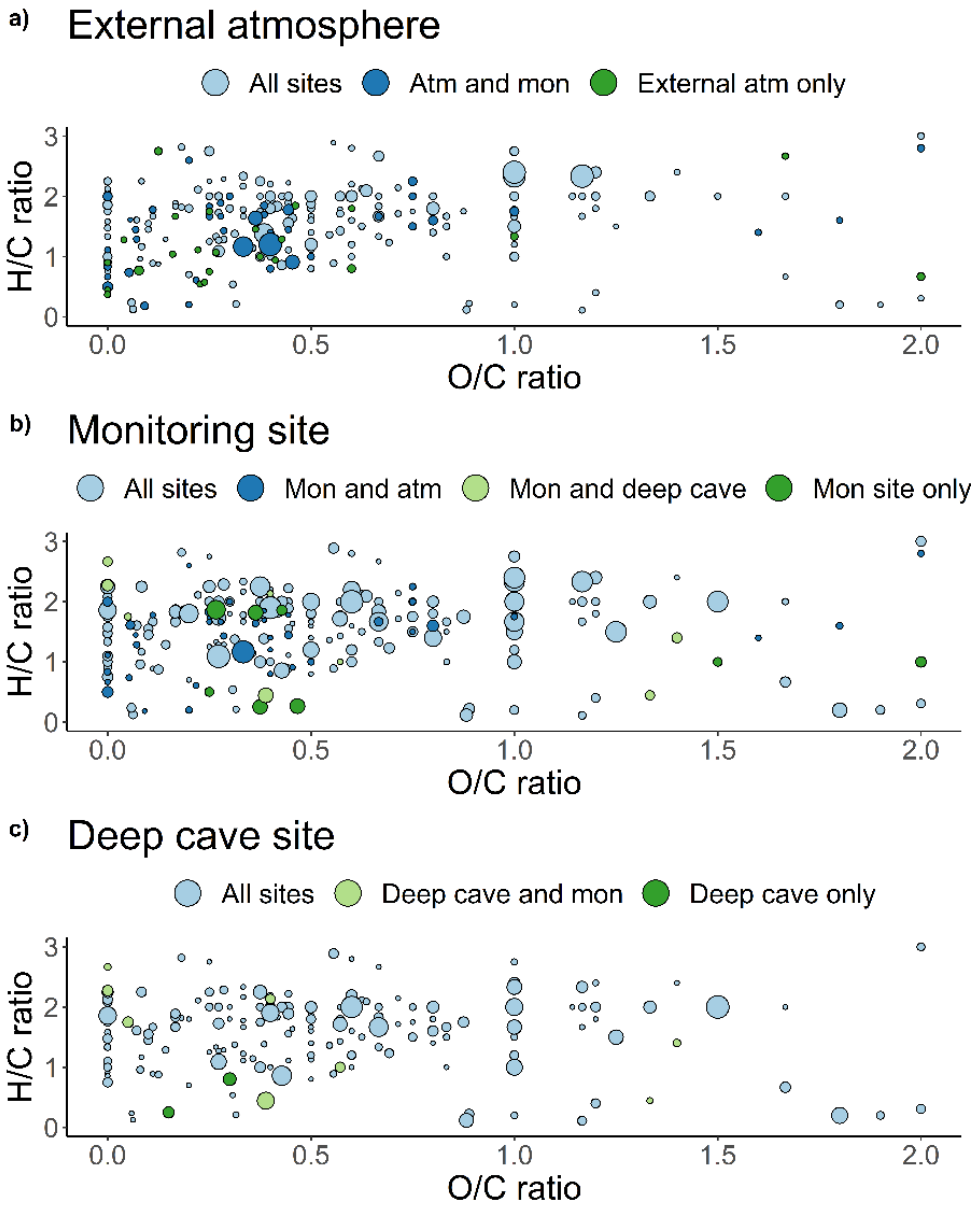

Figure 51: van Krevelen diagrams of compounds detected at the sampling sites (Mon=monitoring site, atm=atmosphere) in the external atmosphere (a), monitoring site in the cave (b), and deep cave site (c). Points are sized depending on signal intensity and colored based on the occurrence at one or more sites simultaneously. For simplification, only data from sampling of interval 3 (44 days) is shown.

6.3.3 Active filter sampling

Beside passive filter sampling, where aerosol collection was mainly controlled by wet and dry deposition, active filter sampling was also conducted, where air was actively pumped through filters. For the active filter sampling three different sampling sites were evaluated: the external atmosphere and monitoring site (as in the passive sampling), and a location in the cave close to the cave entrance instead of the deep cave site. This near-entrance site was chosen to track the pathway of aerosols into the cave more precisely. The mean temperature differences (ΔT) between in-cave and surface temperatures ($\Delta T = T_{CAVE} - T_{EXTERNAL}$, °C) for the three sampling intervals were as followed:

ΔT during sampling external atmosphere: -10.78 ± 1.7°C (28/11/2017, 11:00 am – 3 pm, 4 hours)

ΔT during sampling cave entrance: -15.17 ± 2.9°C (05/12/2017, 11:30 am – 4 pm, 4.5 hours)

ΔT during sampling cave monitoring site: -11.66 ± 0.7°C (12/12/2017, 11:00 am – 3 pm, 4 hours)

The boxplot showing the signal intensities collected on the respective filter samples (Figure 52a and c) confirms the negative correlation between aerosol load and distance from cave entrance, revealing that already at the cave entrance medium intensities were lower than outside the cave. The initial transition of air from the external atmosphere into the cave goes hand in hand with a major decrease of atmospheric aerosol load. Analysis of the elemental composition of compounds showed the highest number of compounds near the cave entrance, followed by the external atmosphere and the monitoring site (Figure 52b). The proportion of CHO, CHOS, and CHONS did not show differences >5%, while the CHON compounds increased from 36.5% at the external atmosphere to 52.8% at the cave entrance and 50.0% at the monitoring site. Most biomolecules in living systems (amino acids, (desoxy-)ribonucleic acid components, proteins) are composed of carbon, hydrogen, nitrogen, and oxygen, and their presence might indicate human influence on the increasing number of these compounds. Because temperature differences between in-cave and surface air were highest during sampling at the cave entrance, enhanced ventilation might also contribute to the higher number of compounds.

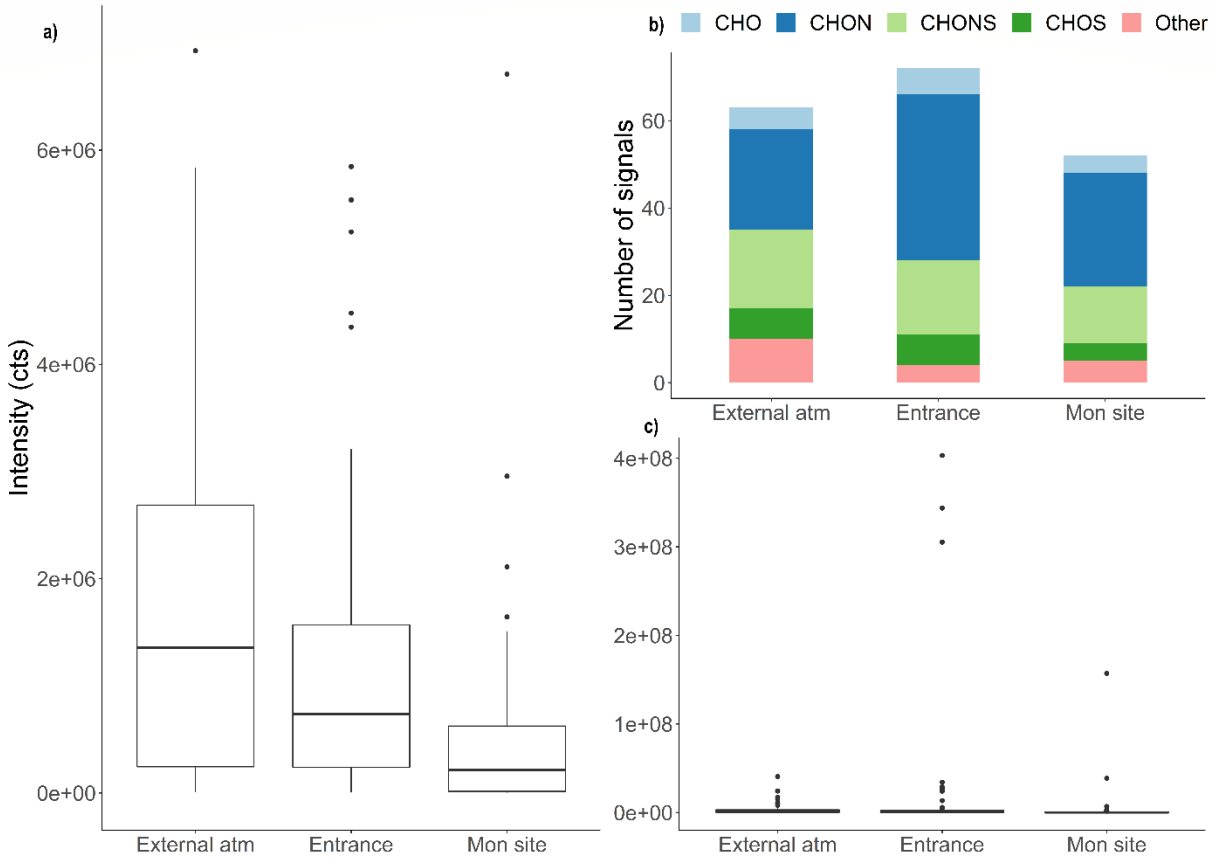

Figure 52: Zoom of boxplot of signal intensities detected on actively sampled filters at sampling sites at the external atmosphere (external atm), cave entrance (entrance), and cave monitoring site (mon site) (a). Stacked barplot of total number of compounds and differentiation between CHO, CHON, CHONS, CHOS and other species at different sampling sites (b). Original boxplot shown in (a) with no zoom on the y-axis (c).

Van Krevelen diagrams of the compounds collected at the different sampling sites provided a more detailed overview on the chemical composition (Figure 53). As shown in Figure 52b, highest signal intensities were detected at the cave entrance, and lowest at the monitoring site. Compounds exclusively detected in the external atmosphere contained low amount of oxygen, while the compounds that underwent transport into the cave (Figure 53a and b, darkblue) showed higher amounts of oxygen and decreasing intensity from external atmosphere into the cave. The most significant intensity difference was observed for the compound $C_3H_6N_{10}O_3$, a nitrogenous urea derivative.

Compounds exclusively detected at the cave entrance were accumulated in the range H/C = 1.7-2.0 and O/C = 0.1-0.3, which in the van Krevelen diagram are associated with lipids and in the range H/C = 0-0.1 and O/C = 0.3-0.4, associated with condensed hydrocarbons. The most prominent of those compounds was $C_{11}H_6N_6O_7$, most probably a purine derivative, and thus most likely introduced by humans or animals to the cave entrance.

Actively filtered sampling revealed only one compound exclusively detected at the monitoring site with a molecular formula of $C_7H_{14}N_{10}O_4$. Compounds detected at the cave entrance and the monitoring site showed generally higher intensities at the latter. The most significant intensity difference was observed for the compound with the molecular formula $C_{11}H_6N_6O_7$, another purine derivative with a different retention time. The highest signal intensity at the monitoring site, the site with the highest frequency of human presence, corroborates anthropogenic introduction of this compound into the cave. Compounds detected at all sampling sites showed decreasing intensity from the external atmosphere into the cave, significantly observable from the external atmosphere to the cave entrance, the most critical part of the aerosol transport. The compound with a molecular formula of $C_3H_8N_6OS_2$ behaved differently with highest intensity at the cave entrance and strongly decreasing intensity at the monitoring site. A database search yielded two structures associated to sulfureous derivatives of urea and guanidine.

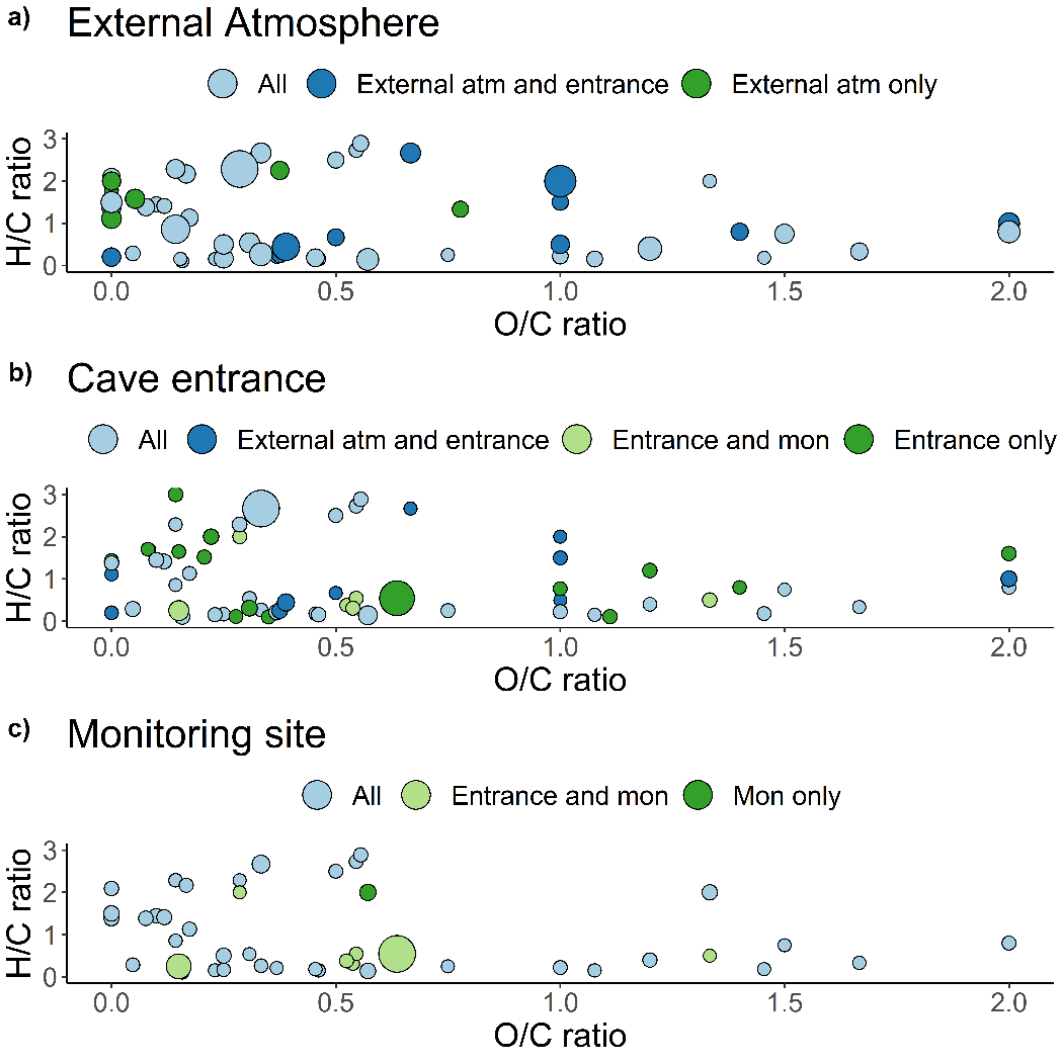

Figure 53: Van Krevelen diagrams of compounds detected on actively sampled filters from the external atmosphere outside of the cave, the cave entrance, and the cave monitoring site. Points were shaped and colored depending on their detection at one or more sampling sites.

Analysis of the chemical composition of actively sampled compounds confirmed that the highest number of compounds collected in the cave had an external atmospheric origin. Furthermore, the initial transition from the atmosphere into the cave represented the largest loss of atmospheric aerosol load. Human presence was clearly reflected by the presence of, e.g., nitrogenous derivatives of urea and guanidine, which showed an intensity increase towards the interior of the cave. The results suggest that active filter sampling is a useful tool to study the influence of local short-term events on the cave atmosphere, including human presence and the pursuit of aerosols through the cave, while long-term passive filter sampling is a useful addition to understand cave ventilation and the influence of atmospheric aerosols on the organic content of growing speleothems.

6.3.4 Hierarchical clustering analysis

A sophisticated tool to determine groups of compounds with similar behavior is hierarchical clustering. The respective signal intensities of the 50 most intense compounds detected on the passively (Figure 54) and actively (Figure S 1) sampled filters were normalized by z-score normalization and hierarchically clustered by their abundance at the respective sampling sites.

Two groups from the hierarchical clustering were associated with compounds externally introduced to the cave (atmospheric entry, Figure 54, blue). The smaller group consisted of three compounds, based on their elemental composition assigned to sugar alcohols, like xylitol ($C_5H_{12}O_5$), and mannitol ($C_6H_{14}O_6$). Mannitol was detected as a molecular tracer for actively wet discharged basidiospores (fungi, which actively discharge their spores with liquid into the air) in the Amazonian atmosphere, with a higher abundance at night during dark and humid conditions, similar conditions as found in a cave (Bauer et al. 2008; Elbert et al. 2010). Alcohol sugars like mannitol and xylitol are the main carbohydrates in lichens and bacteria (Medeiros et al. 2006) and high abundance was documented in sea spray (Hawkins and Russell 2010). The emission of mannitol from fungi as a cave-internal source, was contradicted by the linear decrease of intensity with the distance into the cave. Sea spray aerosols constituted the more potential source of mannitol in the cave atmosphere. Xylitol is associated with wildfires, and has been proposed as a smoke tracer in Antarctic aerosols (Barbaro et al. 2015). It has also been detected as a component associated with savanna fires in southern Africa (Gao et al. 2003). Resuspension of water-soluble sugar alcohols from soil due to agricultural activity is another source of xylitol-containing organic aerosols (Simoneit et al. 2004). Here, xylitol was also detected on actively sampled filters, showing the same intensity decrease (Table 4). Because of this behavior it has been proposed as a promising marker for the influence of local fire events on the cave atmosphere. However, a more comprehensive number of marker compounds is necessary to distinguish between the different aerosol sources from the external atmosphere.

Compounds with a linear intensity increase to the cave interior were classified as “cave-borne” (Figure 54, green). Most elemental compositions agreed with dicarboxylic acids, like adipic acid (Table 4). Adipic acid results from the oxidation of cyclohexene, or the ozonolysis of methylene-cyclohexene or

1-methyl-cyclohexene, and was detected in urban aerosols in Germany, China, and the U.S.A. (Zhang et al. 2010). An urban emission source of the precursor compounds of adipic acid disagreed with the observed abundances in and outside WP. The relative influence of anthropogenic and biogenic sources to organic aerosols can be estimated by the ratio of adipic acid and phthalic acid to azelaic acid (Ho et al. 2006). Molecular formulas consistent with azelaic acid ($C_9H_{16}O_4$) and phthalic acid ($C_8H_6O_4$) were detected on the passively sampled filters from the external atmosphere and the monitoring site. Because differences in transport through the cave and aerosol-aging processes were already observed, only the ratio from the external atmosphere was determined as 0.92, indicating a biogenic, possibly cave-internal source of the detected aerosols.

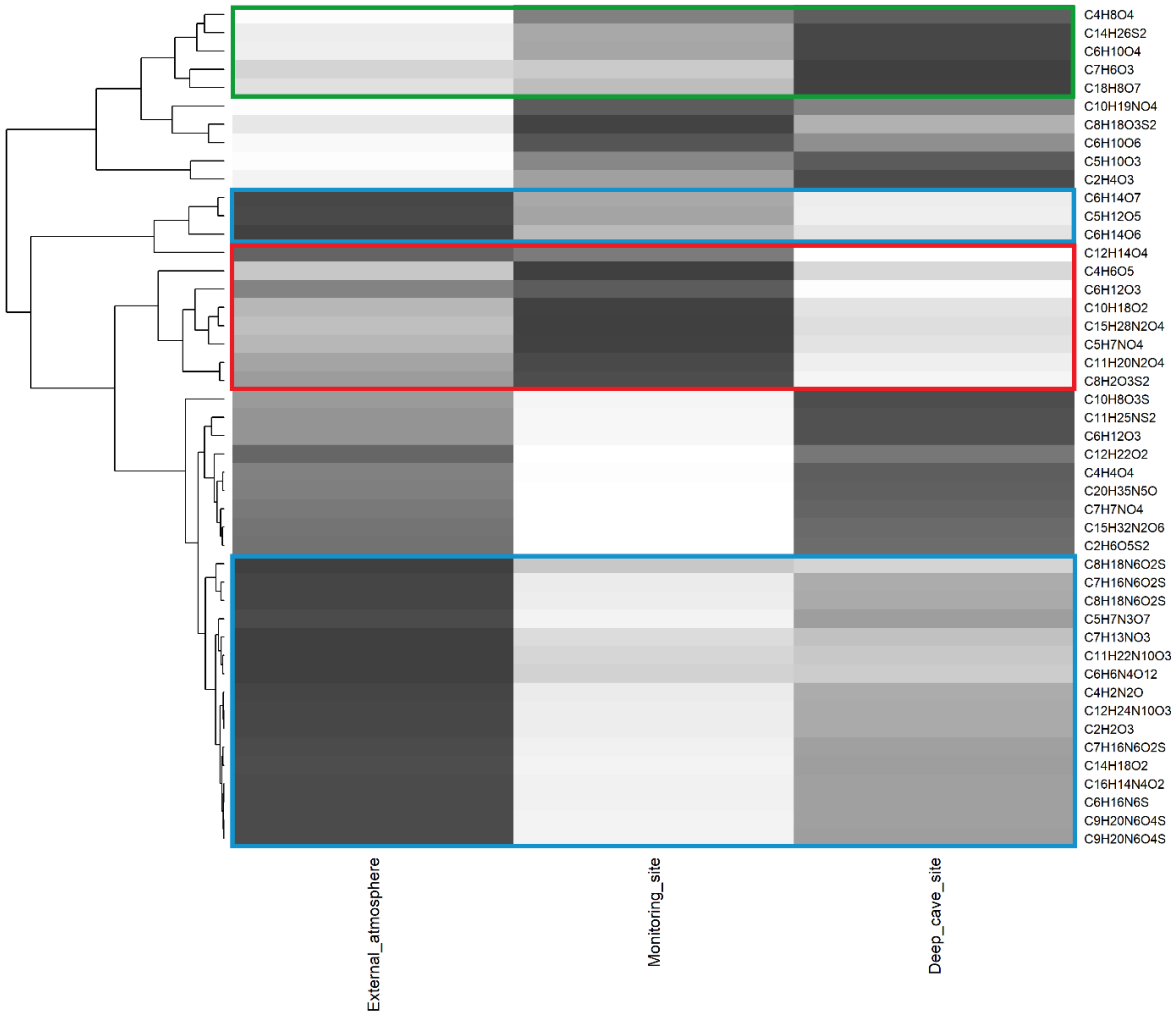

Figure 54: Heatmap of signal intensities of the 50 most intense compounds passively collected on filters at the different sampling sites. Rows were hierarchically clustered based on previous z-score normalization. Columns represent the different sampling sites. Distinct groups of the hierarchical clustering were assigned to compounds of atmospheric entry (blue), human entry (red), and cave-borne (green) based on their intensity distribution.

Hierarchical clustering of the 50 most intense compounds on actively sampled filters revealed a large proportion of compounds that are introduced by humans into the cave, with high intensities only at the monitoring site, almost exclusively nitrogenous with high MW (Figure S 1).

6.3.5 Suspect-target screening for environmentally relevant compounds

The analysis of the H/C and O/C ratios, and hierarchical clustering revealed several relevant molecular formulas representative of different aerosol sources or dynamics in the cave. In addition, comprehensive suspect-target lists were used, that are available by *NORMAN Suspect List Exchange*, representing different groups of environmentally relevant contaminants. The lists mostly cover water contaminants or pharmaceuticals and their transformation products and metabolites. For screening in atmospheric aerosol samples, seven different suspect lists were used including biomarkers, per- and polyfluoroalkyl substances, pesticides, surfactants, mycotoxins, phytotoxins, and insecticides. Additionally, a manually prepared suspect list of natural amino acids was employed. All compounds detected on passively and actively sampled filters, from the respective suspect target lists, proposed identity from the lists, retention time, and intensity at the different sampling sites are shown in Table 4. Depending on the intensity progress at the sampling sites, the entry sources were classified as atmospheric (and accumulative if contrary behavior was observed in active and passive sampling), anthropogenic, and cave-borne.

Atmospheric introduction of compounds into the cave was confirmed by passive and active filter sampling. Thus, compounds classified as atmospherically introduced were not further investigated if not already described elsewhere (e.g., xylitol, phthalic acid).

Three of the five compounds classified as anthropogenically introduced were found by screening for biomarker compounds. Taurine was expected to result from tobacco products, and if so anthropogenic transport of smoke products (Sheu et al. 2020) would be a relevant entry source of taurine into caves. However, the use of taurine in tobacco products is prohibited in the EU (EU Tobacco Products Directive [2014/40/EU]), U.S. (US Home Smoking Prevention and Tobacco Control Act [21 CFR Part 907: Tobacco Products Standards]), and also in New Zealand (Smokefree Environments and Regulated Products Act 1990 – Proposals for regulations), and was neither confirmed in solid tobacco products (Ren et al. 2019) nor in e-cigarette refill solution (Barhdadi et al. 2021). A different source was suggested via human breath, because taurine and its metabolic products were detected in human breath (Martínez-Lozano and de la Mora 2007), and as a natural degradation product of the natural amino acid cysteine which occurs naturally in the human circulatory system. Dehydroascorbic acid is an oxidized form of vitamin C, which is commonly used by humans as a dietary supplement. The intake of secoisolariciresinol by humans via flaxseeds is known (Kezimana et al. 2018), but no data on the excretion is documented. C_{12}-alkyl sulfate was found by screening actively and passively sampled filters as a surfactant. Surfactants are known compounds of atmospheric aerosols, and the surface tension of aerosols is proposed to affect the cloud-condensation properties (Baduel et al. 2012). The C_{12}-alkyl

sulfates are widely used as sodium salts, sodium dodecyl sulfate (SDS), as surfactant or emulsifier in consumer products like cleaning agents or cosmetics. Aerosols emitted from household products and cosmetics (Oh and Kim 2020; Sheu et al. 2021) can be anthropogenically transported into the cave, similar to tobacco smoke products (Sheu et al. 2020) and act as contaminant in the cave environment. Substituted benzothiazole derivatives are ubiquitous contaminants in environmental samples and have been used by the industry for decades, for example as vulcanizing agents in tires (Kumata et al. 2002), biocides, or corrosion inhibitors (Reemtsma et al. 1995). Industrial use did not provide a reasonable explanation for the presence at WP though, especially not at the monitoring site inside WP. After environmental exposure of humans to benzothiazole derivatives, 2-substituted derivatives were found in human breath (García-Gómez et al. 2015) which is a more likely source of 2-benzothiazolsulfonic acid.

Two compounds were found in the surfactant and biomarker suspect list, classified as cave-borne due to their increasing abundance with distance in the cave. Adipic acid was equally observed and has already been described in the hierarchical clustering of compounds passively sampled on filters (chapter 6.3.4). Haloacetic acids like dichloroacetic acid are oxidation products of C_2-halocarbons which are mainly anthropogenically emitted and environmentally toxic. They are well-known pollutants from water disinfection materials and as herbicides. A first laboratory experiment proved that abiotic natural production of chloroacetic acids from soil and humic acids is possible. However, no concluding research was conducted to transfer the experiments from the laboratory to the field (Fahimi et al. 2003). Biosynthesis of dichloroacetic acid was proven in the mushroom species *Russula nigricans* constituting the first natural occurrence of this compound in a living organism (Lajin et al. 2021), and a potential source of cave-borne dichloroacetic acid. Further studies of the microbial abundance in WP are necessary to confirm this observation.

The two main sources of organic matter in speleothems are the overlying environment and microbial communities in the cave (Blyth, 2016). However, the aerosol budget analyzed in this work poses the question of a third entry of organic matter into the speleothem, especially since the industrial revolution and the strongly increased SOA-budget of the atmosphere. It is remarkable that even in WP, an infrequently visited cave, a large proportion of anthropogenically introduced organic compounds was found. In addition, cave ventilation was influenced by stronger temperature deviations on the surface and resulted in increased aerosol entry into the cave and thus a higher probability of inclusion of the aerosol organic matter into the speleothems.

Table 4: Compounds detected by suspect-target screening in samples from active and passive filter sampling. The retention time in min, peak intensity at the different sampling sites, proposed formula, proposed identity (including the respective NORMAN suspect list), and proposed entry source of the respective compounds is listed. Entry sources are classified as atmospheric (atm), accumulative (acc), anthropogenic (anth), cave-borne (cave).

Sampling	t_R (min)	External atm.	Cave entrance	Monitoring site	Deep cave site	Formula	Proposed identity	Entry source
passive	5.2	4.9E+07		1.1E+07	4.5E+06	CH_4O_3S	Methanesulfonic acid[S23]	atm
active	5.2	7.5E+06	8.9E+05	7.7E+06				atm
passive	1.4	8.2E+06		9.0E+06	5.8E+07	$C_4H_6O_4$	Succinic acid[S23]	atm/acc
active	1.4	1.2E+07	1.2E+07	5.6E+06				atm
passive	1.5	1.8E+06		1.1E+06	5.2E+06	$C_5H_8O_4$	Glutaric acid[S23]	atm
passive	4.9	1.8E+06		2.3E+06	2.6E+07	$C_4H_4O_4$	Maleic acid[S23]	atm/acc
active	4.9	5.2E+08	1.8E+07	1.2E+07				atm
passive	0.8	1.9E+07		3.5E+07	1.3E+06	$C_5H_{12}O_5$	Xylitol[S23]	atm
active	0.8	4.9E+07	5.8E+06	4.1E+05				atm
passive	0.8	1.1E+08		3.4E+07	1.9E+06	$C_6H_{14}O_6$	Sorbitol[S23]	atm
active	0.8	1.3E+07						atm
passive	0.8	1.9E+07		3.4E+07	1.5E+06	$C_7H_{10}N_4O_3$	Cymoxanil[S11]	atm/acc.
active	0.8	4.7E+07	5.9E+06	1.6E+05				atm
passive	6.7	6.1E+06		7.8E+06		$C_8H_6O_4$	Phthalic acid[S34]	atm
active	6.7	3.9E+06	2.5E+06					atm
passive	0.7	5.8E+06		2.3E+06	3.1E+04	$C_5H_{10}N_2O_3$	Glutamine[A1]	atm
active	0.9	7.7E+06	2.3E+06	3.8E+04		$C_5H_9NO_4$	Glutamic acid[S23, A1]	atm
active	1.6	2.2E+07	5.4E+05	1.4E+04		$C_6H_{12}O_7$	Sodium gluconate[S23]	atm
passive	0.8	1.4E+06		2.0E+06	5.4E+04	$C_2H_7NO_3S$	Taurine[S34]	atm/anth
passive	19.5	7.1E+05				$C_{12}H_{26}O_4S$	C12-Alkyl Sulfate[S23]	anth
active	19.5	1.5E+06	1.0E+07	1.1E+06				anth
passive	13.3	5.7E+06		1.4E+07	3.6E+06	$C_7H_5NO_3S_2$	2-Benzothiazolsulfonic acid[S12]	anth
passive	8.5	2.0E+05		1.6E+07		$C_6H_6O_6$	L-Dehydroascorbic acid[S34]	anth
active	9.7	6.0E+04		4.0E+05		$C_{20}H_{26}O_6$	Secoisolariciresinol[S34]	anth
passive	2.6	4.1E+05		1.4E+07	2.6E+07	$C_6H_{10}O_4$	Adipic acid[S23]	cave acc
passive	9.1	2.0E+06		2.8E+06	1.9E+07	$C_2H_2Cl_2O_2$	Dichloroacetic acid[S34]	cave/acc

**S11: Insecticides, fungicides, and transformation products* (Moschet 2017)

**S12: Retrospective screening of new emerging contaminants* (Alygizakis et al. 2018)

**S23: Surfactant suspect list from Environmental Institute (Slovakia) and the German Federal Environmental Agency* (Alygizakis 2018)

**S34: Biomarkers from Exposome Explorer* (Nevea et al. 2019)

**A1: Manual list of natural amino acids*

6.4 Conclusion and Outlook

A first study on atmospheric aerosols as a relevant source of organic compounds in the subterranean environment of WP was conducted. The aerosol sampling efficiency on different surrogate surfaces, representing dry cave walls or growing speleothems was evaluated for future investigations. The efficiencies were relying on the duration of sampling and the comparison revealed passive aerosol sampling by wet and dry deposition on filters as the most efficient sampling method. Glass and plastic petri dishes showed a comparable efficiency, while passive aerosol sampling on an aqueous surface showed the least number of compounds and medium intensity independent from the duration of sampling. Sampling in water was intended to represent the surface of growing speleothems but the results suggest that passive aerosol sampling on filters should be conducted to sufficiently sample and recover aerosols from the cave environment. Different number and intensity of signals in the time intervals were associated with changing cave ventilation due to the temperature difference in and outside of the cave. The analysis of the intensity of signals during the three intervals at the different sampling sites showed slightly but linear decreasing intensity with distance to the cave on the filter samples. Signal intensity in the water sampling showed inverse behavior with decreasing intensity from the external atmosphere to the monitoring site and increasing intensity from the monitoring site to the deep cave site. This unexpected behavior, in combination with the low intensity and number of compounds, excluded these samples from further investigation. Analysis of the compounds in van Krevelen diagrams revealed anthropogenically transported aerosols from the external atmosphere, and atmospherically introduced aerosols as the main sources of the sampled organic compounds. The results emphasized the need to carefully evaluate proxies from different speleothems in the same cave.

Active filter sampling was conducted at the external atmosphere, in the cave close to the entrance, and at the monitoring site. The results demonstrated that the transition of aerosols from the external atmosphere into the cave was the most critical part during transport, with the highest loss of signal intensity. Analysis of the chemical composition confirmed external entry of atmospheric aerosols and human presence as the most relevant sources of organic aerosols in the cave. While passive sampling over longer time periods proved useful to collect a broad range of different aerosols, active sampling revealed more information on critical pathways of the air into and through the cave and should be conducted at more consecutive sites and in the same time intervals to maintain comparability of the influence of cave ventilation on the atmospheric aerosol load.

Hierarchical clustering of the most intense compounds detected on the actively and passively sampled filters resulted in the distinction of three different groups of compounds, i) those with an external atmospheric origin, ii) those which were anthropogenically introduced into the cave, and iii) those which appear to have a subterranean origin. Relevant molecular formulas should be targeted by monitoring and, if possible, confirmed by analytical standards or at least mass spectrometric fragmentation behavior.

In addition to hierarchical clustering, suspect target lists were used to screen the samples for environmentally relevant contaminants. Molecular formulas associated to environmentally relevant contaminants, surfactants, insecticides, biomarkers, and amino acids were found and literature search for the individual compounds confirmed a connection of the anthropogenically introduced aerosols to human breath, consumer products, or the human metabolism and a connection of the aerosols classified as “cave-borne” to e.g., a disinfectant, that was recently proven to be produced by fungal species.

Summarizing, cave aerosols are a relevant source for organic compounds in caves and their collection should be included to scientific monitoring of caves either to study their flow into the cave, and where most aerosols are lost due to deposition, or to screen for new environmentally relevant target compounds, whose determination could then be applied to speleothem samples. A comparison of the atmospheric organic content and the organic content of offspring speleothems will be necessary to observe whether aerosols are included into speleothems and to which extent.

Ice core analysis

7. Development and application of trace analysis methods for organic atmospheric marker species in ice cores

7.1 Introduction

Glaciers preserve atmospheric constituents deposited with snowfall and the mined ice cores are valuable climate archives which are elucidated by the analysis of multiple inorganic and organic proxies. Early research focused on inorganic species to determine the effects of enhanced anthropogenic emissions on the atmosphere especially in the transition between the pre-industrial and the industrial age. Sulfate anions were analyzed in Alpine glaciers (Schwikowski et al. 1999; Preunkert et al. 2001a) and Greenland ice cores (Mayewski et al. 1990) by ion chromatography (IC) with conductivity detection and associated with anthropogenic emission and emission of sea salt. Other inorganic proxies associated with anthropogenic activities were heavy metals, analyzed by ICP sector field MS and ammonium ions, analyzed by IC, in Alpine and Arctic glaciers (Barbante et al. 2004; Gabrielli et al. 2005). Halogens and halogenic acids were suspected to result from volcanic activities and oceanic emissions and analyzed by ICP-MS (Preunkert et al. 2001b; Legrand et al. 2018), while methanesulfonic acid was analyzed in an Antarctic ice core by IC and associated to biogenic marine emissions (Wolff et al. 2006).

The first organic compounds of interest were light carboxylate ions like formate and acetate, which were first detected in samples from Col du Dôme (CDD) and further studies connected the concentration of formate, acetate, glycolate, and oxalate in Greenland and Antarctic ice cores to biomass burning, natural emission from terrestrial vegetation, and fuel combustion (Legrand and De Angelis 1996; Legrand et al. 2003; Angelis et al. 2012). Low MW fatty acids were detected by GC-MS in Greenland ice cores and associated with terrestrial higher plant waxes, soil emission, and marine phytoplankton emission (Kawamura et al. 1996). Other organic proxies included PAH and humic-like substances (HULIS). PAH were analyzed by HPLC or GC-MS in European Alpine ice cores and approximately 90% of all PAH emissions in the atmosphere are connected to anthropogenic activities, since they are a thermal degradation product of incomplete fuel combustion (Gabrieli et al. 2010). Humic acids, especially fulvic acid, are one of the most relevant parts of natural surfactants in water, and therefore highly abundant in atmospheric aerosols. They were detected in CDD using UV detection (Guilhermet et al. 2013) and in Antarctic ice cores using Fourier-transform infrared spectroscopy (FT-IR) (Calace et al. 2005).

Naturally emitted vegetation-derived precursor compounds are rapidly oxidized in the atmosphere, and the reaction products undergo gas-to-particle conversion forming SOA. SOA constituents like α-dicarbonyls, dicarboxylic acids, and oxocarboxylic acids were detected in Alpine and Greenland ice cores (Kawamura et al. 2001; Müller-Tautges et al. 2016) and moved the focus of research from the precursor compounds to the variety of transformation products to understand the impact of the

hydrocarbon budget on climate and air quality (Fu et al. 2016). Some of the most abundant precursors are isoprene, terpenes, and sesquiterpenes, which are emitted by all plants. Although the precursors have short atmospheric lifetimes of minutes to a few hours, the long lifetime of the oxidation products, for example pinonic acid and pinic acid, enables long range transport and wet or dry deposition at remote locations (Kesselmeier et al. 2000; Pöschl 2005). Biogenic SOA tracers were detected in ice core samples from Kamchatka (Fu et al. 2016), Alaska (Pokhrel et al. 2016), and the European Alps (Müller-Tautges et al. 2016). SOA ageing results in further oxidation of these compounds to e.g. MBTCA (Müller et al. 2012; Kristensen et al. 2014), which was detected in an ice core from Kamchatka (Fu et al. 2016).

Other important organic aerosol sources are biomass burning events (Simoneit 2002). The reconstruction of paleo fire events provides information on changing fire dynamics as a result of changing climate conditions and enables more reliable prediction of fires in the future (Shakesby and Doerr 2006; Zennaro et al. 2014; Parvin et al. 2019). A fire event changes local plant and microbial productivity, biodiversity (Power et al. 2008), and releases atmospheric aerosols, which act as CCN, influencing the radiative climate forcing (Jimenez et al. 2009). During combustion, the polymeric plant components are disintegrated, and the small, oxidized reaction products are adsorbed by atmospheric aerosols and transported. Lignin is the second most abundant biopolymer, and the combustion products vanillic acid and *p*-hydroxybenzoic acid were detected in Arctic ice cores (Grieman et al. 2016) and in an ice core from Northeast Asia by GC-MS (Kawamura et al. 2012).

The three monomeric precursors for polymeric lignin are coniferyl-, coumaryl-, and sinapyl-alcohol and the ratio of the monomers provides information on the vegetational origin, distinguishing between angiosperm and gymnosperm vegetation, as well as wooden and non-wooden plant species (Hedges and Mann 1979; Jex et al. 2014). Lignin is analyzed in soil (Kögel and Bochter 1985; Bahri et al. 2006), sediments (Goñi and Montgomery 2000), and speleothems (Heidke et al. 2019, 2021). It could provide valuable information on aerosol transport, due to the more precise linkage of aerosols to different classes of vegetation and source regions. In addition, studies revealed that only minor fractions of the organic SOA content are present as individual organic molecules, while the majority is present as oligomeric or polymeric matter (Turpin et al. 2000; Goldstein and Galbally 2007). Despite that no data is currently available on intact polymeric lignin in ice cores.

The most abundant polymeric structure in terrestrial vegetation is cellulose. During cellulose combustion at temperatures >300°C, 1,6-anhydro-β-glucopyranose (Lev) is formed, while its isomers 1,6-anhydro-β-mannopyranose (Man) and 1,6-anhydro-β-galactopyranose (Gal) are formed during combustion of hemicellulose (Simoneit et al. 2000; Simoneit 2002; Fabbri et al. 2009). Due to the distinct formation conditions and source specificity Lev is one of the most important biomass burning markers and thoroughly studied in snow (Kehrwald et al. 2012), soils, sediments (Elias et al. 2001; Hopmans et al. 2013), aerosols (Schkolnik et al. 2005; Puxbaum et al. 2007; Saarnio et al. 2013;

Zangrando et al. 2016; Bhattarai et al. 2019), and ice cores from the Antarctic (Gambaro et al. 2008), a Tibetan ice core (Yao et al. 2013), an ice core from Alaska (Pokhrel et al. 2020), and Greenland ice cores (Zennaro et al. 2014; Parvin et al. 2019). Studies demonstrated an atmospheric lifetime of Lev for several days, allowing long range transport and deposition remotely from the fire location (Hu et al. 2013; Isabel García et al. 2017; Schreuder et al. 2018) even though Lev degradation was observed by photo-oxidation (Zhao et al. 2014), reactions with OH radicals (Hennigan et al. 2010; Hoffmann et al. 2010; Arangio et al. 2015), and reactions with NO_x-radicals (Knopf et al. 2011; Shiraiwa et al. 2012). The ratio among Lev and its isomers Gal and Man provides information on the smoke emission source, distinguishing between liginite burning and biomass burning, hence natural and domestic fuel emissions (Fabbri et al. 2009).

Each individual proxy provides valuable insights into different processes influencing the earths SOA budget and consequently climate conditions. While most studies focused on a distinct fraction to assess certain questions like anthropogenic effects or biomass burning records, recent research aimed towards a more comprehensive analysis of proxies (King et al. 2019b) and the elucidation of the entire molecular composition of ice core samples by non-target analysis (Vogel et al. 2019). Due to the very low concentrations (parts per billion to parts per trillion) of atmospheric marker compounds in ice core samples, efficient sample preparation methods are necessary to enrich the compounds to a quantifiable level. Rotary evaporation under vacuum was utilized in many studies to carefully remove the aqueous matrix of the melted ice core samples without evaporation of the organic compounds (Kawamura et al. 2001, 2012; Pokhrel et al. 2015; Fu et al. 2016; King et al. 2019b). Other methods like stir bar sorptive extraction (Müller-Tautges et al. 2014), LLE (Seki et al. 2015), or SPE in combination with rotary evaporation (Xie et al. 2000) focused on extraction of the trace compounds rather than removal of the matrix. This study was destined to develop a comprehensive workflow to quantify a selected number of organic constituents (Table 5) using a combination of two SPE methods and centrifugal evaporation. Phthalic acid has been detected in a Greenland ice core (Kawamura et al. 2001) and is a secondary atmospheric oxidation product of phthalate, which is frequently used as a plasticizer (Hyder et al. 2012; Hermabessiere et al. 2017). Biomass burning markers of lignin, cellulose, and conifer resin (Kawamura et al. 2012) were included, as well as biogenic SOA markers of isoprene and monoterpene. Mannitol and xylitol are tracers for airborne fungal spores and biomass burning (Bauer et al. 2008; Saarnio et al. 2010). Dodecanoic acid (lauric acid), tetradecanoic acid (myristic acid), hexadecenoic acid (palmitic acid), and methanesulfonic acid were selected as proxies for marine sea spray emission (Meyers 1997; Wolff et al. 2006; King et al. 2019b). In addition, a first study of LOPs from polymeric lignin precursors was aimed. To analyze the monomeric composition lignin was degraded into LOPs (chapter 2.3), which are similar to the biomass burning products of lignin in aerosols and therefore the polymeric lignin was separated from the initially present biomass burning markers in the ice core by two subsequent extraction procedures.

Table 5: Target analytes for method development, their origin (anthrop=anthropogenic, BB=biomass burning, and environmental relevance, molecular formula, *m/z* of the deprotonated species $[M-H]^-$, *m/z* of a fragment from MS^2 measurements for quality control (QC), the respective neutral loss group, the chosen LC-method and the sample preparation method.

Origin	**Analyte**	**Molecular formula**	***m/z* [M-H]$^-$**	***m/z* MS^2 for QC**	**Neutral loss**	**LC**	**Method**
Anthrop.	4-Methylphthalic acid	$C_9H_8O_4$	179.0349			PFP	WAX
Anthrop.	Phthalic acid	$C_8H_6O_4$	165.0193	121.0296	$-CO_2$	HILIC	WAX
Anthrop.	Pimelic acid	$C_7H_{12}O_4$	159.0662	115.0765	$-CO_2$	PFP	WAX
BB cellulose	Gluconic acid	$C_6H_{12}O_7$	195.0510			PFP	WAX
BB cellulose	Hydroxymethyl-furfural	$C_6H_6O_3$	125.0244			HILIC	WAX
BB cellulose	Levoglucosan	$C_6H_{10}O_5$	161.0455			HILIC	Vacuum evap.
BB lignin	Acetovanillon	$C_9H_{10}O_3$	165.0557			PFP	WAX
BB lignin	*trans*-Cinnamic acid	$C_9H_8O_2$	147.0451	121.0297	$-C_2H_2$	HILIC	WAX
BB lignin	*p*-Coumaric acid	$C_9H_8O_3$	163.0400	119.0502	$-CO_2$	PFP	WAX
BB lignin	*trans*-Ferulic acid	$C_{10}H_{10}O_4$	193.0506	149.0608	$-CO_2$	PFP	WAX
BB lignin	*p*-Hydroxy-acetophenon	$C_8H_8O_2$	135.0452	93.0346	$-C_2H_2O$	PFP	WAX
BB lignin	*p*-Hydroxy-benzaldehyde	$C_7H_6O_2$	121.0950			PFP	WAX
BB lignin	*p*-Hydroxybenzoic acid	$C_7H_6O_3$	137.0244	93.0346	$-CO_2$	PFP	WAX
BB lignin	Salicylic acid	$C_7H_6O_3$	137.0244	93.0346	$-CO_2$	PFP	WAX
BB lignin	Syringaldehyde	$C_{10}H_{10}O_4$	181.0506	166.0269	$-CH_3$	PFP	WAX
BB lignin	Syringic acid	$C_9H_{10}O_5$	197.0455	153.0557	$-CO_2$	PFP	WAX
BB lignin	Vanillic acid	$C_8H_8O_4$	167.0349	152.0114	$-CH_3$	PFP	WAX
BB	Vanillin	$C_8H_8O_3$	151.0400	136.0166	$-CH_3$	PFP	WAX

Origin	Analyte	Molecular formula	*m/z* $[M-H]^-$	*m/z* MS^2 for QC	Neutral loss	LC	Method
lignin							
BB lignin	Acetosyringone	$C_{10}H_{12}O_4$	195.0663	165.0193	$-C_2H_6$	PFP	WAX
BB resin	Dehydroabietic acid	$C_{10}H_{28}O_2$	299.2017			HILIC	WAX
Fungal spores	Mannitol	$C_6H_{14}O_6$	181.0718			HILIC	Vacuum evap.
Fungal spores/BB	Xylitol	$C_5H_{12}O_5$	151.0612			HILIC	Vacuum evap.
Isoprene	Erythritol	$C_4H_{10}O_4$	121.0506			HILIC	Vacuum evap.
Mono-terpene	BTCA	$C_7H_{10}O_6$	189.0405			PFP	WAX
Mono-terpene	Ketopinic acid	$C_{10}H_{14}O_3$	181.0870			HILIC	WAX
Mono-terpene	MBTCA	$C_8H_{12}O_6$	203.0561	185.0456	$-H_2O$	PFP	WAX
Mono-terpene	Pinic acid	$C_9H_{14}O_4$	185.0819	141.0922	$-CO_2$	PFP	WAX
Mono-terpene	*cis*-Pinonic acid	$C_{10}H_{16}O_3$	183.1026	141.0922	$-C_2H_2O$	HILIC	WAX
Mono-terpene	Terebic acid	$C_7H_{10}O_4$	157.0506	113.0609	$-CO_2$	PFP	WAX
BSOA	Camphoric acid	$C_{10}H_{16}O_4$	199.0975	155.1078	$-CO_2$	PFP	WAX
BSOA	*trans*-1,2-Cyclohexane-dicarboxylic acid	$C_8H_{12}O_4$	171.0662	127.0765	$-CO_2$	PFP	WAX
BSOA	Malic acid	$C_4H_6O_5$	133.0142			HILIC	WAX
Org. Sulfate	Camphor-sulfonic acid	$C_{10}H_{16}O_4S$	231.0697			HILIC	WAX
Polymeric lignin	Syringaldehyde	$C_{10}H_{10}O_4$	181.0506			PFP	Lignin degradation
Polymeric lignin	Acetosyringone	$C_{10}H_{12}O_4$	195.0663	165.0193	$-C_2H_6$	PFP	Lignin degradation
Polymeric lignin	Syringic acid	$C_9H_{10}O_5$	197.0455	153.0557	$-CO_2$	PFP	Lignin degradation
Polymeric lignin	Vanillin	$C_8H_8O_3$	151.0400	136.0166	$-CH_3$	PFP	Lignin degradation

Origin	Analyte	Molecular formula	*m/z* $[M-H]^-$	*m/z* MS^2 for QC	Neutral loss	LC	Method
Polymeric lignin	Acetovanillon	$C_9H_{10}O_3$	165.0557			PFP	Lignin degradation
Polymeric lignin	Vanillic acid	$C_8H_8O_4$	167.0349	152.0114	$-CH_3$	PFP	Lignin degradation
Polymeric lignin	*p*-Coumaric acid	$C_9H_8O_3$	163.0400	119.0502	$-CO_2$	PFP	Lignin degradation
Polymeric lignin	*trans*-Ferulic acid	$C_{10}H_{10}O_4$	193.0506	149.0608	$-CO_2$	PFP	Lignin degradation
Sea spray	Methanesulfonic acid	CH_4O_3S	94.9808			PFP	WAX
Sea spray	Lauric acid	$C_{12}H_{24}O_2$	199.1703			PFP	WAX
Sea spray	Myristic acid	$C_{14}H_{28}O_2$	227.2017			PFP	WAX
Sea spray	Palmitic acid	$C_{16}H_{32}O_2$	255.2329			PFP	WAX

7.2 Experimental Part

7.2.1 Materials

Lev (>99%), vanillin (99%), 5-hydroxymethyl-2-furaldehyd (98%), formic acid (99%), and *p*-hydroxybenzoic acid (99%) were purchased from Acros Organics (Geel, Belgium). Dodecanoic acid (99.5%) and vanillic acid (98%) were obtained from Alfa Aesar (Karlsruhe, Germany). ACN (LC-MS grade), MeOH (LC-MS grade), and water (LC-MS grade) were purchased from Fisher Scientific (Darmstadt, Germany). Tetradecanoic acid (analytical grade) and 1,2,4-butanetricarboxylic acid (BTCA, >99%) were obtained from Fluka (Munich, Germany). Dehydroabietic acid was purchased from Chemos GmbH (Altdorf, Germany). Ammoniumacetate (98%), ammonium formate (98%), D-L-Malic acid (>99.5%) and hydrochloric acid (30%) were purchased from Merck (Darmstadt, Germany). 3,5-Dimethoxy-4-hydroxyacetophenone (97%), salicylic acid (99%), camphorsulfonic acid (98%), *cis*-pinonic acid (98%), *trans*-cinnamic acid (97%), pimelic acid (96%), *p*-coumaric acid (>98%), *p*-hydroxyacetophenone (>98%), 4-methylphthalic acid (99%), *trans*-ferulic acid (99%), terebic acid, *cis,trans*-pinic acid, hexadecanoic acid (>99%), ammonium hydroxide solution (25%), *p*-hydroxybenzaldehyde (>97.5%), 4-hydroxy-3-methoxyacetophenone (>98%), syringaldehyde (98%), *meso*-erythritol (>99%), mannitol (≥98%), (1S)-(+)-ketopinic acid (99%), phthalic acid (99.5%), methanesulfonic acid (99%), xylitol (≥99%), syringic acid (>95%), D-gluconic acid sodium salt (≥99%), *trans*-cyclohexane-1,2-dicarboxylic acid (95%), dichloromethane (p.a.), and (1R,3S)-(+)-camphoric acid (99%) were purchased from Sigma-Aldrich (Darmstadt, Germany). Formic acid (LC-MS, 99%) was delivered by VWR International GmbH (Darmstadt, Germany). Ultrapure water with 18.2 MΩ resistance was produced by a Milli-Q water system from Merck Millipore (Darmstadt, Germany).

7.2.2 Colle Gnifetti ice core sample preparation

The ice core from Colle Gnifetti (45°55′45.7″N, 7°52′30.5″E) was drilled and recovered in 2015 by a team from the Paul Scherrer Institute (PSI), Villigen, Switzerland. The ice core sections were dated by annual layer counting in combination with the determination of absolute time markers like Saharan dust storm events and the nuclear isotope peak from 1963 (Jenk et al. 2009; Brugger et al. 2021). Samples were stored at -20°C in a cold room at PSI before preparation for analysis. The core was cut in contiguous sections, which were thawed under inert helium atmosphere and filtered through a quartz-fiber filter (Fang et al. 2021). Aliquots of approximately 30 mL were taken and re-frozen in pre-cleaned glass jars with PTFE-coated screw caps (Table S 4). The cleaning procedure included a bake out at 450°C for at least 8 hours, rinsing three times with ultrapure water and three times with MeOH. The screw caps were rinsed three times with ultrapure water and three times with MeOH. After cleaning, the vials and caps were dried under a laminar flowhood. Sample-containing vials were closed with the screw-caps, sealed from the outside with Parafilm and stored at -20°C until analysis. Prior to analysis the samples were melted at room temperature.

7.2.3 Chromatography and mass spectrometry

Method development and analysis was conducted using a Dionex UltiMate 3000 UHPLC system with an HPG-3400 RS pump (Thermo Fisher Scientific). The UHPLC system was coupled to a Q Exactive Orbitrap high resolution MS (Thermo Fisher Scientific) and an additional external pump (High precision pump Model 300 C S) from Gynkotek (Germering, Germany) was used for post-column derivatization. The ESI probe was heated to 150°C to enhance solvent evaporation, the capillary temperature was set to 320°C, sheath gas pressure to 60 psi, auxiliary gas pressure to 20 psi and the spray voltage to -3.5 kV. The mass spectrometer was operated in full scan mode, (*m/z* 80-500), with a mass resolution of 70,000. XCalibur 4.3 and the integrated SII control plugin for the chromatography system was used for instrument control.

Chromatographic separation on RP columns was evaluated on an Acquity UPLC CSH Fluoro-Phenyl (PFP) column (100x2.1 mm, 1.7 µm) from Waters (Milford, USA) and on a Hypersil GOLD column (50x2.1 mm, 1.9 µm) from Thermo Fisher Scientific (Darmstadt, Germany). Eluent A consisted of H_2O/ACN 98:2 (v/v) with 400 µL/L of formic acid, while eluent B consisted of H_2O/ACN 2:98 (v/v). The flowrate was set to 0.4 mL/min, injection volume to 10 µL, and the columns were heated to 30°C during method development. Five different gradients were used on both columns to evaluate the separation efficiency (Table 6), including an isocratic method (gradient A), a linear gradient (gradient C), step gradients (gradient B), and combination of linear and step gradients (gradient D and E). The final method was developed on the PFP column starting with 1% of eluent B which was increased to 99% within 13 minutes and held for one minute. Afterwards, the column was re-equilibrated with the starting conditions of 1% eluent B for one minute.

Table 6: Gradients A-E evaluated on the C_{18} and PFP reversed-phase columns. Eluent B consisted of ACN/H_2O 98:2.

Gradient A		**Gradient B**		**Gradient C**		**Gradient D**		**Gradient E**	
t (min)	*% B*	*t (min)*	*% B*	*t (min)*	*% B*	*t (min)*	*% B*	*t (min)*	*% B*
0	10	0	5	0	10	0	5	0	10
11	10	0.5	10	11	99	0.5	5	2	25
		5	10	12	99	5	15	4	30
		6	15			7	99	8.5	65
		7	30			8	99	9	65
		7.5	50						
		7.55	99						

To evaluate separation of the target compounds on the HILIC columns the iHILIC-Fusion and IHILIC-Fusion(+) columns (both 100x2.1 mm, 1.8 µm) from HILICON AB (Umeå, Sweden) were tested. Five different gradients were evaluated including stepwise and linear decrease of eluent B (Table 7), consisting of ACN, while eluent A was a buffer solution of either ammonium acetate or ammonium formate with concentrations of 5 mM or 10 mM, respectively. The columns were heated to 30°C, injection volume was 10 µL, and the flowrate was set to 0.4 mL/min. The final method included an additional PCF of 0.1 mL/min of a methanolic ammonium hydroxide (50 mM) solution, that was introduced by a T-piece between the column and the MS. The gradient started at an eluent composition of ACN/buffer 97:3 (v/v) from 0-0.5 minutes, before decreasing the ACN content to 50% within 11.5 minutes and holding for two minutes. Afterwards the column was re-equilibrated with starting conditions for 8 minutes.

Table 7: Gradients A-E evaluated on the iHILIC-Fusion and iHILIC-Fusion(+) columns. Eluent B consisted of ACN.

Gradient A		**Gradient B**		**Gradient C**		**Gradient D**		**Gradient E**	
t (min)	*% B*	*t (min)*	*% B*	*t (min)*	*% B*	*t (min)*	*% B*	*t (min)*	*% B*
0	97	0	97	0	97	0	97	0	97
1	97	0.5	97	0.5	97	0.5	97	0.5	97
2	90	1	90	1	90	1	90	1	90
10	80	6	85	6	85	6	85	6	85
12	75	7.5	60	7.5	60	7.5	60	7.5	60
12.5	60	10	60	9	50	9	50	9	50
15	60	10.5	97	9.5	97	10	50	11	50
15.5	97	22	97	20	97	10.5	97	11.5	97
25	97					21	97	22	97

7.2.4 Solid-phase extraction

Several SPE materials were evaluated using different sample preparation protocols for enrichment of a preferably high number of target compounds. Oasis WAX cartridges (3 cc, 60 mg, 30 µm) were used as weak anion-exchange material and purchased from Waters (Milford, USA). The cartridges were conditioned and equilibrated twice with 3 mL of MeOH and twice with formic acid (0.1%). Samples were set to different pH values (pH 6.0, pH 8.0, pH 10.0) and after applying the samples, the cartridges were washed with three portions of 3 mL formic acid (0.1%) and dried for 20 minutes by sucking ambient air through the cartridges using a vacuum manifold. Samples were eluted using 500 µL of MeOH twice, and 500 µL of a methanolic NH_4OH solution (5%) twice.

Oasis MAX cartridges (1 cc, 10 mg, 30 µm) were purchased from Waters (Milford, USA) and evaluated as SAX material using two different protocols and three different sample pH values (pH 6.0, pH 8.0, pH 10.0). In the first method, the cartridges were conditioned and equilibrated using 1 mL of MeOH and 1 mL of H_2O, twice. After applying the samples, the cartridges were washed using three times 500 µL of a 10 mM ammonium acetate solution and dried for 20 minutes. Elution was conducted using 500 µL of MeOH and 500 µL a methanolic formic acid solution (2%), twice. In the second method, conditioning and equilibration was conducted using 1 mL MeOH twice, 1 mL of H_2O, and 1 mL of a 5% NH_4OH solution. After the samples were applied to the cartridges, the cartridges were washed with three portions of 500 µL the 5% NH_4OH solution before being dried for 20 minutes. Cartridges were eluted using three times 500 µL of a methanolic formic acid solution (5%).

For enrichment of polar compounds GCB material was investigated. Supelclean ENVI-Carb cartridges (3 cc, 250 mg) were purchased from Sigma-Aldrich (Darmstadt, Germany) and evaluated using two protocols. The first method started by conditioning and equilibration of the columns using 3 mL of MeOH and 3 mL of H_2O, twice. After applying the samples, the cartridges were washed with 3 mL of H_2O, twice before drying for 20 minutes by vacuum manifold. Elution was conducted using three portions of 500 µL MeOH, three portions of 500 µL MeOH/DCM (8:2, v/v), and three portions of 500 µL MeOH/DCM (2:8, v/v). The order of the MeOH/DCM mixtures was varied in two experiments. During the second method cartridges were conditioned twice with 3 mL of MeOH and twice with 3 mL of formic acid (0.1%). After applying the samples, cartridges were washed twice with 3 mL of formic acid (0.1%) and dried for 20 minutes. Elution was conducted similarly to the first method and accordingly the order of the MeOH/DCM mixtures was varied.

HLB cartridges (3 cc, 60 mg, 30 µm) were purchased from Waters (Milford, USA). Two methods were compared for enrichment of target compounds. In the first method cartridges were conditioned and equilibrated using 3 mL of MeOH and 3 mL of H_2O, twice. After applying the samples, cartridges were washed twice with 3 mL of an aqueous solution containing 5% of MeOH and dried for 20 minutes. Cartridges were eluted with three times 500 µL of MeOH, three times 500 µL of 2% formic acid in MeOH/H_2O (1:1, v/v), and three times 500 µL of 5% NH_4OH in MeOH/H_2O (1:1, v/v). During the

second method cartridges were conditioned twice with 3 mL of MeOH and twice with 3 mL of formic acid (0.1%). After samples were applied, cartridges were washed twice with 3 mL of formic acid (0.1%) and dried for 20 minutes. Elution was conducted using three portions of 500 µL of a methanolic solution containing 2% NH_4OH.

Another reversed-phase material was evaluated using Discovery DSC-18 cartridges (3 cc, 500 mg) purchased from Merck (Darmstadt, Germany). The first method started by conditioning the cartridges twice with 3 mL of MeOH, and 3 mL of H_2O, before the sample was applied. Afterwards, cartridges were washed with 3 mL of an aqueous solution containing 5% of MeOH twice and dried for 20 minutes. Cartridges were eluted using four portions of 500 µL of MeOH. In the second method cartridges were conditioned twice with 3 mL of MeOH and twice with 3 mL of formic acid (0.1%). No washing step was included and after drying for 20 minutes the cartridges were eluted with four portions of 500 µL of MeOH. All elution solvents were evaporated to dryness under a gentle stream of nitrogen and during method development re-constituted in 500 µL of ACN/H_2O (1:1, v/v) prior to measurement by RP-LC and HILIC MS.

7.2.5 Lignin oxidation

Polymeric lignin was extracted from the captured flow-through of the WAX cartridges using HLB cartridges that were conditioned twice with 3 mL of MeOH and twice with 3 mL of formic acid (0.1%). After applying the flow-through, the cartridges were washed twice with 3 mL of H_2O and dried for 20 minutes. Elution was conducted with ten portions of 250 µL of MeOH and after evaporation of the eluate to almost dryness under a gentle stream of nitrogen, the samples were re-constituted in 200 µL of MeOH and sonicated for 10 minutes at 45°C. The solution was transferred to 500 µL PFA vials from Savillex (Eden Prairie, USA). The sample containers were flushed with 100 µL of MeOH, sonicated for 10 minutes at 45°C, and the solution was added to the PFA vials. The solution in the PFA vials was evaporated to dryness under a gentle stream of nitrogen, re-constituted in 200 µL of degassed sodium hydroxide (NaOH, 1 M) and sonicated for 10 minutes at 45°C. Afterwards, the solutions were spiked with 10 µL of $CuSO_4$ solution (10 mM) and 10 µL of ascorbic acid (0.2 M), and the atmosphere in the vials was exchanged with nitrogen. Five PFA vials were placed in respectively one microwave vessel, which was in turn filled with 7 mL of NaOH (1 M) to half the height of the PFA vials for pressure exchange. The temperature program for the oxidation in the GC oven started with an initial temperature of 25°C which was held for 1 minute before increasing temperature to 155°C within 5 minutes and holding this temperature for 90 minutes. After cooling, the sample solutions were neutralized with 40 µL of HCl (30%) before enrichment of LOPs by a second HLB SPE cartridge (1 cc, 30 mg, 30 µm) from Waters (Milford, USA). The cartridges were conditioned twice with 1 mL of MeOH and twice with 1 mL of HCl (0.6%). After applying the samples, cartridges were washed with 500 µL of HCl (0.6%) and dried for 20 minutes by vacuum manifold. Elution was conducted with eight portions of 125 µL of 2%

NH_4OH in ACN. The eluate was evaporated under a gentle stream of nitrogen, re-constituted in 500 µL of H_2O/ACN (9:1, v/v), and analyzed by RP-LC MS.

7.2.6 Centrifugal evaporation

Centrifugal evaporation was conducted using an Eppendorf Concentrator plus purchased from Eppendorf (Hamburg, Germany) at a rotational speed of 1400 rpm. Four temperatures were evaluated (room temperature, 30°C, 45°C, and 60°C) and sample recovery from the centrifugal tubes was investigated using six solvent mixtures, including ACN, ACN/H_2O (9:1, v/v), ACN/H_2O (1:1, v/v), MeOH, MeOH/DCM (8:2, v/v), and MeOH/DCM (1:1, v/v). After evaporation, the centrifugal tubes were flushed with 1.5 mL of solvent and sonicated for 10 minutes at 30°C. The solution was transferred to an HPLC vial and the procedure was repeated. Afterwards, the solution in the vial was evaporated to dryness under a gentle stream of nitrogen and re-constituted in 500 µL ACN/H_2O (95:5, v/v).

7.2.7 Final method

The final sample preparation method consisted of a double-layer SPE for enrichment of SOA marker compounds and separation of lignin burning markers from polymeric lignin on the WAX cartridge and enrichment of polymeric lignin on the HLB cartridge. The flow-through of both SPE cartridges was captured and evaporated by centrifugal evaporation to recover small, hydrophilic compounds like Lev (Figure 55). The two SPE cartridges were conditioned separately with two portions of 3 mL MeOH and two portions of 3 mL formic acid (0.1%). The pH value of the sample was set to a pH value of 8 with aqueous NH_4OH (5%) solution. For applying the sample, the cartridges were connected with the WAX cartridge at the top and the HLB cartridge at the bottom. To prevent drying of the solid material, 1.5 mL of formic acid (0.1%) were applied to the HLB cartridge and 1.5 mL of the sample solution were applied to the WAX cartridge beforehand. The flow-through of the combined cartridges was captured for further preparation by centrifugal evaporation. Afterwards, the combined cartridges were washed twice with 3 mL of H_2O before separate elution. The WAX cartridges were eluted with three portions of 500 µL MeOH and three portions of 500 µL of a methanolic solution containing 5% NH_4OH. The solution was evaporated to dryness under a gentle stream of nitrogen, re-constituted in 200 µL of H_2O/ACN (1:1, v/v), sonicated for 10 minutes at 30°C and filtered by Micropur PTFE filters (3 mm, 0.20 µm) purchased from Altmann-Analytik (München, Germany). The solutions were measured by RP-LC and HILIC MS. The HLB cartridges were eluted with ten portions of 250 µL MeOH. The solution was evaporated to dryness and further prepared according to chapter 5.2.2.1. The flow-through was evaporated to dryness by centrifugal evaporation at 45°C. Afterwards, the centrifugal tubes were flushed with 1.5 mL of ACN and sonicated for 10 minutes at 30°C twice. The transferred solution was evaporated to dryness in the HPLC vial, reconstituted in 200 µL of ACN/H_2O (95:5), sonicated for 10 minutes at 30°C, filtered and measured by HILIC MS.

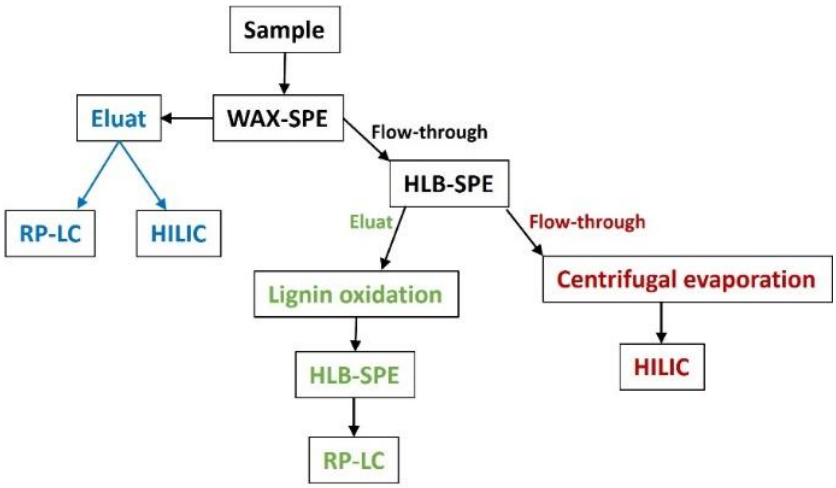

Figure 55: Schematic workflow of the final method including two subsequent solid-phase extractions, and the evaporation of the flow-through by centrifugal evaporation (red). Lignin oxidation is conducted with the eluate of the HLB-SPE (green) and the respective chromatographic method for each sample is presented.

7.3 Results and Discussion

7.3.1 Method development and validation

7.3.1.1 Liquid chromatography

Two RP-LC columns with different stationary phases were evaluated for most efficient separation of the target analytes and the capacity factor (k') of all analytes were determined by optimized gradients (Figure 56). The C_{18}-column is functionalized with aliphatic C_{18}-alkyl chains, while the PFP column is functionalized with fluor-substituted phenyl-residues, enhancing the interaction of aromatic compounds with the stationary phase by additional π-π interactions.

The k' on the PFP-column showed larger distribution than on the C_{18}-column. The regression lines of all analyte groups showed only minor slopes on the y-axis, thus the C_{18}-column did not provide sufficient retention differences for separation, in contrast to the PFP column (Figure 56a). In addition, the medium k' of all target analytes was higher on the PFP-column. The boxplot analysis of the C_{18}-column showed a strong tendency towards lower k', while the PFP-column showed outliers at high k', corresponding to strong retention of these compounds and consequently well separation (Figure 56b).

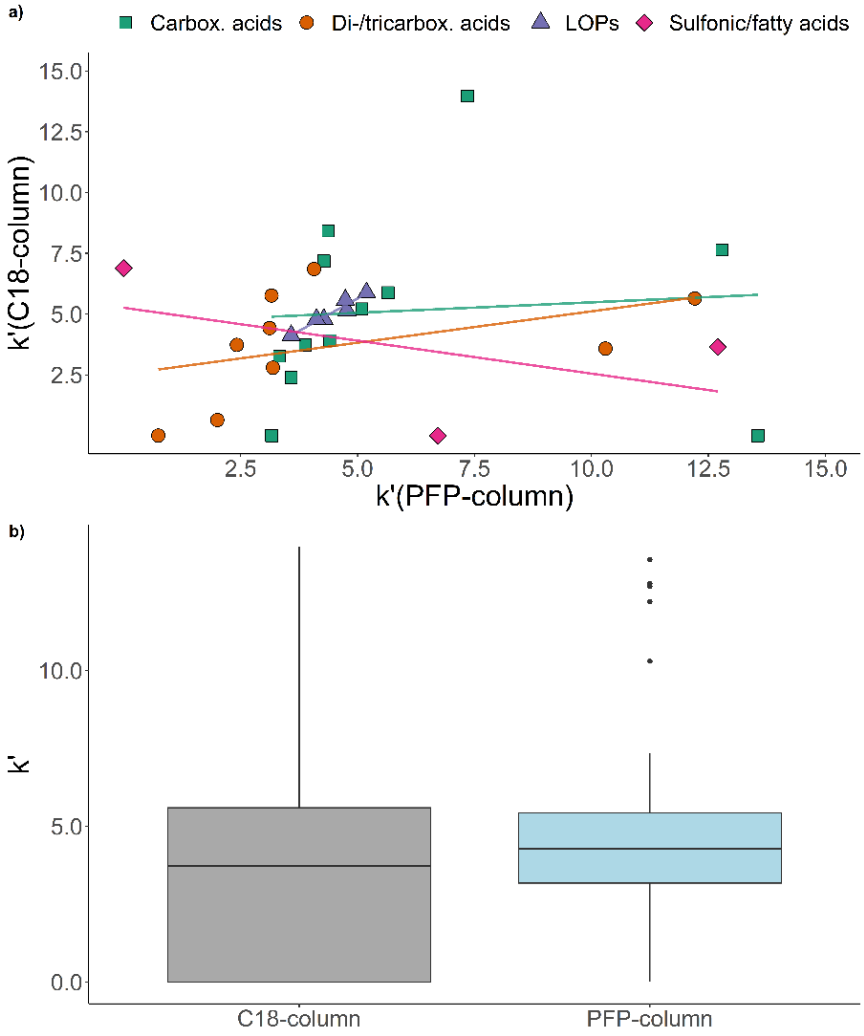

Figure 56: a) Comparison of the capacity factors (k') of analytes with different functionalities on the C_{18}- and PFP-column with respective regression lines visualizing the general retention differences. b) Boxplot of all capacity factors of the target analytes on the C_{18}- and PFP-column (b).

The PFP column was suitable to separate most compounds, but small, polar compounds like Lev, mannitol, or xylitol, were inaccessible using reversed-phase stationary phases. Therefore, two HILIC columns were used to separate the remaining target compounds most efficiently. Retention on HILIC phases depends on several mechanisms and factors like the percentage of water in the eluent, buffer concentration, pH value, or temperature (see chapter 4.2.1). Method development on the HILIC columns was conducted using isocratic solvent conditions of ACN and the respective buffer solutions in a ratio of 97:3 (v/v). Ammonium formate and ammonium acetate were evaluated as buffers with different concentrations (5 mM and 10 mM) at different temperatures (room temperature, 30°C, 40°C) (Figure 57).

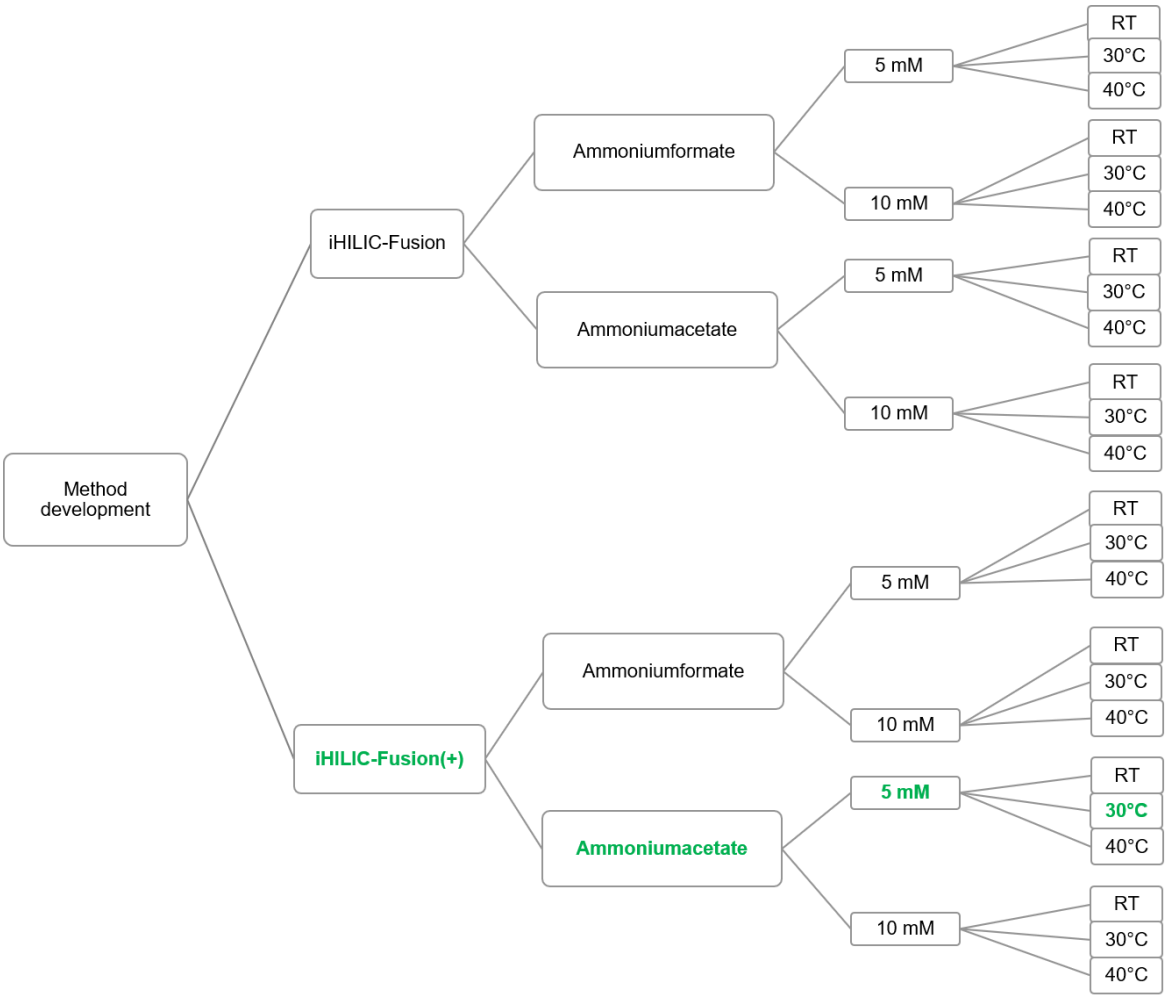

Figure 57: Schematic representation of tested conditions on the HILIC columns during method development. Final conditions are marked in green.

The retention time of each analyte was normalized to the first peak in the chromatogram and defined as the k' which in turn was plotted in logarithmic scale to the respective tested conditions (Figure 58). Heating of the columns to 30°C or 40°C always resulted in a significant increase of k', indicating that the retention was strongly improved by enhancing the diffusion of analytes between the aqueous and the organic phase. For the small organic compounds, the Fusion column showed generally higher k'-values but a significant opposite effect was observable for the fatty acids. Those did not experience sufficient retention on the Fusion column regardless of the conditions. Therefore, the Fusion(+) column was prioritized for further evaluation. Mannitol, erythritol, and xylitol on the one hand, and the three fatty acids on the other hand showed consistent behavior on the Fusion(+) column, while Lev was only analyzable using an ammonium acetate buffer solution with a concentration of 5 mmol/L and a temperature of 30°C, which was therefore chosen as the optimum conditions for separation on the iHILIC-Fusion(+) column.

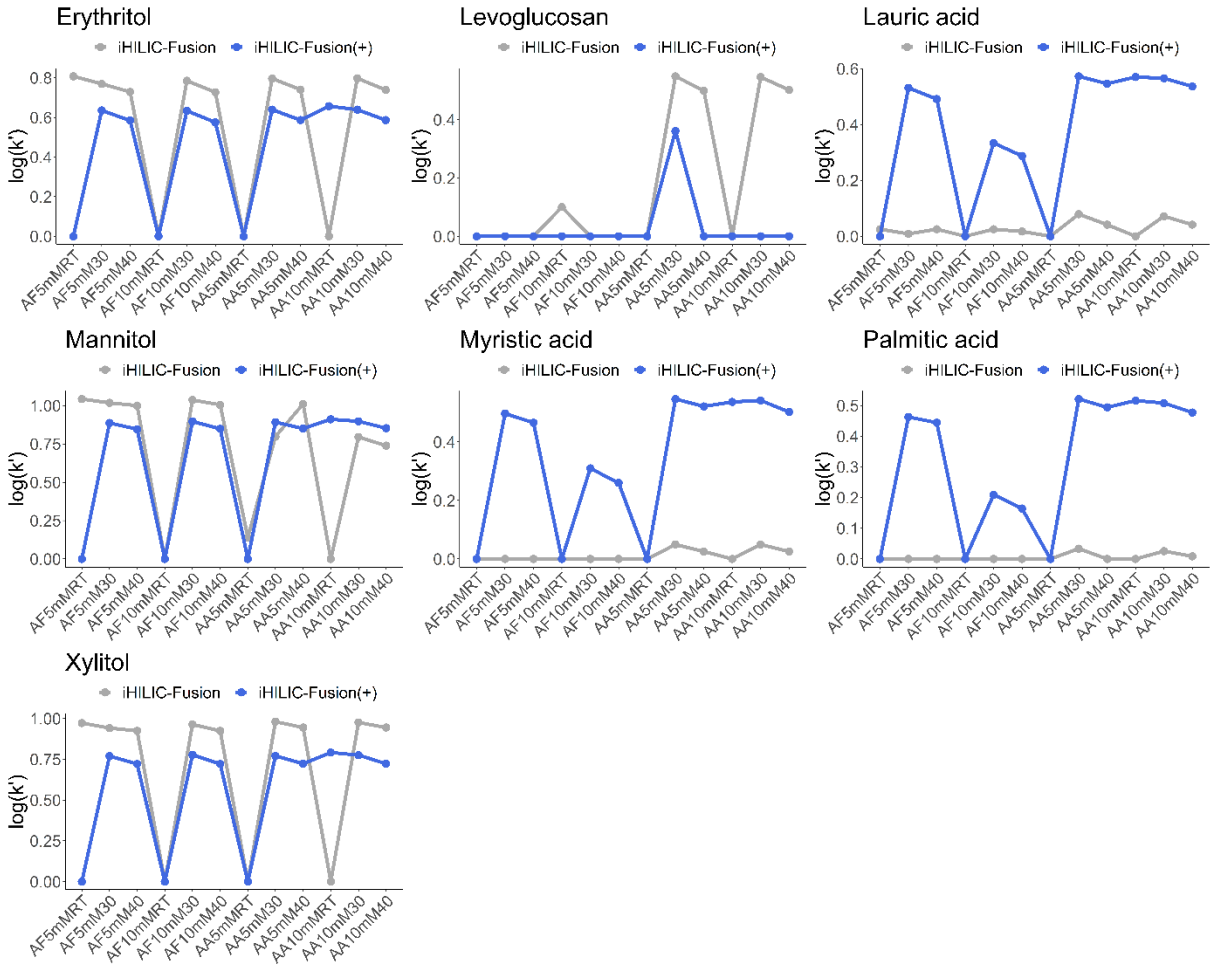

Figure 58: Logarithmic application of the capacity factor (k') on the iHILIC-Fusion (grey) and the iHILIC-Fusion(+) column (blue) of analytes depending on the buffer (AF=ammoniumformate, AA=ammonium acetate), buffer concentration (5 mM, 10 mM), and temperature (RT, 30°C, 40°C).

The degree of ionization of compounds has a significant influence on the intensity of the signal in the mass spectrum. The ESI source is responsible for the creation of desolvated single ions but only partly provides the initial ionization of compounds (see chapter 4.3.1). Ideally, compounds are charged prior to entering the MS in the LC solvents (Cech and Enke 2001). While most target analytes have carboxylic acid, or leastwise phenolic functionalities, facilitating ionization in aqueous solvents, compounds like Lev require strong pH adjustments for deprotonation. Considering the example of Lev, a pH value of 12 would be necessary to dissociate half of the molecules in the solution, but the utilized HILIC column only provided stability to a pH of 10. Therefore, an additional PCF was introduced between the column and the mass spectrometer. MeOH was used as an evaporable solvent with a concentration of 50 mmol/L of ammonium hydroxide solution. The hydroxide ions enhanced the deprotonation of Lev, and the formed reaction products water and ammonia were evaporated in the ESI source. In this way, sufficient ionization was provided not interfering with chromatographic separation. The effect of the PCF on the analytes was evaluated on all columns using a 500 ng/mL standard solution (Figure 59). The mean signal intensities on the C_{18}-column, the PFP column, and the iHILIC-Fusion column were not improved by

the PCF, while iHILIC-Fusion(+) column showed significantly increased average intensity. Therefore, the HILIC method was complemented by a PCF of 0.1 mL/min, while the PFP method did not require an additional pH adjustment for sufficient ionization.

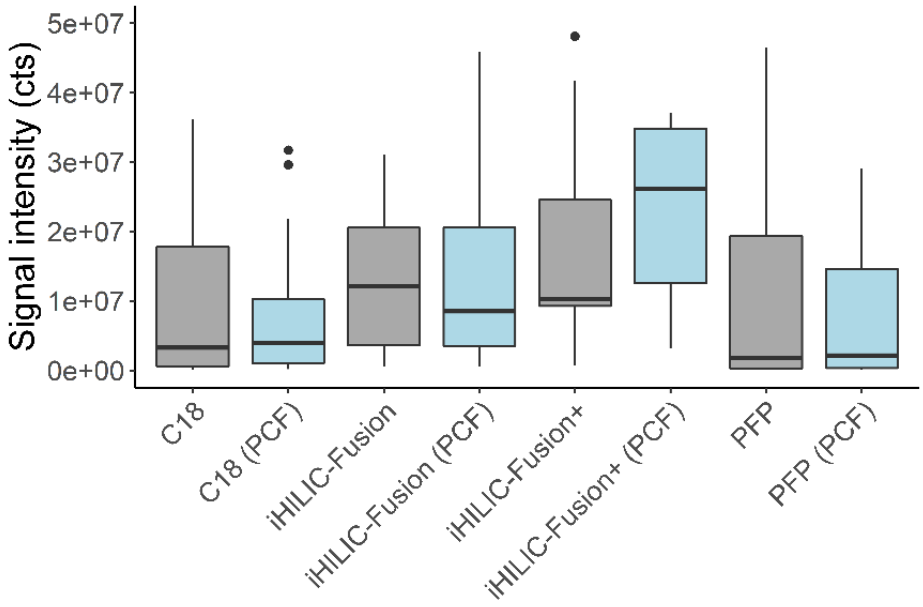

Figure 59: Boxplot of signal intensities of all target analytes on the four different LC columns with PCF (blue) and without PCF (grey)

The TIC of a 500 ng/mL standard solution on the Fusion(+) column revealed only minor differences with or without the PCF. However, the XIC of *m/z* 161.0455 (Lev) without the PCF did not show a peak, while the XIC with PCF revealed a narrow, gaussian peak with a signal-to-noise ratio of 77968.

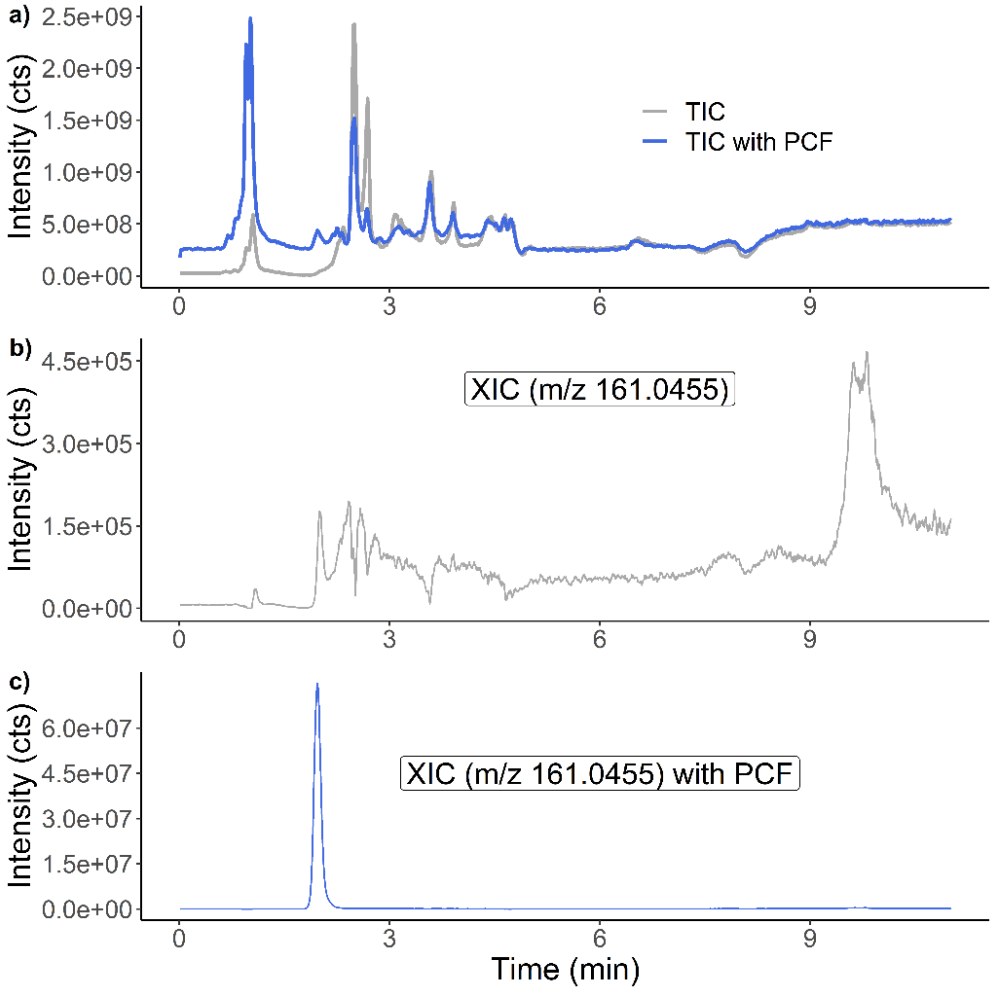

Figure 60: a) TIC of a 500 ng/mL standard solution on the iHILIC-Fusion (+) column with PCF (blue) and without PCF (grey). b) XIC of *m/z* 161.0455 without additional alkaline PCF. c) XIC of *m/z* 161.0455 with an additional PCF of 0.1 mL/min of 50 mM methanolic ammonium hydroxide solution.

Linearity of the two developed LC methods on the HILIC and the PFP column was evaluated by a series of standards with concentrations of 0.1 ng/mL, 0.5 ng/mL, 1 ng/mL, 5 ng/mL, 10 ng/mL, 25 ng/mL, 50 ng/mL, 75 ng/mL, 100 ng/mL, 250 ng/mL, 500 ng/mL, 1000 ng/mL, and 2000 ng/mL. The signal intensity divided by the concentration (I/c) was plotted to the logarithm of the concentration and all I/c values within a 5% deviation range of the mean value of all I/c values were considered as linear (Figure 61, Figure S 2-Figure S 4). Almost all compounds showed sufficient linearity up to the concentration of 2000 ng/mL, while only *p*-hydroxyacetophenone, *p*-hydroxybenzaldehyde, methanesulfonic acid, and Lev showed linearity in a concentration range below 1 ng/mL.

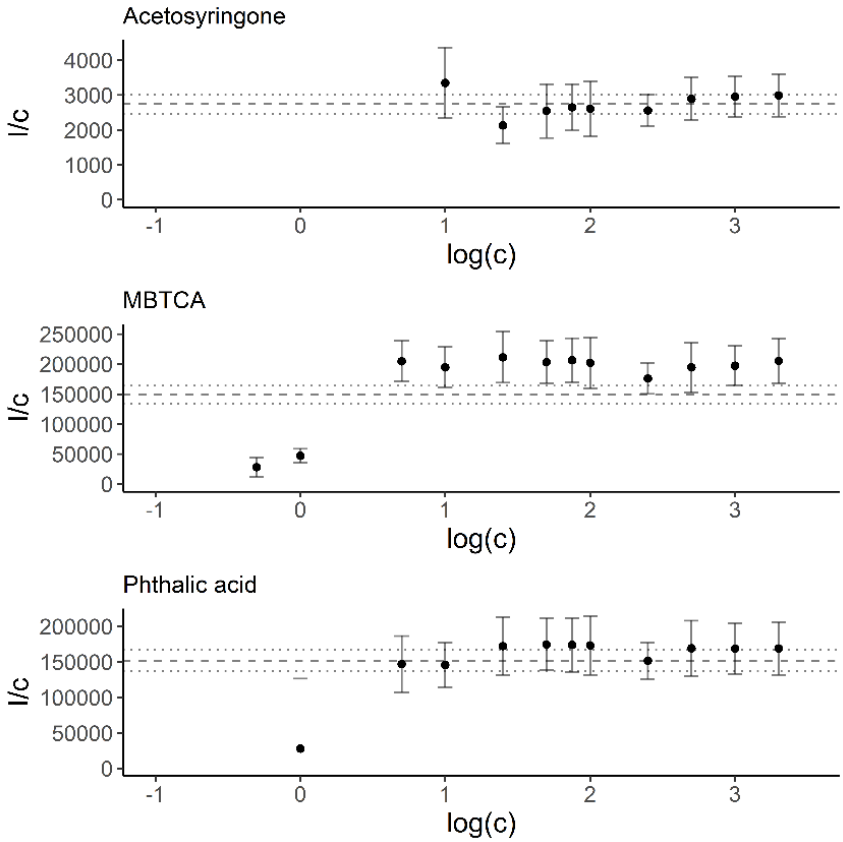

Figure 61: Plots of intensity to concentration ratio (I/c) to the logarithm of concentration of a series of standard solutions with increasing concentrations for evaluation of linearity of the LC-MS methods on the PFP and HILIC column for selected compounds (acetosyringone, MBTCA, phthalic acid).

The slope of the respective linear regression (m), as well as the standard deviation (SD) of a tenfold measurement of a blank solution of H_2O/ACN (1:1, v/v) were used to calculate the limits of detection LOD and LOQ of the respective analytes (Equation 17 and (Equation *18*), which are shown in Table S 3 in the appendix.

$$LOD = \frac{3 \cdot SD(blank)}{m\ (calibration\ curve)}$$

(Equation 17)

$$LOQ = \frac{10 \cdot SD(blank)}{m\ (calibration\ curve)}$$

(Equation 18)

The repeatability of the LC-MS methods was evaluated by fivefold measurements of the standard solutions. A boxplot visualization of the 25 ng/mL standard solution showed adequate repeatability (with relative standard deviations lower than 5%) for compounds with generally low signal intensities (Figure 62a), medium intensities (Figure 62b), and high intensities (Figure 62c).

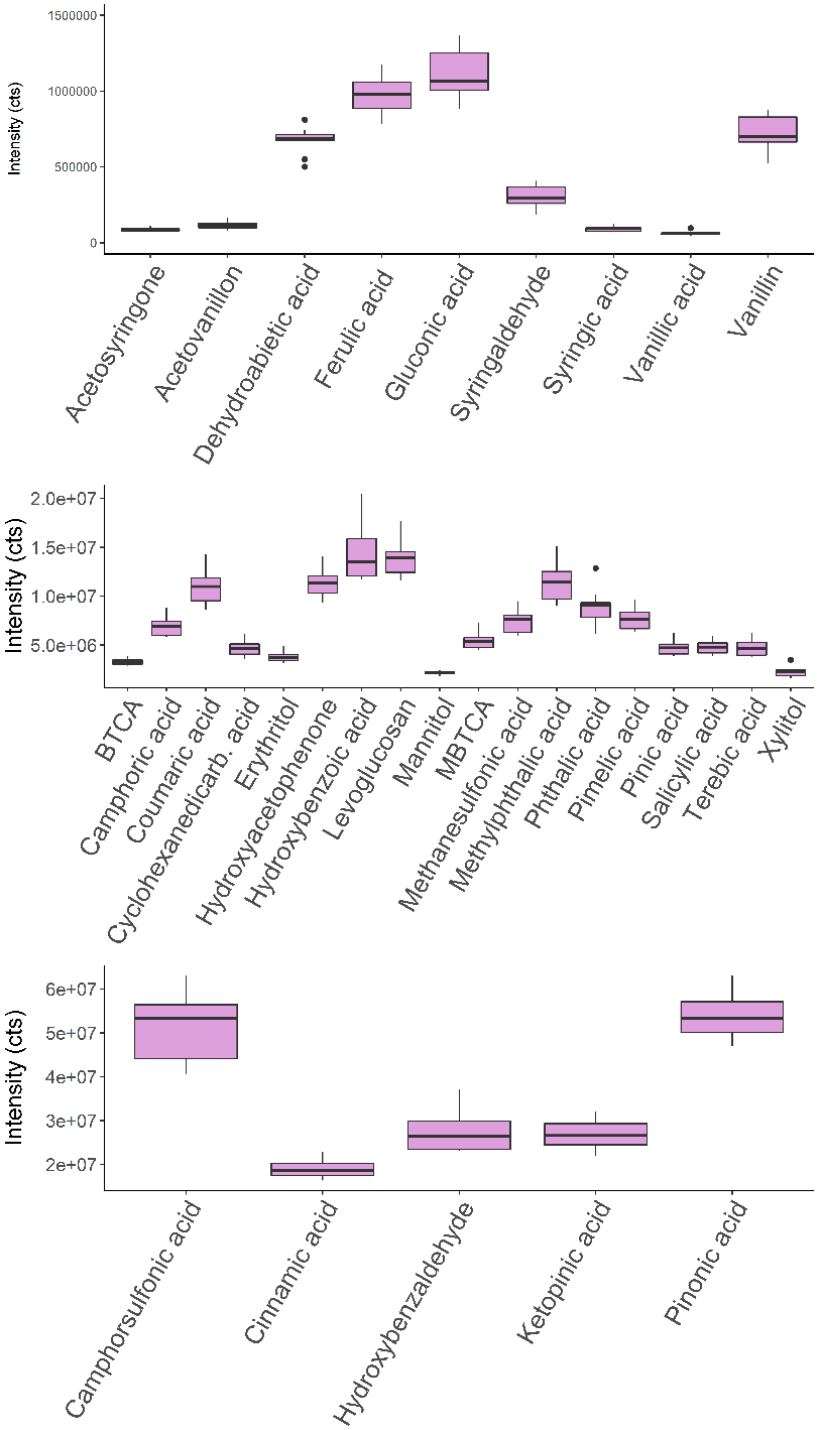

Figure 62: Repeatability of the LC-MS methods evaluated by fivefold measurement of a 25 ng/mL standard solution. a) Repeatability of compounds with low signal intensities. b) Repeatability of compounds with medium intensities. c) Repeatability of compounds with high signal intensities.

7.3.1.2 Solid-phase extraction

To quantify trace concentrations of organic compounds in the ice core samples, proper enrichment is a crucial part of sample preparation. A straightforward approach is SPE, where liquid samples are passed through a solid material and analytes are captured by the solid-phase based on their affinity towards the different functionalities (see chapter 4.1.1). Due to the variety of target compounds several materials were evaluated for the most efficient enrichment of an ideally high number of analytes. GCB material is based on carbon blacks heated at high temperatures (2700-3000°C), with various functional groups on the surface due to the chemisorption of oxygen during and after the heating process. Due to this variety, the interactions between analytes and the material, as well as the proper elution solvents are difficult to predict (Hennion 2000). However, the ability of GCB material to extract strongly hydrophilic compounds from aqueous matrices was demonstrated (Di Corcia and Samperi 1990; Corcia and Marchetti 1991) which is why GCB was included in the screening of SPE materials. As representatives for non-polar surfaces a silica-based C_{18}-functionalized material and a HLB material were chosen. Many analytes contained carboxylic acid functionalities, or at least a phenolic residue. Therefore, two different ion exchange materials were used: SAX and WAX. The difference between these materials was their pH-dependent charge state. SAX material was generally considered for the enrichment of weakly acidic compounds, because of the permanent positive charge of the material by quaternary ammonium groups. Permanently charged strong organic acids are not detachable, while the charge state of weak organic acids is adjusted by the pH value of the elution solvent, allowing high recovery and repeatability. WAX material contains chargeable functional groups, suitable for the enrichment of stronger carboxylic acids, because elution is ensured by discharging of the solid phase and thereby disrupting the ionic interactions. Both anion-exchange materials used in this work were based on a mixed-mode functionality with a basic structure similar to the HLB material (Figure 63).

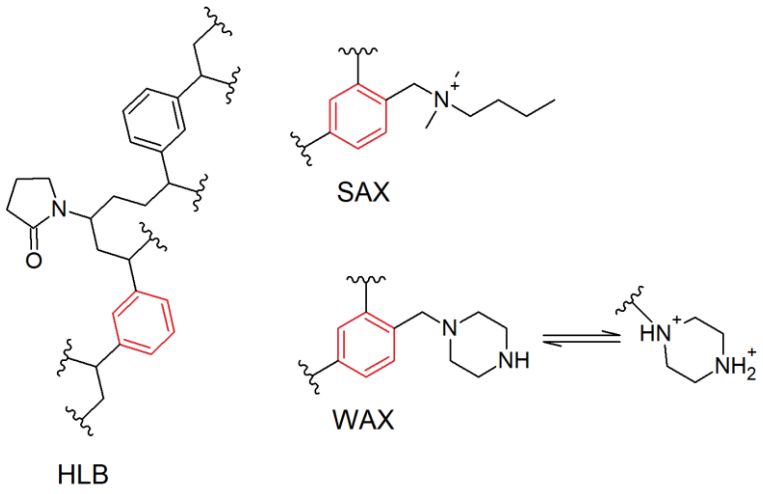

Figure 63: Structure of hydrophilic-lipophilic balanced material (HLB), strong anion exchange (SAX), and weak anion exchange (WAX) material adapted from Waters 2021.

Different conditioning of the cartridges, elution volumes, and elution solvents were evaluated (see chapter 7.2.4) on the different cartridges using 10 mL of deionized water spiked with 100 ng of the respective compounds resulting in a final concentration of 100 ng/mL in the final sample volume of 1 mL by an enrichment factor of 10. The most efficient methods on the respective SPE materials were chosen for comparison of the materials and a heatmap of the recovery of the analytes showed, that e.g., GCB material was only suitable for a minority of compounds (Figure 64). Hierarchical clustering provided more information on similarly behaving compounds on the different materials and similar efficiency of the respective materials. As anticipated, HLB and C_{18}-material showed comparable results, as well as SAX and WAX material. Most compounds were sufficiently recoverable on the WAX and the SAX material, while the non-polar phases did not provide recovery of fatty acids or methanesulfonic acid. The fatty acids were not recoverable from the flow-through of the SPE cartridge, thus the interaction with the solid phase was stronger than the affinity towards the elution solvent. Methanesulfonic acid on the other hand was recovered from the flow-through, so interaction with the solid-phase was too weak for sufficient retention. Malic acid, xylitol, mannitol, Lev, guaiacol, and erythritol (which is not displayed) did not experience retention on the SPE-materials due to their high hydrophilicity and were completely recoverable from the flow-through.

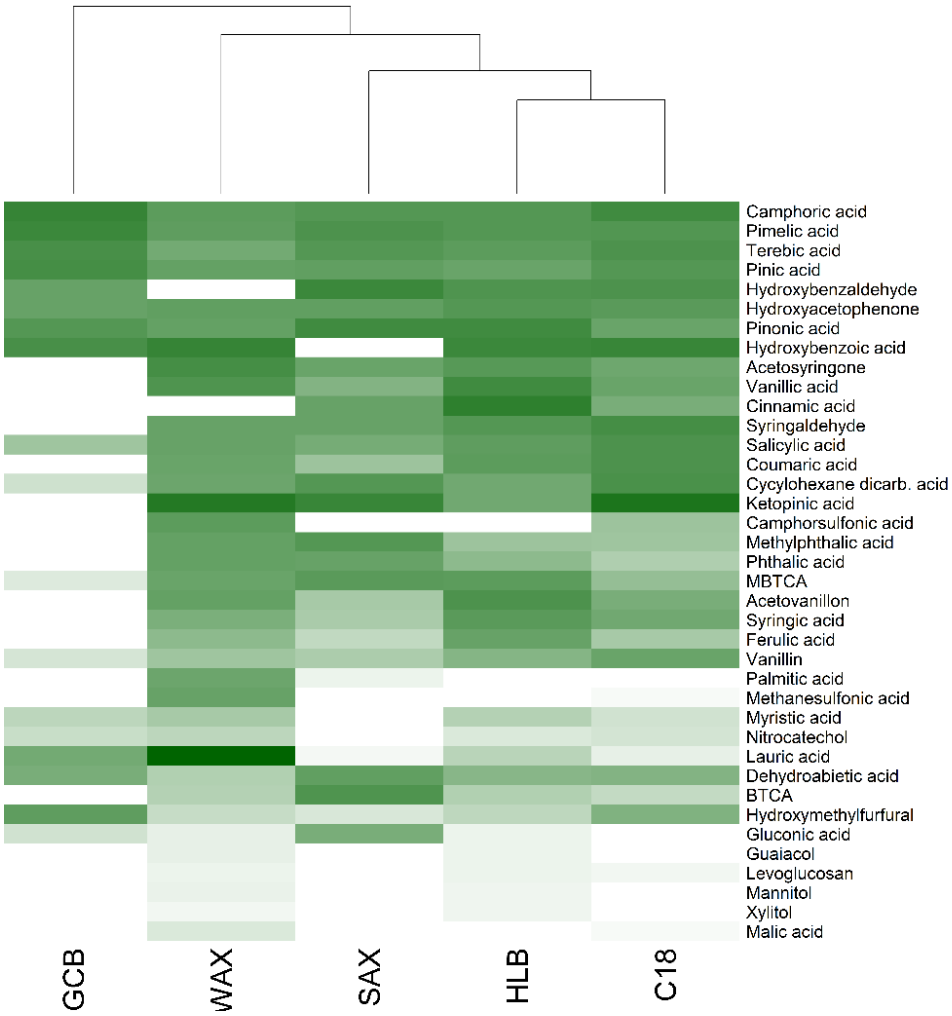

Figure 64: Heatmap of recoveries of the target compounds on different SPE materials. Dendrograms result from hierarchical clustering and grouping of compounds based on their behavior on the different SPE materials and grouping of SPE materials based on their enrichment efficiencies.

The performance of the anion-exchange material was further evaluated with different pH values of the sample solutions destined to enhance the charging of the compounds with high pK_a-values, or the solid phase. No interaction was observable for the small polar compounds on the SAX material, independent from the pH value. Other compounds did not behave significantly different with different pH values and showed rather poor recovery on the SAX material (Figure 65).

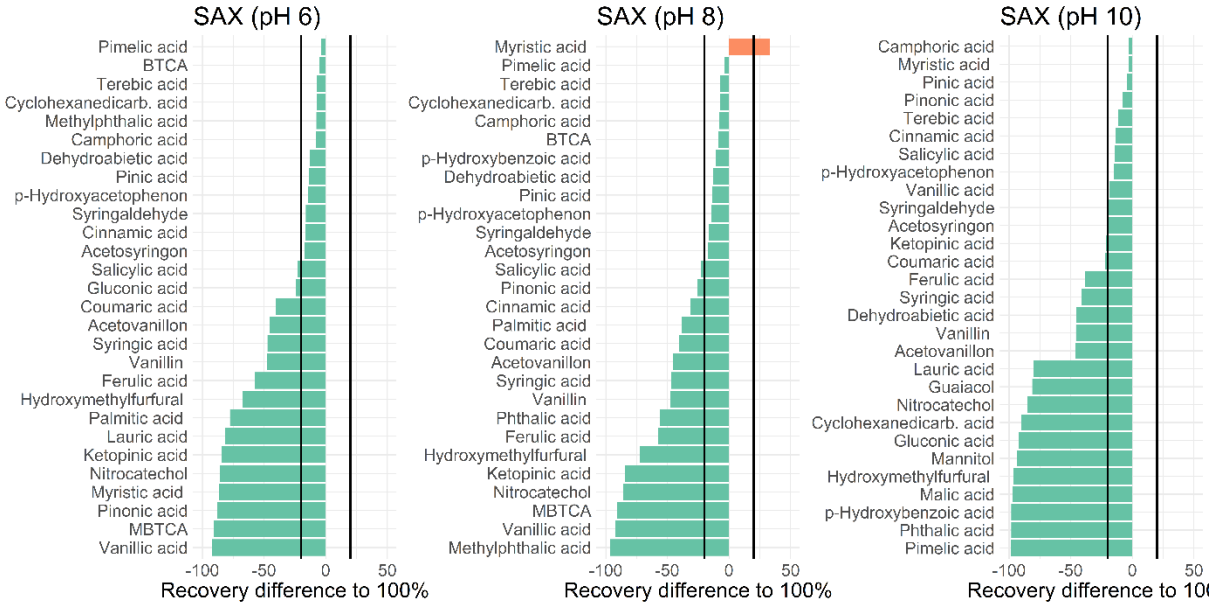

Figure 65: Recovery of target analytes on the SAX material using different sample pH values (pH 6, pH 8, pH 10). Recovery was considered sufficient in a deviation between -20 and 20% (marked in black).

Similar experiments on the WAX material showed high recoveries for most compounds using a pH value of pH 6 or pH 8, while a pH value of pH 10 showed significantly lower recovery because the excess hydroxide ions deprotonated and discharged to piperazine moiety of the WAX material, preventing ionic interactions. Optimum results were achieved on the WAX material adjusting the pH value of the sample solution to pH 8 (Figure 66).

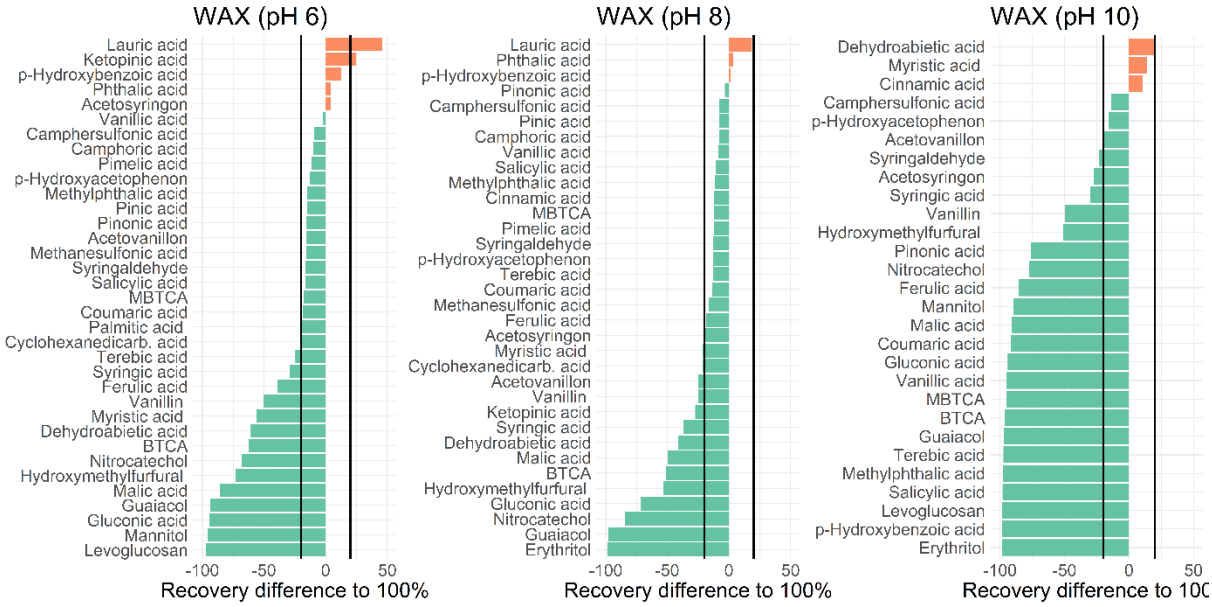

Figure 66: Recovery of target analytes on the WAX material using different sample pH values (pH 6, pH 8, pH 10). Recovery was considered sufficient in a deviation between -20 and 20% (marked in black).

Further SPE experiments were conducted for the enrichment of Lev (and other small, polar compounds) from the aqueous matrix. The pH value of the sample was adjusted to pH 14 with ammonium hydroxide or NaOH to deprotonate Lev. However, the hydrophilicity of the negatively charged Lev was still higher than the ionic interaction with the positively charged solid phase. HILIC-SPE cartridges were evaluated with different percentages of ACN in the sample solution. Sufficient recovery was achieved solely using a matrix of 100% ACN, and even minor percentages of water completely suppressed interactions, thus a HILIC SPE was not applicable. Similar results were obtained using cotton wool as solid phase (Selman et al. 2011).

Method validation of the WAX-SPE was conducted for all recoverable analytes. Linearity was evaluated similarly to the LC-MS method. Ten milliliters of deionized water were spiked with 0.5 ng, 1 ng, 10 ng, 50 ng, 100 ng, 250 ng, 500 ng, and 1000 ng and enriched to a final sample volume of 1 mL. Exemplary, the linearity of acetosyringone, MBTCA and phthalic acid showed sufficient linearity between 10-1000 ng, with a tendency towards lower concentration by acetosyringone and MBTCA (Figure 67, Figure S 5-Figure S 7).

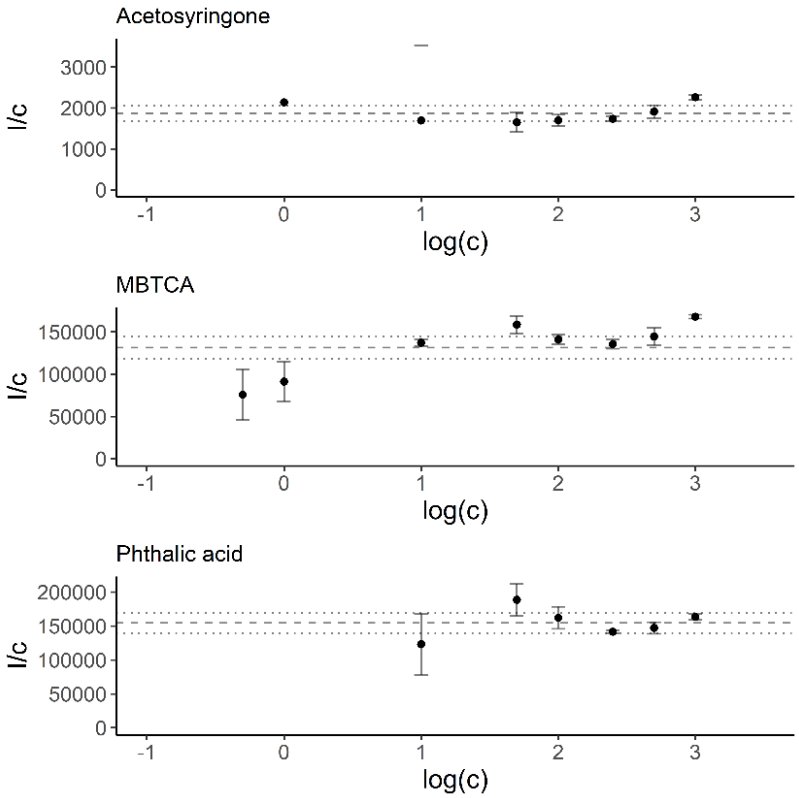

Figure 67: Plots of intensity to concentration ratio (I/c) to the logarithm of concentration of a series of standard solutions prepared by WAX-SPE with increasing concentrations for evaluation of the linearity of the SPE method for selected compounds (acetosyringone, MBTCA, phthalic acid).

In addition to investigation of the linearity, the slopes of the respective calibration curves were used to calculate the mLOQ (Equation 18). The standard deviation of the blank was determined by preparation of five blank samples (10 mL of deionized water) by WAX-SPE. The obtained instrument limits of quantification (iLOQ) and mLOQ values were in comparable concentration ranges for all analytes. The largest differences were observable for vanillic acid, hydroxymethylfurfural, and acetovanillon (Figure 68). The iLOQ and mLOQ values were decisive for the LC-method, as several analytes showed lower iLOQ values on the HILIC column than on the PFP column (Figure 68, grey). The small differences between iLOQ and mLOQ indicated high efficiency of the WAX-SPE enrichment for most analytes.

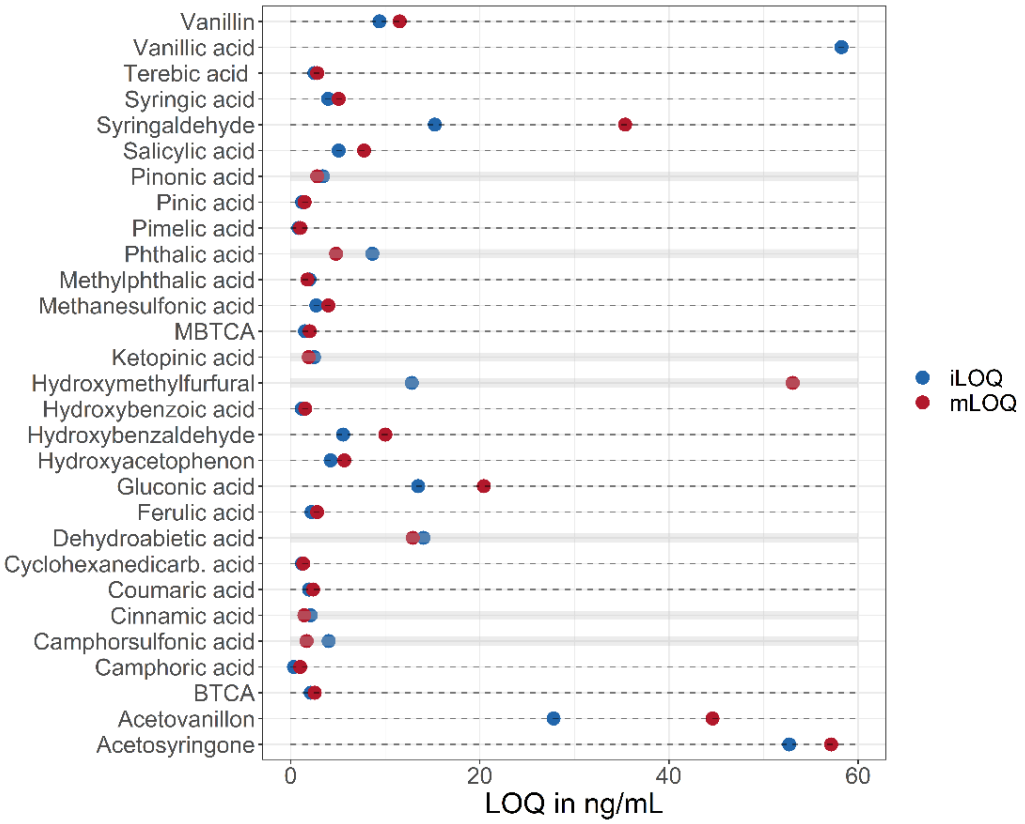

Figure 68: Instrument limit of quantification (iLOQ) of the LC-MS measurement and method limit of quantification (mLOQ) of the WAX-SPE method of target analytes. Analytes showing lower iLOQ values on the HILIC are marked by a grey bar rather than dotted line.

Repeatability of the WAX-SPE was determined by three parallel enrichments of 10 mL water samples spiked with 100 ng of the individual analytes. The compounds with the lowest signal intensities (Figure 69a) showed sufficient repeatability. Compounds with medium intensities (Figure 69b and c) like ferulic acid, *p*-hydroxybenzoic acid, or *p*-hydroxyacetophenon showed higher deviations among the three experiments and evaluation of suchlike compounds in the real samples was therefore conducted carefully with regard to these results.

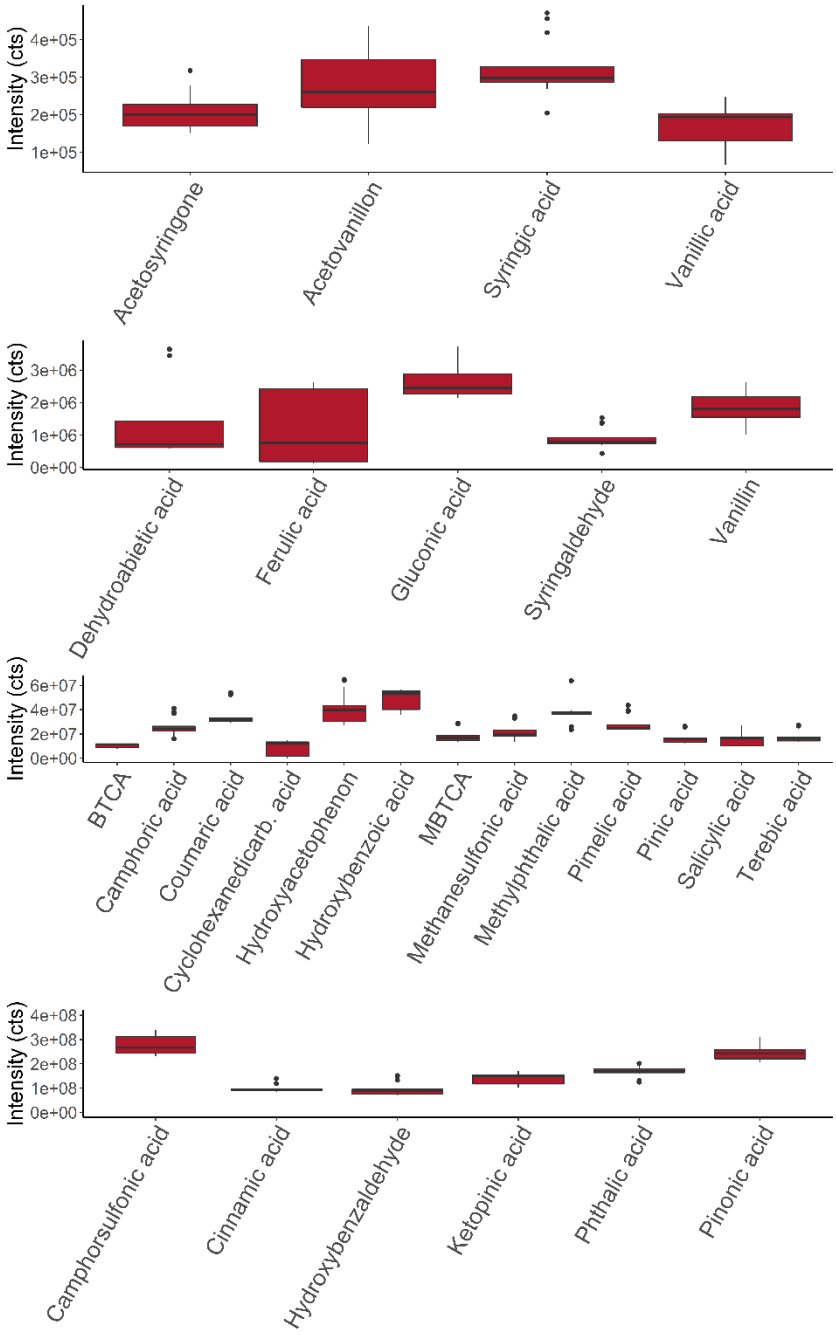

Figure 69: Repeatability of the WAX-SPE method evaluated by threefold enrichment of 10 mL water sample spiked with 100 ng of the respective compounds to 1 mL final volume. a) Repeatability of compounds with low signal intensities. b) and c) Repeatability of compounds with medium intensities. d) Repeatability of compounds with high signal intensities.

Evaluation of the linearity, mLOQ, and repeatability was conducted using a deionized water as an ice core surrogate matrix. To assess the recovery and matrix effects on the WAX-SPE method, a more accurate representation of the ice core matrix was necessary. Therefore, snow samples collected on *Jungfraujoch* in Switzerland (see chapter 8.2.2 for a more detailed description) were used. To evaluate the recovery and matrix effects three different solutions were used, one spiked prior to the SPE (A), one spiked after SPE (B), and a standard solution of similar concentration (C). A/B is calculated to evaluate

the recovery, while B/C is used to evaluate the matrix effects. The recovery was assessed by spiking the solutions with 5 ng, 100 ng, and 500 ng of the compounds in threefold determinations, respectively. Using the low concentration of 5 ng, sufficient recovery between 80-120% was observable for 21 of the 30 compounds (Figure 70a).

The low acidity of syringaldehyde, *p*-hydroxyacetophenon, ferulic acid, cinnamic acid, and coumaric acid resulted in low signal intensity as well as decreased retention due to less ionic interactions. The 100 ng solution exhibited sufficient recovery for all compounds except vanillic acid, ferulic acid, gluconic acid, and 1,2-cyclohexanedicarboxylic acid (Figure 70b). Since 1,2-cyclohexanedicarboxylic acid showed sufficient recovery using the 5 ng solution, here an instrumental or preparative error was more likely than insufficient recovery. Gluconic acid was strongly overdetermined in all three experiments mostly due to chromatographic issues, as strong peak broadening was observable for this compound. The 500 ng solution showed sufficient recovery for all compounds except gluconic acid and ferulic acid, which showed a recovery lower than 50% in all three approaches (Figure 70c). In conclusion recovery improved with higher concentrations, while a concentration close to the mLOQs of most compounds (5 ng/mL) exhibited lower recoveries, which was considered during quantification of lower concentrated compounds in the real samples.

Furthermore, the matrix of a sample has an impact on the ionization of compounds in the ESI source. Matrix components interfere in the competition for excess charges on the ESI droplets and depending on their polarity, gas-phase acidity, proton affinity, and surface activity suppress the proper ionization of the desired analytes. In addition, high concentrations of interfering compounds increase the viscosity and surface tension of the ESI droplets, aggravating the evaporation of ions with lower energy from the droplets in the ion evaporation model (chapter 4.3.1). Non-volatile compounds can form insoluble particles enclosing the analytes. Ions in the matrix can react as ion-pairing reagents with the analytes forming an uncharged complex (Trufelli et al. 2011). Also, the matrix influences the formation of protomers, hence protonation or deprotonation of analytes at different sites resulting in more stable or less stable ions. An example for this effect was thoroughly described for *p*-hydroxybenzoic acid, which can be deprotonated at the phenolic moiety or at the carboxylic acid group (Toma et al. 2012; Xia and Attygalle 2016). Deprotonation at the phenolic moiety results in a more stable ion than at the carboxylic acid group, because the carboxylate anion is prone to the cleavage of CO_2. Since a majority of analytes contains a phenolic moiety, as well as a carboxylic acid functionality, the evaluation of the matrix effects on these compounds was a crucial part of method validation. According to the recovery, matrix effects were evaluated using three different concentrations.

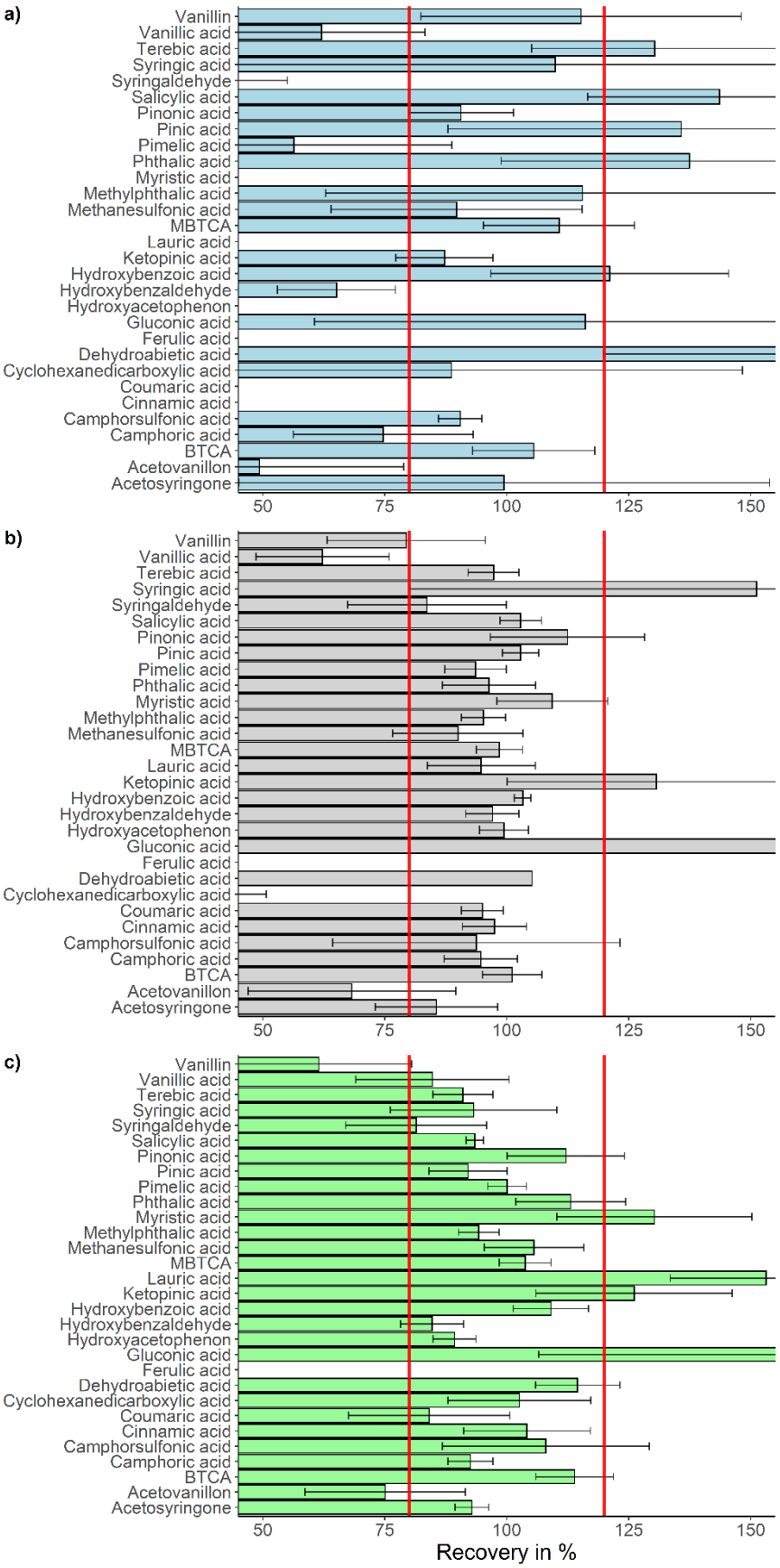

Figure 70: Recovery (%) of the compounds on the WAX-SPE evaluated using snow samples spiked before and after the SPE with 5 ng (a), 100 ng (b), and 500 ng (c).

The 5 ng solution showed strong ion suppression effects for the three fatty acids, aromatic compounds like coumaric acid, and diacids like phthalic acid (Figure 71a). Fatty acids possess of a surfactant-like structure with a polar head and non-polar tail and because of that they were expected to be located at the surface of the ESI droplets. However, a suppression of these ions was observed in all three experiments, indicating the presence of other surfactants in the solution and low gas-phase acidity of the lauric acid, myristic acid, and palmitic acid. The 100 ng solution exhibited lower matrix effects on the analytes in general, with exceptionally high ion suppression of gluconic acid and strong ion enhancement of ferulic acid (Figure 71b). Ion enhancement effects were minimized with higher concentrations, and partly switched towards ion suppression (Figure 71c). The matrix, though not highly complex, had an inconsistent influence on the ionization of the individual compounds in the ESI source.

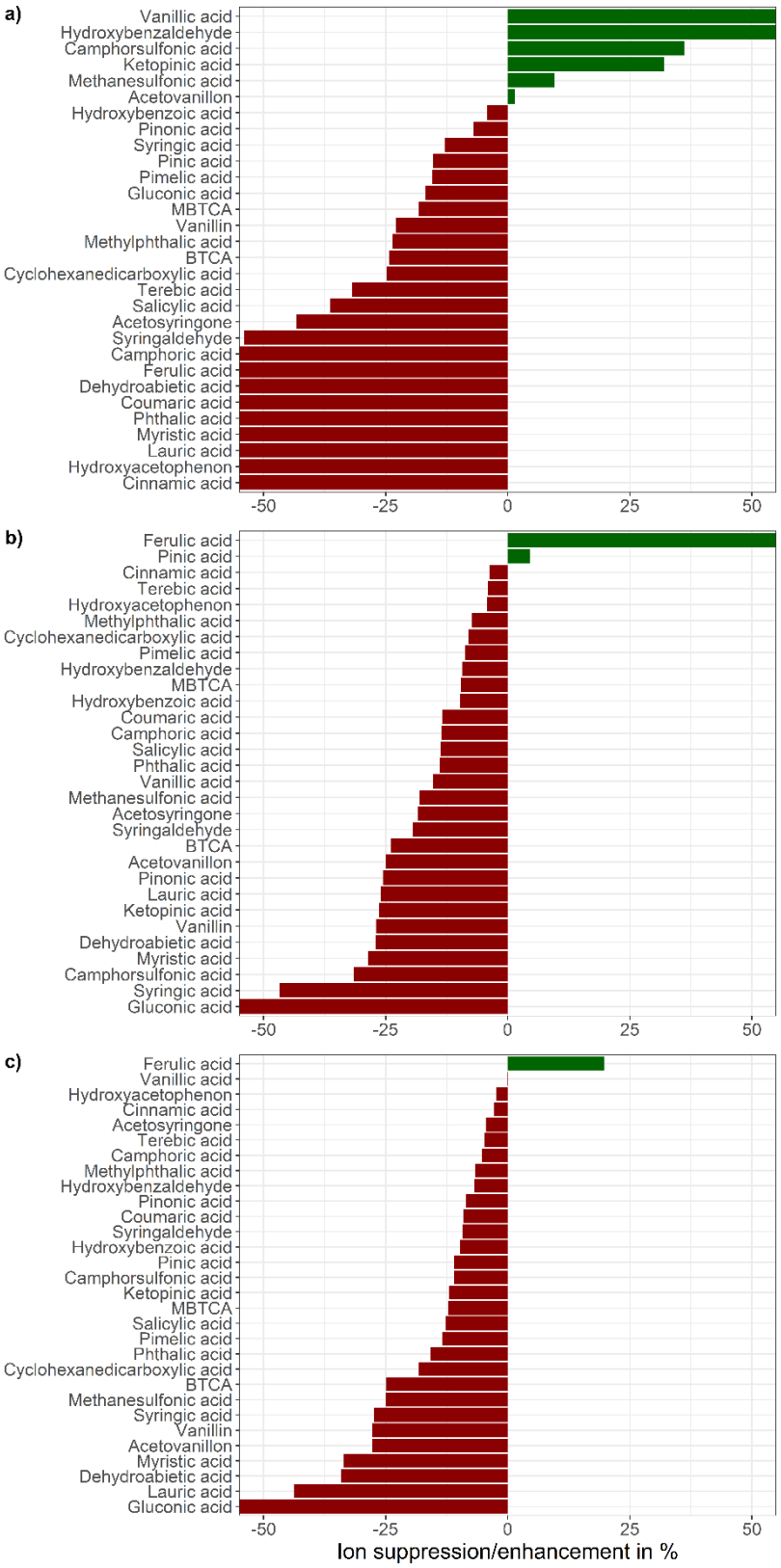

Figure 71: Matrix effects (%) of the compounds on the WAX-SPE evaluated using a snow sample after the SPE with 5 ng (a), 100 ng (b), and 500 ng (c) and a standard solution of similar concentration. Negative matrix effects correspond to ion suppression, while positive matrix effects correspond to ion enhancement.

7.3.1.3 Lignin analysis

The monomeric composition of lignin provides valuable information on the vegetation species. To elucidate the chemical composition, an alkaline oxidation of the polymeric lignin is conducted to recover oxidated products of the initial monomers, the LOPs. LOPs consist of eight compounds (acetosyringone, syringaldehyde, syringic acid, acetovanillone, vanillin, vanillic acid, coumaric acid, ferulic acid) which are further classified in three groups, the S-group, the V-group, and the C-group (see chapter 2.3). The ratios of the C-group to the V-group (C/V) and the S-group to the V-group (S/V) are characteristic for angiosperm or gymnosperm vegetation, and wooden or non-wooden parts of the vegetation (Jex et al. 2014). However, all LOPs are also important biomass burning markers in atmospheric aerosols and for that reason the initially present biomass burning markers must be separated from the polymeric lignin in the samples prior the oxidation, to preserve the individual unique information that these markers provide. Because no analytical lignin standards are available, a qualitative comparison was conducted using industrially produced lignin powder of unknown monomeric composition. The composition of lignin was directly determined by alkaline oxidation and subsequent enrichment and measurement of the LOPs as reference value (Figure 72). To evaluate the behavior of polymeric lignin on the WAX cartridge a stock solution of lignin was used with 10 mg of lignin powder in deionized water (final concentration of 1 mg/mL). Five samples were prepared with a lignin concentration of 1 µg/mL and enriched by WAX-SPE. The flow-through and the eluate of the SPE were prepared similarly to oxidize the polymeric lignin and enrich the LOPs. The LOP concentrations in the eluate were in comparable ranges to the reference values. Only the concentration of acetovanillone, vanillin, and vanillic acid showed high differences between the reference and the SPE results. However, since no quantification of the individual LOPs is forced, but the analysis of the composition of the groups, the WAX-SPE was considered sufficient to quantitatively separate the biomass burning compounds from the flow-through and to equally retain and pass polymeric lignin without distinction by the monomeric composition.

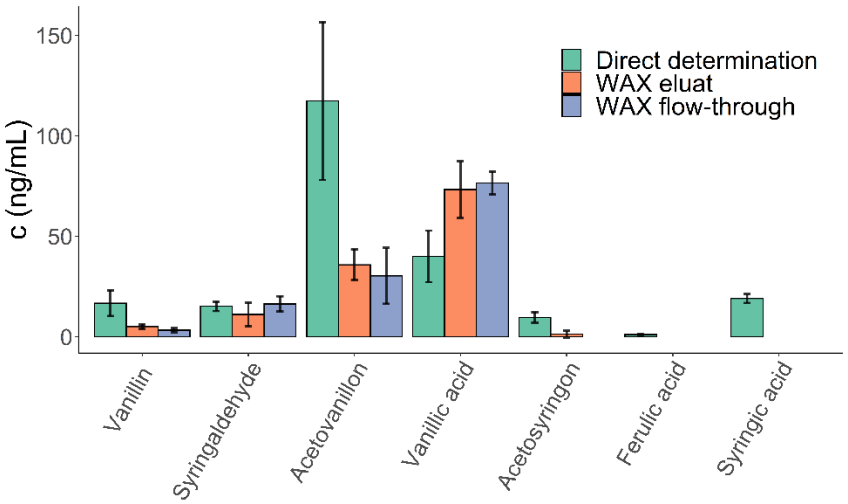

Figure 72: Concentration of LOPs from lignin in the enriched WAX eluat, the WAX flow-through, and a solution of similar concentration directly oxidated without prior preparation by WAX-SPE.

The comparison of the group composition in the lignin powder by direct determination in the WAX flow-through and in the WAX eluate showed only minor differences between the lignin retained by the SPE and the lignin passed through the SPE (Figure 73). Therefore, the flow-through of the WAX-SPE was enriched by a second SPE using HLB material, which was proven successful for lignin analysis (Heidke et al. 2018). The eluate of the HLB-SPE was subjected to the alkaline oxidation procedure (thoroughly described in 5.2.2.1), and the LOPs were enriched by another HLB-SPE (see 5.2.2.1). Linearity, mLOQs, recovery, and matrix effects of the LOP analysis after alkaline oxidation of the polymeric lignin was conducted and the results are shown and discussed elsewhere (chapter 5.3.3).

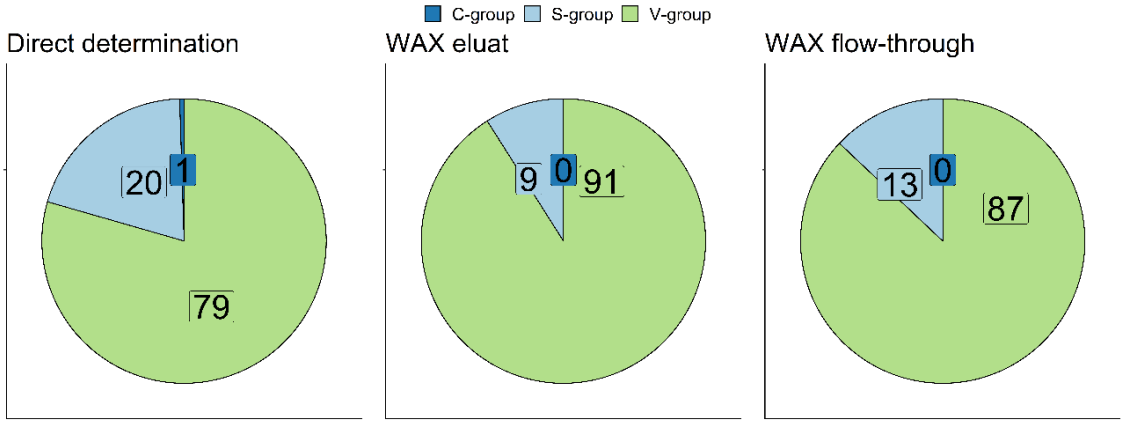

Figure 73: Piechart of the LOP groups from lignin in the enriched WAX eluat, the WAX flow-through, and a solution of similar concentration directly oxidated without prior preparation by WAX-SPE.

7.3.1.4 Centrifugal evaporation

The target compounds erythritol, Lev, mannitol, and xylitol were not recoverable by SPE, and therefore the enrichment approach was replaced by an evaporation of the aqueous matrix. Centrifugal evaporation and N_2-assisted evaporation were compared and showed similar recoveries. The centrifugal evaporation allowed the investigation of a higher number of samples in one batch while maintaining a constant evaporation time for all samples. Therefore, it was further optimized considering the temperature and the solvents for re-constitution (Figure 74). The recovery using ACN/H_2O mixtures to reconstitute and transfer the analytes from the centrifugal tubes to the HPLC vials was higher than using MeOH/DCM mixtures. Xylitol only showed adequate recovery using ACN as a solvent and a temperature of at least 30°C. Therefore, and due to time saving, a temperature of 45°C was chosen, and analytes were transferred using 1.5 mL of ACN twice.

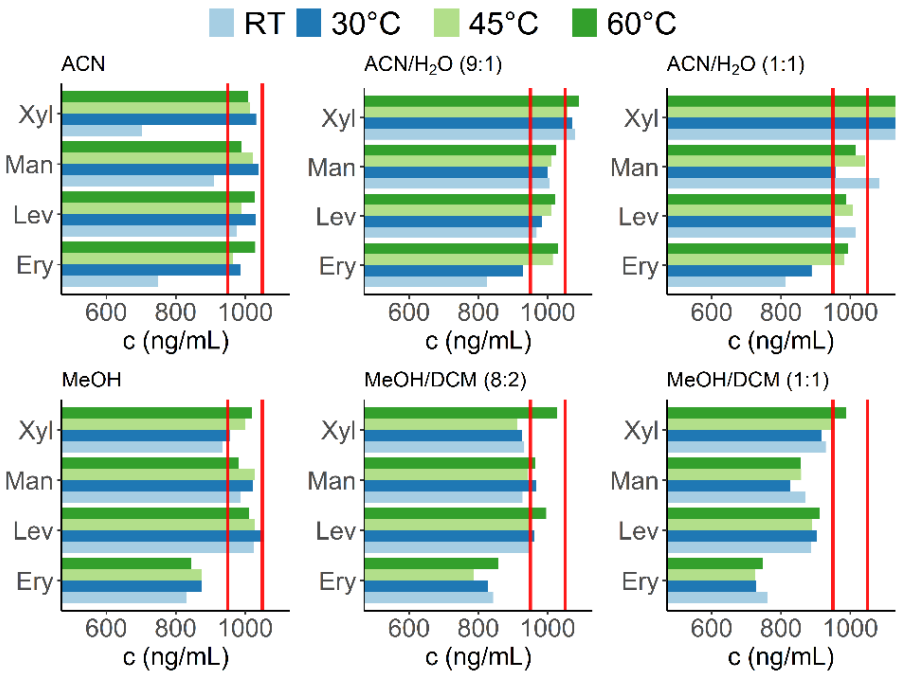

Figure 74: Concentration of xylitol (Xyl), mannitol (Man), levoglucosan (Lev), and erythritol (Ery) after centrifugal evaporation of a 10 mL solution spiked with 1000 ng of the respective compounds at different temperatures and re-constitution and transfer by different solvents to a final volume of 1 mL (final concentration 1000 ng/mL).

Method validation included the determination of the mLOD and mLOQ, as well as the linearity range and the repeatability in a fivefold determination. A series of solutions of 10 mL deionized water were spiked with 0.5 ng, 1 ng, 5 ng, 10 ng, 25 ng, 50 ng, 75 ng, 100 ng, 250 ng, 500 ng, and 1000 ng and enriched to a final concentration of 1 mL. All compounds showed mLOQ values below 10 ng/mL, sufficient repeatability (rel. standard deviation <10%), and a linearity range up to 250 ng/mL (Table 8).

Table 8: Overview on method validation of the centrifugal evaporation including the mLOD (ng/mL), mLOQ (ng/mL), linearity range (ng/mL) and repeatability (%).

Analyte	**mLOD (ng/mL)**	**mLOQ (ng/mL)**	**Linearity range (ng/mL)**	**Repeatability (%)**
Levoglucosan	0.32	1.05	1-250	2.49
Mannitol	0.38	1.27	5-250	5.49
Erythritol	0.1	0.34	1-250	4.06
Xylitol	2.24	7.46	25-250	9.98

Recovery and matrix effects were evaluated using snow samples as surrogate matrix. However, to determine recovery and matrix effects, first the integration of the centrifugal evaporation into the workflow consisting of a prior WAX and HLB SPE was evaluated. Therefore, standard solutions were prepared, the flow-through of both cartridges was captured and the passing of the analytes without retention was proven by recoveries in the flow-through between 86.7-140%. Recovery by centrifugal evaporation individually and after SPE was evaluated by threefold parallel enrichment of 10 mL of

deionized water spiked with 100 ng of the respective analytes and sufficient recovery with adequate standard deviations was observable for all analytes (Figure 75a). Due to the two SPE procedures prior to the centrifugal evaporation the number and quantity of interfering compounds in the matrix was low, which is why ion suppression and ion enhancement effects were lower than 15% for all analytes enabling reliable quantification (Figure 75b). The higher number of samples per batch and reduced time requirement favored the use of centrifugal evaporation to the commonly used rotary evaporation (Kawamura et al. 2012; Pokhrel et al. 2015; Fu et al. 2016; King et al. 2019b). While the recovery of Lev by rotary evaporation and centrifugal evaporation was comparable, a strongly improved recovery was observed for erythritol from 40% by rotary evaporation (King et al. 2019b) to 87.1% by centrifugal evaporation. In addition, repeatability, mLOD, and mLOQ showed better results using centrifugal evaporation compared to rotary evaporation.

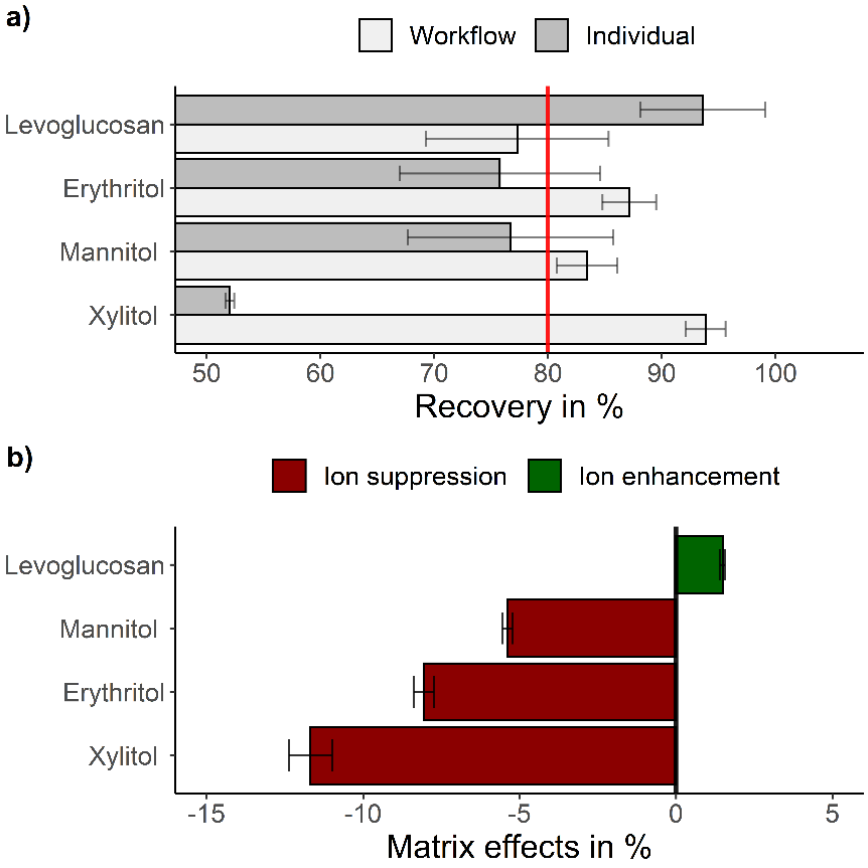

Figure 75: a) Recovery (%) of compounds enriched by centrifugal evaporation individually or integrated into the workflow including prior flow through WAX and HLB-SPE cartridges. b) Matrix effects (ion suppression/ion enhancement) of the centrifugal evaporation in the ionization in the ESI source.

7.3.2 Application Colle Gnifetti Glacier

The method described in chapter 7.2 and 7.3 was applied as proof-of-principle to thirty-three samples from Colle Gnifetti glacier, covering the time between 1844 and 1995 with a gap between 1860 and 1924. The concentrations of the SOA marker compounds were calculated in ng/mL of frozen ice core sample with the assumption of 1 mL thawed ice equal to 1 g of frozen sample and plotted in a timely series.

Monoterpene oxidation markers

The monoterpene oxidation marker BTCA showed two distinct concentration plateaus, with higher concentrations of 0.11-0.25 ng/mL between 1952 to 1995 and lower concentrations of 0.04-0.07 ng/mL between 1844 to 1948. Pinic acid and MBTCA showed a peaking concentration in 1974, and MBTCA and pinonic acid showed an additional peak in 1988. Since MBTCA is formed by OH-initiated oxidation of pinonic acid, a high oxidative capacity of the atmosphere in this year driving aerosol aging is indicated (Zhang et al. 2010; Müller et al. 2012). All three monoterpene oxidation markers showed rather low concentrations in the samples from the 19th century. Terebic acid, ketopinic acid, *trans*-1,2-cyclohexanedicarboxylic acid, and pinonic acid progressed similarly and in comparable concentration ranges (Figure 76, Figure S 13). In the literature, for pinene oxidation products MBTCA, pinic acid, and pinonic acid pronounced seasonal cycles in aerosol field studies and a strong temperature dependency are described (Zhang et al. 2010). According to the mean temperature data provided by the *Federal Office of Meteorology and Climatology MeteoSwiss*, in 1987 to 1988, a sudden shift to a pronounced period of warm winters was observable, consistent with the peaking concentration of temperature dependent markers MBTCA and pinonic acid. Precipitation in the southern Alpine region did not show significant changes during the winters from 1864 to 2021 (MeteoSwiss 2020). MBTCA and pinonic acid were analyzed in samples from Belukha glacier in Siberia from the 19th century and showed comparable concentrations to the results from Colle Gnifetti. In contrast, samples from Kamchatka Peninsula in Russia from 1700-2000 showed lower concentrations of MBTCA in the pg/g range and higher concentrations of pinonic acid. In samples from Aurora Peak in Alaska, MBTCA was not detectable, while pinonic acid showed similar concentrations to Colle Gnifetti. Pinic acid in Belukha glacier and Aurora Peak were in comparable concentration ranges, while Kamchatka was approximately ten times higher. (Fu et al. 2016; Pokhrel et al. 2016; Zuth 2018).

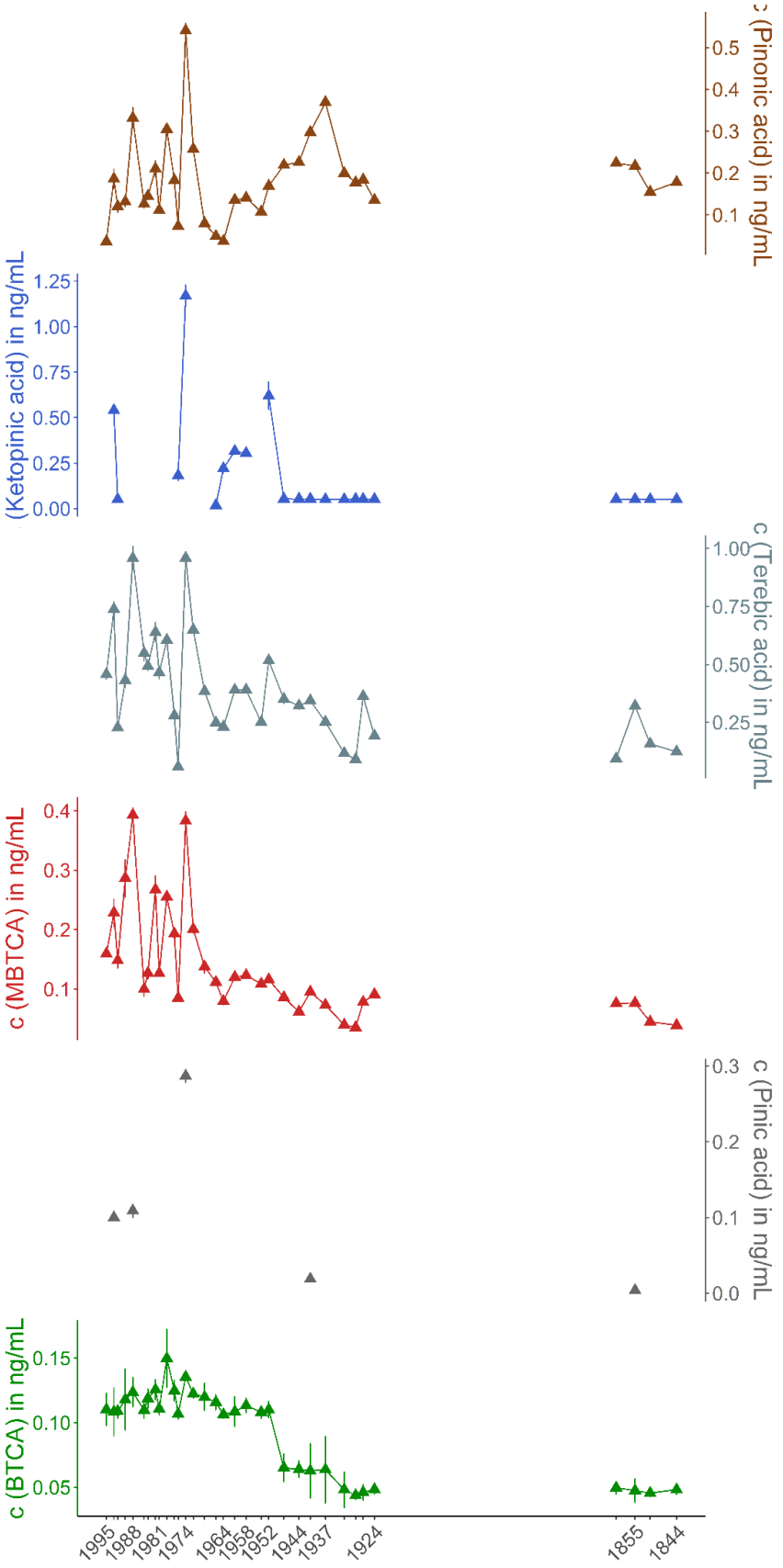

Figure 76: Historic records of monoterpene oxidation products in ng/mL detected in Colle Gnifetti ice core samples from 1844 to 1995.

Anthropogenic emission markers

The concentrations of the anthropogenic marker phthalic acid and *p*-methylphthalic acid were peaking in 1974 and progressing similarly to monoterpene oxidation markers between 1995 to 1929, indicating a connection between aerosol aging and the emission of anthropogenic pollutants to the atmosphere. While *p*-methylphthalic acid showed the historically lowest concentrations in the samples from 1844 to 1860, concentrations of phthalic acid were below the LOQ in these samples. *p*-Methylphthalic acid was already detected in Alpine glacier core from *Grenzgletscher* between 1942-1993 in comparable concentration ranges to Colle Gnifetti from the same mountain range (Müller-Tautges et al. 2016). In the same core phthalic acid concentrations between 0.01 ng/g to 0.3 ng/g were observable. In addition, phthalic acid was detected in a Greenland ice core with a medium concentration of 0.56 ng/g in samples from 1540-1989 (Kawamura et al. 2001). Pimelic acid behaved differently than phthalic acid and *p*-methylphthalic acid, with a peaking concentration in 1948, that was rapidly decreasing from 1948 to 1952 (Figure S 8). Pimelic acid was detected in samples from Belukha glacier (mean 2.23 ng/g, max. 9.8 ng/g), *Grenzgletscher* (mean 0.15 ng/g, max 0.86 ng/g), Greenland (mean 0.18 ng/g, max. 1.01 ng/g), and a sub-Antarctic ice core (0.1-0.4 ng/g) which is comparable to Colle Gnifetti with 0.01-0.3 ng/mL (Kawamura et al. 2001; Müller-Tautges et al. 2016; Zuth 2018; King et al. 2019c).

Biomass burning markers

The concentration of the cellulose burning marker Lev was increasing in 1937 and 1860. In the literature, an increased number of fires and area of burning is described in two cantons from Switzerland in 1937, in accordance to the Lev peak in observed in Colle Gnifetti (Pezzatti et al. 2013). However, the time gap after 1860 does not allow to draw conclusions on the significance of this peak and no literature on fires in this year in Switzerland is available. Lev is a thoroughly analyzed biomass burning marker in aerosols and was also quantified in glacier samples from Kamchatka (1700-2000) and Aurora Peak (1650-2010) with concentrations between 0.1-10 ng/g and 0.5-1.5 ng/g, which is in a comparable concentration range to Colle Gnifetti, yet slightly higher. Also, dehydroabietic acid, a resin burning marker was detected in these glacier cores with a concentration between 0.01-0.5 ng/g in Kamchatka and 0.1-0.4 ng/g in Aurora Peak, which was also slightly higher than the concentrations in the results presented here (Kawamura et al. 2001, 2012; Pokhrel et al. 2020). In this study, dehydroabietic acid was only found in younger samples from 1981 to 1995 with high errors among the threefold determination. Gluconic acid, another cellulose burning marker was only quantifiable in samples from 1974, 1977, and 1982 to 1995 (Figure S 9). In 1974 the highest number of fires and amount of burnt area was recorded between 1904-2008 in Switzerland (Pezzatti et al. 2013). In the obtained data of this study, the only biomass burning markers supporting this observation were gluconic acid and salicylic acid (Figure S 10). However, in 1974 monoterpene oxidation and anthropogenic emission markers showed increased concentrations suggesting a connection between elevated temperatures from biomass burning and monoterpene emission and oxidation. A similar observation was made in historic trends of SOA markers in samples

from *Grenzgletscher*, where the burning markers vanillic acid and *p*-hydroxybenzoic acid were peaking in 1974, as well as pimelic acid and pinic acid (Müller-Tautges et al. 2016). In the data presented here, vanillic acid and *p*-hydroxybenzoic acid did not show a peak in 1974 (Figure S 10 and Figure S 11), but the concentration ranges were similar to those found in *Grenzgletscher*, Aurora Peak, Kamchatka, and Belukha (Kawamura et al. 2012; Müller-Tautges et al. 2016; Zuth 2018; Pokhrel et al. 2020) The historic trend of the lignin burning markers acetosyringone, cinnamic acid, syringaldehyde, and acetovanillon showed two distinct concentration plateaus with similar switching points to BTCA but with inverse concentrations, as they were higher between 1855 to 1948 than between 1952 to 1993 (Figure S 9-Figure S 11). A suchlike shift was not observable in data from fire events or historic records from the nearby *Grenzgletscher*.

Sea spray emission markers

Markers for sea spray emissions included methanesulfonic acid, which was only quantifiable in 1948, 1941, 1937, and 1927, and the three fatty acids lauric acid, myristic acid, and palmitic acid, which were peaking in 1954 and showed similar timely concentration progress (Figure S 12). Methanesulfonic acid is a product of dimethyl sulfide oxidation. Dimethyl sulfide is primarily emitted by marine phytoplankton and concentrations in open water are much higher than beneath ice sheets. Methanesulfonic was detected in a sub-Antarctic ice core in samples from 2001-2016 with a concentration between 0.03-22 ng/mL, in Svalbard ice core from 1800-1997 with a mean concentration of 9.3 ng/mL, and in a Greenland ice core with concentrations >1 ng/mL in samples from 1770 to 1990. These concentrations were much higher than in the obtained data, however all the named ice cores are in closer proximity to the oceans and therefore exposed more strongly to marine emissions. A decrease of methanesulfonic acid over the 20th century was described in the literature and explained by either a decrease of biogenic dimethylsulfide emission or a lower yield of methanesulfonic acid from dimethylsulfide oxidation due to an anthropogenically changed oxidative capacity of the atmosphere (Legrand et al. 1997; Isaksson et al. 2005; King et al. 2019c). Unfortunately, the low data frequency did not allow to support or contradict these theories. Fatty acids have been analyzed in glaciers from Antarctica, Greenland and Alaska. In the sub-Antarctic glacier fatty acids could not be detected above the LOD, while in Aurora Peak from Alaska the mean concentration of lauric acid in samples from 1734-2008 was 4.82 ng/g, myristic acid 15.3 ng/g, and palmitic acid 20.3 ng/g, in ascending concentration consisting with the data from Colle Gnifetti. A correlation of increased fatty acid concentrations with increased Arctic temperature was described in the Greenland ice core. In Colle Gnifetti, a comparable temperature dependency is indicated but more data on fatty acids in Alpine glaciers is necessary to confirm these observations (Kawamura et al. 1996; Pokhrel et al. 2015; King et al. 2019c).

Isoprene and fungal spore emissions

Erythritol as an isoprene derived SOA marker was only detectable in samples from 1966-1993 (Figure S 13). In the literature, *meso*-erythritol is found in a sub-Antarctic glacier core from 2001-2016 with concentrations between 0.1-0.7 ng/g, while in other cores also 2-methylerythritol is used as a marker compound for example in Aurora Peak, Alaska, and Belukha. In samples from Aurora Peak between 1650-2010 the average concentration of 2-methylerythritol was 0.69 ng/mL and maximum concentration was 3.5 ng/mL. In Belukha the average concentration in samples from the 19th century was 0.104 ng/g (Pokhrel et al. 2016; Zuth 2018; King et al. 2019c). Erythritol concentration in the Colle Gnifetti samples is by factor 50-100 lower than concentrations described in the literature, however no further data in Alpine ice cores is available to elucidate the different driving forces for isoprene derived SOA markers in remote glaciers and glaciers strongly influenced by anthropogenic emissions. A temperature dependency of 2-methylerythritol concentration in ice cores was observed which is consistent with the data from Colle Gnifetti as erythritol was only detectable in a time period of elevated temperature, even confirmed by temperature proxy data in a core from Colle Gnifetti in the literature (MeteoSwiss 2020; Brugger et al. 2021). The concentrations of mannitol and xylitol, which are intended as markers for fungal spore emissions, were below the LOQ in samples from the 19th century, and while xylitol concentrations showed a comparably constant behavior, mannitol showed a significant peak in 1976. A detection of mannitol is described in the literature in samples from Aurora Peak, Alaska, in samples from 1734-2008, however no data on the concentration was published yet (Pokhrel et al. 2015).

Lignin analysis

The data presented herein is the first analysis of intact polymeric lignin in ice core samples. Historic records of the sum of eight LOPs, the LOPs from the S-group, C-group, and V-group, as well as the C/V ratio and S/V ratio were analyzed. The LOP sum showed a peaking concentration in the sample from 1985, here driven by an increase in V-group LOPs, and in the sample from 1992, driven by an increase in the S-group LOPs. In general, the C-group showed lower concentrations, than the S- and V-group. For all three groups, and accordingly the sum of LOPs, increased concentrations were observable in the younger samples between 1985 and 1993 and comparable concentration progress in the older samples (Figure 77). This elevation could either result from a higher abundance of vegetation and corresponding emission of lignin or from cold winters in Southern Switzerland in the beginning of the 1980s and the beginning of the 1990s leading to increased wood stove heating (MeteoSwiss 2020; Brugger et al. 2021). The overall trend of elevating LOP concentrations in the investigated samples is consistent with the increased forest cover in Switzerland in recent decades. On average, all regions of the Alps showed increased forest cover of 3.7% per decade since 1930 and 4.3% since 1990, with a minimum in the middle of the 19th century (Kulakowski et al. 2011; Bebi et al. 2017). In the Southern Alps an increase of 17.1% per decade was recorded between 1993/95 to 2009/13 (Abegg et al. 2020) and the LOP concentration in Colle Gnifetti showed an average increase of 51.8% (±45.03%) per decade. The

strongest increase was observable from the 1970s to the 1980s. Changing forest cover and species is only minorly influenced by temperature but rather by changes in land use like declining agricultural industry and the switch from wood to coal burning (Gellrich et al. 2007; Bebi et al. 2017).

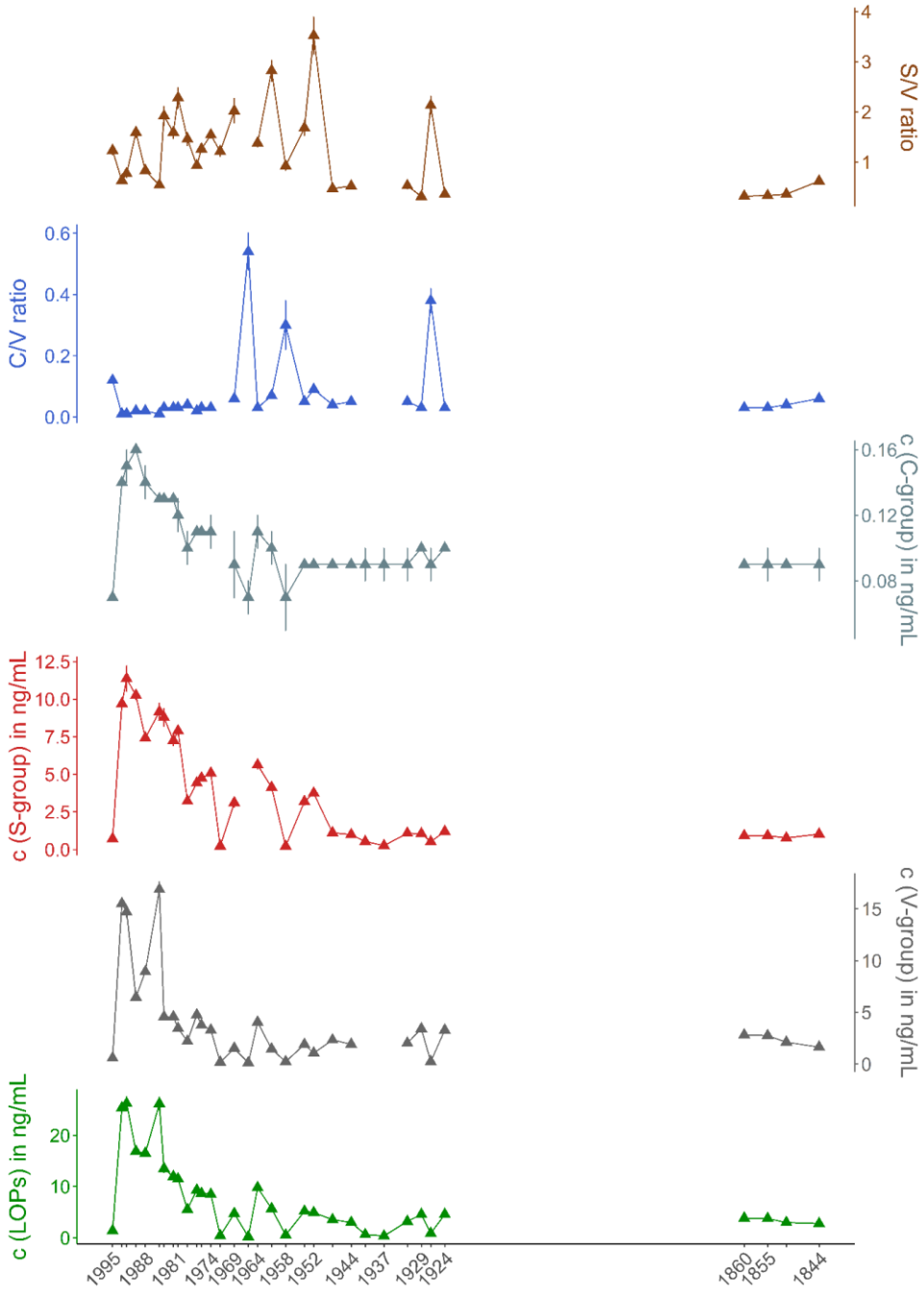

Figure 77: Historic records of the S/V ratio, C/V ratio, C-group, S-group, V-group and sum of LOPs from intact polymeric lignin after alkaline oxidative degradation in Colle Gnifetti samples from 1844 to 1995.

The C/V ratio was significantly rising in the samples from 1927, 1958 and 1966, while constantly remaining on low level in the remaining samples. In 1927 also the S/V ratio was increased, and in general the S/V ratio showed stronger variance in the historic record. In the same year, temperature records from Southern Switzerland showed lower temperatures in winter, which supports the assumption of increased domestic wood burning during lower temperatures, especially since no increase of biomass burning

events was observable in the available fire records from the cantons Valais and Ticino (Pezzatti et al. 2013; MeteoSwiss 2020). In contrast, the C/V ratio in 1966 could be explained by a biomass burning event, as here an increased number of fires was recorded (Pezzatti et al. 2013). It is however important to consider, that the emergence of biomass burning events in the Alps is strongly regionally affected. In the Southern Alps, fires occur mainly in dry winters and by anthropogenically induced ignition, while in the Central Alps, fires are more frequent in the summer due to the high abundance of ignitable Scots pines and lightning strikes (Bebi et al. 2017). Therefore, the available fire data from the two cantons in Valais und Ticino in Southern Switzerland is not representative for biomass burning events in the entire Alpine region.

The plotting of the S/V ratio to the C/V ratio provides further information on the type of vegetation, since certain areas in a suchlike plot are associated to different species. Gymnosperm and angiosperm vegetation is distinguished by the S/V ratio, while wooden and non-wooden vegetation species are distinguished by the C/V ratio. Most of the samples were grouped at low C/V ratios corresponding to wooden vegetation, and consistent with the high forest cover of the Alps. On average the most abundant species are the broad-leafed European beech and the coniferous silver fir, Norway spruce, and mountain pine, with strong regional differences (Bebi et al. 2017; Conedera et al. 2017). Samples with peaking C/V ratios were from 1927, 1958 and 1966, and showed different S/V ratios. The sample from 1966 was located close to the area of non-wooden gymnosperm vegetation in the plot, while the other outlier samples were rather associated with non-wooden angiosperm vegetation (Figure 78a). Older samples from 1844 to 1932 (excluding the outlier from 1927) were all grouped in range of C/V 0.02-0.06 and S/V 0.25-0.6 before younger samples starting from the 1950s were all shifted to lower C/V and higher S/V ratios indicating higher abundance of wooden angiosperm vegetation according to a decline of spruce by 0.9% and increase of beech by 0.9% between 1993/95 to 2009/13 (Abegg et al. 2020). During the 19th century, pollen records from Colle Gnifetti showed a declining percentage of trees on the overall vegetation while also forest records showed a minimum land cover (Kulakowski et al. 2011; Brugger et al. 2021) which is consistent with the observation from Colle Gnifetti, that show a small shift towards non-wooden vegetation in older samples (Figure 78b). Considering the S/V ratio, which distinguishes between the vegetation species angiosperm and gymnosperm, the older samples showed a tendency towards gymnosperm vegetation, while younger samples were shifted towards angiosperm vegetation, consistently with data on decreasing coniferous vegetation from the pre-industrial period before 1880 and industrial period after 1880 (Bebi et al. 2017).

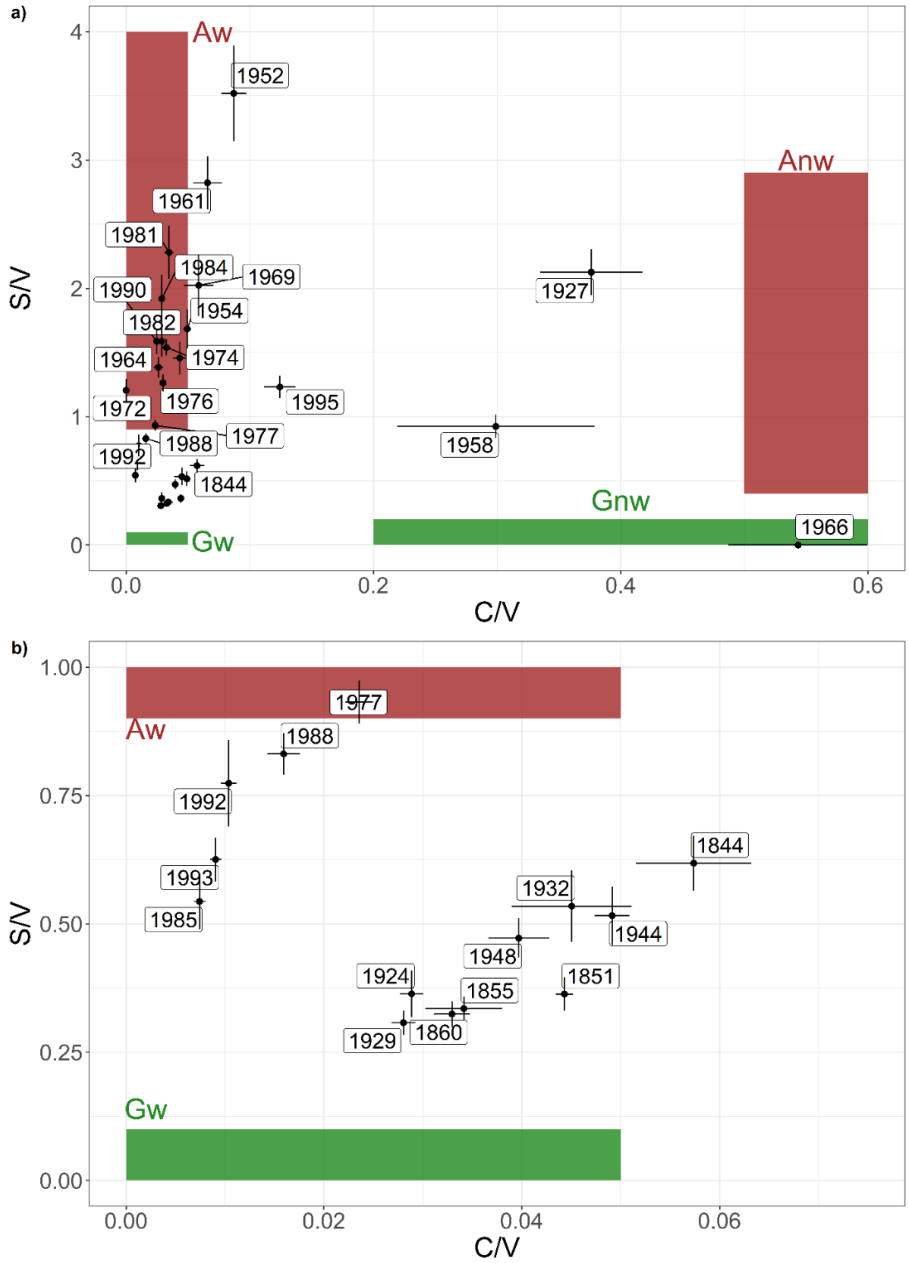

Figure 78: a) Scatterplot of the S/V and C/V ratios analyzed in samples from Colle Gnifetti glacier from 1844 to 1995. (Aw=woody angiosperm vegetation, Anw= non-woody angiosperm vegetation, Gw=woody gymnosperm vegetation, Gnw=non-woody gymnosperm vegetation). b) Zoom of scatterplot a) from S/V 0-1 and C/V 0-0.07.

Principal component analysis (see 7.3.2.2 for more detailed methodic description) including only lignin markers was conducted showing that 95.8% of the total variance were described by PC1, which was loaded by the sum of LOPs, the S-group LOPs, and the V-group LOPs, and thus summarized as abundance of vegetation. Only 3.9% were described by PC2, including the C-group, as well as the C/V and S/V ratio, which was summarized as vegetation type. Clustering by k-means analysis showed that the abundance of vegetation grouped the samples by age and younger samples were strongly influenced by the abundance of vegetation and samples from the 1970-1980s were especially prone to the S-group concentration and S/V ratio, hence the differentiation between angiosperm and gymnosperm vegetation.

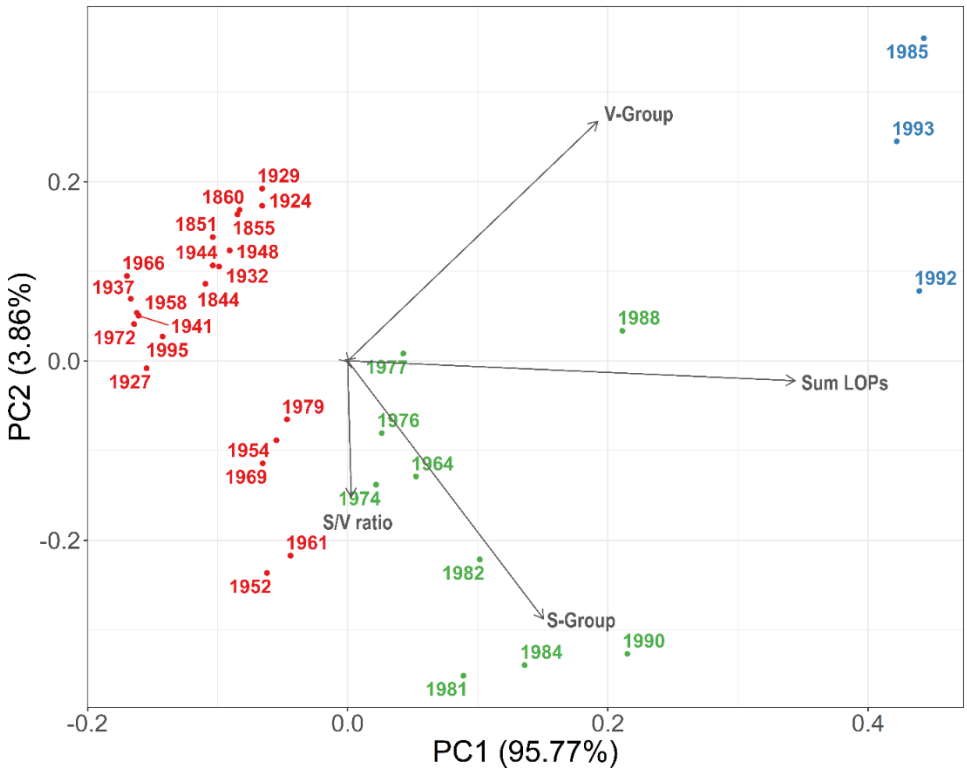

Figure 79: Principal component analysis of Colle Gnifetti glacier samples including all variables associated with polymeric lignin: S/V ratio, C/V ratio, S-group concentration, V-group concentration, C-group concentration, and sum of LOP concentration. The highest loadings on the principal components are labelled. Samples were clustered into three groups by the k-means algorithm.

The results from lignin analysis show that lignin is a promising vegetation marker, not only in climate archives like speleothems and sediments, but also in ice cores. The data mirrored a change in vegetation abundance and vegetation species that is consistent with available data on forest cover and composition in Switzerland before and after 1880. It is however important to further elucidate the lignin emission. Possible modifications of the monomeric lignin composition during emission and atmospheric transport would disturb a proper preservation of the vegetation signature und should be further evaluated. In addition, the atmospheric stability of polymeric lignin is important to evaluate the possibility of long-range transport and hence the potential of lignin as a marker for changing vegetation on a larger trans-regional scale.

7.3.2.1 Correlation analysis

A correlogram of all SOA markers and polymeric lignin concentrations offered a more detailed insight into the behaviors of all compounds among each other (Figure 80). The fatty acids lauric acid, myristic acid and palmitic acid, which represent markers of sea spray emission showed an anti-correlation to lignin markers and the monoterpene and isoprene derived SOA markers, for example lauric acid and erythritol ($r=-0.6$, $p< 0.01$). This observed anti-correlation is consistent with data from Aurora Peak, Alaska, and demonstrates, that fatty acid concentration in Colle Gnifetti ice core is not driven by vegetation but rather as proposed by sea spray (Pokhrel et al. 2015, 2016). In Colle Gnifetti, a positive

correlation of monoterpene oxidation markers to each other was observed, as well as a linkage of mannitol to erythritol ($r=0.7$, $p<0.01$), BTCA ($r=0.6$, $p<0.01$) and MBTCA ($r=0.5$, $p<0.01$), consistent to observations from the Alaskan glacier (Pokhrel et al. 2016). Lev only showed a correlation to pinonic acid ($r=0.5$, $p<0.01$), while for gluconic acid, a different cellulose burning marker, positive correlation to monoterpene derived SOA markers was observable. A missing linkage between Lev and the lignin burning markers *p*-hydroxybenzoic acid and vanillic acid is consistent with the literature. However in Aurora Peak glacier a correlation between vanillic acid and dehydroabietic acid, and in data from *Grenzgletscher* a correlation between vanillic acid and *p*-hydroxybenzoic acid was described, which was not found in data from Colle Gnifetti (Müller-Tautges et al. 2016; Pokhrel et al. 2020). In *Grenzgletscher* an additional correlation between *p*-hydroxybenzoic acid and pinic acid was observed and concluded to a biomass burning derived source of pinic acid. This was not confirmed by data from Colle Gnifetti, where instead a correlation of pinic acid to anthropogenic emission markers like phthalic acid ($r=0.7$, $p<0.01$) and *p*-methylphthalic acid ($r=0.9$, $p<0.01$) was observed.

In addition, compounds were hierarchically clustered based on their correlations among each other. The monoterpene oxidation markers were clustered with other biogenic SOA markers and showed a positive correlation to the grouped anthropogenic emission markers phthalic acid and *p*-methylphthalic acid. This indicates a strong anthropogenic influence on the oxidation of monoterpene derived precursors in the atmosphere and SOA abundance. The lignin markers were grouped and the LOPs showed positive correlation to erythritol ($r=0.7$, $p<0.01$), mannitol ($r=0.5$, $p<0.01$), *p*-hydroxybenzoic acid ($r=0.5$, $p<0.01$), and gluconic acid ($r=0.5$, $p<0.01$). Due to the additional anti-correlation to lauric acid ($r=-0.5$, $p<0.01$), and palmitic acid ($r=-0.5$, $p<0.01$) emission of polymeric lignin is proposed either as a result of biomass burning (domestic or natural), as indicated by the correlation to the biomass burning markers gluconic acid and *p*-hydroxybenzoic acid, or a result of microbial degradation of lignin, according to the correlation with mannitol. Latter would complicate the association of lignin composition to vegetation species, as microbial degradation modifies the monomeric composition (Opsahl and Benner 1995; Jex et al. 2014).

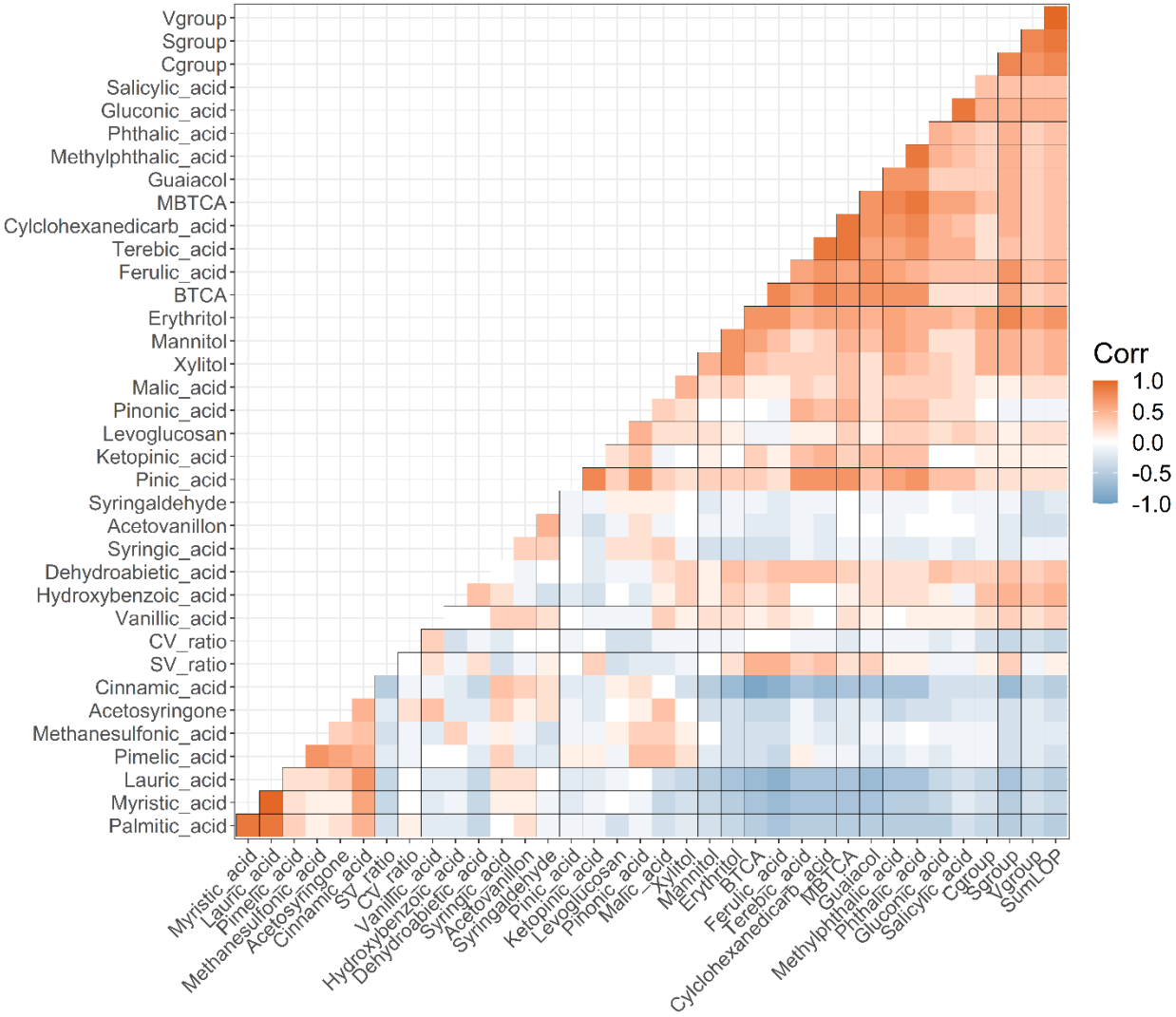

Figure 80: Correlogram of SOA markers and lignin oxidation products analyzed in Colle Gnifetti glacier samples from 1844 to 1955. Regression coefficients are colorized in a gradient from -1.0 (blue) to 1.0 (red) and compounds were clustered hierarchically using an R clustering algorithm.

7.3.2.2 Principal Component analysis

For further elucidation of the influence of individual compound on the clustering in the correlogram, a principal component analysis (PCA) was performed on the data using the “prcomp” command from package “stats” in R (v.4.0.3). PCA is performed to summarize a high number of individual variables into principal components (PC), that describe the overall variance of variables in the data as simplified as possible. Data points are collected in a two-dimensional coordinate system and a line is drawn through the data, minimizing the average square distance of each data point to the line. Each line that can be drawn in a simplified manner represents a principal component and is to a certain percentage able to describe the overall variance and group samples according to their degree of bias from the individual PCs (Bro and Smilde 2014).

Using all available data from SOA and lignin markers, 78.2% of the variance were explained by PC1 and 17.18% by PC2. The highest negative loadings on PC1 were given by palmitic acid and myristic acid, while the highest positive loadings on PC1 were given by the LOP concentration, as well as S-group, and V-group concentrations. Hence, PC1 was summarized as influence of vegetation abundance and sea spray emission. Similar contributions of these compounds were observable on PC2, yet with inverse significance and all as negative loadings with a factor |>0.1| (Table 9). Clustering of samples into three groups by the k-means algorithm revealed a discrimination between older samples from the mid-19th century with samples from the mid-20th century. This group was strongly influenced by the three fatty acids, especially the sample from 1932. A second group included samples from approximately the 1940s to the 1970s, with outliers like the sample from 1855, 1860, or 1995. This group was only marginally impacted by PC1. The third group was composed of the youngest samples from 1981 to 1993, which experienced the strongest positive impact from PC1 (Figure 81a).

Table 9: PCA component matrix of all analytes with factor loadings >|0.1|

Compound	**PC1**	**PC2**	**PC3**	**PC4**	**PC5**
S-Group	0.146	-0.298	-0.110	0.672	-0.147
V-Group	0.143	-0.458		-0.603	
LOP	0.289				
S/V ratio				0.327	
trans-1,2-cylclohexanedicarboxylic acid					0.293
Palmitic acid	-0.783	-0.284	-0.547		
Myristic acid	-0.460	-0.207	0.702	0.201	0.429

Due to the high factor loadings of lignin and sea spray markers, the effect of other SOA markers could not be visualized with this PCA. Therefore, a second, reduced PCA was performed excluding the highest factor loadings (Table 10). This analysis revealed an explained variance of 55.81% by PC1 and 24.26% by PC2.

Table 10: Reduced component matrix of PCA with all analytes except for sea spray markers (lauric acid, myristic acid, palmitic acid) and lignin markers (only factor loadings >|0.1| are displayed)

Compound	**PC1**	**PC2**	**PC3**	**PC4**	**PC5**
Pimelic acid					-0.118
Pinic acid					-0.132
trans-1,2-cylclohexanedicarboxylic acid	-0.560	0.405	0.178	-0.602	0.153
Terebic acid	-0.173		0.101	-0.193	0.130
Xylitol	-0.364	-0.476	-0.760	-0.235	
Ketopinic acid		0.148			-0.926
Pinonic acid					-0.173
Phthalic acid	-0.631	0.231		0.727	
Malic acid	-0.324	-0.719	0.601		

The highest loadings on PC1 were phthalic acid and cyclohexanedicarboxylic acid, therefore PC1 was summarized as anthropogenic influence, while PC2 was rather influenced by malic acid and xylitol and therefore summarized as biomass burning. PC1 had the strongest impact on the sample from 1974. In this year, increased concentrations of pinic acid, phthalic acid, *p*-methylphthalic acid, cyclohexanedicarboxylic acid, and MBTCA concentration were observed and in accordance with the fire records from Switzerland these concentrations were associated with a biomass burning event (Pezzatti et al. 2013; MeteoSwiss 2020). Other grouped samples which were strongly influenced by PC1, hence anthropogenic emissions, were between 1972 and 1993. The other two groups did not show a clear distinction between older and younger samples (Figure 81b).

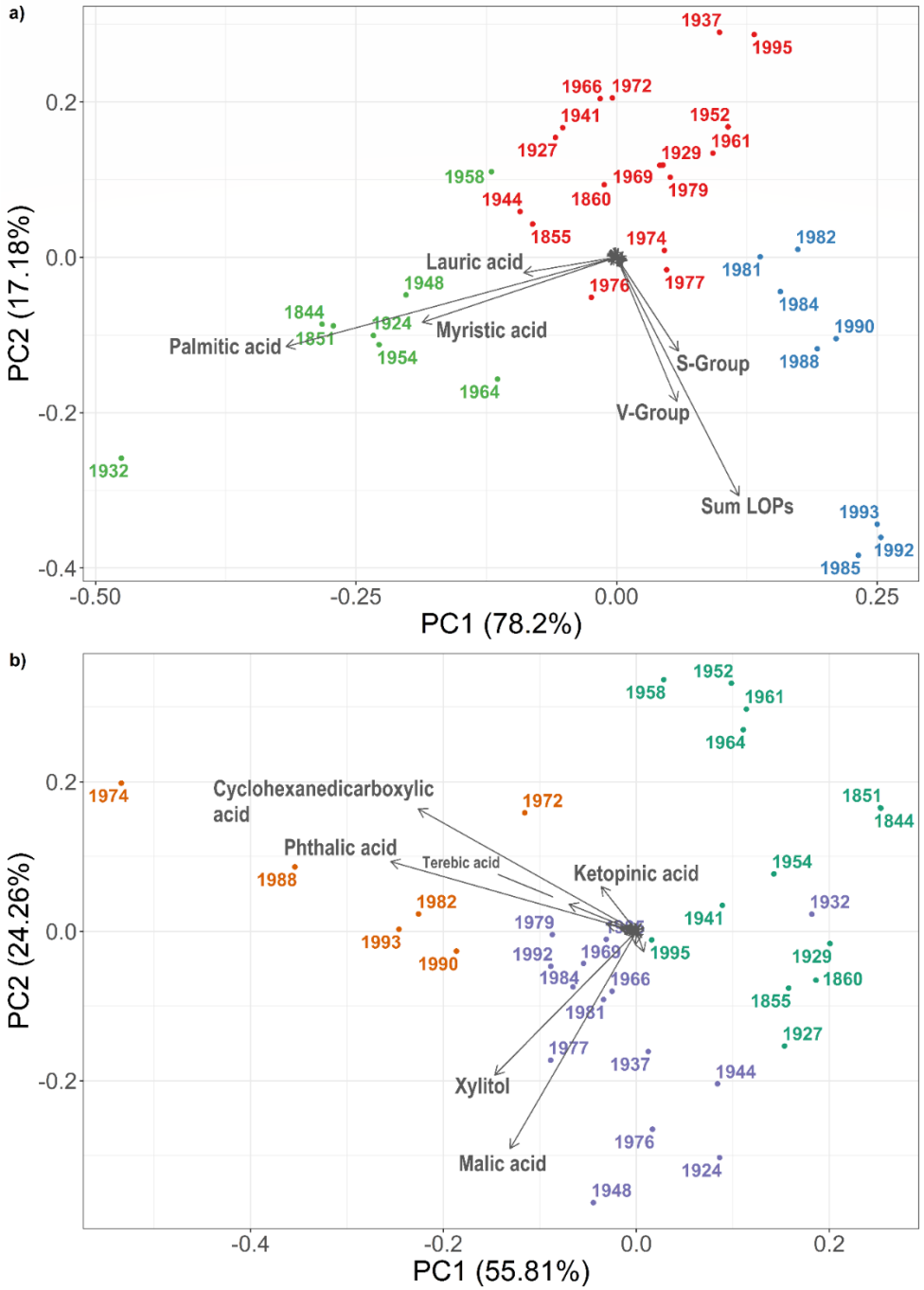

Figure 81: Principal component analysis of Colle Gnifetti glacier samples. a) Analysis including all SOA markers and lignin oxidation products with the highest loadings on the principal components labelled. Samples were clustered into three groups by the k-means algorithm. b) Principal component analysis without the highest loadings from plot a), samples were again clustered by the k-means algorithm.

7.4 Conclusion and Outlook

In this chapter, the development and application of a novel trace analysis method for simultaneous detection of SOA markers and polymeric lignin in ice cores was presented. Two chromatographic methods were developed on a pentafluorophenyl column with reversed-phase functionality and a HILIC method to cover analytes of higher polarity. For the HILIC method different columns, buffers and pH values were evaluated. The final method included a PCF of methanolic ammonium hydroxide solution to significantly increase the ionization efficiency of polar compounds like Lev. Sufficient repeatability and linearity was obtained for trace concentrations down to 1 ng/mL. Different SPE materials were evaluated for enrichment of SOA marker compounds and separation of lignin burning markers from intact polymeric lignin. Thereby different workflows, pH values, and combinations of material were tested. The final method consisted of a double layer SPE with a WAX material for enrichment of SOA markers and HLB material for enrichment of lignin. Highly polar compounds like mannitol, xylitol, levoglucosan, and erythritol could not be enriched by SPE and were recovered in the flow-through, which is why a novel approach was introduced using centrifugal evaporation for the evaporation of the aqueous matrix. Method validation of the double layer SPE and centrifugal evaporation confirmed sufficient linearity, repeatability, and recovery for trace concentrations. Analysis of lignin was conducted using a catalyzed alkaline oxidation approach with soluble $CuSO_4$ as a catalyst. The oxidation procedure and subsequent SPE was suitable to analyze the monomeric composition with good repeatability. Further experiments could be conducted to evaluate the accuracy of the lignin analysis by using lignin derived from different plant parts (wood, leaves, needles) and different vegetation species. Furthermore, more potential SOA markers could be included to the target analytes like sesquiterpene oxidation markers, products of dimerization, organosulfates, or a variety of fatty acids. For Lev analysis, a method for the separation of the three isomers Lev, Gal and Man is available and could be used on ice core samples with higher initial Lev concentration.

Application of the method to thirty-three samples from Alpine glacier Colle Gnifetti from 1844 to 1995 showed a good correlation of monoterpene derived SOA marker among each other and similar concentration ranges to other ice core studies in the literature. A temperature dependency was observed for monoterpene and isoprene derived SOA markers, while the concentration of the isoprene oxidation marker erythritol was much lower in Colle Gnifetti than in other ice cores described in the literature. Correlation of monoterpene oxidation markers (MBTCA) and anthropogenic derived SOA markers revealed a strong influence of the abundance of anthropogenic pollutants in the atmosphere on aerosol aging. In addition, in 1974 an increased number of fires was described in the literature and in Colle Gnifetti, monoterpene oxidation markers showed an increased concentration, indicating an influence of biomass burning on monoterpene emission and oxidation, presumably due to the strongly elevated temperature. A peaking Lev concentration in the sample from 1937 was consistent with increased number of fires in this year confirming the potential of Lev as a biomass burning marker in ice cores. PCA distinguished between anthropogenic influence (PC1), describing 56% of the total variance and

biomass burning describing 25% of the variance (PC2), and clustered the samples according to their age. Younger samples were influenced strongest by anthropogenic emissions. In the future, more older samples from Colle Gnifetti glacier will be analyzed to complement the data on changing aerosol constituents in the pre-industrial and industrial age and validate the impact of anthropogenic pollutants in the atmosphere. In addition, samples from Belukha glacier in the Altai Mountain range will be analyzed that cover a larger period of time. Here, concentrations of monoterpene and isoprene derived markers are expected to be higher and enable the analysis of the enantiomeric ratio of pinic acid, derived from either α- or β-pinene, by chiral chromatography. Furthermore, the remote location of Belukha glacier compared to the Alpine Colle Gnifetti will provide further information on climate change on a global scale.

The presented data from lignin analysis is the first data on polymeric lignin in ice core samples. On average, the overall concentration of LOPs increased continuously per decade from the 1930s on according to higher forest cover in the Alps due to changed land use, decreasing agricultural activity and a switch from domestic wood to coal burning. The low C/V ratio is consistent with the high forestation of the Alpine region and the S/V ratio increased from older to younger samples, which was in accordance with data on forest development in the Southern Swiss Alps, where the abundance of beech species increased and coniferous species decreased. PCA on lignin markers showed a higher influence of vegetation abundance than vegetation type on the overall sample variance. In summary, first analyses of lignin in ice core samples showed a high potential of lignin as a marker for changes in vegetation abundance and vegetation species on a regional scale. More experiments are necessary to elucidate the emission source, that we postulate by biomass burning or microbial degradation of wood. Furthermore, the atmospheric stability of lignin should be analyzed to evaluate the potential of lignin as a marker for vegetation on a trans-regional to global scale.

8. Non-target and suspect-target screening for organic compounds in ice core samples from Colle Gnifetti core

Chapter 8.1 to 8.4 is a reprint of the article

Towards comprehensive non-target screening using heart-cut two-dimensional liquid chromatography for the analysis of organic atmospheric tracers in ice cores

Anja Beschnitt, Margit Schwikowski, Thorsten Hoffmann

published in "Journal of Chromatography A" (doi:10.1016/j.chroma.2021.462706).

Abstract

Non-target screening of secondary organic aerosol compounds in ice cores is used to reconstruct atmospheric conditions and sources and is a valuable tool to elucidate the chemical profiles of samples with the aim to obtain as much information as possible from one mass spectrometric measurement. The coupling of mass spectrometry to chromatography limits the results of a non-target screening to signals of compounds within a certain polarity range based on the utilized stationary phases of the columns. Comprehensive two-dimensional liquid chromatography (LCxLC) introduces a second column of different functionality to enable the analysis of a broader range of analytes. Conventional LCxLC requires complex instrumental setups and is difficult to implement for most laboratories. In this work we demonstrate an approach to approximate a comprehensive non-target screening using a simple instrumental setup employing two columns of orthogonal functionalities (HILIC and reversed-phase), an additional pump, and an additional six-port valve. The void volume of the first dimension is transferred to the reversed-phase column to analyze low-polarity compounds during the re-equilibration of the HILIC. Method validation showed adequate repeatability and detection limits for two selected void volume markers and application to snow samples collected at the high-alpine research station *Jungfraujoch* yielded a total of 270 signals. Comparison to the one-dimensional HILIC approach revealed 175 signals exclusively detected in the two-dimensional method, of which 23 were detected in the second dimension. Detailed analysis of the chemical composition showed consistency with expected compounds in snow samples like lignin or cellulose combustion products from biomass burning or secondary organic aerosol constituents. The results confirmed that one-dimensional chromatography was not sufficient to cover the entire range of compounds and the developed two-dimensional approach will improve the information content from non-target screening while maintaining time of analysis and a simple instrumental setup.

8.1 Introduction

Ice cores are valuable environmental archives which are used to study paleoclimatic conditions to improve the understanding and predictions of climate change in the past, present and in the future. They preserve the organic and inorganic compounds deposited with snow (wet deposition) or wind (dry deposition) in annual layers which can be dated back over several thousand years (Jenk et al. 2009; Fang et al. 2021). The main sources of organic compounds found in environmental archives are atmospheric aerosols. Aerosols influence the radiative budget of the earth's atmosphere either by scattering of solar radiation (direct effect) or by influencing the lifetime and amount of clouds by acting as cloud condensation nuclei (indirect effect) (Pöschl 2005). Primary aerosols are directly emitted into the atmosphere as particles, while secondary (organic) aerosols (SOA) are formed in the atmosphere by oxidation of volatile organic compounds (VOC) into less volatile species which undergo gas-to-particle conversion (Houghton J.T., Ding, Y., Griggs, D.J., Noguer, M., van der Linden, P.J., Dai, X., Maskell, K., Johnson 2001; Lohmann and Feichter 2005; Pöschl 2005). Selected well-known oxidation products of VOCs are used as SOA-markers and assigned to certain sources, such as pinic acid as an oxidation product of α- or β-pinene representing contributions from terrestrial vegetation (Glasius et al. 2000; Yasmeen et al. 2010). Other compounds, such as 1,6-anhydro-β-glucopyranose (levoglucosan), are used as markers for primary aerosol emissions, in this case from biomass burning (Dye and Yttri 2005; Saarnio et al. 2013; Bhattarai et al. 2019), or mannitol, as a tracer for airborne fungal spores (Bauer et al. 2008; Fu et al. 2013). The detailed investigation of the molecular composition of organic aerosols is also a valuable tool to investigate anthropogenic effects on atmospheric chemistry (Kourtchev et al. 2014). The atmospheric lifetimes of organic markers in the particle phase range from less than a day to more than 10 days, enabling long-range atmospheric transport (Donahue et al. 2013). The concentration of the individual marker compounds in ice core samples are extremely low and the access to precious ice samples is often limited leading to low sample volumes, which arises an urgent need for highly sensitive analytical methods for quantification of trace compounds. In addition, due to the high number of VOCs precursors from various sources, and an additional chemical processing (ageing), the molecular composition of organic aerosols is very complex, consisting of thousands of individual compounds. While on the one hand this increases the requirements for trace analytical method development, on the other hand it means that the precise characterization of the composition can provide further information about aerosol sources but also atmospheric chemical processes, which targeted analysis would not provide. Therefore, non-targeted analysis of organic matter in ice core samples, with simultaneous detection of also very different polar analytes, is a novel and important tool to elucidate the changing chemical profile over time (Vogel et al. 2019).

Comprehensive, non-targeted analysis of complex samples is a rapidly emerging field in organic trace analysis. However, while data interpretation, sensitivity, and selectivity of the HR-MS are continuously improving, chromatographic separation is the limiting factor for this analytical approach. Most publications dealing with sophisticated non-target screenings (NTS) use reversed-phase liquid

chromatography (RP-LC) methods (Hug et al. 2014; Ruff et al. 2015; Nürenberg et al. 2015; Vogel et al. 2019). RP-LC coupled with an electrospray ionization (ESI) mass spectrometry (MS) system is well suited for the analysis of a wide range of compounds. However, small, polar compounds in particular, which are of great interest in areas such as environmental chemistry, water analysis, or pharmaceutical analysis, can usually not be detected because they do not experience sufficient retention on RP-columns. Researchers working with such analytes circumvent this problem by using, for example hydrophilic interaction liquid chromatography (HILIC) (Minkus et al. 2021), or mixed-mode columns (Montes et al. 2017). Switching to other column functionalities is an instrumentally simple solution and allows the analysis of different groups of analytes but does not solve the problem of incomplete sample profiling. Since ice core samples are composed of an aqueous matrix, polar constituents are expected to predominate, making HILIC the method of choice for an initial overview of the chemical composition. However, a serious disadvantage of HILIC chromatography is the long re-equilibration time when working with solvent gradients. To make good use of this extra time, the present work introduces a second chromatography step that runs during the re-equilibration time of the HILIC column. In this way, compounds with low polarity that do not experience sufficient retention on the HILIC column and elute in the void volume become accessible for analysis. Otherwise, these compounds would be subject to strong matrix effects (ion suppression/ion amplification) (Mallet et al. 2004; Antignac et al. 2005). In the present work, the void volume is collected in an additional sample loop and transferred to an RP-LC column, resulting in quasi-comprehensive two-dimensional liquid chromatography (*q*2D-LC).

2D-LC is generally distinguished between heart-cut 2D-LC (LC-LC) and comprehensive 2D-LC (LCxLC). LC-LC is used to separate small, distinct fractions of the 1D effluent on a second dimension with a different functionality, e.g., cardiolipins on an additional RP-column (Helmer et al. 2020), or enantiomers on an additional chiral column in the second dimension (Lee et al. 2013; Lin et al. 2020). For LC-LC, a conventional LC-MS instrument requires only an additional six-port valve (and, depending on the output device a second LC-pump) equipped with a storage device, such as a sample loop or a trapping column, to perform LC-LC experiments. In addition to single-heart cut 2D-LC, in which only a specific fraction of the effluent is collected, multiple-heart-cut (mLC-LC) methods are also used to evaluate the peak purity of chiral pharmaceutical compounds (Lee et al. 2013), or to analyze antibody-drug conjugates in bioanalysis (Sandra et al. 2016). (m)LC-LC is suitable for separating compounds that are difficult to resolve in one dimension in complex sample matrices but cannot be used for the analysis of non-target compounds because only a certain known fraction of the first dimension is transferred and analyzed on the second column, while the remaining information from the first dimension is neglected.

To combine the information of the first and second dimension and to obtain a comprehensive overview of the compounds in a sample, the simplest setup is a serial coupling of two columns with an additional pump that introduces the correct mobile phase for the second dimension through a T-piece between the columns. The columns used can have similar (Herrero et al. 2008) or orthogonal functionalities (Louw et al. 2008; Greco et al. 2013). However, serial coupling of columns can lead to mutual cancellation of separation on the respective columns (Alvarez-Segura et al. 2016; Stoll et al. 2017). Another approach is to couple columns of orthogonal functionalities in parallel and then re-combine the outflows upstream of the MS. In an exemplary work, the collected fraction of the 1D effluent is the void volume of the HILIC column, which is transferred to the RP-LC column to analyze polar and non-polar compounds simultaneously (Rampler et al. 2018).

In an LCxLC experiment, on the other hand, the entire effluent of the first dimension is transferred to the second dimension in small, separate fractions. This requires a much more complex instrumental setup, including at least one valve with eight ports and two sample loops. While one sample loop is filled with a portion of the 1D effluent, the second loop transfers the previously collected effluent to the second dimension. Therefore, the volume of collected fractions is limited to the capacity of the respective sample loops (see Pirok et al. 2019 and Stoll and Carr 2017 for detailed reviews of instrumental aspects of LC-LC and LCxLC). LCxLC significantly increases peak capacity compared to one-dimensional chromatography by combining (orthogonal) column functionalities (e.g., RPLCxNPLC) but is associated with challenging instrument settings and data evaluations. All described two-dimensional chromatography methods are available not only for LC, but also for gas chromatography (see (Dallüge et al. 2003) for a detailed overview), e.g., in the analysis of pyrolysis products of bio-oils (Staš et al. 2021).

In this work, we present a novel approach that combines the advantages of LC-LC and LCxLC to obtain a more comprehensive chemical sample profile without extended analysis time with a straightforward instrumental setup involving only an additional six-port valve, sample loop, and pump. NTS was performed on fresh snow samples collected on the *Jungfraufirn* near to the high-alpine research station *Jungfraujoch* (Switzerland) as a surrogate for ice core samples and results from the *q*2D-LC method were compared to the previously used HILIC NTS approach, and to the individually measured LC methods, which were manually evaluated for matching signals. The new method showed comparable results to the individually measured chromatography methods and an enhanced number of signals compared to the HILIC approach for the same amount of time. Thus, it is a promising approach, to utilize the unused HILIC equilibration time and will be applied to ice core in the future.

8.2 Materials and Methods

8.2.1 Chemicals

Levoglucosan (>99%), vanillin (99%), and *p*-hydroxybenzoic acid (99%) were purchased from Acros Organics (Geel, Belgium). Dodecanoic acid (99.5%) and vanillic acid (98%) were obtained from Alfa Aesar (Karlsruhe, Germany). Acetonitrile (LC-MS grade), methanol (LC-MS grade), and water (LC-MS grade) were purchased from Fisher Scientific (Darmstadt, Germany). Tetradecanoic acid (analytical grade) and 1,2,4-butanetricarboxylic acid (>99%) were obtained from Fluka (Munich, Germany). Ammoniumacetate (98%) was purchased from Merck (Darmstadt, Germany). 3,5-Dimethoxy-4-hydroxyacetophenone (97%), salicylic acid (99%), camphorsulfonic acid (98%), *cis*-pinonic acid (98%), *trans*-cinnamic acid (97%), pimelic acid (96%), *p*-coumaric acid (>98%), *p*-hydroxyacetophenone (>98%), 4-methylphthalic acid (99%), *trans*-ferulic acid (99%), terebic acid, *cis,trans*-pinic acid, hexadecanoic acid (>99%), ammonium hydroxide solution (25%), *p*-hydroxybenzaldehyde (>97.5%), 4-hydroxy-3-methoxyacetophenone (>98%), syringaldehyde (98%), *meso*-erythritol (>99%), mannitol (≥98%), (1S)-(+)-ketopinic acid (99%), phthalic acid (99.5%), methanesulfonic acid (99%), xylitol (≥99%), syringic acid (>95%), and (1R,3S)-(+)-camphoric acid (99%) were purchased from Sigma-Aldrich (Darmstadt, Germany). Formic acid (LC-MS, 99%) was delivered by VWR International GmbH (Darmstadt, Germany). Ultrapure water with 18.2 MΩ resistance was produced by a Milli-Q water system from Merck Millipore (Darmstadt, Germany).

8.2.2 Sample preparation

Surface snow samples for method validation were collected on Jungfraufirn near the high-alpine research station *Jungfraujoch* (46°32’ N, 7° 59’ E) on the 21st of January 2020 at an altitude of 3460 m a.s.l. (see Osmont et al. (Osmont et al. 2021) for detailed information of the study site and meteorological conditions). Winter snow samples are expected to present the greatest challenge for method development, since impurity concentrations are extremely low compared to summer snow. This is due to the strong atmospheric stability, decoupling high-altitude sites from the low-elevation sources (Bukowiecki et al. 2016). Samples were transferred into glass containers, covered with aluminum foil, closed with screw-caps, and stored at -25°C until analysis. The glass containers were pre-cleaned with ultrapure water three times, and twice with LC-MS grade acetonitrile (ACN), afterwards they were heated at 450°C for 8 hours to remove contamination with fatty acids (Bosle et al. 2014). 1.5 mL of thawed snow samples were evaporated under a fine stream of nitrogen and re-constituted in 500 µL (enrichment by a factor of 3) of H_2O/ACN (1:1, v/v). One sample was spiked with 10 µL of a multi-component (see chapter 3.4), standard solution (10 µg/mL).

8.2.3 Chromatography and mass spectrometry

Method development and analysis was conducted using a Dionex UltiMate 3000 ultrahigh-performance liquid chromatography (UHPLC) system consisting of an HPG-3400 RS pump and an HPG-3400 SD pump (both Thermo Fisher Scientific). The UHPLC system was coupled to a Q Exactive Orbitrap high resolution MS (Thermo Fisher Scientific) and an additional external pump (High precision pump Model 300 C S) from Gynkotek (Germering, Germany) was used for post-column derivatization. The ESI probe was heated to 150°C (HESI) to enhance solvent evaporation, the capillary temperature was set to 320°C, sheath gas pressure to 60 psi, auxiliary gas pressure to 20 psi and the spray voltage to -3.5 kV. The mass spectrometer was operated in full scan mode, (*m/z* 80-500), with a mass resolution of 140,000. XCalibur 4.3 and the integrated SII control plugin for the chromatography system was used for instrument control and for NTS the open-source software MZmine 2 (version 2.53) was used for peak detection and sum formula prediction.

8.2.3.1 One-dimensional separation

Chromatographic separation was conducted on an iHILIC-Fusion(+) column (100x2.1 mm, 1.8 µm) from HILICON AB (Umeå, Sweden) and an Acquity UPLC CSH Fluoro-Phenyl column (100x2.1 mm, 1.7 µm) from Waters (Milford, USA), respectively. The flowrate in both methods was set to 0.4 mL/min and the columns were heated to 30°C during separation. The injection volume was 10 µL. For HILIC separation a buffer solution ammonium acetate (5mM, pH 6.0) (A) and pure ACN (B) were used as the mobile phase. Additionally, to enhance ionization a post-column flow (PCF) of a methanolic NH_4OH (50 mM) solution was introduced by a T-piece between the column and the mass spectrometer. Data was recorded from 0 to 14 min, and afterwards the column was re-equilibrated for 8 min with the starting conditions for the next run. Separation on the RP column was conducted using H_2O/ACN (98:2, v/v) with 400 µL/L of formic acid (A) and H_2O/ACN (2:98, v/v) (B). The respective gradients are shown in Table 11.

Table 11: Optimized gradients of one-dimensional separation on the HILIC column (left) and the RP-LC column (right). Eluent B refers to ammonium acetate buffer (5mM, pH 6.0) for the HILIC and H_2O/ACN (98:2, v/v) for the RP-LC.

HILIC (1D)		**RP-LC (1D)**	
Time in min	*%B*	*Time in min*	*%B*
0	97	0	1
0.5	97	13	99
12	50	14	99
14	50	14.5	1
14.5	97	15	1
22	97		

8.2.3.2 Two-dimensional HILICxRP separation

Two-dimensional HILIC-RP separation was performed on the same columns as described for one-dimensional separation. An additional six-port valve equipped with a 500 µL sample loop was used to switch between position A, where the first dimension (HILIC) was transferred directly to the MS, position B, where the sample loop was filled with a certain volume (here the void volume) of the first dimension, and position C where the second pump was switched on to transfer the content of the sample loop to the second dimension (RP) for separation of low polarity compounds (Figure 82). During a chromatographic run, the positions of the six-port valves were set in the order A→B→A→C.

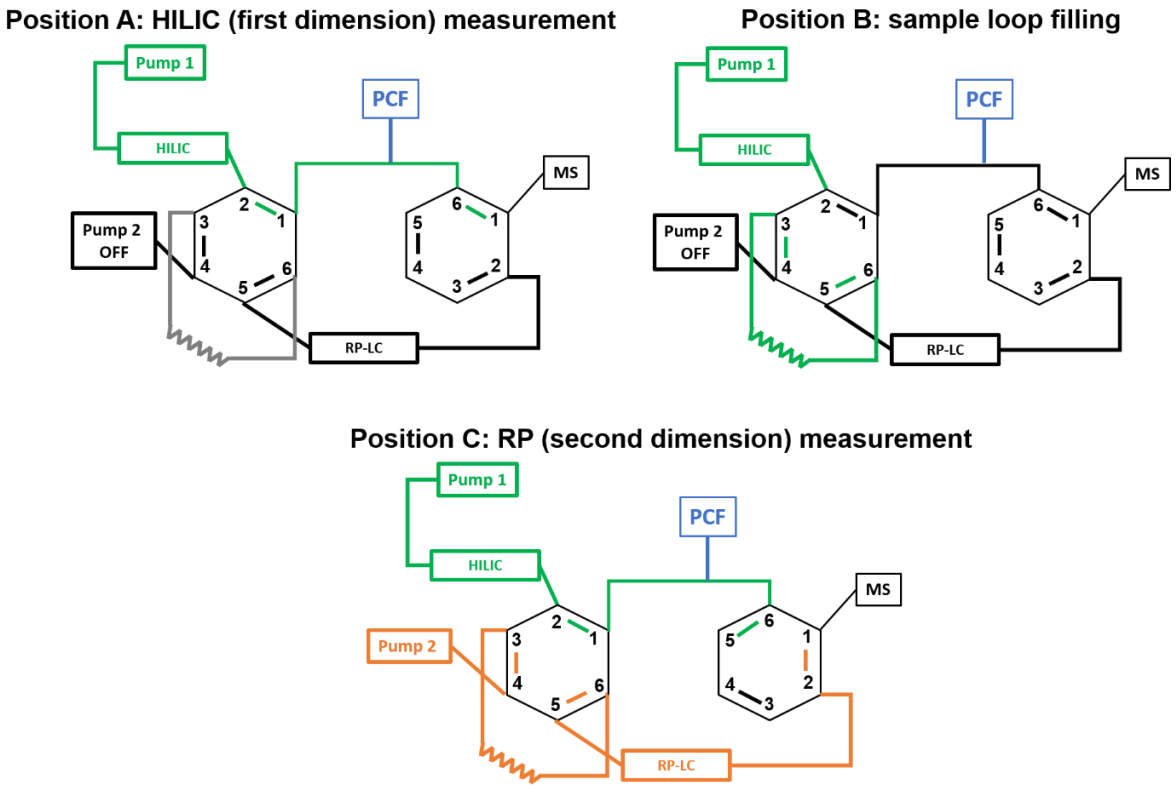

Figure 82: Instrumental setup of the quasi-comprehensive 2D-LC method. Position A: Only the first dimension is transferred to the MS (green) with an additional post-column flow (PCF) between the HILIC Column and the MS (blue), while the second pump is switched off and the path of the second dimension is not used (black). Position B: The sample loop is filled with the void volume of the first dimension (green). Position C: The second pump is turned on, the content of the sample loop is transferred to the second column and measured in the MS (orange), the HILIC column is re-equilibrating with the initial conditions and is going to waste. During a chromatographic run, the sequence of positions is A→B→A→C.

During the measurement of the second dimension, the HILIC column was re-equilibrated with the initial conditions of the subsequent measurement. To capture the void volume, the time window of position B was set to 0.7-1.3 min, resulting in a captured volume of 240 µL. To counteract peak broadening on the second dimension, an "injection flowrate" of 0.7 mL/min was set at the beginning of the measurement of the second dimension to transfer the volume as focused as possible (Table 12). The injection volume to the first dimension was 10 µL and both columns were placed in the same column oven and heated to

30°C. As in the one-dimensional methods, a PCF of methanolic ammonium hydroxide solution (50 mM) was introduced between the HILIC column and the MS to enhance ionization.

Table 12: Optimized gradient conditions of the two-dimensional LC for pump 1 operating the first dimension with the HILIC column, and pump 2 for the second dimension using a RP column. The positions of the valves for transfer between the two dimensions (valve 1) and between the MS and waste (valve 2) depending on the time are shown.

Pump 1 (HILIC)				**Pump 2 (RP)**				**Valve 1**	
Time in min	*Flow in mL/min*	*%A*	*%B*	*Time in min*	*Flow in mL/min*	*%C*	*%D*	*Time in min*	*Position*
0	0.4	3	97	0	0	95	5	0	1_2
0.5	0.4	3	97	10.6	0	95	5	0.7	6_1
1.0	0.4	10	90	11.0	0.7	95	5	1.3	1_2
6.0	0.4	15	85	11.5	0.7	95	5		
7.5	0.4	40	60	11.6	0.4	95	5	**Valve 2**	
9.0	0.4	50	50	18.0	0.4	95	5	*Time in min*	*Position*
11.0	0.4	50	50	18.5	0.4	50	50	0	6_1
11.5	0.4	3	97	20.0	0.4	50	50	11	1_2
25.0	0.4	3	97	20.5	0.4	95	5		
				24.5	0.4	95	5		
				25	0	95	5		

8.2.3.3 Data processing with MZmine and Matlab

Data of the high-resolution MS measurements were processed using the open-source software MZmine 2 (version 2.53). Settings were optimized for the respective samples in terms of noise levels and resulting peak shapes. Peak detection was performed using the automated data analysis pipeline (ADAP) chromatogram builder module (Pluskal et al. 2010; Myers et al. 2017). The minimum group size in number of scans was set to 5, *m/z* tolerance to 2 ppm, minimum highest intensity to 5.0E4 (according to the noise level of the samples), and the minimum group intensity threshold to 5.0E3. The chromatograms were deconvoluted by the local minimum search algorithm with a chromatographic threshold of 85%, a minimum relative height of 10%, and a minimum ratio of peak top to peak edge of 1.6. The minimum absolute height was set according to the sample noise levels to 5.0E4. Isotopic features were removed by isotope peak grouping with an *m/z* tolerance of 5 ppm, and a retention time tolerance of 0.2 min. Joined alignment was conducted with an *m/z* tolerance of 2 ppm, a minimum intensity of 1.0E3, and a minimum score of 70%. Formula prediction was set to a range of C (1-50), H (0-100), O (0-40), N (0-5), and S (0-2). A minimum absolute intensity of 1.0E3 was set and a minimum score of 70%.

Blank subtraction was conducted using an in-house Matlab script, so only signals of significant difference from blank samples (H_2O/ACN, 1:1) were further analyzed. The script set a signal/blank ratio of >3, removed signals which were only detected in one of the fivefold measurements, and removed signals with an intensity <1.0E4.

8.3 Results and Discussion

The main goal of the developed two-dimensional method was to obtain a larger amount of information from one measurement in a time comparable to one-dimensional chromatography. To evaluate the amount and quality of the data obtained from the two-dimensional approach, first efficient one-dimensional separation methods were developed on the HILIC and RP columns.

8.3.1 Evaluation of one-dimensional LC methods on the HILIC and RP column

8.3.1.1 Method development on the individual HILIC and RP columns

Two different HILIC columns were selected for separation of atmospherically relevant marker substances: the iHILIC-Fusion column, which is a silica-based column substituted with hydroxyethyl amide chains, and charged with ammonium and sulphate moieties on the surface, and the iHILIC-Fusion(+) column which is similarly structured but with excess positive charges on the surface for improved retention of negatively charged compounds. Both columns can be used between pH 2 and 8, a maximum operation temperature of 60°C, and maximum back pressure of 650 bar at room temperature. Performance of the columns was assessed by retention time, peak resolution of target compounds, and signal intensity. Different aqueous buffer solutions (ammonium acetate and ammonium formate) with different concentrations (5 mM and 10 mM) at different temperatures (25°C, 30°C, 40°C) were tested under isocratic conditions (ACN/buffer solution: 97:3, v/v). Most effective separation was obtained using an aqueous ammonium acetate buffer solution (5 mM) at 30°C on the iHILIC-Fusion(+) column. To improve the time of analysis, different gradients were tested, and most efficient separation was achieved using the gradient shown in Table 11. A selection of relevant extracted ion chromatograms (XIC) of target compounds is shown in Figure 83. The very early eluting compounds were *p*-hydroxybenzaldehyde (*m/z* 121.0506) and other phenolic aldehydes and ketones (e.g., 4-hydroxy-3-methoxyacetophenone, vanillin). Carboxylic acids like coumaric acid (*m/z* 163.0400), dehydroabietic acid (*m/z* 299.2017), or terebic acid (*m/z* 157.0506) eluted between 2.5 and 5.5 min. In this time range, separation proved most difficult, as many of the compounds showed similar polarities. Strongly retained compounds, eluting later than 8 min were dicarboxylic acids like pimelic acid (*m/z* 159.0662), pinic acid (*m/z* 185.0819), or 1,2-cyclohexanedicarboxylic acid (*m/z* 171.0662).

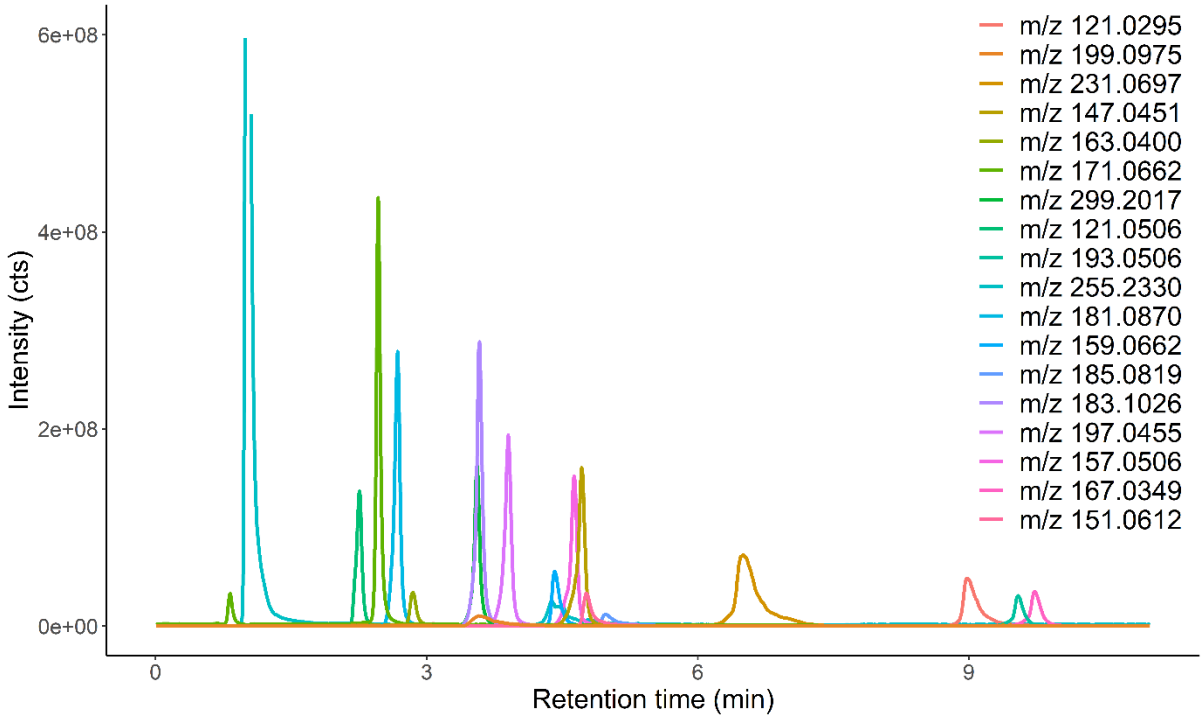

Figure 83: Selection of extracted ion chromatograms (XIC) of relevant SOA markers separated on the iHILIC-Fusion(+) with optimized gradient, temperature, and solvent conditions. The y-axis was cut at 6.0E8 for better visualization of smaller peaks.

Screening for all relevant target compounds in the respective chromatograms revealed a missing compound, levoglucosan (1,6-anhydro-β-glucopyranose), an important biomass burning marker (Fabbri et al. 2009; Bhattarai et al. 2019). This small, polar compound was expected to be sufficiently retained on HILIC columns (You et al. 2016) but was not visible as a peak in the respective XIC (Figure 84a). Although ACN is a suitable solvent for ESI, due to its low surface tension and high volatility, its aprotic character does not support the charging of neutral compounds in the solution. The hydroxy groups of levoglucosan have pKa values of 12.21, 13.22, and 14.74, hence the initial number of ions in the HILIC solvent was very low. A suitably high pH value for deprotonation could not be set to the mobile phase, because the pH stability of the iHILIC-Fusion(+) column ranged from pH 2 to 8. Therefore, a PCF of a methanolic ammonium hydroxide solution (50 mM) between the column and the mass spectrometer was introduced with a flowrate of 0.1 mL/min (Zuth 2018), which resulted in a narrow peak of high intensity at 1.97 min of levoglucosan in the XIC (Figure 84b). Since more compounds with similar properties to levoglucosan were expected in ice core samples, the PCF for NTS was employed in both the one- and two-dimensional approaches.

For RP separation, a C_{18}-column and a pentafluorophenyl (PFP) column were evaluated using H_2O/ACN (2:98, v/v) and H_2O/ACN (98:2, v/v, with 400 µL/L formic acid) as solvents, respectively. Here, only different gradients were evaluated at a temperature of 30°C (for comparability with the HILIC separation) and the optimized gradient is shown in Table 11, consisting of a continuous increase of the ACN content along the runtime on the PFP column.

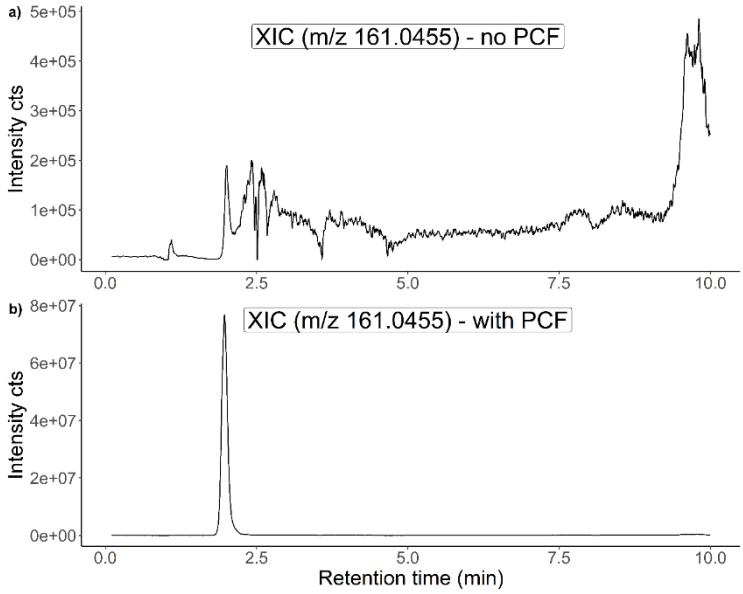

Figure 84: XIC of *m/z* 161.0455 (levoglucosan) analyzed on the HILIC column without an additional PCF (a) and with an additional PCF a methanolic ammonium hydroxide solution (50 mM).

8.3.1.2 Comparison of HILIC and RP-LC separation

Two chromatographic methods (Table 11) with high separation power were available for NTS of snow samples, as surrogate matrix for ice cores samples. To compare the two functionalities of the stationary phases of the RP and the HILIC column, six-fold measurements of the samples and three-fold measurements of blank samples were conducted. After peak detection by MZmine, the mean values of the measurements were determined, blank signals subtracted (see chapter 2.3.3), signals with a retention time <0.5 min neglected, and the remaining signals were plotted by their *m/z* values and retention times (Figure 85). Figure 85a shows the results obtained by the HILIC chromatography. Signals were distributed between 0.5 and 14 min and in the entire mass range of *m/z* 80-500, with most signals in the *m/z* range of 150-300 and 0.5-4 min, in accordance with the target compounds, which were also acquired in this time window. A large proportion of compounds eluted between 0.5 and 1 min in or near the void volume (green area), which is problematic, because compounds in or near the void volume experience strong ion suppression or enhancement effects, which distorts the results (Mallet et al. 2004; Antignac et al. 2005).

Figure 85b shows the signals obtained from the RP-LC measurements. Here, the signals were more evenly distributed over time, but the *m/z* values were slightly higher on average. Only one signal was detected near the void volume at a retention time of less than one minute. The compounds in the aqueous snow samples were expected to be more polar, and consequently more signals were found with the HILIC method than with the RP-LC.

Manual matching of retention times revealed the consistency of nine compounds found with both methods. Nine of 178 signals in the HILIC method, marked as red triangles in Figure 85a, and nine out of 64 signals in the RP-LC, marked as black triangles and red diamond shapes in Figure 85b. The results

show that one-dimensional LC methods in this case do not cover the full range of compounds in the samples, and only a small percentage (5% for HILIC, 14% for RP-LC) was detected by both methods. Therefore, it was essential to combine the two methods in order to increase the amount of information obtained from a measurement. Four of the nine compounds eluted near the void volume in the HILIC but were sufficiently retained on the RP-column. Therefore, the new two-dimensional approach should capture and further analyze the void volume of the HILIC on the RP column, to maintain the information from the HILIC while gaining additional information about more nonpolar compounds from the second RP dimension.

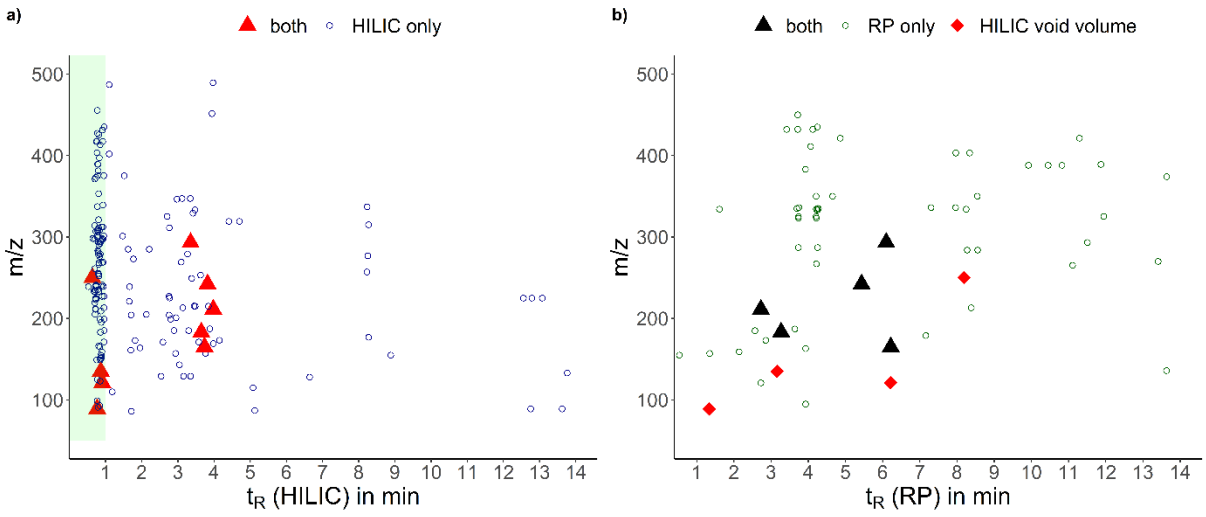

Figure 85*: m/z* plotted against retention time of signals detected in NTS of snow samples detected on the HILIC-Fusion(+) column (a), and on the PFP column (b). Nine signals were found in both methods and confirmed by matching retention times, marked in red in (a). Of the nine signals four were eluting in or close to the void volume on the HILIC column (red diamond shapes in (b)).

8.3.2 Method development of heart-cut two-dimensional LC (*q*2D-LC)

The main goal of the *q*2D-LC method was to obtain a more comprehensive overview by transferring the void volume of the HILIC column, containing non-polar compounds to the second dimension consisting of a suitable RP-column. For this reason, the void volume of the HILIC column had to be cut out of the first dimension in a suitable time window. The total ion chromatogram (TIC) of the multi-component standard showed a signal of high intensity at approximately 0.8 min (Figure 86a), which was targeted for the transfer onto the second dimension as representative for the void volume. First experiments were conducted using a sample loop of 100 µL, resulting in time windows of 0.25 min (due to the flowrate of 0.4 mL/min on the HILIC column). Three different time windows (Figure 86b) around the retention time of 0.8 min were tested and time window B (green), was suitable to cut out the peak of the void volume and resulted in a signal of high intensity in the TIC of the *q*2D-LC in the second dimension at approximately 12 min (Figure 86c). However, although the peak was successfully transferred, to the

second dimension, the retention on the column was low, and the peak shape in the TIC was rather broad. To evaluate further optimization of the *q*2D-LC method standard compounds were necessary as representatives of the void volume. Screening of the respective XICs of all standard compounds revealed, that the *m/z* values of *p*-hydroxybenzaldehyde (*m/z* 121.0295) and *p*-hydroxyacetophenone (*m/z* 135.0452) showed signals of similar shape and retention time to the void volume peak in Figure 86a. Therefore, these two compounds were used to evaluate the effects of the different chromatographic conditions tested to optimize the method (Table S 5 in the supplementary material).

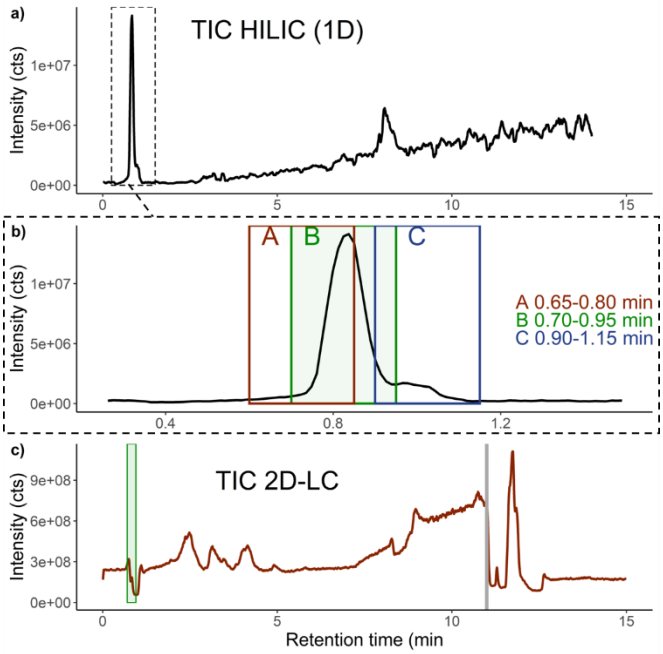

Figure 86: a) Total ion chromatogram (TIC) of the one-dimensional HILIC method. b) Zoom (0.25-1.5 min) of TIC (HILIC 1D). Three different time windows A, B, and C are shown which were tested to transfer the void volume to the second dimension using a 100 µL sample loop. Time window B (0.70-0.95 minutes was suitable to enclose the peak which disappears in the first dimension the TIC of the 2D-LC (c) and recurs on the second dimension (marked by grey line at 11 min). All measurements shown were conducted using a temperature of 30°C, HILIC flowrate of 0.4 mL/min, and the RP gradient presented in Table 12.

Further optimization of the method was performed using a 500 µL sample loop with the possibility of larger time windows and sample volumes. In addition, the larger volume of the sample loop should prevent early diffusion into the RP column before the flow from the second pump starts. The length and position of the time window (and the resulting sample volume), the initial composition of the mobile phase on the RP column, gradient on the RP column, temperature of both columns, injection flow, and modulation volume were tested. The sample volume ranged from 200 to 400 µL with a total time of 0.1-1.5 min to capture the entirety of the peak in the smallest possible volume, which was achieved with a time window of 0.7-1.3 min (240 µL). To improve the initial retention of the compounds on the RP column, the composition of the mobile phase was varied to reduce the elution strength by keeping the ACN content as low as possible between 1 and 10%. Here, a ratio of H_2O/ACN (95:5, v/v) resulted in

improved retention and peak shape with a retention time of the two void volume markers of about 13.5 and 13.7 min (Figure 87). In addition, different gradients were evaluated on the RP column: Gradient A (Table 11), Gradient B consisting of a linear increase in the ACN content up to a final H_2O/ACN ratio of 1:99 (v/v), and Gradient C, which is isocratic and defined by the respective initial composition of the mobile phase. While the overall retention of the compounds was not strongly affected by the different gradients, the strongest separation was observed under isocratic conditions.

In addition to the retention on the second column, the peak shapes were also subjected to optimization. Due to the large volume of the sample loop (compared to e.g., 10 µL injection volume in a 1D chromatography), the column can be overloaded in the second dimension, leading to peak-fronting. Diffusion in the solution during the residence time in the sample loop also negatively affects the peak shape, but not as much as originally expected. To improve peak shape, an injection flowrate was introduced to transfer the contents of the sample loop to the second dimension in a focused manner. To this end, the initial flow rate of the second dimension was set to 0.7 mL/min for 0.5 min. Afterwards, the flow rate was set to a final flow rate of 0.4 mL/min within 0.1 min. Another factor that was expected to affect the results more severely was the high elution power of the solvent from the HILIC column (97% ACN) on the RP column (due to the orthogonality of the methods). However, experiments to evaluate solvent modulation within the sample loop, where 50-300 µL of aqueous solvent was added to the trapped void volume to dilute and weaken the injection solvent (Stoll et al. 2017) did not result in improved peak shape or retention on the RP column. The TIC of the 250 ng/mL multi-component standard recorded by the final *q*2D-LC method, and the XICs of the two void volume markers are shown in Figure 87.

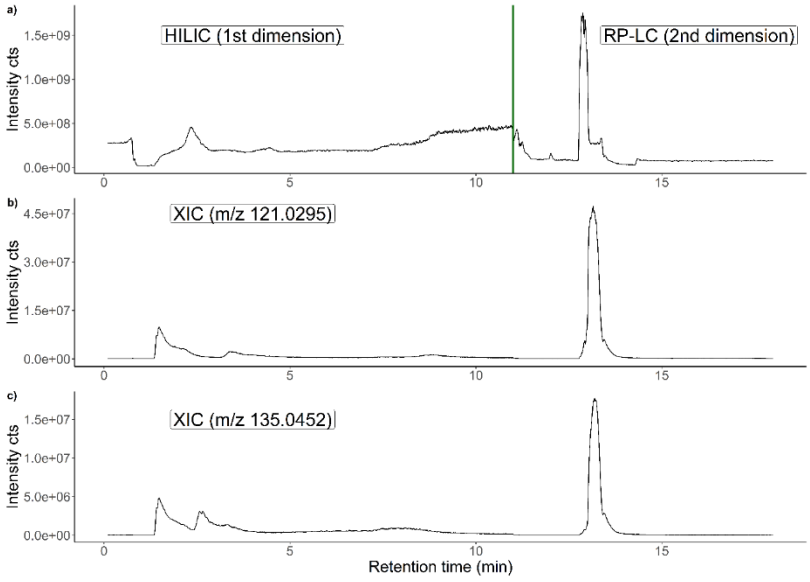

Figure 87: TIC of a 250 ng/mL multi-component standard solution measured with optimized 2D-LC conditions. The switch between first and second dimension is marked in green. b) XIC of *m/z* 121.0295 (*p*-hydroxybenzaldehyde) and c) XIC of *m/z* 135.0452 (*p*-hydroxyacetophenone) both used as void volume marker of the first dimension.

8.3.3 Two-dimensional LC method validation

As mentioned in the introduction, the present *q*2D-LC approach was developed for qualitative NTS of ice core samples. Therefore, the method validation did not focus on quantitative aspects, but qualitatively evaluated the transfer from the first to the second dimension using the void volume markers *p*-hydroxybenzaldehyde and *p*-hydroxyacetophenone. A calibration function was obtained using the multi-component standard with the following concentrations: 10 ng/mL, 50 ng/mL, 100 ng/mL, 250 ng/mL, and 500 ng/mL, respectively set in 1 mL of H_2O/ACN (1:1, v/v). In addition, a blank sample consisting of 1 mL H_2O/ACN (1:1, v/v) was measured to determine the limit of detection (LOD). To assess the linearity of the method, the signal intensity of the standards divided by the respective concentrations (I/c) was plotted against the logarithm of the concentration (Figure 88). In addition to the regression coefficient, determined to be 0.9975 for *p*-hydroxybenzaldehyde and 0.9952 for *p*-hydroxyacetophenone, the plot shows adequate linearity with a deviation less than five percent from the mean of all I/c values, for all standard solutions.

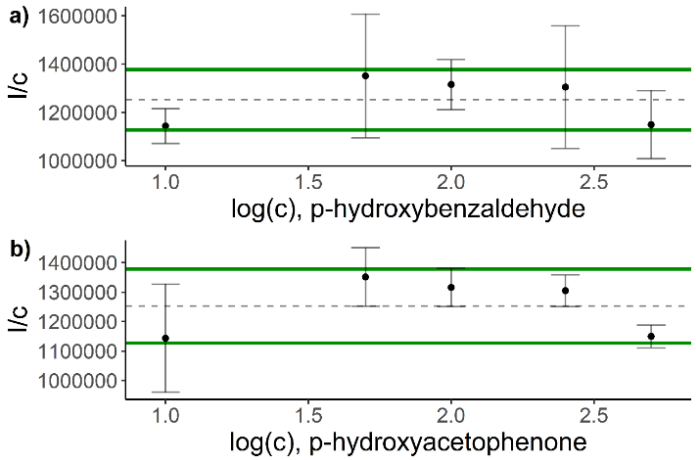

Figure 88: Plots of signal intensity divided by concentration (I/c) to the logarithm of the concentration (log c) of a series of standard solutions to evaluate the linearity of the 2D-LC method for *p*-hydroxybenzaldehyde (a) and *p*-hydroxyacetophenone (b). The mean value of all I/c values is marked, as well as 5% tolerance (green). Sufficient linearity was assumed for all standard solutions within the 5% range.

In addition, the repeatability of the q2D-LC method for all target compounds was evaluated by calculating the relative standard deviation when the 100 ng/mL standard was measured ten times, and the LOD was determined by dividing the threefold standard deviation of the blank signals by the slope of the calibration curve of the respective target compounds (Table 13). 1,2,4-Butanetricarboxylic acid (BTCA) had a high retention time of 10.69 min and therefore exhibited strong peak broadening. The peak integration was complicated. However, with the exception of BTCA, all target compounds showed adequate repeatability with standard deviations less than 15%. LOD values ranged from 0.02 ng/mL (salicylic acid) to 32.34 ng/mL (hexadecanoic acid). Hexadecanoic acid is the most abundant saturated fatty acid and therefore a ubiquitous contaminant in laboratories (Carta et al. 2017). Although the glassware used was baked to minimize the effect (Müller-Tautges et al. 2014), high blank levels were

still observed, resulting in high LOD values. The void volume marker *p*-hydroxybenzaldehyde and *p*-hydroxyacetophenone showed repeatable results with standard deviations of less than 5% and LOD values of 0.14 ng/mL and 0.08 ng/mL, respectively.

Table 13: Trivial name, proposed atmospheric origin, sum formula, *m/z* value ($[M-H]^-$), log P, retention time in minutes, repeatability in percent, and limit of detection in ng/mL of all SOA markers evaluated by the *q*2D-LC method.

Name	**Atmospheric origin**	**Sum formula**	***m/z* $[M-H]^-$**	**log P**	**t_R in min**	**Rep. in %**	**LOD in ng/mL**
Levoglucosan	Cellulose combustion *(Kawamura et al. 2012; Pokhrel et al. 2020)*	$C_6H_{10}O_5$	161.0455	-0.68	1.84	6.57	1.12
Acetovanillon	Lignin combustion *(Kawamura et al. 2012)*	$C_9H_{10}O_3$	165.0557	1.33	2.18	7.29	0.09
Vanillin	Lignin combustion (*Kawamura et al. 2012)*	$C_8H_8O_3$	151.0400	1.19	2.22	4.88	0.11
Dehydroabietic acid	Resin combustion *(Kawamura et al. 2012; Pokhrel et al. 2020)*	$C_{20}H_{28}O_2$	299.2017	6.35	2.32	4.73	N.A.
Hexadecanoic acid	Sea spray *(Meyers 1997; Wolff et al. 2006)*	$C_{16}H_{32}O_2$	255.2330	5.03	2.36	4.77	32.34
Tetradecanoic acid	Sea spray *(Meyers 1997; Wolff et al. 2006)*	$C_{14}H_{28}O_2$	227.2017	6.09	2.37	6.17	2.87
Dodecanoic acid	Sea spray *(Meyers 1997; Wolff et al. 2006)*	$C_{12}H_{24}O_2$	199.1704	7.15	2.41	8.38	6.95
***p*-Hydroxybenzoic acid**	Lignin combustion *(Kawamura et al. 2012; Pokhrel et al. 2020)*	$C_7H_6O_3$	137.0244	1.42	2.44	7.94	0.10
Salicylic acid	Lignin combustion *(Kawamura et al.*	$C_7H_6O_3$	137.0224	2.06	4.21	8.07	0.02

Name	Atmospheric origin	Sum formula	*m/z* $[M-H]^-$	log P	t_R in min	Rep. in %	LOD in ng/mL
	2012; Pokhrel et al. 2020)						
Acetosyringone	Lignin combustion *(Kawamura et al. 2012)*	$C_{10}H_{12}O_4$	195.0663	1.23	2.52	8.26	0.08
Camphorsulfonic acid	Sulfated biogenic SOA *(Iinuma et al. 2007a; Kristensen and Glasius 2011)*	$C_{10}H_{16}O_4S$	231.0697	-0.57	2.61	14.75	N.A.
4-Methylphthalic acid	Anthropogenic *(Kawamura et al. 2001; Hyder et al. 2012; Hermabessiere et al. 2017)*	$C_9H_8O_4$	179.0349	1.27	2.61	11.53	2.15
Syringaldehyde	Lignin combustion *(Kawamura et al. 2012)*	$C_9H_{10}O_4$	181.0506	0.86	2.63	5.92	0.12
Erythritol	Isoprene oxidation *(Claeys et al. 2004)*	$C_4H_{10}O_4$	121.0506	-3.0	2.77	6.28	N.A.
Mannitol	Fungal spores *(Bauer et al. 2008)*	$C_6H_{14}O_6$	181.0718	-4.67	2.81	8.25	N.A.
***cis*-Pinonic acid**	Monoterpene oxidation *(Zhang et al. 2010; Feltracco et al. 2021)*	$C_{10}H_{16}O_3$	183.1026	1.07	3.16	5.82	0.24
Ketopinic acid	Monoterpene oxidation *(Kleindienst et al. 2007; King et al. 2019a)*	$C_{10}H_{14}O_3$	181.0870	0.70	3.19	9.79	0.35
Phthalic acid	Anthropogenic *(Kawamura et al. 2001; Hyder et al.*	$C_8H_6O_4$	165.0193	0.81	3.39	7.59	0.52

Name	Atmospheric origin	Sum formula	*m/z* $[M-H]^-$	log P	t_R in min	Rep. in %	LOD in ng/mL
	2012; Hermabessiere et al. 2017)						
Methanesulfonic acid	Sea spray *(Meyers 1997; Wolff et al. 2006)*	CH_4O_3S	94.9808	-1.89	3.42	13.94	8.29
Xylitol	Fungal spores *(Saarnio et al. 2010)*	$C_5H_{12}O_5$	151.0612	-3.77	3.44	10.61	N.A.
***trans*-Cinnamic acid**	Lignin combustion *(Kawamura et al. 2012)*	$C_9H_8O_2$	147.0451	2.41	3.61	5.86	0.03
***trans*-Ferulic acid**	Lignin combustion *(Kawamura et al. 2012)*	$C_{10}H_{10}O_4$	193.0506	1.64	3.95	10.63	0.21
***p*-Coumaric acid**	Lignin combustion *(Kawamura et al. 2012)*	$C_9H_8O_3$	163.0400	2.43	4.13	7.07	0.23
Vanillic acid	Lignin combustion *(Kawamura et al. 2012)*	$C_8H_8O_4$	167.0349	1.33	4.20	9.98	0.43
Terebic acid	Monoterpene oxidation *(Kahnt et al. 2014; Sato et al. 2016)*	$C_7H_{10}O_4$	157.0506	-0.39	4.37	9.83	0.07
Syringic acid	Lignin combustion *(Kawamura et al. 2012)*	$C_9H_{10}O_5$	197.0455	1.13	4.51	12.41	0.29
Camphoric acid	Biogenic SOA (Fu et al. 2016)	$C_{10}H_{16}O_4$	199.0975	1.47	4.94	7.39	0.24
***trans*-1,2-cyclohexanedicarbox. acid**	Biogenic SOA (Fu et al. 2016)	$C_8H_{12}O_4$	171.0662	0.64	8.37	12.44	2.57
***cis,trans*-Pinic acid**	Monoterpene oxidation	$C_9H_{14}O_4$	185.0819	0.94	8.79	11.75	7.40

Name	Atmospheric origin	Sum formula	*m/z* $[M-H]^-$	log P	t_R in min	Rep. in %	LOD in ng/mL
	(Zhang et al. 2010; Feltracco et al. 2021)						
Pimelic acid	Anthropogenic *(Kawamura and Yasui 2005; van Pinxteren and Herrmann 2007)*	$C_7H_{12}O_4$	159.0662	0.27	8.97	12.88	16.74
MBTCA	Monoterpene oxidation (Müller et al. 2012)	$C_8H_{12}O_6$	203.0561	-0.63	9.03	12.97	8.05
BTCA	Monoterpene oxidation (Müller et al. 2012)	$C_7H_{10}O_6$	189.0405	-0.90	10.69	24.18	22.95
***p*-Hydroxybenz-aldehyde**	Lignin combustion *(Kawamura et al. 2012)*	$C_7H_6O_2$	121.0295	1.39	13.13	2.87	0.14
***p*-Hydroxyaceto-phenone**	Lignin combustion *(Kawamura et al. 2012)*	$C_8H_8O_2$	135.0452	1.42	13.19	4.93	0.08

8.3.4 Two-dimensional LC method performance

To evaluate the performance of the *q*2D-LC method, the results of the NTS of the snow sample using the 1D HILIC approach were compared with the *q*2D-LC results of the similar sample. Data analysis was performed as described in 2.3.3., and the resulting signals were plotted by *m/z* and retention time (Figure 89a), and in a van-Krevelen plot (Kim et al. 2003) by H/C ratio and O/C ratio (Figure 89b). In addition, the signals obtained by both methods (1D and 2D) were plotted according to their retention time to observe the retention time shift due to the longer delay time in the *q*2D-LC as well as the retention time of transferred signals from the void volume in the second dimension (Figure 89c). Evaluation of the *m/z* to retention time plot revealed a total of 270 signals in the *q*2D-LC method and 177 signals in the 1D-HILIC method. Ninety-five of the respective signals were detected by both methods, resulting in 82 signals detected exclusively in the 1D-HILIC method and 175 signals detected exclusively in the *q*2D-LC method, of which 23 were found at a retention time >11 min, and thus in the second dimension.

In both methods, many signals were detected at lower retention times (<1.0 min), but more signals were observed at higher retention times in the *q*2D-LC method. One explanation for this could be the data analysis by MZmine. By eliminating the empty volume peak, the relative height of the smaller peaks increased, so more signals were detected using the same threshold as the 1D-LC approach. Although the recovery of SOA markers from the evaporation procedure described in chapter 2.2 proved sufficient, a loss of highly volatile compounds cannot be entirely ruled out. However, replacing the evaporation procedure by solid-phase extraction did not provide sufficient recovery for highly polar compounds from the aqueous matrix. Application of the evaporation method to ice core samples in the future requires the usage of an appropriate internal standard like ^{13}C-substituted levoglucosan.

The van-Krevelen plot provides more detailed information about the chemical properties of the respective signals. Most compounds detected by both methods were in the range of H/C 1 to 2 and O/C 0 to 0.5. These ranges are assigned to lipids, peptides, and unsaturated hydrocarbons (Brockman et al. 2018; Rivas-Ubach et al. 2018). Compounds detected only in the *q*2D-LC were mainly grouped in the range of H/C 0 to 2.0 and O/C 0.5 to 1.0, which is partially assigned to carbohydrates, lignins, and tannins, all of which belong to groups of important environmental compounds not covered by the 1D-HILIC method. A closer look at the retention times of signals detected by both methods reveals signals that were similarly detected on the HILIC column and are near the regression line in Figure 89c. However, the elimination of interfering compounds from the void volume improved retention of compounds in the first dimension, which is observable in a positive shift in retention time. One signal can be observed that was transferred from the first to the second dimension, with a low retention time on the y-axis, and a retention time >11 min on the x-axis. However, the 23 additional signals in the second dimension represent the main added value of the *q*2D-LC approach, which generally has better information content compared to 1D-HILIC. The 23 signals in the second dimension ranged from H/C 0.1 to 1.6, and O/C 0 to 1.3, so no saturated hydrocarbons were found. The ring and double bond equivalents (RDBE) ranged from 3 to 11, confirming this observation. 13 of the signals had *m/z* values >300. Database screening of the molecular formulas revealed many steroidal functionalities, cyclic structures, and carbohydrate functionalities. In general, the analysis of compounds detected in the second dimension was consistent with the assumption that important information has been lost in the void volume of HILIC, which is now accessible by the *q*2D-LC method.

Finally, a time-consuming manual data analysis was performed to combine all signals acquired individually in the HILIC and RP-LC measurements. Here, retention times had to be matched manually to distinguish between similar and different compounds with the same molecular formulas which is not suitable for routine analyses or large datasets. However, the combined data yielded a total of 101 signals detectable only by individual analysis on both columns, including 34 on the RP column and 67 on the HILIC column. Forty-one of the 67 signals (61%) had retention times of less than one minute and since they are expected to be subject to matrix effects in the void volume, their information value was considered negligible.

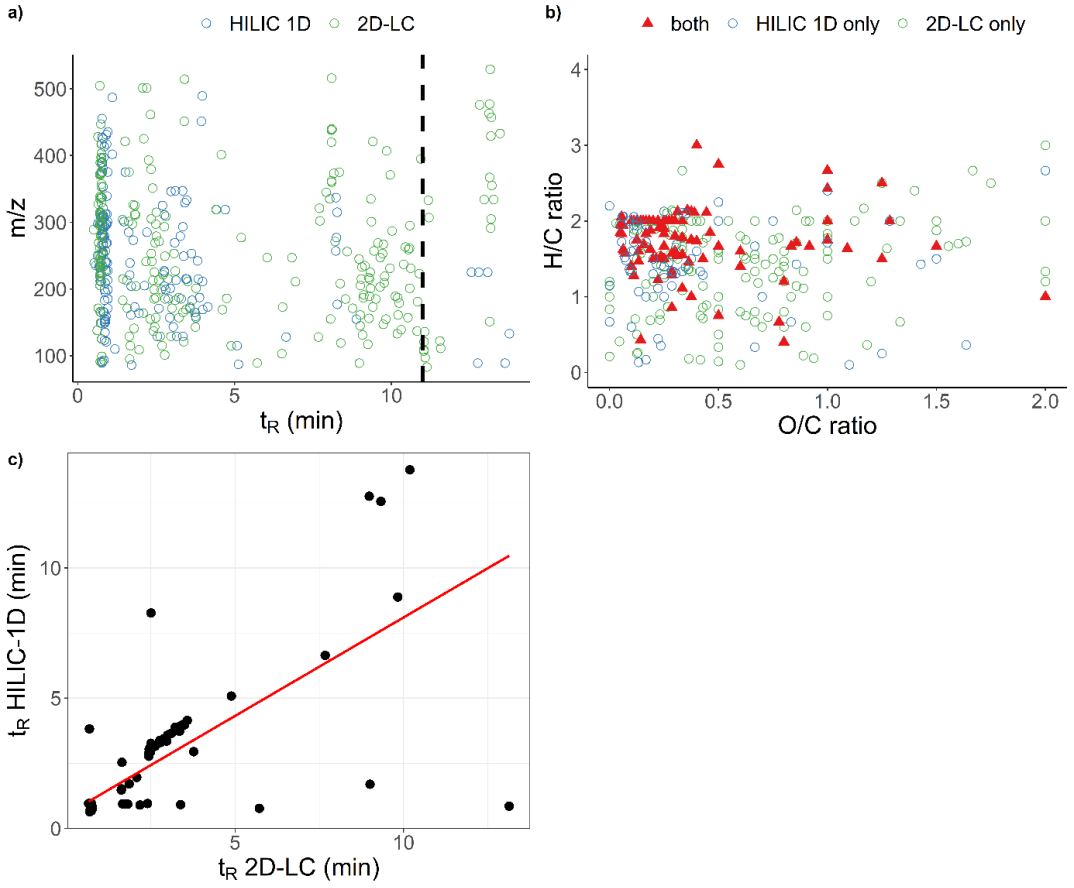

Figure 89: a) plot of *m/z* to retention time (t_R) of signals detected only in the one-dimensional HILIC method (blue) and only in the two-dimensional approach (green). The switch between the two dimensions is marked at the retention time of 11 minutes (black). b) Van-Krevelen plot of H/C to O/C ratios of all signals detected in the one-dimensional HILIC method (blue), 2D-LC method (green), and signals detected by both methods (red). c) Retention times of signals detected in both methods in the one-dimensional method (y-axis) and the 2D-LC (x-axis). The regression line (red) visualizes the shift of retention time in the two methods due to the higher delay time.

8.4 Conclusions

Environmental archives such as ice cores contain large amounts of organic compounds that provide information about climate changes in the past, which in turn contributes to understanding and predicting climate change in the present and future. Here we present a *q*2D-LC approach that can expand the amount of information obtained from NTS into a more comprehensive overview, while maintaining a simple instrumental setup and analysis time no longer than a one-dimensional HILIC measurement. NTS approaches are necessary to search for new target compounds and to get an overview of the chemical profile of the samples. However, the chromatographic resolution is a limiting factor, due to the one-dimensional functionalities of the stationary phase. In this *q*2D-LC, a second (orthogonal) stationary phase is introduced to cover compounds of different polarities. Here, the first dimension consists of a HILIC column and the second dimension of an RP column. The void volume of the HILIC column is collected in a sample loop, and while the HILIC column is running in re-equilibration settings,

the void volume is analyzed by the second dimension. In this way, all the information from the first dimension is preserved, and additional information on lower polarity compounds is provided, without increasing the run time. The transfer between the two dimensions was tested for linearity and repeatability, and detection limits were determined for a selection of several important atmospheric marker compounds. Linearity was evaluated using two void-volume marker compounds and proved sufficient. The repeatability ranged between 2.87% for *p*-hydroxybenzaldehyde and 24.28% for BTCA (relative standard deviations), while the detection limits were determined between 0.02 ng/mL for salicylic acid and 22.95 ng/mL for BTCA. Application to snow samples showed that *q*2D-LC increased the number of signals from the NTS and that chemical properties of the additional compounds on the second dimension matched their expected polarities. The one-dimensional HILIC method yielded 177 signals, 82 exclusively detected in this approach, while the *q*2D-LC method yielded a total of 270 signals, of which 175 were exclusively detected using the *q*2D-LC approach. Further evaluation of the retention times revealed that 23 of the additional signals were detected on the second dimension and therefore constitute the additional benefit of the developed *q*2D-LC method.

8.5 Application of *q*2D-LC to samples from Colle Gnifetti

The *q*2D-LC method described in chapter 8.1 to 8.4 was applied to thirty-three timely consecutive samples (with a gap between 1860 and 1924) from the Alpine ice core Colle Gnifetti as proof-of-principle for non-targeted and suspect-targeted analysis. To exclude contaminations from the sample containers and sample preparation, a process blank was measured that was stored and prepared according to the samples. 1.5 mL of thawed ice core samples (or Milli-Q water as blank solution) were evaporated under a stream of nitrogen and re-constituted in 200 µL of H_2O/ACN (1:1, v/v), before filtering and analysis by *q*2D-LC. Each sample was analyzed by threefold determination and further processed according to 8.2.3.3.

8.5.1 Non-target screening

The first part of non-targeted analysis aimed the elucidation of the general chemical composition. For that, mean-values of the threefold determinations were calculated and a process blank was subtracted to a minimum signal-to-noise ratio of 10 and a cutoff threshold of $1x10^7$. Signals with a retention time lower than one minute were excluded from analysis. All remaining sum formulas were checked for their chemical consistency by the seven golden rules filter from Fiehn Lab (Kind and Fiehn 2007). The number of remaining compounds was then compared to the mean value of all signal intensities (Figure 90). A trend of declining number of signals from the 1990s to the 1950s was observable, however, the mean signal intensity behaved differently. Here, the intensities were fluctuating between 1970 and 1995, and stable between 1930 and 1980, with a high peaking mean intensity in 1927. This indicates either an overall higher intensity of all signals, due to increased emissions or a number of signals with substantially high intensity due to a burning or other environmentally relevant event. A potential biomass burning event is supported by the peaking concentration of the lignin burning marker vanillic

acid in 1927 (see chapter 7.3.2 and Figure S 10) but could not be confirmed by the available fire records from Switzerland, as no increased number of fires was recorded in 1927 (Pezzatti et al. 2013). In the older samples, the highest number of signals was found in the sample from 1860 and lowest number in the older samples and overall, in 1844.

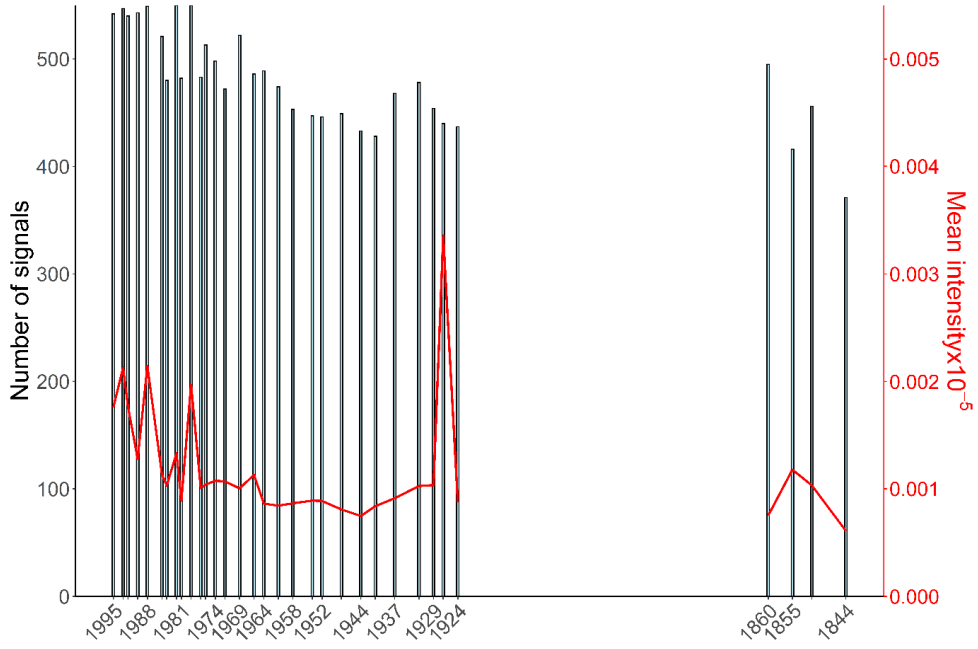

Figure 90: Number of signals from NTS in Colle Gnifetti ice core samples after blank subtraction and seven golden rules filtering (left axis) and mean intensity ($x10^{-5}$) of the signals (right axis). For better clarity, the standard deviation of mean signal intensity was not displayed.

For a better understanding of the chemical composition, the mean values of the OSc (Equation 13 and Equation 14), H/C, ratio and O/C ratio were calculated for all compounds detected in the respective samples (Figure 91). The OSc of compounds in samples from 1980-1990 was negative and showed a switch from positive to negative oxidation state in the middle of the 1970s. The OSc is calculated by the oxidation numbers of the carbon atoms in the molecule, which in turn depend on the amount of chemically bonded hydrogen and oxygen and the resulting the partial negative charging of the carbon atoms. Therefore, a higher OSc indicates lower degree of oxidation of the molecules in older samples, which is supported by the mean H/C and O/C ratios. The H/C ratio showed a strong decrease between 1930 to 1920, hence the overall degree of saturation decreased. However, this was not induced by a higher ratio of oxygen, since the O/C ratio did not show a similarly clear trend. This indicates either a lower oxidation strength of the atmosphere or an increased number of anthropogenic atmospheric contaminations introducing other heteroatoms like sulfur or nitrogen. Highest amount of oxygen was found in the samples from 1972 and 1984. The increased oxygen ratio is consistent with higher overall oxidation states in these samples. Temperature records from Colle Gnifetti showed a change from negative to positive mean temperature consistent with the observed changing of the OSc and the mean temperature over Europe showed an increase of the temperature from the 1980s on that is similar to the

increased average O/C ratio (Stocker et al. 2013; Brugger et al. 2021). In addition, records of black carbon and spheroidal carbonaceous particles from fossil fuel combustion showed a strong increase between approximately 1920 to 1990 (Brugger et al. 2021). These anthropogenic emissions from fossil burning strongly contribute to the overall chemical composition of the atmosphere and hence SOA formation and aging that was also confirmed by the NTS data from Colle Gnifetti.

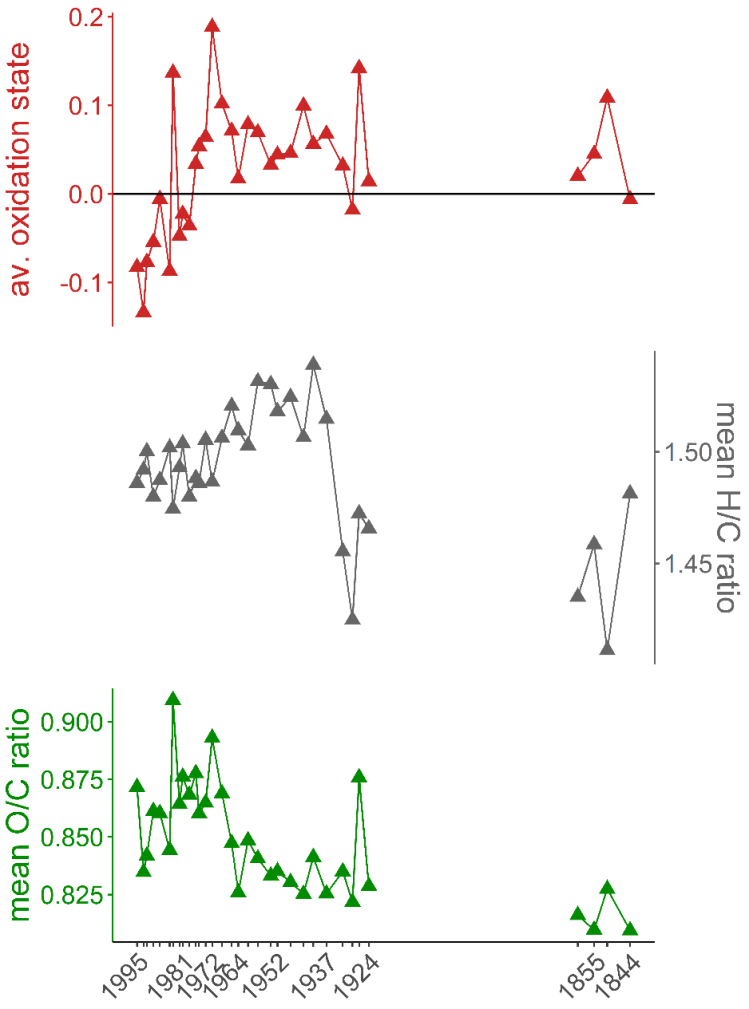

Figure 91: Mean values of O/C ratio (green), H/C ratio (grey) and average oxidation state (red) of all signals from NTS of Colle Gnifetti ice core samples over time.

The second part of NTS focused on the identification of environmentally relevant compounds which in conclusion could be added to the targeted analysis in the future. For that, compounds were prioritized by PCA and the highest weighing on PC1 to PC5 (Table S 6). With this analysis, 19 compounds were selected and plotted in a biplot to elucidate their influence on the sample variance (Figure 92). This biplot confirmed the sample from 1929 as a significant outlier, that was also grouped individually by k-means clustering. The strongest loadings on this sample were represented by the compounds with the molecular formulas $C_5H_7NO_3$, $C_6H_6N_2O_2$ and $C_9H_{10}NO_4$, all of which consist of the general molecular formula $C_xH_yN_zO_i$. The abundance of CHON species is mainly controlled by the concentration of NO_x

in the atmosphere at daytime, which is in turn influenced by anthropogenic emissions, like gas-phase ammonia from agricultural activities (O'Brien et al. 2013; Kourtchev et al. 2014).

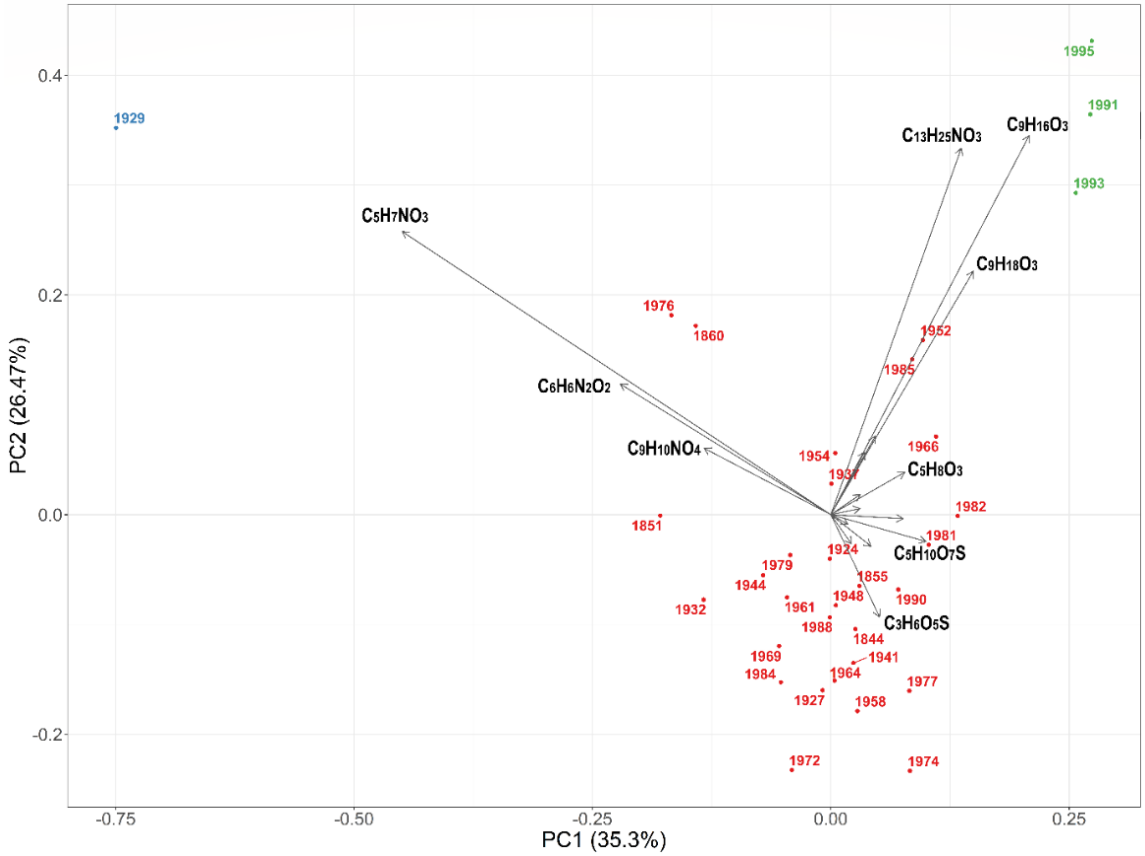

Figure 92: Biplot of principal component analysis of prioritized compounds (see Table S 6). Samples were grouped by k-means analysis and highest loadings on PC1 and PC2 were labelled.

The second group consisted of samples from 1991, 1993 and 1995, and here the highest loadings were represented by the compounds with molecular formulas $C_{13}H_{25}NO_3$, $C_9H_{16}O_3$ and $C_9H_{18}O_3$. Database search associated the $C_{13}H_{25}NO_3$ compound with amide functionalities, while most of the possible chemical structures of $C_9H_{16}O_3$ and $C_9H_{18}O_3$ contained a carboxylic acid functionality. One possible structure of $C_9H_{18}O_3$ is hydroxynonanoic acid, which is a known biotransformation product of oleic acid, which is a homologue of the fatty acids lauric acid, myristic acid and palmitic acid that are associated with sea spray emissions. However, correlation analysis of the three fatty acids with the probable transformation product of oleic acid did not show significant correlation coefficients. The third and largest group contained all remaining samples and was mostly subjected to compounds containing sulfur like $C_3H_6O_5S$ and $C_5H_{10}O_7S$, both of which contain sulfonic acid functionalities. According to high loadings of CHON and CHONS compounds, PC2 was summarized as anthropogenic emissions.

Correlation analysis of the prioritized compounds with the known target compounds showed a strong correlation of $C_3H_6O_5S$ and $C_5H_{10}O_7S$ with trans-1,2-cyclohexanedicarboxylic acid, MBTCA, terebic acid, methylphthalic acid, and phthalic acid (Table 14), a combination of markers for aerosol aging and anthropogenic SOA markers. Five further compounds showed significant correlation to target analytes,

mainly between biogenic and anthropogenic SOA markers to sulfur-containing compounds. The compound $C_3H_4O_4$ showed similar correlations to anthropogenic and biogenic SOA markers and database search assigned one structure of this molecular formula to malonic acid, which was already detected in PM2.5 collected in Singapore (Yang and Yu 2008). The compounds $C_5H_8O_3$ and $C_6H_{10}O_3$ are correlating with S-group lignin markers, the sum of LOPs, and aerosol aging markers (BTCA and MBTCA). Since here first data on polymeric lignin in aerosols is presented and the source of polymeric lignin in the atmosphere is not elucidated, a clear conclusion could not be drawn from these observations.

Table 14: Results of correlation analysis of prioritized NTS compounds with target compounds. Correlations were classified as significant when $R \geq |0.7|$ and $p<0.05$.

	$C_3H_4O_4$	**$C_3H_6O_5S$**	**$C_4H_{10}O_5S$**	**$C_5H_{10}O_7S$**	**$C_5H_{12}O_7S$**	**$C_5H_8O_3$**	**$C_6H_{10}O_3$**
S-Group							0.8
LOPs						0.7	0.7
BTCA		0.7	0.8				0.7
Cyclohexane-dicarboxylic acid	0.7	0.8	0.8	0.8	0.7		
MBTCA	0.9	0.7	0.7	0.8	0.8		0.7
Terebic acid	0.7	0.7	0.7	0.8	0.7		
Methylphthalic acid	0.8	0.7	0.7	0.7	0.8		
Lauric acid						-0.7	-0.7
Phthalic acid	0.9	0.7	0.7	0.8	0.8		

The prioritized compounds were subjected to hierarchical clustering analysis. Here, the sample from 1929 was an outlier, and clustering of the remaining samples did not change significantly to the k-means clustering in the PCA biplot. The compounds on the other hand were clustered according to their elemental composition. Sulfur-containing compounds were clustered on the left and were responsible for distinction of two main groups of samples, from old to young. Nitrogen-containing compounds were clustered and clustering was consistent with the observations from the PCA analysis, as they were the unique feature of the sample from 1929 (Figure 93). Although both elemental compositions, CHON and CHONS are associated with anthropogenic emissions, here these compounds are clearly distinguished by the clustering. Different sources for nitrogen-containing contaminants, most probable from agricultural emissions, and sulfur-containing contaminants from fossil fuel burning were indicated (Surratt et al. 2008; Kourtchev et al. 2014). The compound assigned to malonic acid was here clustered with sulfur-containing compounds and therefore constitutes a promising candidate for anthropogenic

SOA emissions, for which analytical standards are available, complementary to organosulfate compounds.

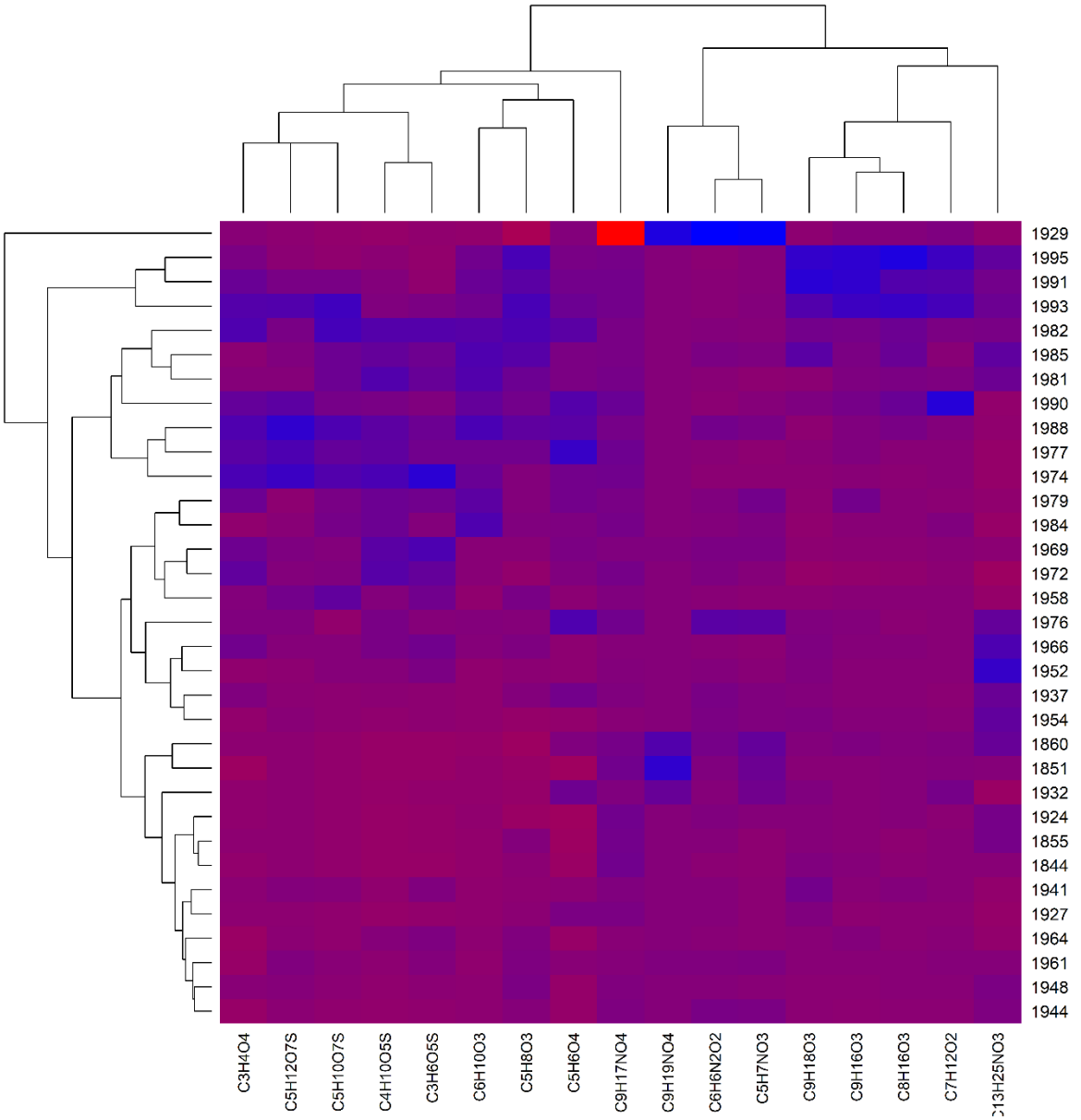

Figure 93: Hierachical clustering of significant compounds from principal component analysis in Colle Gnifetti ice core samples with column-wise color scaling.

8.5.2 Suspect-target screening

Data from NTS was searched for suspected target compounds for which no analytical standards are available. The suspect-target lists contained products from dimerization of atmospheric organic compounds (Table S 7), organosulfates (Table S 8) and sesquiterpene oxidation markers (Table S 9). The *m/z* values of the dimerization markers did not show peaks of significant height and S/N ratio in the chromatograms after blank subtraction. Two *m/z* values from the organosulfate suspect list were detected and quantified using camphorsulfonic acid as a surrogate standard compound (Kristensen and Glasius 2011), one of which was already included in the prioritized NTS compound list. In addition, the

m/z value associated to *β*-caryophyllinic acid, a sesquiterpene oxidation marker, was detected and quantified using ketopinic acid as a surrogate standard compound. For all compounds, an enrichment factor of 7.5 was considered due to the evaporation of 1.5 mL sample solution and re-constitution in 200 µL of solvent. The two organosulfate species showed comparable fluctuations in the younger sample from the 1970s on. The species of *m/z* 154.9660 ($C_2H_4O_6S$) is proposed in the literature either as an adduct between glyoxal and sulfuric acid (Surratt et al. 2008) or as glycolic acid sulfate (Olson et al. 2011). However, in both laboratory experiments it was exclusively yielded from isoprene derived SOA. Between 1932 and 1969, a constant low concentration was found while from 1969 to 1995 strong deviations with maximum concentrations in 1972, 1979, 1984, and 1990. The species of *m/z* 213.066 ($C_5H_{10}O_7S$) showed generally higher variations in the historic record with a maximum concentration in 1974 (Figure 94). The suggested precursor for this compound is isoprene and it was the most abundant compound in tropospheric aerosols analyzed by on-line single particle MS (Froyd et al. 2010; Kristensen and Glasius 2011). In laboratory experiments it was detected in the photooxidation of isoprene under low NO_x concentration in the presence of acidified sulfate seed aerosol (Surratt et al. 2008). A strong correlation of organosulfate abundance and the presence of MBTCA is described in the literature, indicating that photochemical aging of aerosols is an important process in organosulfate formation. In addition, the abundance of anthropogenic pollutants in the atmosphere (NO_x or SO_2) has an influence the abundance of organosulfates as NO_X controls the formation of first order isoprene oxidation products and SO_2 is the main source of sulfur in the atmosphere (Kourtchev et al. 2014; Wang et al. 2020c; Bryant et al. 2021). This is consistent with the correlation of $C_5H_{10}O_7S$ with MBTCA found in Colle Gnifetti. In addition, the correlation of $C_5H_{10}O_7S$ with phthalic acid and methylphthalic acid was conclusive as it represents a connection between isoprene derived organosulfate abundance and anthropogenic emission. Here, seasonal ice core samples would be useful for proof-of-principle analysis, as the anthropogenically dependent organosulfate formation shows a strong seasonality, that was not yet recovered from climate archives (Wang et al. 2020c).

For the species of *m/z* 253.1445 ($C_{14}H_{22}O_4$), associated with *β*-caryophillinic acid a significantly increasing concentration was observable starting in the sample from 1988 until 1955, to a concentration ten times higher after 1988 than before (Figure 94). Caryophyllene is one of the most abundant sesquiterpene and in laboratory oxidation experiments *β*-caryophillinic acid, *β*-nocaryophillinic acid and *β*-caryophillonic acid were produced, however *β*-caryophillonic acid was not included here due to its significantly lower abundance by comparison (Helmig et al. 2006, 2007; van Eijck et al. 2013). *β*-caryophillinic acid and *β*-nocaryophillonic acid were detected in ambient air samples from Finland, PM2.5 samples from the USA and marine aerosols over the Arctic ocean (Jaoui et al. 2007; Fu et al. 2013; van Eijck et al. 2013). However, the lack of available analytical standards impedes the quantitative analysis and can only be circumvented by organic synthesis of the oxidation products (van Eijck et al. 2013) or the use of surrogate standards like pinic acid (Jaoui et al. 2007). The semi-quantitative presented data from Colle Gnifetti is consistent with a study from Belukha ice core from the Altai

mountain range, where β-caryophillinic acid concentration was measured using synthesized standards and ranged between 0.004 ng/g and 0.103 ng/g ice under the assumption that one milliliter of frozen ice core sample equals one gram of frozen ice (Zuth 2018). In contrast, the study from Belukha ice core observed a correlation of the sesquiterpene marker with α-pinene oxidation products, which was not found in Colle Gnifetti due to the different sources of organic material in a remote ice core and an Alpine ice core. Sesquiterpene emissions increase with elevated ambient temperature, which was confirmed by increasing ambient β-caryophillinic acid in PM2.5 samples and is consisting with the presented results, as temperature records from Colle Gnifetti and the mean temperature on the European continent show rising temperatures at the end of the 20th century similarly to the recorded β-caryophillinic acid concentration (Helmig et al. 2006, 2007; Jaoui et al. 2007; Stocker et al. 2013; Brugger et al. 2021).

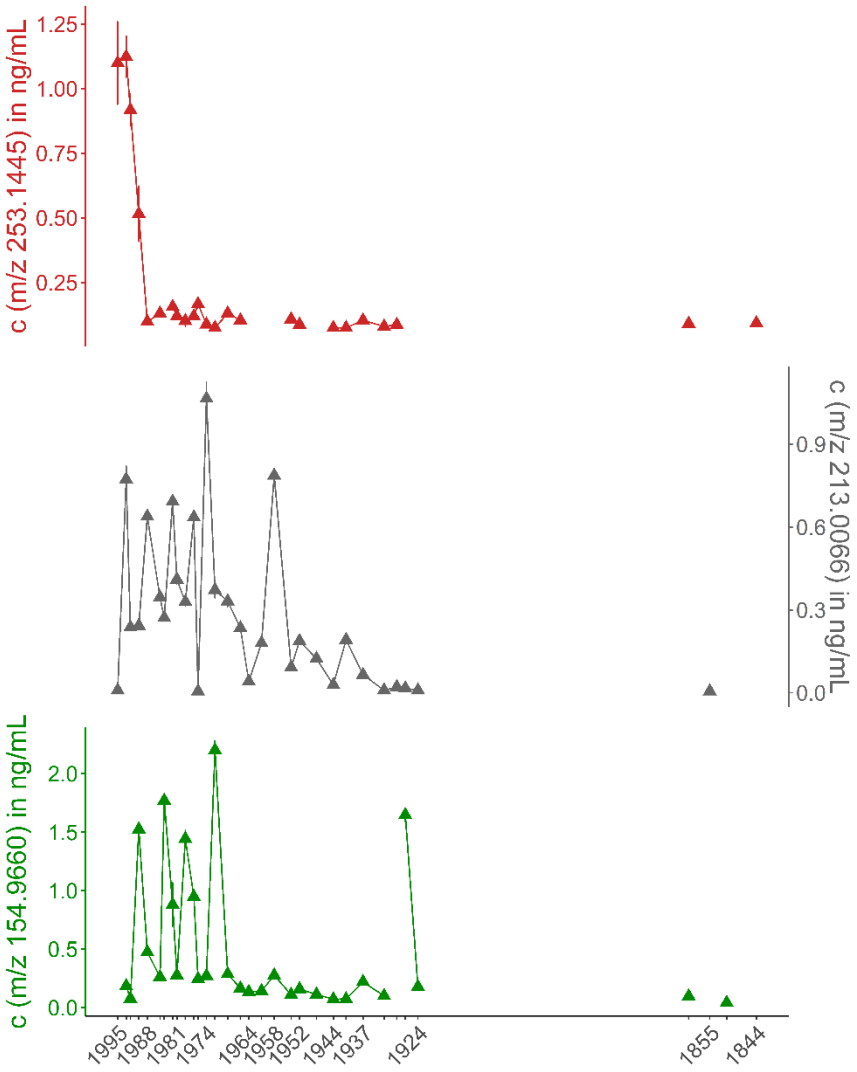

Figure 94: Historic records of compounds detected in suspect-target screening of Colle Gnifetti ice core samples. Two organosulfate compounds *m/z* 154.9660 (green) and *m/z* 213.0066 (grey) were detected as well the *m/z* value associated with β-caryophyllinic acid (*m/z* 253.1445, red). Semi-quantitative data in ng/mL was obtained by calibration and quantification with surrogate standard compounds (camphorsulfonic acid and ketopinic acid).

8.5.3 Conclusion

The application of the developed *q*2D-LC method to samples from Alpine ice core Colle Gnifetti addressed two key goals. First, the chemical composition of the samples over time was elucidated to detect significant changes and associate them to changing temperature or anthropogenic activity. The second part aimed the determination of prospective SOA markers as target compounds. As first proof-of-principle, different number of signals, as well as different mean intensities were determined in the data from NTS. Here, the sample from 1927 showed a strongly increased mean intensity while number of signals was consistent. A connection to a biomass burning event was proposed, as also the lignin burning marker vanillic acid showed a peaking concentration in this sample. However, lack of data from the literature of that time did not allow to draw final conclusions. The chemical composition of the samples was further studied by the historic records of the mean OSc, mean H/C ratio and mean O/C ratio. A behavior corresponding to temperature change, increased black carbon emission, and increased carbonaceous particle emissions was confirmed by the literature.

The second part of the analysis focused on a prioritization of compounds for further investigation. Therefore, a PCA was conducted and based on the loadings on PC1-PC5 nineteen compounds remained. Among those compounds the group of CHON had a strong impact on the sample from 1929 suggesting a high NO_x concentration in the atmosphere at that time. PC1 described 35.3% of the total variance but could not be assigned to certain effects. PC2 described 26.5% of the total variance and was summarized as anthropogenic emission factors, since it was primarily loaded by CHON and CHONS compounds. Correlation analysis of NTS compounds with target compounds revealed correlation of CHOS compounds with anthropogenic markers and markers of SOA aging like MBTCA. Hierarchical clustering, using only previously prioritized compounds showed a clear distinction between CHON and CHOS compounds, so even though the abundance of both groups is controlled by anthropogenic emissions, a further discrimination was indicated proposedly an agricultural origin of CHON compounds and fossil fuel burning as the main driver of CHOS abundance.

STS included a list of dimers, organosulfates and sesquiterpene markers. Only two organosulfates were detected and one sesquiterpene marker. All STS compounds were semi-quantified using surrogate standard compounds. Both isoprene derived organosulfates were correlating with anthropogenic SOA markers and MBTCA, as indicated by the literature their abundance was controlled by SOA aging and the presence of anthropogenic pollutants in the atmosphere. *β*-caryophillinic acid was detected in similar concentrations as a previous ice core study from Belukha glacier and a significant concentration shift was confirmed by temperature records because sesquiterpene emission increased with rising temperature.

In the future, more and older samples should be analyzed to observe clearer trends in the historic records and to compare the records with available data on biomass burning from Europe. In addition, a sample preparation step could be included to detect lower concentrations of compounds. However, this sample

preparation should cover a broad range of analytes, otherwise the benefit of the *q*2D-LC method is neglected. Promising candidates like malonic acid, where analytical standards are available, could be added to the target analysis.

9. Conclusions and Outlook

In this work, different highly sensitive and selective methods for trace analysis of organic marker species in different climate archives were developed using UHPLC-ESI-HRMS. The degradation of polymeric lignin in speleothems was optimized following the principles of "Green Chemistry", by replacing the reaction-catalyzing reagent CuO with soluble $CuSO_4$ and thereby strongly decreasing the amount of chemicals, solvents, and waste. The comparison of both methods showed similar lignin concentration and composition, but the evaluation of possible side reactions, contaminations, and batch-to-batch variability yielded better performance of the $CuSO_4$ oxidation approach. In addition, a method for the analysis of levoglucosan in speleothems was developed, to evaluate the influence of paleo-fire events on the vegetation. A HILIC method was used to separate levoglucosan from the isomers galactosan and mannosan, evaluating different buffers, temperatures and pH values. An additional alkaline post-column flow supported the deprotonation of levoglucosan and strongly improved the sensitivity of the method. In the future, the extraction and enrichment of levoglucosan in speleothems should be improved for example by liquid-liquid extraction with the dissolved speleothem solution or solid-liquid extraction with organic solvents. Application of the methods to flowstone samples from Daves Cave and Waipuna Cave in New Zealand showed that lignin abundance was changing during wet and dry periods, hence different transport mechanisms of lignin through the soil depending on the amount of precipitation were postulated. During drier conditions, lignin was predominantly transported by adsorption to soil particles, while increased precipitation resulted in dominantly aqueous transfer. Further studies should be conducted to support these observations and to investigate lignin alteration depending on the transport mechanism. Levoglucosan showed a correlation to the C/V ratio of lignin, hence to non-wooden vegetation of higher flammability, which was conclusive and demonstrating the suitability of levoglucosan as a biomass burning marker in speleothems. The data from the two analyzed flowstones did not provide useful information on the transport of levoglucosan through the soil and further studies should be conducted comparing the levoglucosan concentration and isomer ratio in different depths of the soil and drip water. The inclusion mechanisms of both proxies into growing speleothems should be evaluated in artificial cave setups to elucidate the influence of crystal formation and prior calcite precipitation on the levoglucosan and lignin concentration in speleothems.

A first non-targeted study on the chemical composition of aerosols in Waipuna Cave was conducted to evaluate atmospheric aerosols as a source of organic compounds in speleothems and different sampling methods as surrogate surfaces of speleothems. Aerosols were sampled on filter, water, plastic, and glass surfaces and filter sampling proved most efficient. Plotting in van Krevelen diagrams and hierarchical clustering revealed a correlation of the aerosol load with cave ventilation and a dependency to the location in the cave. Three different classes of aerosol sources were postulated: externally introduced aerosols, aerosols related to human activity and "caveborne" aerosols. Externally introduced aerosols by cave ventilation and anthropogenically introduced aerosols were the main sources of the detected

organic compounds. A suspect-target screening revealed the presence of environmentally relevant contaminants, which were assigned to surfactants, insecticides, biomarkers, and amino acids connected to human breath, consumer products, or the human metabolism. Further aerosol studies should be conducted at the same cave site and compounds of significant intensity should be evaluated in the outer layers of growing speleothems to evaluate the relevance of organic aerosols as a source of organic compounds in speleothems.

For organic trace analysis in ice cores, two LC methods (HILIC and reversed-phase) were developed to analyze a broad range of analytes of different polarities and functionalities. The separation of initially present lignin oxidation products, which are also representative for lignin burning, from polymeric lignin was realized by two consecutive extractions. Here, the lignin degradation approach was successfully adapted from speleothem to ice core samples. Several solid-phase functionalities were evaluated for the enrichment of small, polar compounds like levoglucosan, erythritol, mannitol, or xylitol. Finally, those compounds were accessible by centrifugal evaporation. Application of the methods on samples from Alpine glacier Colle Gnifetti showed a good correlation of monoterpene derived SOA markers among each other and a correlation of monoterpene with anthropogenically derived SOA markers, indicating a connection between anthropogenic pollutants in the atmosphere and aerosol aging. Furthermore, a temperature dependency of monoterpene and isoprene oxidation was revealed. The historic trend of Lev was consistent with fire records from Southern Switzerland, showing an increased concentration in 1937, where a strongly increased number of fires was recorded. Other observations were peaking concentrations of monoterpene markers in 1974, another year of high fire frequency, which was associated to an increased monoterpene oxidation due to the high temperature from the burning. First data on polymeric lignin in ice core samples was presented and confirmed the potential of lignin as a vegetation marker in ice cores. The data was consistent with the literature displaying an increased LOP concentration along with increased forest cover in the Alps, as well as in increase of beech species in the forests, that was observable in an increasing S/V ratio from older to younger samples.

Suspect- and non-target screening is an important analytical tool to elucidate the chemical profile of samples and to detect novel marker compounds. Suchlike screening approaches were aimed for the analysis of the Colle Gnifetti ice core samples. Since the chromatography is the limiting factor when aiming a comprehensive overview of all organic compounds, a 2D-LC method was developed consisting of two chromatographic columns with orthogonal functionalities. In this method, the void volume of the HILIC column in the first dimension was transferred to the second dimension consisting of a PFP column with reversed-phase functionality. The new method yielded a higher number of signals in representative fresh snow samples from *Jungfraujoch* without increasing the duration of the method and was applied for NTS and STS of organic compounds in Colle Gnifetti ice core samples. In the historic records, NTS revealed the presence of multiple CHON and CHONS compounds among others that were correlated to aerosol aging markers like MBTCA and markers for anthropogenic emissions like phthalic acid, indicating the necessity of atmospheric pollutants in the atmosphere and aerosol aging for the

presence of organosulfates and organonitrates in the atmosphere. Analysis by hierarchal clustering and PCA showed an overall grouping of samples per age and a distinction of CHON and CHONS compounds though both emerge from the reactions of SOA with anthropogenic pollutants during aerosol aging. In addition, NTS aimed the detection of novel target compounds. Here, malonic acid was found a promising marker, where analytical standards are available, that was correlating with organosulfates. In STS for organosulfates, dimers, and sesquiterpene oxidation markers, two organosulfates as well as one sesquiterpene marker were detected and semi-quantified with surrogate standard compounds. The analyzed sesquiterpene oxidation marker showed comparable concentration to a previous study conducted on samples from Belukha glacier from the Altai Mountain range in Siberia.

In the future, the novel trace analysis approaches and non-target screening methods will be applied to samples from Belukha ice core in Siberia to compare the concentration and progress of the marker compounds and the chemical profiles in remote regions and regions which are strongly influenced by agricultural and industrial emissions. Thereby, the data from Colle Gnifetti represents environmental and climate changes on a regional scale, while samples from Belukha will be used to assess these effects on a global scale. Furthermore, available chiral separation techniques could be used to distinguish between different isomers of the target compounds to assign them to natural or anthropogenic emissions based on the enantiomeric ratio. The influence of freezing and re-freezing of samples during transportation and storage on the analyte concentration should be evaluated to prevent misinterpretation of the data. NTS and STS will be continued using the developed *q*2D-LC approach. Malonic acid should be included into the target analysis as a compound correlating with organosulfates. Sample preparation techniques could be introduced here, however an enrichment of a broad range of analytes is necessary to exploit the full advantage of the *q*2D-LC method, which already proved difficult for the target analysis.

10. References

Abbott PM, Plunkett G, Corona C, et al (2021) Cryptotephra from the Icelandic Veiðivötn 1477 CE eruption in a Greenland ice core: Confirming the dating of volcanic events in the 1450s CE and assessing the eruption's climatic impact. Clim Past 17:565–585. https://doi.org/10.5194/cp-17-565-2021

Abegg M, Brändli U, Cioldi F, et al (2020) Schweizerisches Landesforstinventar LFI. Ergebnistabellen und Karten der LFI-Erhebungen 1983–2017 (LFI1, LFI2, LFI3, LFI4). http://www.lfi.ch/resultate/. Accessed 2 Feb 2022

Alpert AJ (1990) Hydrophilic-interaction chromatography for the separation of peptides, nucleic acids and other polar compounds. J Chromatogr A 499:177–196. https://doi.org/10.1016/S0021-9673(00)96972-3

Alvarez-Segura T, Torres-Lapasió JR, Ortiz-Bolsico C, García-Alvarez-Coque MC (2016) Stationary phase modulation in liquid chromatography through the serial coupling of columns: A review. Anal Chim Acta 923:1–23. https://doi.org/10.1016/j.aca.2016.03.040

Alygizakis N (2018) S23 | EIUBASURF | Surfactant Suspect List from EI and UBA. https://doi.org/10.5281/ZENODO.2648765

Alygizakis NA, Samanipour S, Hollender J, et al (2018) Exploring the Potential of a Global Emerging Contaminant Early Warning Network through the Use of Retrospective Suspect Screening with High-Resolution Mass Spectrometry. Environ Sci Technol 52:5135–5144. https://doi.org/10.1021/acs.est.8b00365

Amad MH, Cech NB, Jackson GS, Enke CG (2000) Importance of gas-phase proton affinities in determining the electrospray ionization response for analytes and solvents. J Mass Spectrom 35:784–789. https://doi.org/10.1002/1096-9888(200007)35:7<784::AID-JMS17>3.0.CO;2-Q

Anastasio C, McGregor KG (2001) Chemistry of fog waters in California's Central Valley: 1. In situ photoformation of hydroxyl radical and singlet molecular oxygen. Atmos Environ 35:1079–1089. https://doi.org/10.1016/S1352-2310(00)00281-8

Andersson-Sköld Y, Simpson D (2001) Secondary organic aerosol formation in northern Europe: A model study. J Geophys Res Atmos 106:7357–7374. https://doi.org/10.1029/2000JD900656

Andreae MO, Jones CD, Cox PM (2005) Strong present-day aerosol cooling implies a hot future. Nature 435:1187–1190. https://doi.org/10.1038/nature03671

Andreae MO, Rosenfeld D, Artaxo P, et al (2004) Smoking Rain Clouds over the Amazon. Science (80-) 303:1337–1342. https://doi.org/10.1126/science.1092779

Angelis MD, Traversi R, Udisti R (2012) Long-term trends of mono-carboxylic acids in Antarctica: comparison of changes in sources and transport processes at the two EPICA deep drilling sites. Tellus B Chem Phys Meteorol 64:17331. https://doi.org/10.3402/tellusb.v64i0.17331

Antignac JP, De Wasch K, Monteau F, et al (2005) The ion suppression phenomenon in liquid chromatography-mass spectrometry and its consequences in the field of residue analysis. Anal Chim Acta 529:129–136. https://doi.org/10.1016/j.aca.2004.08.055

Arakaki T, Faust BC (1998) Sources, sinks and mechanisms of hydroxyl radical (OH) photoproduction and consumption in authentic acidic continental cloud waters from Whiteface Mountain, New York: the role of Fe(r) (r=II, III) photochemical cycle. J Geophys Res Atmos 103:3487–3504. https://doi.org/10.1029/97JD02795

Arakaki T, Kuroki Y, Okada K, et al (2006) Chemical composition and photochemical formation of hydroxyl radicals in aqueous extracts of aerosol particles collected in Okinawa, Japan. Atmos Environ 40:4764–4774. https://doi.org/10.1016/j.atmosenv.2006.04.035

Arangio AM, Slade JH, Berkemeier T, et al (2015) Multiphase chemical kinetics of OH radical uptake by molecular organic markers of biomass burning aerosols: Humidity and temperature dependence, surface reaction, and bulk diffusion. J Phys Chem A 119:4533–4544. https://doi.org/10.1021/jp510489z

Arndt S, Jørgensen BB, LaRowe DE, et al (2013) Quantifying the degradation of organic matter in marine sediments: A review and synthesis. Earth-Science Rev 123:53–86. https://doi.org/10.1016/J.EARSCIREV.2013.02.008

Atkinson R (2007) Rate constants for the atmospheric reactions of alkoxy radicals: An updated estimation method. Atmos Environ 41:8468–8485. https://doi.org/10.1016/j.atmosenv.2007.07.002

Atkinson R, Arey J (2003) Gas-phase tropospheric chemistry of biogenic volatile organic compounds: a review. Atmos Environ 37:197–219. https://doi.org/10.1016/S1352-2310(03)00391-1

Augustin L, Barbante C, Barnes PRF, et al (2004) Eight glacial cycles from an Antarctic ice core. Nature 429:623–628. https://doi.org/https://doi.org/10.1038/nature02599.

Badino G (2004) Clouds in caves. Speleogenes Evol Karst Aquifers 2:1–8

Baduel C, Nozière B, Jaffrezo JL (2012) Summer/winter variability of the surfactants in aerosols from Grenoble, France. Atmos Environ 47:413–420. https://doi.org/10.1016/j.atmosenv.2011.10.040

Bahri H, Dignac M-F, Rumpel C, et al (2006) Lignin turnover kinetics in an agricultural soil is monomer specific. Soil Biol Biochem 38:1977–1988. https://doi.org/10.1016/j.soilbio.2006.01.003

Baldini JUL, Lechleitner FA, Breitenbach SFM, et al (2021) Detecting and quantifying palaeoseasonality in stalagmites using geochemical and modelling approaches. Quat Sci Rev 254:. https://doi.org/10.1016/j.quascirev.2020.106784

Barbante C, Schwikowski M, Döring T, et al (2004) Historical record of European emissions of heavy metals to the atmosphere since the 1650s from alpine snow/ice cores drilled near Monte Rosa. Environ Sci Technol 38:4085–4090. https://doi.org/10.1021/es049759r

Barbaro E, Kirchgeorg T, Zangrando R, et al (2015) Sugars in Antarctic aerosol. Atmos Environ 118:135–144. https://doi.org/10.1016/j.atmosenv.2015.07.047

Barhdadi S, Moens G, Canfyn M, et al (2021) Impact of the Revised European Tobacco Product Directive on the Quality of E-cigarette Refill Liquids in Belgium. Nicotine Tob Res 23:227–234. https://doi.org/10.1093/ntr/ntaa023

Barsanti KC, Pankow JF (2004) Thermodynamics of the formation of atmospheric organic particulate matter by accretion reactions - Part 1: Aldehydes and ketones. Atmos Environ 38:4371–4382. https://doi.org/10.1016/j.atmosenv.2004.03.035

Bashir MEH, Lui JH, Palnivelu R, et al (2013) Pollen Lipidomics: Lipid Profiling Exposes a Notable Diversity in 22 Allergenic Pollen and Potential Biomarkers of the Allergic Immune Response. PLoS One 8:1–23. https://doi.org/10.1371/journal.pone.0057566

Bateman KP, Kellmann M, Muenster H, et al (2009) Quantitative-Qualitative Data Acquisition Using a Benchtop Orbitrap Mass Spectrometer. J Am Soc Mass Spectrom 20:1441–1450. https://doi.org/10.1016/j.jasms.2009.03.002

Bauer H, Claeys M, Vermeylen R, et al (2008) Arabitol and mannitol as tracers for the quantification of airborne fungal spores. Atmos Environ 42:588–593. https://doi.org/10.1016/j.atmosenv.2007.10.013

Bauer SE, Menon S (2012) Aerosol direct, indirect, semidirect, and surface albedo effects from sector contributions based on the IPCC AR5 emissions for preindustrial and present-day conditions. J Geophys Res 117:1–15. https://doi.org/10.1029/2011JD016816

Bebi P, Seidl R, Motta R, et al (2017) Changes of forest cover and disturbance regimes in the mountain forests of the Alps. For Ecol Manage 388:43–56. https://doi.org/10.1016/j.foreco.2016.10.028

Beck M, Hoffmann T (2016) A detailed MSn study for the molecular identification of a dimer formed from oxidation of pinene. Atmos Environ 130:120–126. https://doi.org/10.1016/j.atmosenv.2015.09.012

Bell D, Wu C, Bertrand A, et al (2021) Particle-phase processing of α-pinene NO_3 secondary organic aerosol in the dark. Atmos Chem Phys Discuss 1–28. https://doi.org/10.5194/acp-2021-379

Benner R, Kaiser K (2012) Characterization of Lignin by Gas Chromatography and Mass Spectrometry Using a Simplified CuO Oxidation Method. Anal Chem 84:459–464. https://doi.org/dx.doi.org/10.1021/ac202004r

Benson DR, Yu JH, Markovich A, Lee SH (2011) Ternary homogeneous nucleation of H2SO4, NH 3, and H2O under conditions relevant to the lower troposphere. Atmos Chem Phys 11:4755–4766. https://doi.org/10.5194/acp-11-4755-2011

Bernstein JA, Alexis N, Barnes C, et al (2004) Health effects of air pollution. J Allergy Clin Immunol 114:1116–1123. https://doi.org/10.1016/j.jaci.2004.08.030

Bhattarai H, Saikawa E, Wan X, et al (2019) Levoglucosan as a tracer of biomass burning: Recent progress and perspectives. Atmos Res 220:20–33. https://doi.org/10.1016/j.atmosres.2019.01.004

Bianchi F, Tröstl J, Junninen H, et al (2016) New particle formation in the free troposphere: A question of chemistry and timing. Science (80-) 352:1109–1112. https://doi.org/10.1126/science.aad5456

Blyth AJ, Asrat A, Baker A, et al (2007) A new approach to detecting vegetation and land-use change using high-resolution lipid biomarker records in stalagmites. Quat Res 68:314–324. https://doi.org/10.1016/j.yqres.2007.08.002

Blyth AJ, Baker A, Collins MJ, et al (2008) Molecular organic matter in speleothems and its potential as an environmental proxy. Quat Sci Rev 27:905–921. https://doi.org/10.1016/j.quascirev.2008.02.002

Blyth AJ, Baker A, Thomas LE, Van Calsteren P (2011) A 2000-year lipid biomarker record preserved in a stalagmite from north-west Scotland. J Quat Sci 26:326–334. https://doi.org/10.1002/jqs.1457

Blyth AJ, Farrimond P, Jones M (2006) An optimised method for the extraction and analysis of lipid biomarkers from stalagmites. Org Geochem 37:882–890. https://doi.org/10.1016/j.orggeochem.2006.05.003

Blyth AJ, Hartland A, Baker A (2016) Organic proxies in speleothems – New developments, advantages and limitations. Quat Sci Rev 149:1–17. https://doi.org/10.1016/j.quascirev.2016.07.001

Blyth AJ, Watson JS (2009) Thermochemolysis of organic matter preserved in stalagmites: A preliminary study. Org Geochem 40:1029–1031. https://doi.org/10.1016/j.orggeochem.2009.06.007

Boerjan W, Ralph J, Baucher M (2003) Lignin Biosynthesis. Annu Rev Plant Biol 54:519–546. https://doi.org/10.1146/annurev.arplant.54.031902.134938

Bond TC, Streets DG, Yarber KF, et al (2004a) A technology-based global inventory of black and organic carbon emissions from combustion. J Geophys Res Atmos 109:1–43. https://doi.org/10.1029/2003JD003697

Bond WJ, Dickinson KJM, Mark AF (2004b) What limits the spread of fire-dependent vegetation? Evidence from geographic variation of serotiny in a New Zealand shrub. Glob Ecol Biogeogr 13:115–127. https://doi.org/10.1111/j.1466-882X.2004.00070.x

Bond WJ, Keeley JE (2005) Fire as a global "herbivore": The ecology and evolution of flammable ecosystems. Trends Ecol Evol 20:387–394. https://doi.org/10.1016/j.tree.2005.04.025

Bonn B, Moortgat GK (2002) New particle formation during α- and β-pinene oxidation by O3, OH and NO3, and the influence of water vapour: Particle size distribution studies. Atmos Chem Phys 2:183–196. https://doi.org/10.5194/acp-2-183-2002

Bonn B, Schuster G, Moortgat GK (2002) Influence of water vapor on the process of new particle formation during monoterpene ozonolysis. J Phys Chem A 106:2869–2881. https://doi.org/10.1021/jp012713p

Bosle JM, Mischel SA, Schulze AL, et al (2014) Quantification of low molecular weight fatty acids in cave drip water and speleothems using HPLC-ESI-IT/MS-development and validation of a selective method. Anal Bioanal Chem 406:3167–3177. https://doi.org/10.1007/s00216-014-7743-6

Bowman DMJS, Balch JK, Artaxo P, et al (2009) Fire in the earth system. Science (80-) 324:481–484. https://doi.org/10.1126/science.1163886

Brebu M, Vasile C (2010) Thermal degradation of lignin - a review. Cellul Chem Technol 44:353–363

Breitenbach SFM, Adkins JF, Meyer H, et al (2010) Strong influence of water vapor source dynamics on stable isotopes in precipitation observed in Southern Meghalaya, NE India. Earth Planet Sci Lett 292:212–220. https://doi.org/10.1016/j.epsl.2010.01.038

Breitenbach SFM, Rehfeld K, Goswami B, et al (2012) Constructing proxy records from age models (COPRA). Clim Past 8:1765–1779. https://doi.org/10.5194/cp-8-1765-2012

Bro R, Smilde AK (2014) Principal component analysis. Anal Methods 6:2812–2831. https://doi.org/10.1039/c3ay41907j

Brockman SA, Roden E V, Hegeman AD (2018) Van Krevelen diagram visualization of high resolution-mass spectrometry metabolomics data with OpenVanKrevelen. Metabolomics 14:1–15. https://doi.org/10.1007/s11306-018-1343-y

Brown SA (1969) Biochemistry of Lignin Formation. Bioscience 19:115–121. https://doi.org/10.2307/1294669

Brüggemann M, Poulain L, Held A, et al (2017) Real-time detection of highly oxidized organosulfates and BSOA marker compounds during the F-BEACh 2014 field study. Atmos Chem Phys 17:1453–1469. https://doi.org/10.5194/acp-17-1453-2017

Brüggemann M, Xu R, Tilgner A, et al (2020) Organosulfates in Ambient Aerosol: State of Knowledge and Future Research Directions on Formation, Abundance, Fate, and Importance. Environ Sci Technol 54:3767–3782. https://doi.org/10.1021/acs.est.9b06751

Brugger SO, Schwikowski M, Gobet E, et al (2021) Alpine Glacier Reveals Ecosystem Impacts of Europe's Prosperity and Peril Over the Last Millennium. Geophys Res Lett 48:1–12. https://doi.org/10.1029/2021gl095039

Bryant DJ, Elzein A, Newland M, et al (2021) Importance of Oxidants and Temperature in the Formation of Biogenic Organosulfates and Nitrooxy Organosulfates. ACS Earth Sp Chem 5:2291–2306. https://doi.org/10.1021/acsearthspacechem.1c00204

Bukowiecki N, Weingartner E, Gysel M, et al (2016) A review of more than 20 years of aerosol observation at the high altitude research station Jungfraujoch, Switzerland (3580 m asl). Aerosol Air Qual Res 16:764–788. https://doi.org/10.4209/aaqr.2015.05.0305

Burney DA, Burney LP (1993) Modern pollen deposition in cave sites: experimental results from New York State. New Phytol 124:523–535. https://doi.org/10.1111/j.1469-8137.1993.tb03844.x

Buszewski B, Noga S (2012) Hydrophilic interaction liquid chromatography (HILIC)-a powerful separation technique. Anal Bioanal Chem 402:231–247. https://doi.org/10.1007/s00216-011-5308-5

Calace N, Cantafora E, Mirante S, et al (2005) Transport and modification of humic substances present in Antarctic snow and ancient ice. J Environ Monit 7:1320–1325. https://doi.org/10.1039/b507396k

Camel V (2003) Solid phase extraction of trace elements. Spectrochim Acta - Part B At Spectrosc 58:1177–1233. https://doi.org/10.1016/S0584-8547(03)00072-7

Carlton AG, Turpin BJ, Altieri KE, et al (2007) Atmospheric oxalic acid and SOA production from glyoxal: Results of aqueous photooxidation experiments. Atmos Environ 41:7588–7602. https://doi.org/10.1016/J.ATMOSENV.2007.05.035

Carlton AG, Wiedinmyer C, Kroll JH (2009) A review of Secondary organic aerosol (SOA) formation from isoprene. Atmos Chem Phys 9:4987–5005. https://doi.org/10.5194/acp-9-4987-2009

Carta G, Murru E, Banni S, Manca C (2017) Palmitic acid: Physiological role, metabolism and nutritional implications. Front Physiol 8:1–14. https://doi.org/10.3389/fphys.2017.00902

Casale MT, Richman AR, Elrod MJ, et al (2007) Kinetics of acid-catalyzed aldol condensation reactions of aliphatic aldehydes. Atmos Environ 41:6212–6224. https://doi.org/10.1016/j.atmosenv.2007.04.002

Caseldine CJ, McGarry SF, Baker A, et al (2008) Late Quaternary speleothem pollen in the British Isles. J Quat Sci 23:193–200. https://doi.org/10.1002/JQS.1121

Cech NB, Enke CG (2001) Practical implications of some recent studies in electrospray ionization fundamentals. Mass Spectrom Rev 20:362–387. https://doi.org/10.1002/mas.10008

Cheng H, Edwards RL, Sinha A, et al (2016) The Asian monsoon over the past 640,000 years and ice age terminations. Nature 534:640–646. https://doi.org/10.1038/nature18591

Cheng Y, Brook JR, Li SM, Leithead A (2011) Seasonal variation in the biogenic secondary organic aerosol tracer cis-pinonic acid: Enhancement due to emissions from regional and local biomass burning. Atmos Environ 45:7105–7112. https://doi.org/10.1016/j.atmosenv.2011.09.036

Choi SS, Kim MC, Kim YK (2011) Influence of silica on formation of levoglucosan from carbohydrates by pyrolysis. J Anal Appl Pyrolysis 90:56–62. https://doi.org/10.1016/j.jaap.2010.10.009

Claeys M, Graham B, Vas G, et al (2004) Formation of Secondary Organic Aerosols Through Photooxidation of Isoprene. Science (80-) 303:1173–1176. https://doi.org/10.1126/science.1092805

Claeys M, Iinuma Y, Szmigielski R, et al (2009) Terpenylic acid and related compounds from the oxidation of α-pinene: Implications for new particle formation and growth above forests. Environ Sci Technol 43:6976–6982. https://doi.org/10.1021/es9007596

Claeys M, Szmigielski R, Kourtchev I, et al (2007) Hydroxydicarboxylic acids: Markers for secondary organic aerosol from the photooxidation of α-pinene. Environ Sci Technol 41:1628–1634. https://doi.org/10.1021/es0620181

Claeys M, Wang W, Vermeylen R, et al (2010) Chemical characterisation of marine aerosol at Amsterdam Island during the austral summer of 2006-2007. J Aerosol Sci 41:13–22. https://doi.org/10.1016/j.jaerosci.2009.08.003

Cole-Filipiak NC, O'Connor AE, Elrod MJ (2010) Kinetics of the hydrolysis of atmospherically relevant isoprene-derived hydroxy epoxides. Environ Sci Technol 44:6718–6723. https://doi.org/10.1021/es1019228

Coleborn K, Spate A, Tozer M, et al (2016) Effects of wildfire on long-term soil CO2 concentration: implications for karst processes. Environ Earth Sci 75:1–12. https://doi.org/10.1007/s12665-015-4874-9

Coles GM, Gilbertson DD, Hunt CO, Jenkinson RDS (1989) Taphonomy and the palynology of cave deposits. Cave Sci 16:83–89

Comont L, Laggoun-Défarge F, Disnar JR (2006) Evolution of organic matter indicators in response to major environmental changes: The case of a formerly cut-over peat bog (Le Russey, Jura Mountains, France). Org Geochem 37:1736–1751. https://doi.org/10.1016/j.orggeochem.2006.08.005

Conedera M, Colombaroli D, Tinner W, et al (2017) Insights about past forest dynamics as a tool for present and future forest management in Switzerland. For Ecol Manage 388:100–112. https://doi.org/10.1016/j.foreco.2016.10.027

Corcia A Di, Marchetti M (1991) Multiresidue Method for Pesticides in Drinking Water Using a Graphitized Carbon Black Cartridge Extraction and Liquid Chromatographic Analysis. Anal Chem 63:580–585. https://doi.org/10.1021/ac00006a007

Core JE, Cooper JA, Neulicht RM (1984) Current and Projected Impacts of Residential Wood Combustion on Pacific Northwest Air Quality. J Air Pollut Control Assoc 34:138–143. https://doi.org/10.1080/00022470.1984.10465735

Coulter SE, Pilcher JR, Plunkett G, et al (2012) Holocene tephras highlight complexity of volcanic signals in Greenland ice cores. J Geophys Res Atmos 117:1–11. https://doi.org/10.1029/2012JD017698

Dallüge J, Beens J, Brinkman UAT (2003) Comprehensive two-dimensional gas chromatography: A powerful and versatile analytical tool. J Chromatogr A 1000:69–108. https://doi.org/10.1016/S0021-9673(03)00242-5

Dansgaard W (1964) Stable isotopes in precipitation. Tellus 16:436–468. https://doi.org/10.3402/tellusa.v16i4.8993

Darer AI, Cole-Filipiak NC, O'Connor AE, Elrod MJ (2011) Formation and stability of atmospherically relevant isoprene-derived organosulfates and organonitrates. Environ Sci Technol 45:1895–1902. https://doi.org/10.1021/es103797z

Das S, Giorgi F, Giuliani G, et al (2020) Near-Future Anthropogenic Aerosol Emission Scenarios and Their Direct Radiative Effects on the Present-Day Characteristics of the Indian Summer Monsoon. J Geophys Res Atmos 125:1–19. https://doi.org/10.1029/2019JD031414

Davies SM, Wastegård S, Abbott PM, et al (2010) Tracing volcanic events in the NGRIP ice-core and synchronising North Atlantic marine records during the last glacial period. Earth Planet Sci Lett 294:69–79. https://doi.org/10.1016/j.epsl.2010.03.004

Depalma JW, Horan AJ, Hall Iv WA, Johnston M V (2013) Thermodynamics of oligomer formation: Implications for secondary organic aerosol formation and reactivity. Phys Chem Chem Phys 15:6935–6944. https://doi.org/10.1039/c3cp44586k

Di Corcia A, Samperi R (1990) Determination of Chloroaniline Traces in Environmental Waters by Selective Extraction with Two Traps in Tandem and Liquid Chromatography. Anal Chem 62:1490–1494. https://doi.org/10.1021/ac50031a001

Dinh NP, Jonsson T, Irgum K (2011) Probing the interaction mode in hydrophilic interaction chromatography. J Chromatogr A 1218:5880–5891. https://doi.org/10.1016/j.chroma.2011.06.037

Dole M, Mack LL, Hines RL, et al (1968) Molecular beams of macroions. J Chem Phys 49:2240–2249. https://doi.org/10.1063/1.1670391

Donahue NM, Chuang W, Epstein SA, et al (2013) Why do organic aerosols exist? Understanding aerosol lifetimes using the two-dimensional volatility basis set. Environ Chem 10:151–157. https://doi.org/10.1071/EN13022

Donahue NM, Huff Hartz KE, Chuong B, et al (2005) Critical factors determining the variation in SOA yields from terpene ozonolysis: A combined experimental and computational study. Faraday Discuss 130:295–309. https://doi.org/10.1039/b417369d

Donahue NM, Robinson AL, Stanier CO, Pandis SN (2006) Coupled partitioning, dilution, and chemical aging of semivolatile organics. Environ Sci Technol 40:2635–2643. https://doi.org/10.1021/es052297c

Dredge J, Fairchild IJ, Harrison RM, et al (2013) Cave aerosols: Distribution and contribution to speleothem geochemistry. Quat. Sci. Rev. 63:23–41

Dreybrodt W, Gabrovsek F, Perne M (2005) Condensation Corrosion : a Theoretical Approach. Acta Carsologica 34/2:317–348. https://doi.org/10.3986/ac.v34i2.262

Dreyfus GB, Parrenin F, Lemieux-Dudon B, et al (2007) Anomalous flow below 2700 m in the EPICA Dome C ice core detected using δ18O of atmospheric oxygen measurements. Clim Past 3:341–353. https://doi.org/10.5194/cp-3-341-2007

Dunbar NW (2003) Tephra layers in the Siple Dome and Taylor Dome ice cores, Antarctica: Sources and correlations. J Geophys Res 108:. https://doi.org/10.1029/2002jb002056

Dye C, Yttri KE (2005) Determination of Monosaccharide Anhydrides in Atmospheric Aerosols by Use of High-Performance Liquid Chromatography Combined with High-Resolution Mass Spectrometry. Anal Chem 77:1853–1858. https://doi.org/10.1021/ac049461j

Edwards RL, Chen JH, Ku TL, Wasserburg GJ (1987) Precise timing of the last interglacial period from mass spectrometric determination of thorium-230 in corals. Science (80-) 236:1547–1553. https://doi.org/10.1126/SCIENCE.236.4808.1547

Eichler A, Schwikowski M, Gaggeler HW, et al (2000) Glaciochemical dating of an ice core from upper Grenzgletscher (4200 m a.s.l.). J Glaciol 46:507–515. https://doi.org/10.3189/172756500781833098

Elbert W, Taylor PE, Andreae MO, Pöschl U (2010) Contribution of fungi to primary biogenic aerosols in the atmosphere: active discharge of spores, carbohydrates, and inorganic ions by Asco- and Basidiomycota. Atmos Chem Phys Discuss 6:11317–11355. https://doi.org/10.5194/acpd-6-11317-2006

Elias VO, Simoneit BRT, Cordeiro RC, Turcq B (2001) Evaluating levoglucosan as an indicator of biomass burning in Carajás, Amazônia: A comparison to the charcoal record. Geochim Cosmochim Acta 65:267–272. https://doi.org/10.1016/S0016-7037(00)00522-6

Fabbri D, Torri C, Simoneit BRT, et al (2009) Levoglucosan and other cellulose and lignin markers in emissions from burning of Miocene lignites. Atmos Environ 43:2286–2295. https://doi.org/10.1016/j.atmosenv.2009.01.030

Fahimi IJ, Keppler F, Schöler HF (2003) Formation of chloroacetic acids from soil, humic acid and phenolic moieties. Chemosphere 52:513–520. https://doi.org/10.1016/S0045-6535(03)00212-1

Faimon J, Lang M (2013) Variances in airflows during different ventilation modes in a dynamic U-shaped cave. Int J Speleol 42:115–122. https://doi.org/10.5038/1827-806X.42.2.3

Faimon J, Ličbinský R, Lang M, et al (2019) Cave microclimatology: diurnal variations in aerosol particle concentrations. Theor Appl Climatol 137:2841–2852. https://doi.org/10.1007/s00704-019-02776-1

Faimon J, Štelcl J, Sas D (2006) Anthropogenic CO2-flux into cave atmosphere and its environmental impact: A case study in the Císařská Cave (Moravian Karst, Czech Republic). Sci Total Environ 369:231–245. https://doi.org/10.1016/j.scitotenv.2006.04.006

Fairbanks RG, Mortlock RA, Chiu TC, et al (2005) Radiocarbon calibration curve spanning 0 to 50,000 years BP based on paired 230Th/234U/238U and 14C dates on pristine corals. Quat Sci Rev 24:1781–1796. https://doi.org/10.1016/j.quascirev.2005.04.007

Fairchild IJ, Baker A (2012) Speleothem Science. John Wiley & Sons, Ltd, Chichester

Fairchild IJ, Smith CL, Baker A, et al (2006) Modification and preservation of environmental signals in speleothems. Earth-Science Rev 75:105–153. https://doi.org/10.1016/j.earscirev.2005.08.003

Fairchild IJ, Spötl C, Frisia S, et al (2010) Petrology and geochemistry of annually laminated stalagmites from an Alpine cave (Obir, Austria): seasonal cave physiology. Geol Soc London Spec Publ 336:295–321. https://doi.org/10.1144/SP336.16

Fairchild IJ, Treble PC (2009) Trace elements in speleothems as recorders of environmental change. Quat Sci Rev 28:449–468. https://doi.org/10.1016/j.quascirev.2008.11.007

Fang L, Jenk TM, Singer T, et al (2021) Radiocarbon dating of alpine ice cores with the dissolved organic carbon (DOC) fraction. Cryosph 15:1537–1550. https://doi.org/10.5194/tc-15-1537-2021

Feltracco M, Barbaro E, Spolaor A, et al (2021) Year-round measurements of size-segregated low molecular weight organic acids in Arctic aerosol. Sci Total Environ 763:. https://doi.org/10.1016/j.scitotenv.2020.142954

Fohlmeister J, Voarintsoa NRG, Lechleitner FA, et al (2020) Main controls on the stable carbon isotope composition of speleothems. Geochim Cosmochim Acta 279:67–87. https://doi.org/10.1016/j.gca.2020.03.042

Froyd KD, Murphy SM, Murphy DM, et al (2010) Contribution of isoprene-derived organosulfates to free tropospheric aerosol mass. PNAS 107:21360–21365. https://doi.org/10.1073/pnas.1012561107

Fu P, Kawamura K, Seki O, et al (2016) Historical Trends of Biogenic SOA Tracers in an Ice Core from Kamchatka Peninsula. Environ Sci Technol Lett 3:351–358. https://doi.org/10.1021/acs.estlett.6b00275

Fu PQ, Kawamura K, Chen J, et al (2013) Organic molecular composition of marine aerosols over the Arctic Ocean in summer: Contributions of primary emission and secondary aerosol formation. Biogeosciences 10:653–667. https://doi.org/10.5194/bg-10-653-2013

Fu TM, Jacob DJ, Wittrock F, et al (2008) Global budgets of atmospheric glyoxal and methylglyoxal, and implications for formation of secondary organic aerosols. J Geophys Res Atmos 113:1–17. https://doi.org/10.1029/2007JD009505

Gabrieli J, Vallelonga P, Cozzi G, et al (2010) Post 17th-century changes of european pah emissions recorded in high-altitude alpine snow and ice. Environ Sci Technol 44:3260–3266. https://doi.org/10.1021/es903365s

Gabrielli P, Barbante C, Boutron C, et al (2005) Variations in atmospheric trace elements in Dome C (East Antarctica) ice over the last two climatic cycles. Atmos Environ 39:6420–6429. https://doi.org/10.1016/J.ATMOSENV.2005.07.025

Gambaro A, Zangrando R, Gabrielli P, et al (2008) Direct determination of levoglucosan at the picogram per milliliter level in antarctic ice by high-performance liquid chromatography/electrospray ionization triple quadrupole mass spectrometry. Anal Chem 80:1649–1655. https://doi.org/10.1021/ac701655x

Gao S, Hegg DA, Hobbs P V., et al (2003) Water-soluble organic components in aerosols associated with savanna fires in southern Africa: Identification, evolution, and distribution. J Geophys Res Atmos 108:1–15. https://doi.org/10.1029/2002JD002324

Gao S, Ng NL, Keywood M, et al (2004) Particle phase acidity and oligomer formation in secondary organic aerosol. Environ Sci Technol 38:6582–6589. https://doi.org/10.1021/es049125k

García-Gómez D, Bregy L, Nussbaumer-Ochsner Y, et al (2015) Detection and Quantification of Benzothiazoles in Exhaled Breath and Exhaled Breath Condensate by Real-Time Secondary Electrospray Ionization-High-Resolution Mass Spectrometry and Ultra-High Performance Liquid Chromatography. Environ Sci Technol 49:12519–12524. https://doi.org/10.1021/acs.est.5b03809

Garland RM, Elrod MJ, Kincaid K, et al (2006) Acid-catalyzed reactions of hexanal on sulfuric acid particles: Identification of reaction products. Atmos Environ 40:6863–6878. https://doi.org/10.1016/j.atmosenv.2006.07.009

Gellrich M, Baur P, Koch B, Zimmermann NE (2007) Agricultural land abandonment and natural forest re-growth in the Swiss mountains: A spatially explicit economic analysis. Agric Ecosyst Environ 118:93–108. https://doi.org/10.1016/j.agee.2006.05.001

Genty D, Baker A, Massault M, et al (2001a) Dead carbon in stalagmites: Carbonate bedrock paleodissolution vs. ageing of soil organic matter. Implications for 13C variations in speleotherms. Geochim Cosmochim Acta 65:3443–3457. https://doi.org/10.1016/S0016-7037(01)00697-4

Genty D, Baker A, Vokal B (2001b) Intra- and inter-annual growth rate of modern stalagmites. Chem Geol 176:191–212. https://doi.org/10.1016/S0009-2541(00)00399-5

Genty D, Blamart D, Ouahdi R, et al (2003) Precise dating of Dansgaard-Oeschger climate oscillations in western Europe from stalagmite data. Nature 421:833–837. https://doi.org/10.1038/nature01391

George IJ, Chang RYW, Danov V, et al (2009) Modification of cloud condensation nucleus activity of organic aerosols by hydroxyl radical heterogeneous oxidation. Atmos Environ 43:5038–5045. https://doi.org/10.1016/j.atmosenv.2009.06.043

Giorio C, Kehrwald N, Barbante C, et al (2018) Prospects for reconstructing paleoenvironmental conditions from organic compounds in polar snow and ice. Quat Sci Rev 183:1–22. https://doi.org/10.1016/j.quascirev.2018.01.007

Glasius M, Lahaniati M, Calogirou A, et al (2000) Carboxylic acids in secondary aerosols from oxidation of cyclic monoterpenes by ozone. Environ Sci Technol 34:1001–1010. https://doi.org/10.1021/es990445r

Goldstein AH, Galbally IE (2007) Known and unexplored organic constituents in the Earth's atmosphere. Environ Sci Technol 41:1514–1521. https://doi.org/10.1021/es072476p

Goldstein SJ, Stirling CH (2003) Techniques for Measuring Uranium-series Nuclides: 1992–2002. Rev Mineral Geochemistry 52:23–57. https://doi.org/https://doi.org/10.2113/0520023

Goñi MA, Montgomery S (2000) Alkaline CuO oxidation with a microwave digestion system: Lignin analyses of geochemical samples. Anal Chem 72:3116–3121. https://doi.org/10.1021/ac991316w

González NJD, Borg-Karlson AK, Artaxo P, et al (2014) Primary and secondary organics in the tropical Amazonian rainforest aerosols: Chiral analysis of 2-methyltetraols. Environ Sci Process Impacts 16:1413–1421. https://doi.org/10.1039/c4em00102h

González NJD, Borg-Karlson AK, Redeby JP, et al (2011) New method for resolving the enantiomeric composition of 2-methyltetrols in atmospheric organic aerosols. J Chromatogr A 1218:9288–9294. https://doi.org/10.1016/j.chroma.2011.10.069

Goujon C, Barnola JM, Ritz C (2003) Modelling the densification of polar firn including heat diffusion: Application to close-off characteristics and gas isotopic fractionation for Antarctica and Greenland sites. J Geophys Res D Atmos 108:4792. https://doi.org/10.1029/2002jd003319

Graham B, Mayol-Bracero OL, Guyon P, et al (2002) Water-soluble organic compounds in biomass burning aerosols over Amazonia 1. Characterization by NMR and GC-MS. J Geophys Res Atmos 107:1–16. https://doi.org/10.1029/2001JD000336

Graham J., Rickwood D (2002) Biological Centrifugation. Springer Verlag, Heidelberg

Greco G, Grosse S, Letzel T (2013) Serial coupling of reversed-phase and zwitterionic hydrophilic interaction LC/MS for the analysis of polar and nonpolar phenols in wine. J Sep Sci 36:1379–1388. https://doi.org/10.1002/jssc.201200920

Grgić I, Iskra I, Podkrajšek B, Gerjevič VD (2014) Measurements of aerosol particles in the Škocjan Caves, Slovenia. Environ Sci Pollut Res 21:1915–1923. https://doi.org/10.1007/s11356-013-2080-4

Grieman MM, Aydin M, Fritzsche D, et al (2016) Aromatic acids in a Eurasian Arctic ice core: a 3000-year proxy record of biomass burning. Clim Past Discuss 14:1–29. https://doi.org/10.5194/cp-2016-126

Griffin RJ, Cocker DR, Flagan RC, Seinfeld JH (1999) Organic aerosol formation from the oxidation of biogenic hydrocarbons. J Geophys Res Atmos 104:3555–3567. https://doi.org/10.1029/1998JD100049

Gross JH (2017) Mass Spectrometry: A Textbook, 3rd edn. Springer International Publishing AG, Cham, Switzerland

Guenther A (1995) A global model of natural volatile organic compound emissions. J Geophys Res 100:8873–8892. https://doi.org/10.1029/94JD02950

Guilhermet J, Preunkert S, Voisin D, et al (2013) Major 20th century changes of water-soluble humic-like substances (HULIS WS) aerosol over Europe inferred from Alpine ice cores. J Geophys Res Atmos 118:3869–3878. https://doi.org/10.1002/jgrd.50201

Gutiérrez G, Benito JM, Coca J, Pazos C (2010) Vacuum evaporation of surfactant solutions and oil-in-water emulsions. Chem Eng J 162:201–207. https://doi.org/10.1016/j.cej.2010.05.029

Haeberli W, Funk M (1991) Borehole temperatures at the Colle Gnifetti core-drilling site (Monte Rosa, Swiss Alps). J Glaciol 37:37–46. https://doi.org/10.1017/S0022143000042775

Hall IV WA, Johnston M V. (2011) Oligomer content of α-pinene secondary organic aerosol. Aerosol Sci Technol 45:37–45. https://doi.org/10.1080/02786826.2010.517580

Halliday AN, Lee DC, Christensen JN, et al (1998) Applications of multiple collector-ICPMS to cosmochemistry, geochemistry, and paleoceanography. Geochim Cosmochim Acta 62:919–940. https://doi.org/10.1016/S0016-7037(98)00057-X

Hallquist M, Wenger JC, Baltensperger U, et al (2009) The formation, properties and impact of secondary organic aerosol: current and emerging issues. Atmos Chem Phys 9:5155–5236. https://doi.org/10.5194/acp-9-5155-2009

Hansen AMK, Hong J, Raatikainen T, et al (2015) Hygroscopic properties and cloud condensation nuclei activation of limonene-derived organosulfates and their mixtures with ammonium sulfate. Atmos Chem Phys 15:14071–14089. https://doi.org/10.5194/acp-15-14071-2015

Hansen M, Scholz D, Froeschmann ML, et al (2017) Carbon isotope exchange between gaseous CO2 and thin solution films: Artificial cave experiments and a complete diffusion-reaction model. Geochim Cosmochim Acta 211:28–47. https://doi.org/10.1016/j.gca.2017.05.005

Hao Z, Xiao B, Weng N (2008) Impact of column temperature and mobile phase components on selectivity of hydrophilic interaction chromatography (HILIC). J Sep Sci 31:1449–1464. https://doi.org/10.1002/jssc.200700624

Harju J, Winnberg A, Wouterloot JGA (2000) The distribution of OH in Taurus Molecular Cloud-1. Astron Astrophys 353:1065–1073

Hartland A, White J (2019) Geochemistry of Waipuna Cave. In: Lowe, D.J., Pittari, A. (editors), Field Trip Guides. Geosciences 2019 Conference, Hamilton, New Zealand (24-29 November). Geosci Soc New Zeal Misc Publ 155B:1–7

Hartog N, van Bergen PF, de Leeuw JW, Griffioen J (2004) Reactivity of organic matter in aquifer sediments: Geological and geochemical controls. Geochim Cosmochim Acta 68:1281–1292. https://doi.org/10.1016/j.gca.2003.09.004

Hawkins LN, Russell LM (2010) Polysaccharides, Proteins, and Phytoplankton Fragments: Four Chemically Distinct Types of Marine Primary Organic Aerosol Classified by Single Particle Spectromicroscopy. Adv Meteorol 2010:1–14. https://doi.org/10.1155/2010/612132

Heaton KJ, Dreyfus MA, Wang S, Johnston M V. (2007) Oligomers in the early stage of biogenic secondary organic aerosol formation and growth. Environ Sci Technol 41:6129–6136. https://doi.org/10.1021/es070314n

Hedges JI, Erte JR (1982) Characterization of Lignin by Gas Capillary Chromatography. Am Chemlcal Soc Anal Chem 54:174–178. https://doi.org/10.1021/ac00239a007

Hedges JI, Mann DC (1979) The characterization of plant tissues by their lignin oxidation products. Geochim Cosmochim Acta 43:1803–1807. https://doi.org/10.1016/0016-7037(79)90028-0

Hedges JI, Parker PL (1976) Land-derived organic matter in surface sediments from the Gulf of Mexico. Geochim Cosmochim Acta 40:1019–1029. https://doi.org/10.1016/0016-7037(76)90044-2

Heidke I, Hartland A, Scholz D, et al (2021) Lignin oxidation products in soil, dripwater and speleothems from four different sites in New Zealand. Biogeosciences 18:2289–2300. https://doi.org/10.5194/bg-18-2289-2021

Heidke I, Scholz D, Hoffmann T (2019) Lignin oxidation products as a potential proxy for vegetation and environmental changes in speleothems and cave drip water - a first records from the Herbstlabyrinth, central Germany. Clim Past 15:1025–1037. https://doi.org/10.5194/cp-15-1025-2019

Heidke I, Scholz D, Hoffmann T (2018) Quantification of lignin oxidation products as vegetation biomarkers in speleothems and cave drip water. Biogeosciences 15:5831–5845. https://doi.org/10.5194/bg-15-5831-2018

Hellén H, Praplan AP, Tykkä T, et al (2018) Long-term measurements of volatile organic compounds highlight the importance of sesquiterpenes for the atmospheric chemistry of a boreal forest. Atmos Chem Phys 18:13839–13863. https://doi.org/10.5194/acp-18-13839-2018

Hellstrom J, McCulloch M, Stone J (1998) A detailed 31,000-year record of climate and vegetation change, from the isotope geochemistry of two New Zealand speleothems. Quat Res 50:167–178. https://doi.org/10.1006/qres.1998.1991

Hellstrom JC, McCulloch MT (2000) Multi-proxy constraints on the climatic significance of trace element records from a New Zealand speleothem. Earth Planet Sci Lett 179:287–297. https://doi.org/10.1016/S0012-821X(00)00115-1

Helmer PO, Wienken CM, Korf A, Hayen H (2020) Mass spectrometric investigation of cardiolipins and their oxidation products after two-dimensional heart-cut liquid chromatography. J Chromatogr A 1619:1–10. https://doi.org/10.1016/j.chroma.2020.460918

Helmig D, Ortega J, Duhl T, et al (2007) Sesquiterpene emissions from pine trees - Identifications, emission rates and flux estimates for the contiguous United States. Environ Sci Technol 41:1545–1553. https://doi.org/10.1021/es0618907

Helmig D, Ortega J, Guenther A, et al (2006) Sesquiterpene emissions from loblolly pine and their potential contribution to biogenic aerosol formation in the Southeastern US. Atmos Environ 40:4150–4157. https://doi.org/10.1016/j.atmosenv.2006.02.035

Hemström P, Irgum K (2006) Hydrophilic interaction chromatography. J Sep Sci 29:1784–1821. https://doi.org/10.1002/jssc.200600199

Hennigan CJ, Sullivan AP, Collett JL, Robinson AL (2010) Levoglucosan stability in biomass burning particles exposed to hydroxyl radicals. Geophys Res Lett 37:. https://doi.org/10.1029/2010GL043088

Hennion MC (2000) Graphitized carbons for solid-phase extraction. J Chromatogr A 885:73–95. https://doi.org/10.1016/S0021-9673(00)00085-6

Hermabessiere L, Dehaut A, Paul-Pont I, et al (2017) Occurrence and effects of plastic additives on marine environments and organisms: A review. Chemosphere 182:781–793. https://doi.org/10.1016/j.chemosphere.2017.05.096

Hernes PJ, Kaiser K, Dyda RY, Cerli C (2013) Molecular trickery in soil organic matter: Hidden lignin. Environ Sci Technol 47:9077–9085. https://doi.org/10.1021/es401019n

Hernes PJ, Robinson AC, Aufdenkampe AK (2007) Fractionation of lignin during leaching and sorption and implications for organic matter “freshness.” Geophys Res Lett 34:. https://doi.org/10.1029/2007GL031017

Herrero M, Cacciola F, Donato P, et al (2008) Serial coupled columns reversed-phase separations in high-performance liquid chromatography. Tool for analysis of complex real samples. J Chromatogr A 1188:208–215. https://doi.org/10.1016/j.chroma.2008.02.039

Ho KF, Lee SC, Cao JJ, et al (2006) Dicarboxylic acids, ketocarboxylic acids and dicarbonyls in the urban roadside area of Hong Kong. Atmos Environ 40:3030–3040. https://doi.org/10.1016/j.atmosenv.2005.11.069

Hodge EJ, Richards DA, Smart PL, et al (2008) Effective precipitation in southern Spain (~ 266 to 46 ka) based on a speleothem stable carbon isotope record. Quat Res 69:447–457. https://doi.org/10.1016/j.yqres.2008.02.013

Hoffmann D, Tilgner A, Iinuma Y, Herrmann H (2010) Atmospheric stability of levoglucosan: A detailed laboratory and modeling study. Environ Sci Technol 44:694–699. https://doi.org/10.1021/es902476f

Hoffmann DL, Prytulak J, Richards DA, et al (2007) Procedures for accurate U and Th isotope measurements by high precision MC-ICPMS. Int J Mass Spectrom 264:97–109. https://doi.org/10.1016/j.ijms.2007.03.020

Hoffmann T, Bandur R, Marggraf U, Linscheid M (1998) Molecular composition of organic aerosols formed in the α-pinene/O3 reaction: Implications for new particle formation processes. J Geophys Res Atmos 103:25569–25578. https://doi.org/10.1029/98JD01816

Hopmans EC, dos Santos RAL, Mets A, et al (2013) A novel method for the rapid analysis of levoglucosan in soils and sediments. Org Geochem 58:86–88. https://doi.org/10.1016/j.orggeochem.2013.02.003

Houghton J.T., Ding, Y., Griggs, D.J., Noguer, M., van der Linden, P.J., Dai, X., Maskell, K., Johnson CA (2001) Climate Change 2001: The Scientific Basis (Contribution of Working Group I to the Third Assessment Report of the Intergovernmental Panel on Climate Change). Cambridge Univ Press

Hu D, Bian Q, Li TWY, et al (2008) Contributions of isoprene, monoterpenes, β-caryophyllene, and toluene to secondary organic aerosols in Hong Kong during the summer of 2006. J Geophys Res Atmos 113:1–14. https://doi.org/10.1029/2008JD010437

Hu QH, Xie ZQ, Wang XM, et al (2013) Levoglucosan indicates high levels of biomass burning aerosols over oceans from the Arctic to Antarctic. Sci Rep 3:1–7. https://doi.org/10.1038/srep03119

Hua Q (2009) Radiocarbon: A chronological tool for the recent past. Quat Geochronol 4:378–390. https://doi.org/10.1016/J.QUAGEO.2009.03.006

Huang Y, Fairchild IJ, Borsato A, et al (2001) Seasonal variations in Sr, Mg and P in modern speleothems (Grotta di Ernesto, Italy). Chem Geol 175:429–448. https://doi.org/10.1016/S0009-2541(00)00337-5

Hug C, Ulrich N, Schulze T, et al (2014) Identification of novel micropollutants in wastewater by a combination of suspect and nontarget screening. Environ Pollut 184:25–32. https://doi.org/10.1016/j.envpol.2013.07.048

Hughey CA, Hendrickson CL, Rodgers RP, et al (2001) Kendrick mass defect spectrum: A compact visual analysis for ultrahigh-resolution broadband mass spectra. Anal Chem 73:4676–4681. https://doi.org/10.1021/ac010560w

Hyder M, Genberg J, Sandahl M, et al (2012) Yearly trend of dicarboxylic acids in organic aerosols from south of Sweden and source attribution. Atmos Environ 57:197–204. https://doi.org/10.1016/j.atmosenv.2012.04.027

Iguiniz M, Heinisch S (2017) Two-dimensional liquid chromatography in pharmaceutical analysis. Instrumental aspects, trends and applications. J Pharm Biomed Anal 145:482–503. https://doi.org/10.1016/j.jpba.2017.07.009

Iinuma Y, Müller C, Berndt T, et al (2007a) Evidence for the existence of organosulfates from β-pinene ozonolysis in ambient secondary organic aerosol. Environ Sci Technol 41:6678–6683. https://doi.org/10.1021/es070938t

Iinuma Y, Müller C, Böge O, et al (2007b) The formation of organic sulfate esters in the limonene ozonolysis secondary organic aerosol (SOA) under acidic conditions. Atmos Environ 41:5571–5583. https://doi.org/10.1016/j.atmosenv.2007.03.007

Immenhauser A, Buhl D, Richter D, et al (2010) Magnesium-isotope fractionation during low-Mg calcite precipitation in a limestone cave - Field study and experiments. Geochim Cosmochim Acta 74:4346–4364. https://doi.org/10.1016/j.gca.2010.05.006

Iribarne J V., Thomson BA (1976) On the evaporation of small ions from charged droplets. J Chem Phys 64:2287–2294. https://doi.org/10.1063/1.432536

Isabel García M, Van Drooge BL, Rodríguez S, Alastuey A (2017) Speciation of organic aerosols in the Saharan Air Layer and in the free troposphere westerlies. Atmos Chem Phys 17:8939–8958. https://doi.org/10.5194/acp-17-8939-2017

Isaksson E, Kekonen T, Moore J, Mulvaney R (2005) The methanesulfonic acid (MSA) record in a Svalbard ice core. Ann Glaciol 42:345–351. https://doi.org/10.3189/172756405781812637

Ivanovich M, Harmon RS (1992) Uranium-series disequilibrium: applications to earth, marine, and environmental sciences 2 ed. Clarendon Press, United Kingdom

James JM, Patsalides E, Cox G (1994) Amino acid composition of stromatolitic stalagmites. Geomicrobiol J 12:183–194. https://doi.org/10.1080/01490459409377985

Jaoui M, Lewandowski M, Kleindienst TE, et al (2007) ß-caryophyllinic acid: An atmospheric tracer for ß-caryophyllene secondary organic aerosol. Geophys Res Lett 34:1–4. https://doi.org/10.1029/2006GL028827

Jara IA, Newnham RM, Vandergoes MJ, et al (2015) Pollen-climate reconstruction from northern South Island, New Zealand (41°S), reveals varying high- and low-latitude teleconnections over the last 16 000 years. J Quat Sci 30:817–829. https://doi.org/10.1002/jqs.2818

Jenk TM, Szidat S, Bolius D, et al (2009) A novel radiocarbon dating technique applied to an ice core from the Alps indicating late Pleistocene ages. J Geophys Res Atmos 114:1–8. https://doi.org/10.1029/2009JD011860

Jenkin ME (2004) Modelling the formation and composition of secondary organic aerosol from α- and β-pinene ozonolysis using MCM v3. Atmos Chem Phys 4:1741–1757. https://doi.org/10.5194/acp-4-1741-2004

Jenkin ME, Shallcross DE, Harvey JN (2000) Development and application of a possible mechanism for the generation of cis-pinic acid from the ozonolysis of α- and β-pinene. Atmos Environ 34:2837–2850. https://doi.org/10.1016/S1352-2310(00)00087-X

Jex CN, Pate GH, Blyth AJ, et al (2014) Lignin biogeochemistry: From modern processes to Quaternary archives. Quat Sci Rev 87:46–59. https://doi.org/10.1016/j.quascirev.2013.12.028

Jiang W, Appelblad P, Jonsson T, Hemström P (2011) Analysis of Aminoglycosides with a Zwitterionic HILIC Stationary Phase and Mass Spectrometry Detection. Chromatogr today 26–28

Jimenez JL, Canagaratna MR, Donahue NM, et al (2009) Evolution of organic aerosols in the atmosphere. Science (80-) 326:1525–1529. https://doi.org/10.1126/science.1180353

Johnson D, Marston G (2008) The gas-phase ozonolysis of unsaturated volatile organic compounds in the troposphere. Chem Soc Rev 37:699–716. https://doi.org/10.1039/b704260b

Jonsson ÅM, Hallquist M, Ljungström E (2006) Impact of humidity on the ozone initiated oxidation of limonene, Δ3-carene, and α-pinene. Environ Sci Technol 40:188–194. https://doi.org/10.1021/es051163w

Jose S, Nair VS, Babu SS (2020) Anthropogenic emissions from South Asia reverses the aerosol indirect effect over the northern Indian Ocean. Sci Rep 10:18360. https://doi.org/10.1038/s41598-020-74897-x

Kahnt A, Iinuma Y, Blockhuys F, et al (2014) 2-hydroxyterpenylic acid: An oxygenated marker compound for α-pinene secondary organic aerosol in ambient fine aerosol. Environ Sci Technol 48:4901–4908. https://doi.org/10.1021/es500377d

Karatapanis AE, Fiamegos YC, Stalikas CD (2010) Study of the behavior of water-soluble vitamins in HILIC on a diol column. Chromatographia 71:751–759. https://doi.org/10.1365/s10337-010-1564-3

Kaufmann G, Dreybrodt W (2004) Stalagmite growth and palaeo-climate: An inverse approach. Earth Planet Sci Lett 224:529–545. https://doi.org/10.1016/j.epsl.2004.05.020

Kawamura K, Izawa Y, Mochida M, Shiraiwa T (2012) Ice core records of biomass burning tracers (levoglucosan and dehydroabietic, vanillic and p-hydroxybenzoic acids) and total organic carbon for past 300years in the Kamchatka Peninsula, Northeast Asia. Geochim Cosmochim Acta 99:317–329. https://doi.org/10.1016/j.gca.2012.08.006

Kawamura K, Suzuki I, Fujii Y, Watanabe O (1996) Ice core record of fatty acids over the past 450 years in Greenland. Geophys Res Lett 23:2665–2668. https://doi.org/10.1029/96gl02428

Kawamura K, Yasui O (2005) Diurnal changes in the distribution of dicarboxylic acids, ketocarboxylic acids and dicarbonyls in the urban Tokyo atmosphere. Atmos Environ 39:1945–1960. https://doi.org/10.1016/j.atmosenv.2004.12.014

Kawamura K, Yokoyama K, Fujii Y, Watanabe O (2001) A Greenland ice core record of low molecular weight dicarboxylic acids, ketocarboxylic acids, and α-dicarbonyls: A trend from Little Ice Age to the present (1540 to 1989 A.D.). J Geophys Res Atmos 106:1331–1345. https://doi.org/10.1029/2000JD900465

Kebarle P, Tang L (1993) From Ions in Solution to Ions in the Gas Phase: The Mechanism of Electrospray Mass Spectrometry. Anal Chem 65:972A-986A. https://doi.org/10.1021/ac00070a001

Kehrwald N, Zangrando R, Gabrielli P, et al (2012) Levoglucosan as a specific marker of fire events in Greenland snow. Tellus, Ser B Chem Phys Meteorol 64:. https://doi.org/10.3402/tellusb.v64i0.18196

Kertész Z, Borbély-Kiss I, Hunyadi I (1999) Study of aerosols collected in a speleotherapeutic cave situated below Budapest, Hungary. Nucl Instruments Methods Phys Res Sect B Beam Interact with Mater Atoms 150:384–391. https://doi.org/10.1016/S0168-583X(98)00899-4

Kesselmeier J, Kuhn U, Wolf A, et al (2000) Atmospheric volatile organic compounds (VOC) at a remote tropical forest site in central Amazonia. Atmos Environ 34:4063–4072. https://doi.org/10.1016/S1352-2310(00)00186-2

Kezimana P, Dmitriev AA, Kudryavtseva A V, et al (2018) Secoisolariciresinol diglucoside of flaxseed and its metabolites: Biosynthesis and potential for nutraceuticals. Front Genet 9:1–9. https://doi.org/10.3389/fgene.2018.00641

Kim KH, Kabir E, Kabir S (2015) A review on the human health impact of airborne particulate matter. Environ. Int. 74:136–143

Kim S, Kramer RW, Hatcher PG (2003) Graphical Method for Analysis of Ultrahigh-Resolution Broadband Mass Spectra of Natural Organic Matter, the Van Krevelen Diagram. Anal Chem 75:5336–5344. https://doi.org/10.1021/ac034415p

Kind T, Fiehn O (2007) Seven Golden Rules for heuristic filtering of molecular formulas obtained by accurate mass spectrometry. BMC Bioinformatics 8:. https://doi.org/10.1186/1471-2105-8-105

King ACF, Giorio C, Wolff E, et al (2019a) Direct injection liquid chromatography high-resolution mass spectrometry for determination of primary and secondary terrestrial and marine biomarkers in ice cores. Anal Chem 91:5051–5057. https://doi.org/10.1021/acs.analchem.8b05224

King ACF, Giorio C, Wolff E, et al (2019b) A new method for the determination of primary and secondary terrestrial and marine biomarkers in ice cores using liquid chromatography high-resolution mass spectrometry. Talanta 194:233–242. https://doi.org/10.1016/j.talanta.2018.10.042

King ACF, Thomas ER, Pedro JB, et al (2019c) Organic Compounds in a Sub-Antarctic Ice Core: A Potential Suite of Sea Ice Markers. Geophys Res Lett 46:9930–9939. https://doi.org/10.1029/2019GL084249

Kingdon KH (1923) A Method for the Neutralization of Electron Space Charge by Positive Ionization at Very Low Gas Pressures. Phys Rev 21:408. https://doi.org/10.1103/PhysRev.21.408

Kirchgeorg T, Schüpbach S, Kehrwald N, et al (2014) Method for the determination of specific molecular markers of biomass burning in lake sediments. Org Geochem 71:1–6. https://doi.org/10.1016/J.ORGGEOCHEM.2014.02.014

Kleindienst TE, Jaoui M, Lewandowski M, et al (2007) Estimates of the contributions of biogenic and anthropogenic hydrocarbons to secondary organic aerosol at a southeastern US location. Atmos Environ 41:8288–8300. https://doi.org/10.1016/j.atmosenv.2007.06.045

Knopf DA, Forrester SM, Slade JH (2011) Heterogeneous oxidation kinetics of organic biomass burning aerosol surrogates by O3, NO2, N2O5, and NO3. Phys Chem Chem Phys 13:21050–21062. https://doi.org/10.1039/c1cp22478f

Knox JH, Pryde A (1975) Performance and selected applications of a new range of chemically bonded packing materials in high-performance liquid chromatography. J Chromatogr A 112:171–188. https://doi.org/10.1016/S0021-9673(00)99951-5

Kögel-Knabner I (2002) The macromolecular organic composition of plant and microbial residues as inputs to soil organic matter. Soil Biol Biochem 34:139–162. https://doi.org/10.1016/j.soilbio.2016.08.011

Kögel I, Bochter R (1985) Characterization of lignin in forest humus layers by high-performance liquid chromatography of cupric oxide oxidation products. Soil Biol Biochem 17:637–640. https://doi.org/10.1016/0038-0717(85)90040-9

Kołodziejczyk A, Pyrcz P, Błaziak K, et al (2020) Physicochemical Properties of Terebic Acid, MBTCA, Diaterpenylic Acid Acetate, and Pinanediol as Relevant α-Pinene Oxidation Products. ACS Omega 5:7919–7927. https://doi.org/10.1021/acsomega.9b04231

Kourtchev I, Hellebust S, Bell JM, et al (2011) The use of polar organic compounds to estimate the contribution of domestic solid fuel combustion and biogenic sources to ambient levels of organic carbon and PM2.5 in Cork Harbour, Ireland. Sci Total Environ 409:2143–2155. https://doi.org/10.1016/j.scitotenv.2011.02.027

Kourtchev I, O'Connor IP, Giorio C, et al (2014) Effects of anthropogenic emissions on the molecular composition of urban organic aerosols: An ultrahigh resolution mass spectrometry study. Atmos Environ 89:525–532. https://doi.org/10.1016/j.atmosenv.2014.02.051

Krauss M, Singer H, Hollender J (2010) LC-high resolution MS in environmental analysis: From target screening to the identification of unknowns. Anal Bioanal Chem 397:943–951. https://doi.org/10.1007/s00216-010-3608-9

Kristensen K, Cui T, Zhang H, et al (2014) Dimers in α-pinene secondary organic aerosol: Effect of hydroxyl radical, ozone, relative humidity and aerosol acidity. Atmos Chem Phys 14:4201–4218. https://doi.org/10.5194/acp-14-4201-2014

Kristensen K, Glasius M (2011) Organosulfates and oxidation products from biogenic hydrocarbons in fine aerosols from a forest in North West Europe during spring. Atmos Environ 45:4546–4556. https://doi.org/10.1016/j.atmosenv.2011.05.063

Kristensen K, N. Jensen L, L. J. Quéléver L, et al (2020) The Aarhus Chamber Campaign on Highly Oxygenated Organic Molecules and Aerosols (ACCHA): Particle formation, organic acids, and dimer esters from α-pinene ozonolysis at different temperatures. Atmos Chem Phys 20:12549–12567. https://doi.org/10.5194/acp-20-12549-2020

Kristensen K, Watne ÅK, Hammes J, et al (2016) High-Molecular Weight Dimer Esters Are Major Products in Aerosols from α-Pinene Ozonolysis and the Boreal Forest. Environ Sci Technol Lett 3:280–285. https://doi.org/10.1021/acs.estlett.6b00152

Kristensen K, Worton DR, Glasius M, et al (2013) Formation and occurrence of dimer esters of pinene oxidation products in atmospheric aerosols. Atmos Chem Phys 13:3763–3776. https://doi.org/10.5194/acp-13-3763-2013

Kroll JH, Donahue NM, Jimenez JL, et al (2011) Carbon oxidation state as a metric for describing the chemistry of atmospheric organic aerosol. Nat Chem 3:133–139. https://doi.org/10.1038/nchem.948

Kroll JH, Ng NL, Murphy SM, et al (2006) Secondary organic aerosol formation from isoprene photooxidation. Environ Sci Technol 40:1869–1877. https://doi.org/10.1021/es0524301

Kroll JH, Seinfeld JH (2008) Chemistry of secondary organic aerosol: Formation and evolution of low-volatility organics in the atmosphere. Atmos Environ 42:3593–3624. https://doi.org/10.1016/j.atmosenv.2008.01.003

Kulakowski D, Bebi P, Rixen C (2011) The interacting effects of land use change, climate change and suppression of natural disturbances on landscape forest structure in the Swiss Alps. Oikos 120:216–225. https://doi.org/10.1111/j.1600-0706.2010.18726.x

Kulmala M, Vehkamäki H, Petäjä T, et al (2004) Formation and growth rates of ultrafine atmospheric particles: A review of observations. J Aerosol Sci 35:143–176. https://doi.org/10.1016/j.jaerosci.2003.10.003

Kumata H, Yamada J, Masuda K, et al (2002) Benzothiazolamines as tire-derived molecular markers: Sorptive behavior in street runoff and application to source apportioning. Environ Sci Technol 36:702–708. https://doi.org/10.1021/es0155229

Kundu S, Kawamura K, Andreae TW, et al (2010) Molecular distributions of dicarboxylic acids, ketocarboxylic acids and α-dicarbonyls in biomass burning aerosols: Implications for photochemical production and degradation in smoke layers. Atmos Chem Phys 10:2209–2225. https://doi.org/10.5194/acp-10-2209-2010

Lajin B, Braeuer S, Borovička J, Goessler W (2021) Is the water disinfection by-product dichloroacetic acid biosynthesized in the edible mushroom Russula nigricans? Chemosphere 281:130819. https://doi.org/10.1016/j.chemosphere.2021.130819

Lamarque JF, Bond TC, Eyring V, et al (2010) Historical (1850-2000) gridded anthropogenic and biomass burning emissions of reactive gases and aerosols: Methodology and application. Atmos Chem Phys 10:7017–7039. https://doi.org/10.5194/acp-10-7017-2010

Larsen BR, Di Bella D, Glasius M, et al (2001) Gas-phase OH oxidation of monoterpenes: Gaseous and particulate products. J Atmos Chem 38:231–276. https://doi.org/10.1023/A:1006487530903

Lechleitner FA, Breitenbach SFM, Cheng H, et al (2017) Climatic and in-cave influences on δ18O and δ13C in a stalagmite from northeastern India through the last deglaciation. Quat Res (United States) 88:458–471. https://doi.org/10.1017/qua.2017.72

Lee C, Zang J, Cuff J, et al (2013) Application of Heart-Cutting 2D-LC for the Determination of Peak Purity for a Chiral Pharmaceutical Compound by HPLC. Chromatographia 76:5–11. https://doi.org/10.1007/s10337-012-2367-5

Legrand M, Cachier H, Wagenbach D, et al (2003) A historical record of formate and acetate from a high-elevation Alpine glacier: Implications for their natural versus anthropogenic budgets at the European scale. J Geophys Res 108:4788. https://doi.org/10.1029/2003jd003594

Legrand M, De Angelis M (1996) Light carboxylic acids in Greenland ice: A record of past forest fires and vegetation emissions from the boreal zone. J Geophys Res Atmos 101:4129–4145. https://doi.org/10.1029/95JD03296

Legrand M, Hammer C, De Angelis M, et al (1997) Sulfur-containing species (methanesulfonate and SO4) over the last climatic cycle in the Greenland Ice Core Project (central Greenland) ice core. J Geophys Res Ocean 102:26663–26679. https://doi.org/10.1029/97JC01436

Legrand M, Mayewski P (1997) Glaciochemistry of Polar Ice Cores: A review. Rev Geophys 35:219–243. https://doi.org/10.1029/96RG03527

Legrand M, McConnell JR, Preunkert S, et al (2018) Alpine ice evidence of a three-fold increase in atmospheric iodine deposition since 1950 in Europe due to increasing oceanic emissions. PNAS 115:12136–12141. https://doi.org/10.1073/pnas.1809867115

Legrand M, Preunkert S, Schock M, et al (2007) Major 20th century changes of carbonaceous aerosol components (EC, WinOC, DOC, HULIS, carboxylic acids, and cellulose) derived from Alpine ice cores. J Geophys Res Atmos 112:1–12. https://doi.org/10.1029/2006JD008080

Lehmann J, Kleber M (2015) The contentious nature of soil organic matter. Nature 528:60–68. https://doi.org/10.1038/nature16069

Leppla D, Zannoni N, Kremper L, et al (2021) Varying chiral ratio of Pinic acid enantiomers above the Amazon rainforest. Atmos Chem Phys Discuss [preprint] 1–19. https://doi.org/10.5194/acp-2021-150

Li SH, Liu S, Colmenares JC, Xu YJ (2016) A sustainable approach for lignin valorization by heterogeneous photocatalysis. Green Chem 18:594–607. https://doi.org/10.1039/c5gc02109j

Lide DR (2011) CRC Handbook of Chemistry and Physics, 90th edn. CRC Press, Boca Raton

Liggio J, Li SM (2006) Organosulfate formation during the uptake of pinonaldehyde on acidic sulfate aerosols. Geophys Res Lett 33:13808. https://doi.org/10.1029/2006GL026079

Lim Y Bin, Ziemann PJ (2005) Products and mechanism of secondary organic aerosol formation from reactions of n-alkanes with OH radicals in the presence of NO x. Environ Sci Technol 39:9229–9236. https://doi.org/10.1021/es051447g

Lin J, Tsang C, Lieu R, Zhang K (2020) Fast chiral and achiral profiling of compounds with multiple chiral centers by a versatile two-dimensional multicolumn liquid chromatography (LC–mLC) approach. J Chromatogr A 1620:460987. https://doi.org/10.1016/j.chroma.2020.460987

Lohmann U, Feichter J (2005) Global indirect aerosol effects: A review. Atmos Chem Phys 5:715–737. https://doi.org/10.5194/acp-5-715-2005

Louw S, Pereira AS, Lynen F, et al (2008) Serial coupling of reversed-phase and hydrophilic interaction liquid chromatography to broaden the elution window for the analysis of pharmaceutical compounds. J Chromatogr A 1208:90–94. https://doi.org/10.1016/j.chroma.2008.08.058

Lüthi MP, Funk M (2001) Modelling heat flow in a cold, high-altitude glacier: Interpretation of measurements from Colle Gnifetti, Swiss Alps. J Glaciol 47:314–324. https://doi.org/10.3189/172756501781832223

Ma Y, Willcox TR, Russell AT, Marston G (2007) Pinic and pinonic acid formation in the reaction of ozone with α-pinene. Chem Commun 1328–1330. https://doi.org/10.1039/b617130c

Maggi V, Orombelli G, Stenni B, et al (1998) 70 years of northern Victoria Land (Antarctica) accumulation rate. Ann Glaciol 27:215–219. https://doi.org/10.3189/1998aog27-1-215-219

Makarov A (2000) Electrostatic axially harmonic orbital trapping: A high-performance technique of mass analysis. Anal Chem 72:1156–1162. https://doi.org/10.1021/ac991131p

Makarov A, Scigelova M (2010) Coupling liquid chromatography to Orbitrap mass spectrometry. J Chromatogr A 1217:3938–3945. https://doi.org/10.1016/j.chroma.2010.02.022

Mallet CR, Lu Z, Mazzeo JR (2004) A study of ion suppression effects in electrospray ionization from mobile phase additives and solid-phase extracts. Rapid Commun Mass Spectrom 18:49–58. https://doi.org/10.1002/rcm.1276

Maltsev V (1997) Speleothems of aerosol origin: discussion. J Cave Karst Stud 59:45–47

Marlon JR, Bartlein PJ, Daniau AL, et al (2013) Global biomass burning: A synthesis and review of Holocene paleofire records and their controls. Quat Sci Rev 65:5–25. https://doi.org/10.1016/j.quascirev.2012.11.029

Martínez-Lozano P, de la Mora JF (2007) Electrospray ionization of volatiles in breath. Int J Mass Spectrom 265:68–72. https://doi.org/10.1016/J.IJMS.2007.05.008

Masson O, Piga D, Gurriaran R, D'Amico D (2010) Impact of an exceptional Saharan dust outbreak in France: PM10 and artificial radionuclides concentrations in air and in dust deposit. Atmos Environ 44:2478–2486. https://doi.org/10.1016/j.atmosenv.2010.03.004

Matley KA, Sniderman JK, Drinnan AN, Hellstrom JC (2020) Late-Holocene environmental change on the Nullarbor Plain, southwest Australia, based on speleothem pollen records. Holocene 30:672–681. https://doi.org/10.1177/0959683619895589

Mayewski PA, Lyons WB, Spencer MJ, et al (1990) An ice-core record of atmospheric response to anthropogenic sulphate and nitrate. Nature 346:554–556. https://doi.org/10.1038/346554a0

Mayfield KJ, Shalliker RA, Catchpoole HJ, et al (2005) Viscous fingering induced flow instability in multidimensional liquid chromatography. J Chromatogr A 1080:124–131. https://doi.org/10.1016/j.chroma.2005.04.093

McCalley D V. (2010) Study of the selectivity, retention mechanisms and performance of alternative silica-based stationary phases for separation of ionised solutes in hydrophilic interaction chromatography. J Chromatogr A 1217:3408–3417. https://doi.org/10.1016/j.chroma.2010.03.011

McCalley D V., Neue UD (2008) Estimation of the extent of the water-rich layer associated with the silica surface in hydrophilic interaction chromatography. J Chromatogr A 1192:225–229. https://doi.org/10.1016/j.chroma.2008.03.049

McDermott F (2004) Palaeo-climate reconstruction from stable isotope variations in speleothems: A review. Quat Sci Rev 23:901–918. https://doi.org/10.1016/j.quascirev.2003.06.021

McDermott F, Frisia S, Huang Y, et al (1999) Holocene climate variability in Europe: Evidence from δ18O, textural and extension-rate variations in three speleothems. Quat Sci Rev 18:1021–1038. https://doi.org/10.1016/S0277-3791(98)00107-3

McGarry SF, Caseldine C (2004) Speleothem Palynology: an undervalued tool in Quaternary studies. Quat Sci Rev 23:2389–2404. https://doi.org/10.1016/J.QUASCIREV.2004.06.007

Medeiros PM, Conte MH, Weber JC, Simoneit BRT (2006) Sugars as source indicators of biogenic organic carbon in aerosols collected above the Howland Experimental Forest, Maine. Atmos Environ 40:1694–1705. https://doi.org/10.1016/J.ATMOSENV.2005.11.001

Meskhidze N, Nenes A (2006) Phytoplankton and Cloudiness in the Southern Ocean. Science (80-) 314:1419–1423. https://doi.org/10.1177/1455072596013005-611

MeteoSwiss FO of M and C (2020) Temperature and precipitation trends. https://www.meteoswiss.admin.ch/home/climate/climate-change-in-switzerland/temperature-and-precipitation-trends.html. Accessed 1 Feb 2022

Meyer V (2010) Practical High-Performance Liquid Chromatography, 5th edn. John Wiley & Sons, Ltd, Chichester

Meyers PA (1997) Organic geochemical proxies of paleoceanographic, paleolimnologic, and paleoclimatic processes. Org Geochem 27:213–250. https://doi.org/10.1016/S0146-6380(97)00049-1

Minerath EC, Casale MT, Elrod MJ (2008) Kinetics feasibility study of alcohol sulfate esterification reactions in tropospheric aerosols. Environ Sci Technol 42:4410–4415. https://doi.org/10.1021/es8004333

Minerath EC, Elrod MJ (2009) Assessing the potential for diol and hydroxy sulfate ester formation from the reaction of epoxides in tropospheric aerosols. Environ Sci Technol 43:1386–1392. https://doi.org/10.1021/es8029076

Minkus S, Bieber S, Letzel T (2021) (Very) polar organic compounds in the Danube river basin: A non-target screening workflow and prioritization strategy for extracting highly confident features. Anal Methods 13:2044–2054. https://doi.org/10.1039/d1ay00434d

Mischel SA, Scholz D, Spötl C, et al (2017) Holocene climate variability in Central Germany and a potential link to the polar North Atlantic: A replicated record from three coeval speleothems. Holocene 27:509–525. https://doi.org/10.1177/0959683616670246

Montes R, Aguirre J, Vidal X, et al (2017) Screening for Polar Chemicals in Water by Trifunctional Mixed-Mode Liquid Chromatography-High Resolution Mass Spectrometry. Environ Sci Technol 51:6250–6259. https://doi.org/10.1021/acs.est.6b05135

More AF, Spaulding NE, Bohleber P, et al (2017) Next-generation ice core technology reveals true minimum natural levels of lead (Pb) in the atmosphere: Insights from the Black Death. GeoHealth 1:211–219. https://doi.org/10.1002/2017GH000064

Moschet C (2017) S11 | SWISSPEST | Swiss Insecticides, Fungicides and TPs. https://doi.org/10.5281/zenodo.2623741#.YROpJCwYmmM.mendeley. Accessed 11 Aug 2021

Müller-Tautges C, Eichler A, Schwikowski M, et al (2016) Historic records of organic compounds from a high Alpine glacier: Influences of biomass burning, anthropogenic emissions, and dust transport. Atmos Chem Phys 16:1029–1043. https://doi.org/10.5194/acp-16-1029-2016

Müller-Tautges C, Eichler A, Schwikowski M, Hoffmann T (2014) A new sensitive method for the quantification of glyoxal and methylglyoxal in snow and ice by stir bar sorptive extraction and liquid desorption-HPLC-ESI-MS. Anal Bioanal Chem 406:2525–2532. https://doi.org/10.1007/s00216-014-7640-z

Müller, L.; Reinnig, M.; Hayen, H.; Hoffman T (2009) Characterization of oligomeric compounds in secondary organic aerosol using liquid chromatography coupled to electrospray ionization Fourier transform ion cyclotron resonance mass spectrometry. Rapid Commun Mass Spectrom 23:971979. https://doi.org/10.1002/rcm.3957

Müller L, Reinnig MC, Naumann KH, et al (2012) Formation of 3-methyl-1,2,3-butanetricarboxylic acid via gas phase oxidation of pinonic acid - A mass spectrometric study of SOA aging. Atmos Chem Phys 12:1483–1496. https://doi.org/10.5194/acp-12-1483-2012

Müller L, Reinnig MC, Warnke J, Hoffmann T (2008) Unambiguous identification of esters as oligomers in secondary organic aerosol formed from cyclohexene and cyclohexene/α-pinene ozonolysis. Atmos Chem Phys 8:1423–1433. https://doi.org/10.5194/acp-8-1423-2008

Murakami H, Sugiyama T, Miki Y, et al (2020) Development and Evaluation of HILIC-type Sorbents Modified with Hydrophilic Copolymers for Solid-phase Extraction. Anal Sci 36:1185–1190. https://doi.org/10.2116/analsci.20P084

Murray KK, Boyd RK, Eberlin MN, et al (2013) Standard Definitions of Terms Related to Mass Spectrometry. Pure Appl Chem 85:1515–1609. https://doi.org/10.1515/ci.2004.26.3.23a

Myers OD, Sumner SJ, Li S, et al (2017) One Step Forward for Reducing False Positive and False Negative Compound Identifications from Mass Spectrometry Metabolomics Data: New Algorithms for Constructing Extracted Ion Chromatograms and Detecting Chromatographic Peaks. Anal Chem 89:. https://doi.org/10.1021/acs.analchem.7b00947

Nardin R, Severi M, Amore A, et al (2021) Dating of the GV7 East Antarctic ice core by high-resolution chemical records and focus on the accumulation rate variability in the last millennium. Clim Past 17:2073–2089. https://doi.org/10.5194/cp-17-2073-2021

Nava-Fernandez C, Hartland A, Gázquez F, et al (2020) Pacific climate reflected in Waipuna Cave drip water hydrochemistry. Hydrol Earth Syst Sci 24:3361–3380. https://doi.org/10.5194/hess-24-3361-2020

Navarro C, Carrión JS, Munuera M, Prieto AR (2001) Cave surface pollen and the palynological potential of karstic cave sediments in palaeoecology. Rev Palaeobot Palynol 117:245–265. https://doi.org/10.1016/S0034-6667(01)00095-1

Navarro Camacho C, Carrión JS, Navarro J, et al (2000) An experimental approach to the palynology of cave deposits. J Quat Sci 15:603–619. https://doi.org/10.1002/1099-1417(200009)15:6<603::AID-JQS544>3.0.CO;2-F

Nevea V, Salek R, Williams A, Schymanski E (2019) S34 | EXPOSOMEXPL | Biomarkers from Exposome Explorer. https://doi.org/10.5281/ZENODO.2653032

Ng NL, Chhabra PS, Chan AWH, et al (2007a) Effect of NOx level on secondary organic aerosol (SOA) formation from the photooxidation of terpenes. Atmos Chem Phys 7:5159–5174. https://doi.org/10.5194/acp-7-5159-2007

Ng NL, Kroll JH, Chan AWH, et al (2007b) Secondary organic aerosol formation from m-xylene, toluene, and benzene. Atmos Chem Phys 7:3909–3922. https://doi.org/10.5194/acp-7-3909-2007

Ng NL, Kwan AJ, Surratt JD, et al (2008) Secondary organic aerosol (SOA) formation from reaction of isoprene with nitrate radicals (NO3). Atmos Chem Phys 8:4117–4140. https://doi.org/10.5194/acp-8-4117-2008

Nolte CG, Schauer JJ, Cass GR, Simoneit BRT (2001) Highly polar organic compounds present in wood smoke and in the ambient atmosphere. Environ Sci Technol 35:1912–1919. https://doi.org/10.1021/es001420r

Nováková L, Matysová L, Solich P (2006) Advantages of application of UPLC in pharmaceutical analysis. Talanta 68:908–918. https://doi.org/10.1016/j.talanta.2005.06.035

Nozière B, Ekström S, Alsberg T, Holmström S (2010) Radical-initiated formation of organosulfates and surfactants in atmospheric aerosols. Geophys Res Lett 37:1–6. https://doi.org/10.1029/2009GL041683

Nozière B, Finessi E, D'Anna B, et al (2015) The Molecular Identification of Organic Compounds in the Atmosphere: State of the Art and Challenges. Chem Rev 115:3919–3983. https://doi.org/10.1021/cr5003485

Nürenberg G, Schulz M, Kunkel U, Ternes TA (2015) Development and validation of a generic nontarget method based on liquid chromatography - high resolution mass spectrometry analysis for the evaluation of different wastewater treatment options. J Chromatogr A 1426:77–90. https://doi.org/10.1016/j.chroma.2015.11.014

O'Brien RE, Laskin A, Laskin J, et al (2013) Molecular characterization of organic aerosol using nanospray desorption/electrospray ionization mass spectrometry: CalNex 2010 field study. Atmos Environ 68:265–272. https://doi.org/10.1016/j.atmosenv.2012.11.056

O'Dowd CD, de Leeuw G (2007) Marine aerosol production: a review of the current knowledge. Math Phys Eng Sci 365:1753–1774. https://doi.org/10.1098/rsta.2007.2043

Odum JR, Hoffmann T, Bowman F, et al (1996) Gas/particle partitioning and secondary organic aerosol yields. Environ Sci Technol 30:2580–2585. https://doi.org/10.1021/es950943+

Oh HJ, Kim J (2020) Characterization of inhalable aerosols from cosmetic powders and sustainability in cosmetic products. Sustainability 12:1–15. https://doi.org/10.3390/su12198187

Olsen J V, Macek B, Lange O, et al (2007) Higher-energy C-trap dissociation for peptide modification analysis. Nat Methods 4:709–712. https://doi.org/10.1038/nmeth1060

Olson CN, Galloway MM, Yu G, et al (2011) Hydroxycarboxylic acid-derived organosulfates: Synthesis, stability, and quantification in ambient aerosol. Environ Sci Technol 45:6468–6474. https://doi.org/10.1021/es201039p

Opsahl S, Benner R (1995) Early diagenesis of vascular plant tissues: Lignin and cutin decomposition and biogeochemical implications. Geochim Cosmochim Acta 59:4889–4904. https://doi.org/10.1016/0016-7037(95)00348-7

Oros DR, Mazurek MA, Baham JE, Simoneit BRT (2002) Organic tracers from wild fire residues in soils and rain/river wash-out. Water Air Soil Pollut 137:203–233. https://doi.org/10.1023/A:1015557301467

Osmont D, Brugger S, Gilgen A, et al (2021) Tracing devastating fires in Portugal to a snow archive in the Swiss Alps: A case study. Cryosphere 14:3731–3745. https://doi.org/10.5194/tc-14-3731-2020

Pancost RD, Boot CS (2004) The palaeoclimatic utility of terrestrial biomarkers in marine sediments. Mar Chem 92:239–261. https://doi.org/10.1016/J.MARCHEM.2004.06.029

Pandey MP, Kim CS (2011) Lignin Depolymerization and Conversion: A Review of Thermochemical Methods. Chem Eng Technol 34:29–41. https://doi.org/10.1002/ceat.201000270

Pankow JF (1994) An absorption model of the gas/aerosol partitioning involved in the formation of secondary organic aerosol. Atmos Environ 28:189–193. https://doi.org/10.1016/1352-2310(94)90094-9

Pankow JF, Asher WE (2008) SIMPOL.1: A simple group contribution method for predicting vapor pressures and enthalpies of vaporization of multifunctional organic compounds. Atmos Chem Phys 8:2773–2796. https://doi.org/10.5194/acp-8-2773-2008

Parazols M, Marinoni A, Amato P, et al (2007) Speciation and role of iron in cloud droplets at the puy de Dôme station. J Atmos Chem 54:267–281. https://doi.org/10.1007/s10874-006-9026-x

Parrenin F, Barker S, Blunier T, et al (2012) On the gas-ice depth difference (Δdepth) along the EPICA Dome C ice core. Clim Past 8:1239–1255. https://doi.org/10.5194/cp-8-1239-2012

Parshintsev J, Hyötyläinen T, Hartonen K, et al (2010) Solid-phase extraction of organic compounds in atmospheric aerosol particles collected with the particle-into-liquid sampler and analysis by liquid chromatography-mass spectrometry. Talanta 80:1170–1176. https://doi.org/10.1016/j.talanta.2009.09.004

Parvin F, Seki O, Fujita K, et al (2019) Assessment for paleoclimatic utility of biomass burning tracers in SE-Dome ice core, Greenland. Atmos Environ 196:86–94. https://doi.org/10.1016/J.ATMOSENV.2018.10.012

Pearson A (2020) The terrestrial carbon cycle in transition: tracking changes using novel tracers on multiple timescales. The University of Waikato

Perry, R.H.; Cooks, R.G.; Noll RJ (2008) Orbitrap Mass Spectrometry: Instrumentation, Ion motion, and applications. Mass Spectrom Rev 27:661–699

Petroff A, Mailliat A, Amielh M, Anselmet F (2008) Aerosol dry deposition on vegetative canopies. Part I: Review of present knowledge. Atmos. Environ. 42:3625–3653

Pettersen RC (1984) The Chemical Compostition of Wood. Chem Solid Wood 2:57–216

Pezzatti GB, Zumbrunnen T, Bürgi M, et al (2013) Fire regime shifts as a consequence of fire policy and socio-economic development: An analysis based on the change point approach. For Policy Econ 29:7–18. https://doi.org/10.1016/j.forpol.2011.07.002

Pirok BWJ, Stoll DR, Schoenmakers PJ (2019) Recent Developments in Two-Dimensional Liquid Chromatography: Fundamental Improvements for Practical Applications. Anal. Chem. 91:240–263

Pluskal T, Castillo S, Villar-Briones A, Orešič M (2010) MZmine 2: Modular framework for processing, visualizing, and analyzing mass spectrometry-based molecular profile data. BMC Bioinformatics 395:11. https://doi.org/10.1186/1471-2105-11-395

Pokhrel A, Kawamura K, Kunwar B, et al (2020) Ice core records of levoglucosan and dehydroabietic and vanillic acids from Aurora Peak in Alaska since the 1660s: A proxy signal of biomass-burning activities in the North Pacific Rim. Atmos Chem Phys 20:597–612. https://doi.org/10.5194/acp-20-597-2020

Pokhrel A, Kawamura K, Ono K, et al (2016) Ice core records of monoterpene- and isoprene-SOA tracers from Aurora Peak in Alaska since 1660s: Implication for climate change variability in the North Pacific Rim. Atmos Environ 130:105–112. https://doi.org/10.1016/j.atmosenv.2015.09.063

Pokhrel A, Kawamura K, Seki O, et al (2015) Ice core profiles of saturated fatty acids (C12:0-C30:0) and oleic acid (C18:1) from southern Alaska since 1734 AD: A link to climate change in the Northern Hemisphere. Atmos Environ 100:202–209. https://doi.org/10.1016/j.atmosenv.2014.11.007

Polag D, Scholz D, Mühlinghaus C, et al (2010) Stable isotope fractionation in speleothems: Laboratory experiments. Chem Geol 279:31–39. https://doi.org/10.1016/j.chemgeo.2010.09.016

Poole CF (2003) New trends in solid-phase extraction. TrAC - Trends Anal. Chem. 22:362–373

Pöschl U (2005) Atmospheric aerosols: Composition, transformation, climate and health effects. Angew Chemie - Int Ed 44:7520–7540. https://doi.org/10.1002/anie.200501122

Power MJ, Marlon J, Ortiz N, et al (2008) Changes in fire regimes since the last glacial maximum: An assessment based on a global synthesis and analysis of charcoal data. Clim Dyn 30:887–907. https://doi.org/10.1007/s00382-007-0334-x

Preunkert S, Legrand M, Wagenbach D (2001a) Sulfate trends in a Col du Dôme (French Alps) ice core: A record of anthropogenic sulfate levels in the European midtroposphere over the twentieth century. J Geophys Res Atmos 106:31991–32004. https://doi.org/10.1029/2001JD000792

Preunkert S, Legrand M, Wagenbach D (2001b) Causes of enhanced fluoride levels in Alpine ice cores over the last 75 years: Implications for the atmosphere fluoride bugget. J Geophys Res 106:619–632

Puxbaum H, Caseiro A, Sánchez-Ochoa A, et al (2007) Levoglucosan levels at background sites in Europe for assessing the impact of biomass combustion on the European aerosol background. J Geophys Res Atmos 112:23–5. https://doi.org/10.1029/2006JD008114

Raes F, Van Dingenen R, Vignati E, et al (2000) Formation and cycling of aerosols in the global troposphere. Atmos. Environ. 34:4215–4240

Ralph J, Lundquist K, Brunow G, et al (2004) Lignins: Natural polymers from oxidative coupling of 4-hydroxyphenyl- propanoids. Phytochem Rev 3:29–60. https://doi.org/10.1023/B:PHYT.0000047809.65444.a4

Ramanathan V, Crutzen PJ, Kiehl JT, Rosenfeld D (2001) Aerosols, Climate, and the Hydrological Cycle. Science (80-) 294:2119–2124

Rampler E, Schoeny H, Mitic BM, et al (2018) Simultaneous non-polar and polar lipid analysis by on-line combination of HILIC, RP and high resolution MS. Analyst 143:1250–1258. https://doi.org/10.1039/c7an01984j

Reemtsma T, Fiehn O, Kalnowski G, Jekel M (1995) Microbial Transformations and Biological Effects of Fungicide-Derived Benzothiazoles Detemrined in Industrial Wastewater. Environ Sci Technol 29:478–485. https://doi.org/10.1021/es00002a025

Reinnig MC, Warnke J, Hoffmann T (2009) Identification of organic hydroperoxides and hydroperoxy acids in secondary organic aerosol formed during the ozonolysis of different monoterpenes and sesquiterpenes by on-line analysis using atmospheric pressure chemical ionization ion trap mass spectrom. Rapid Commun Mass Spectrom 23:1735–1741. https://doi.org/10.1002/rcm.4065

Ren H, Chen Y, Wang H, et al (2019) Simultaneous Determination of Caffeine, Taurine and Five Water-Soluble Vitamins in Tobacco Products by HPLC–MS/MS. Chromatographia 82:1665–1675. https://doi.org/10.1007/s10337-019-03799-6

Rey F, Gobet E, Schwörer C, et al (2019) Causes and mechanisms of synchronous succession trajectories in primeval Central European mixed Fagus sylvatica forests. J Ecol 107:1392–1408. https://doi.org/10.1111/1365-2745.13121

Richards DA, Dorale JA (2003) Uranium-series chronology and environmental applications of speleothems. Rev Mineral Geochemistry 52:407–460. https://doi.org/10.2113/0520407

Riechelmann S, Buhl D, Schröder-Ritzrau A, et al (2012) The magnesium isotope record of cave carbonate archives. Clim Past 8:1849–1867. https://doi.org/10.5194/cp-8-1849-2012

Rinaldi M, Decesari S, Finessi E, et al (2010) Primary and Secondary Organic Marine Aerosol and Oceanic Biological Activity: Recent Results and New Perspectives for Future Studies. Adv Meteorol 2010:1–10. https://doi.org/10.1155/2010/310682

Rissanen MP, Ehrhart S, Guida R, et al (2016) Ion-induced nucleation of pure biogenic particles. Nature 533:521–526. https://doi.org/10.1038/nature17953

Riva M, Budisulistiorini SH, Chen Y, et al (2016) Chemical Characterization of Secondary Organic Aerosol from Oxidation of Isoprene Hydroxyhydroperoxides. Environ Sci Technol 50:9889–9899. https://doi.org/10.1021/acs.est.6b02511

Rivas-Ubach A, Liu Y, Bianchi TS, et al (2018) Moving beyond the van Krevelen Diagram: A New Stoichiometric Approach for Compound Classification in Organisms. Anal Chem 90:6152–6160. https://doi.org/10.1021/acs.analchem.8b00529

Robinson AL, Donahue NM, Shrivastava MK, et al (2007) Rethinking organic aerosols: Semivolatile emissions and photochemical aging. Science (80-) 315:1259–1262. https://doi.org/10.1126/science.1133061

Rogers GM, Walker S, Basher LM, Lee WG (2007) Frequency and impact of Holocene fire in eastern South Island, New Zealand. N Z J Ecol 31:129–142

Rudich Y, Donahue NM, Mentel TF (2007) Aging of organic aerosol: Bridging the gap between laboratory and field studies. Annu Rev Phys Chem 58:321–352. https://doi.org/10.1146/annurev.physchem.58.032806.104432

Ruff M, Mueller MS, Loos M, Singer HP (2015) Quantitative target and systematic non-target analysis of polar organic micro-pollutants along the river Rhine using high-resolution mass-spectrometry - Identification of unknown sources and compounds. Water Res 87:145–154. https://doi.org/10.1016/j.watres.2015.09.017

Saarnio K, Teinilä K, Aurela M, et al (2010) High-performance anion-exchange chromatography-mass spectrometry method for determination of levoglucosan, mannosan, and galactosan in atmospheric fine particulate matter. Anal Bioanal Chem 398:2253–2264. https://doi.org/10.1007/s00216-010-4151-4

Saarnio K, Teinilä K, Saarikoski S, et al (2013) Online determination of levoglucosan in ambient aerosols with particle-into-liquid sampler - High-performance anion-exchange chromatography - Mass spectrometry (PILS-HPAEC-MS). Atmos Meas Tech 6:2839–2849. https://doi.org/10.5194/amt-6-2839-2013

Salvador CM, Chou CCK, Ho TT, et al (2020) Contribution of terpenes to ozone formation and secondary organic aerosols in a subtropical forest impacted by urban pollution. Atmosphere (Basel) 11:. https://doi.org/10.3390/atmos11111232

Sandra K, Vanhoenacker G, Vandenheede I, et al (2016) Multiple heart-cutting and comprehensive two-dimensional liquid chromatography hyphenated to mass spectrometry for the characterization of the antibody-drug conjugate ado-trastuzumab emtansine. J Chromatogr B Anal Technol Biomed Life Sci 1032:119–130. https://doi.org/10.1016/j.jchromb.2016.04.040

Sato K, Jia T, Tanabe K, et al (2016) Terpenylic acid and nine-carbon multifunctional compounds formed during the aging of β-pinene ozonolysis secondary organic aerosol. Atmos Environ 130:127–135. https://doi.org/10.1016/j.atmosenv.2015.08.047

Schauer JJ, Rogge WF, Hildemann LM, et al (1996) Source apportionment of airborne particulate matter using organic compounds as tracers. Atmos Environ 30:3837–3855. https://doi.org/10.1016/1352-2310(96)00085-4

Scheirs J, Camino G, Tumiatti W (2001) Overview of water evolution during the thermal degradation of cellulose. Eur Polym J 37:933–942. https://doi.org/10.1016/S0014-3057(00)00211-1

Schindelka J, Iinuma Y, Hoffmann D, Herrmann H (2013) Sulfate radical-initiated formation of isoprene-derived organosulfates in atmospheric aerosols. Faraday Discuss 165:237–259. https://doi.org/10.1039/c3fd00042g

Schkolnik G, Falkovich AH, Rudich Y, et al (2005) New analytical method for the determination of levoglucosan, polyhydroxy compounds, and 2-methylerythritol and its application to smoke and rainwater samples. Environ Sci Technol 39:2744–2752. https://doi.org/10.1021/es048363c

Schmitt-Kopplin P, Liger-Belair G, Koch BP, et al (2012) Dissolved organic matter in sea spray: A transfer study from marine surface water to aerosols. Biogeosciences 9:1571–1582. https://doi.org/10.5194/bg-9-1571-2012

Scholz D, Hoffmann D (2008) 230Th/U-dating of fossil corals and speleothems. Quat Sci J 57:52–76. https://doi.org/10.3285/eg.57.1-2.3

Scholz D, Hoffmann DL (2011) StalAge - An algorithm designed for construction of speleothem age models. Quat Geochronol 6:369–382. https://doi.org/10.1016/j.quageo.2011.02.002

Schreuder LT, Hopmans EC, Stuut JBW, et al (2018) Transport and deposition of the fire biomarker levoglucosan across the tropical North Atlantic Ocean. Geochim Cosmochim Acta 227:171–185. https://doi.org/10.1016/j.gca.2018.02.020

Schwander J, Sowers T, Barnola JM, et al (1997) Age scale of the air in the summit ice: Implication for glacial-interglacial temperature change. J Geophys Res Atmos 102:19483–19493. https://doi.org/10.1029/97jd01309

Schwikowski M, Döscher A, Gäggeler HW, Schotterer U (1999) Anthropogenic versus natural sources of atmospheric sulphate from an Alpine ice core. Tellus, Ser B Chem Phys Meteorol 51:938–951. https://doi.org/10.1034/j.1600-0889.1999.t01-4-00006.x

Schwikowski M, Seibert P, Baltensperger U, Gaggeler HW (1995) A study of an outstanding Saharan dust event at the high-alpine site Jungfraujoch, Switzerland. Atmos Environ 29:1829–1842. https://doi.org/10.1016/1352-2310(95)00060-C

Schymanski EL, Singer HP, Slobodnik J, et al (2015) Non-target screening with high-resolution mass spectrometry: Critical review using a collaborative trial on water analysis. Anal Bioanal Chem 407:6237–6255. https://doi.org/10.1007/s00216-015-8681-7

Seinfeld J, Pandis S (2006) Atmospheric Chemistry and Physics: From Air Pollution to Climate Change, 3rd edn. John Wiley & Sons, New Jersey

Seinfeld JH, Pandis SN (1998) Atmospheric Chemistry and Physics, 3rd edn. John Wiley & Sons Inc., Hoboken, NJ, USA

Seki O, Kawamura K, Bendle JAP, et al (2015) Carbonaceous aerosol tracers in ice-cores record multi-decadal climate oscillations. Sci Rep 5:14450. https://doi.org/10.1038/srep14450

Selman MHJ, Hemayatkar M, Deelder AM, Wuhrer M (2011) Cotton HILIC SPE microtips for microscale purification and enrichment of glycans and glycopeptides. Anal Chem 83:2492–2499. https://doi.org/10.1021/ac1027116

Shakesby RA, Doerr SH (2006) Wildfire as a hydrological and geomorphological agent. Earth-Science Rev 74:269–307. https://doi.org/10.1016/j.earscirev.2005.10.006

Shang J, Passananti M, Dupart Y, et al (2016) SO2 Uptake on Oleic Acid: A New Formation Pathway of Organosulfur Compounds in the Atmosphere. Environ Sci Technol Lett 3:67–72. https://doi.org/10.1021/acs.estlett.6b00006

Sheu R, Fortenberry CF, Walker MJ, et al (2021) Evaluating Indoor Air Chemical Diversity, Indoor-to-Outdoor Emissions, and Surface Reservoirs Using High-Resolution Mass Spectrometry. Environ Sci Technol 55:10255–10267. https://doi.org/10.1021/acs.est.1c01337

Sheu R, Stönner C, Ditto JC, et al (2020) Human transport of thirdhand tobacco smoke: A prominent source of hazardous air pollutants into indoor nonsmoking environments. Sci Adv 6:. https://doi.org/10.1126/sciadv.aay4109

Shilling JE, King SM, Mochida M, et al (2007) Mass spectral evidence that small changes in composition caused by oxidative aging processes alter aerosol CCN properties. J Phys Chem A 111:3358–3368. https://doi.org/10.1021/jp068822r

Shiraiwa M, Garland RM, Pöschl U (2009) Kinetic double-layer model of aerosol surface chemistry and gas-particle interactions (K2-SURF): Degradation of polycyclic aromatic hydrocarbons exposed to O3, NO2, H2O, OH and NO3. Atmos Chem Phys 9:9571–9586. https://doi.org/10.5194/acp-9-9571-2009

Shiraiwa M, Pöschl U, Knopf DA (2012) Multiphase chemical kinetics of NO 3 radicals reacting with organic aerosol components from biomass burning. Environ Sci Technol 46:6630–6636. https://doi.org/10.1021/es300677a

Simoneit BRT (2002) Biomass burning - A review of organic tracers for smoke from incomplete combustion. Appl Geochemistry 17:129–162. https://doi.org/10.1016/S0883-2927(01)00061-0

Simoneit BRT, Elias VO, Kobayashi M, et al (2004) Sugars - Dominant water-soluble organic compounds in soils and characterization as tracers in atmospheric participate matter. Environ Sci Technol 38:5939–5949. https://doi.org/10.1021/es0403099

Simoneit BRT, Oros DR, Elias VO (2000) Molecular tracers for smoke from charring/burning of chitin biopolymer. Chemosph - Glob Chang Sci 2:101–105. https://doi.org/10.1016/S1465-9972(99)00049-5

Simoneit BRT, Rogge WF, Mazurek MA, et al (1993) Lignin Pyrolysis Products, Lignans, and Resin Acids as Specific Tracers of Plant Classes in Emissions from Biomass Combustion. Environ Sci Technol 27:2533–2541. https://doi.org/10.1021/es00048a034

Škeříková V, Jandera P (2010) Effects of the operation parameters on Hydrophilic Interaction Liquid Chromatography separation of phenolic acids on zwitterionic monolithic capillary columns. J Chromatogr A 1217:7981–7989. https://doi.org/10.1016/j.chroma.2010.07.061

Sleighter R, Hatcher P (2007) The application of electrospray ionization coupled to ultrahigh resolution mass spectrometry for the molecular characterization of natural organic matter. J Mass Spectrom 42:559–574. https://doi.org/10.1002/jms.1221

Smith AC, Wynn PM, Barker PA (2013) Natural and anthropogenic factors which influence aerosol distribution in Ingleborough Show Cave, UK. Int J Speleol 42:49–56. https://doi.org/10.5038/1827-806X.42.1.6

Sniderman JMK, Woodhead JD, Hellstrom J, et al (2016) Pliocene reversal of late Neogene aridification. Proc Natl Acad Sci U S A 113:1999–2004. https://doi.org/10.1073/pnas.1520188113

Spötl C, Fairchild IJ, Tooth AF (2005) Cave air control on dripwater geochemistry, Obir Caves (Austria): Implications for speleothem deposition in dynamically ventilated caves. Geochim Cosmochim Acta 69:2451–2468. https://doi.org/10.1016/j.gca.2004.12.009

Spötl C, Mangini A (2002) Stalagmite from the Austrian Alps reveals Dansgaard-Oeschger events during isotope stage 3: Implications for the absolute chronology of Greenland ice cores. Earth Planet Sci Lett 203:507–518. https://doi.org/10.1016/S0012-821X(02)00837-3

Spötl C, Mangini A, Richards DA (2006) Chronology and paleoenvironment of Marine Isotope Stage 3 from two high-elevation speleothems, Austrian Alps. Quat Sci Rev 25:1127–1136. https://doi.org/10.1016/j.quascirev.2005.10.006

Spötl C, Scholz D, Mangini A (2008) A terrestrial U/Th-dated stable isotope record of the Penultimate Interglacial. Earth Planet Sci Lett 276:283–292. https://doi.org/10.1016/j.epsl.2008.09.029

Staš M, Auersvald M, Vozka P (2021) Two-Dimensional Gas Chromatography Characterization of Pyrolysis Bio-oils: A Review. Energy and Fuels 35:8541–8557. https://doi.org/10.1021/acs.energyfuels.1c00553

Stocker TF, Qin D, Plattner G-K, et al (2013) IPCC, 2013: Climate Change 2013: The Physical Science Basis. Contribution of Working Group I to the Fifth Assessment Report of the Intergovernmental Panel on Climate Change. Cambridge (UK) and New York (USA)

Stoll DR, Carr PW (2017) Two-Dimensional Liquid Chromatography: A State of the Art Tutorial. Anal Chem 89:519–531. https://doi.org/10.1021/acs.analchem.6b03506

Stoll DR, Shoykhet K, Petersson P, Buckenmaier S (2017) Active Solvent Modulation: A Valve-Based Approach to Improve Separation Compatibility in Two-Dimensional Liquid Chromatography. Anal Chem 89:9260–9267. https://doi.org/10.1021/acs.analchem.7b02046

Sun D, Tan W, Pei Y, et al (2011) Late Quaternary environmental change of Yellow River Basin: An organic geochemical record in Bohai Sea (North China). Org Geochem 42:575–585. https://doi.org/10.1016/j.orggeochem.2011.04.011

Surratt JD, Gómez-González Y, Chan AWH, et al (2008) Organosulfate formation in biogenic secondary organic aerosol. J Phys Chem A 112:8345–8378. https://doi.org/10.1021/jp802310p

Surratt JD, Kroll JH, Kleindienst TE, et al (2007) Evidence for organosulfates in secondary organic aerosol. Environ Sci Technol 41:517–527. https://doi.org/10.1021/es062081q

Surratt JD, Murphy SM, Kroll JH, et al (2006) Chemical composition of secondary organic aerosol formed from the photooxidation of isoprene. J Phys Chem A 110:9665–9690. https://doi.org/10.1021/jp061734m

Swartz ME (2005) UPLC: An Introduction and Review. J Liq Chromatogr Relat Technol 28:1253–1263

Synder LR, Kirkland JJ (1979) Introduction to Modern Liquid Chromatography, 2nd edn. John Wiley & Sons Inc., New York

Szmigielski R, Surratt JD, Gómez-González Y, et al (2007) 3-methyl-1,2,3-butanetricarboxylic acid: An atmospheric tracer for terpene secondary organic aerosol. Geophys Res Lett 34:2–7. https://doi.org/10.1029/2007GL031338

Takemura T (2012) Distributions and climate effects of atmospheric aerosols from the preindustrial era to 2100 along Representative Concentration Pathways (RCPs) simulated using the global aerosol model SPRINTARS. Atmos Chem Phys 12:11555–11572. https://doi.org/10.5194/acp-12-11555-2012

Tarabanko VE, Petukhov DV, Selyutin GE (2004) New Mechanism for the Catalytic Oxidation of Lignin to Vanillin. Kinet Catal 45:569–577

Tarabanko VE, Tarabanko N (2017) Catalytic oxidation of lignins into the aromatic aldehydes: General process trends and development prospects. Int J Mol Sci 18:1–29. https://doi.org/10.3390/ijms18112421

Tarvainen V, Hakola H, Hellén H, et al (2005) Temperature and light dependence of the VOC emissions of Scots pine. Atmos Chem Phys 5:989–998. https://doi.org/10.5194/acp-5-989-2005

Thevenot M, Dignac MF, Rumpel C (2010) Fate of lignins in soils: A review. Soil Biol Biochem 42:1200–1211. https://doi.org/10.1016/J.SOILBIO.2010.03.017

Thompson JE (2018) Airborne Particulate Matter: Human Exposure and Health Effects

Thomsen D, Elm J, Rosati B, et al (2021) Large Discrepancy in the Formation of Secondary Organic Aerosols from Structurally Similar Monoterpenes. ACS Earth Sp Chem 5:632–644. https://doi.org/10.1021/acsearthspacechem.0c00332

Thurén A, Larsson P (1990) Phthalate Esters in the Swedish Atmosphere. Environ Sci Technol 24:554–559. https://doi.org/10.1021/es00074a015

Tian H, Xu J, Guan Y (2008) Comprehensive two-dimensional liquid chromatography (NPLC x RPLC) with vacuum-evaporation interface. J Sep Sci 31:1677–1685. https://doi.org/10.1002/jssc.200700559

Tinner W, Conedera M, Ammann B, et al (1998) Pollen and charcoal in lake sediments forest fires in southern Switzerland. The Holocene 8:31–42

Tobias HJ, Ziemann PJ (2000) Thermal desorption mass spectrometric analysis of organic aerosol formed from reactions of 1-tetradecene and O3 in the presence of alcohols and carhoxylic acids. Environ Sci Technol 34:2105–2115. https://doi.org/10.1021/es9907156

Toma HE, Szulejko JE, Sa GF, et al (2012) Protomers: formation, separation and characterization via travelling wave ion mobility mass spectrometry. J Mass Spectrom 47:712–719. https://doi.org/10.1002/jms.2999

Toth AJ, Haaz E, Szilagyi B, et al (2018) COD reduction of process wastewater with vacuum evaporation. Waste Treat Recover 3:1–7. https://doi.org/10.1515/wtr-2018-0001

Treble P, Shelley JMG, Chappell J (2003) Comparison of high resolution sub-annual records of trace elements in a modern (1911-1992) speleothem with instrumental climate data from southwest Australia. Earth Planet Sci Lett 216:141–153. https://doi.org/10.1016/S0012-821X(03)00504-1

Treble PC, Chappell J, Gagan MK, et al (2005) In situ measurement of seasonal d 18 O variations and analysis of isotopic trends in a modern speleothem from southwest Australia. https://doi.org/10.1016/j.epsl.2005.02.013

Trufelli H, Palma P, Famiglini G, Cappiello A (2011) An Overview of Matrix Effects in Liquid Chromatography-Mass Spectrometry. Mass Spectrom Rev 30:491–509

Tsigaridis K, Kanakidou M (2003) Global modelling of secondary organic aerosol in the troposphere: A sensitivity analysis. Atmos Chem Phys 3:1849–1869. https://doi.org/10.5194/acp-3-1849-2003

Tsigaridis K, Krol M, Dentener FJ, et al (2006) Change in global aerosol composition since preindustrial times. Atmos Chem Phys 6:5143–5162. https://doi.org/10.5194/acp-6-5143-2006

Turpin BJ, Saxena P, Andrews E (2000) Measuring and simulating particulate organics in the atmosphere: Problems and prospects. Atmos Environ 34:2983–3013. https://doi.org/10.1016/S1352-2310(99)00501-4

Uglietti C, Zapf A, Jenk TM, et al (2016) Radiocarbon dating of glacier ice: Overview, optimisation, validation and potential. Cryosphere 10:3091–3105. https://doi.org/10.5194/tc-10-3091-2016

van Beynen PE, Soto L, Pace-Graczyk K (2008) Paleoclimate reconstruction derived from speleothem strontium and δ13C in Central Florida. Quat Int 187:76–83. https://doi.org/10.1016/j.quaint.2007.03.019

Van Der Werf GR, Randerson JT, Giglio L, et al (2010) Global fire emissions and the contribution of deforestation, savanna, forest, agricultural, and peat fires (1997-2009). Atmos Chem Phys 10:11707–11735. https://doi.org/10.5194/acp-10-11707-2010

Van Dingenen R, Raes F, Putaud JP, et al (2004) A European aerosol phenomenology - 1: Physical characteristics of particulate matter at kerbside, urban, rural and background sites in Europe. Atmos Environ 38:2561–2577. https://doi.org/10.1016/j.atmosenv.2004.01.040

van Eijck A, Opatz T, Taraborrelli D, et al (2013) New tracer compounds for secondary organic aerosol formation from β-caryophyllene oxidation. Atmos Environ 80:122–130. https://doi.org/10.1016/j.atmosenv.2013.07.060

van Pinxteren D, Herrmann H (2007) Determination of functionalised carboxylic acids in atmospheric particles and cloud water using capillary electrophoresis/mass spectrometry. J Chromatogr A 1171:112–123. https://doi.org/10.1016/j.chroma.2007.09.021

Vanholme R, Demedts B, Morreel K, et al (2010) Lignin biosynthesis and structure. Plant Physiol 153:895–905. https://doi.org/10.1104/pp.110.155119

Veres D, Bazin L, Landais A, et al (2013) The Antarctic ice core chronology (AICC2012): An optimized multi-parameter and multi-site dating approach for the last 120 thousand years. Clim Past 9:1733–1748. https://doi.org/10.5194/cp-9-1733-2013

Vestenius M, Hellén H, Levula J, et al (2014) Acidic reaction products of monoterpenes and sesquiterpenes in atmospheric fine particles in a boreal forest. Atmos Chem Phys 14:7883–7893. https://doi.org/10.5194/acp-14-7883-2014

Vogel AL, Lauer A, Fang L, et al (2019) A Comprehensive Nontarget Analysis for the Molecular Reconstruction of Organic Aerosol Composition from Glacier Ice Cores. Environ Sci Technol 53:12565–12575. https://doi.org/10.1021/acs.est.9b03091

Vollweiler N, Scholz D, Mühlinghaus C, et al (2006) A precisely dated climate record for the last 9 kyr from three high alpine stalagmites, Spannagel Cave, Austria. Geophys Res Lett 33:. https://doi.org/10.1029/2006GL027662

Vonk RJ, Gargano AFG, Davydova E, et al (2015) Comprehensive Two-Dimensional Liquid Chromatography with Stationary-Phase-Assisted Modulation Coupled to High-Resolution Mass Spectrometry Applied to Proteome Analysis of Saccharomyces cerevisiae. https://doi.org/10.1021/acs.analchem.5b00708

Wang F, Ming J, Edwards R, et al (2020a) The fallout from Fukushima Daiichi nuclear accident profiles a new dating reference in ice and comparison with the Chernobyl accident. Environ Res Lett 15:84016. https://doi.org/10.1088/1748-9326/ab83a9

Wang H, Xie SP, Zheng XT, et al (2020b) Dynamics of Southern Hemisphere Atmospheric Circulation Response to Anthropogenic Aerosol Forcing. Geophys Res Lett 47:1–10. https://doi.org/10.1029/2020GL089919

Wang W, Kourtchev I, Graham B, et al (2005a) Characterization of oxygenated derivatives of isoprene related to 2-methyltetrols in Amazonian aerosols using trimethylsilylation and gas chromatography/ion trap mass spectrometry. Rapid Commun Mass Spectrom 19:1343–1351. https://doi.org/10.1002/RCM.1940

Wang Y, Cheng H, Lawrence Edwards R, et al (2005b) The Holocene Asian Monsoon: Link to Solar Changes and North Atlantic Climate. Science (80-) 308:854–857. https://doi.org/10.1029/2002GL014910

Wang Y, Hu M, Wang YC, et al (2020c) Comparative Study of Particulate Organosulfates in Contrasting Atmospheric Environments: Field Evidence for the Significant Influence of Anthropogenic Sulfate and NOx. Environ Sci Technol Lett 7:787–794. https://doi.org/10.1021/acs.estlett.0c00550

Wang Y, Ren J, Huang XHH, et al (2017) Synthesis of Four Monoterpene-Derived Organosulfates and Their Quantification in Atmospheric Aerosol Samples. Environ Sci Technol 51:6791–6801. https://doi.org/10.1021/acs.est.7b01179

Waters (2012) Waters Oasis SPE. In: Homepage Produktbeschreibung. http://www.waters.com/waters/de_DE/Waters-Oasis-Sample-Extraction-SPE-Products/nav.htm?cid=513209&locale=de_DE. Accessed 15 Mar 2021

Waters (2021) No Title. https://www.waters.com/waters/en_US/Waters-Oasis-Sample-Extraction-SPE-Products/nav.htm?cid=513209&locale=en_US. Accessed 27 Aug 2021

Went FW (1960) Blue hazes in the atmosphere. Nature 187:641–643. https://doi.org/10.1038/187641a0

Wesely ML, Hicks BB (2000) A review of the current status of knowledge on dry deposition. Atmos Environ 34:2261–2282. https://doi.org/10.1016/S1352-2310(99)00467-7

Wiedner E, Scholz D, Mangini A, et al (2008) Investigation of the stable isotope fractionation in speleothems with laboratory experiments. Quat Int 187:15–24. https://doi.org/10.1016/j.quaint.2007.03.017

Wilcox LJ, Highwood EJ, Dunstone NJ (2013) The influence of anthropogenic aerosol on multi-decadal variations of historical global climate. Environ Res Lett 8:. https://doi.org/10.1088/1748-9326/8/2/024033

Williams J, De Reus M, Krejci R, et al (2002) Application of the variability-size relationship to atmospheric aerosol studies: Estimating aerosol lifetimes and ages. Atmos Chem Phys 2:133–145. https://doi.org/10.5194/acp-2-133-2002

Woiwode U, Reischl RJ, Buckenmaier S, et al (2018) Imaging Peptide and Protein Chirality via Amino Acid Analysis by Chiral × Chiral Two-Dimensional Correlation Liquid Chromatography. Anal Chem 90:7963–7971. https://doi.org/10.1021/acs.analchem.8b00676

Wolff EW, Fischer H, Fundel F, et al (2006) Southern Ocean sea-ice extent, productivity and iron flux over the past eight glacial cycles. Nature 440:491–496. https://doi.org/10.1038/nature04614

Wong CI, Breecker DO (2015) Advancements in the use of speleothems as climate archives. Quat Sci Rev 127:1–18. https://doi.org/10.1016/j.quascirev.2015.07.019

Wozniak AS, Bauer JET, Sleighter RL, et al (2008) Technical Note: Molecular characterization of aerosol-derived water soluble organic carbon using ultrahigh resolution electrospray ionization Fourier transform ion cyclotron resonance mass spectrometry. Atmos Chem Phys 8:5099–5111. https://doi.org/10.5194/acp-8-5099-2008

Xia H, Attygalle AB (2016) Effect of Electrospray Ionization Source Conditions on the Tautomer Distribution of Deprotonated p-Hydroxybenzoic Acid in the Gas Phase. Anal Chem 88:6035–6043. https://doi.org/10.1021/acs.analchem.6b01230

Xie S, Yao T, Kang S, et al (2000) Geochemical analyses of a Himalayan snowpit profile: Implications for atmospheric pollution and climate. Org Geochem 31:15–23. https://doi.org/10.1016/S0146-6380(99)00133-3

Xu C, Arneil R, Arancon D, et al (2014) Lignin depolymerisation strategies: towards valuable chemicals and fuels. Chem Soc Rev 43:7485–7500. https://doi.org/10.1039/c4cs00235k

Yan G, Kaiser K (2018a) A rapid and sensitive method for the analysis of lignin phenols in environmental samples using ultra-high performance liquid chromatography-electrospray ionization-tandem mass spectrometry with multiple reaction monitoring. Anal Chim Acta 1023:74–80. https://doi.org/10.1016/j.aca.2018.03.054

Yan G, Kaiser K (2018b) Ultralow Sample Volume Cupric Sulfate Oxidation Method for the Analysis of Dissolved Lignin. Anal Chem 90:9289–9295. https://doi.org/10.1021/acs.analchem.8b01867

Yang H, Ding W, Zhang CL, et al (2011) Occurrence of tetraether lipids in stalagmites: Implications for sources and GDGT-based proxies. Org Geochem 42:108–115. https://doi.org/10.1016/J.ORGGEOCHEM.2010.11.006

Yang J, Li G, Rao W, Ji J (2009) Isotopic evidences for provenance of East Asian Dust. Atmos Environ 43:4481–4490. https://doi.org/10.1016/j.atmosenv.2009.06.035

Yang L, Yu LE (2008) Measurements of oxalic acid, oxalates, malonic acid, and malonates in atmospheric particulates. Environ Sci Technol 42:9268–9275. https://doi.org/10.1021/es801820z

Yao P, Schwab VF, Roth VN, et al (2013) Levoglucosan concentrations in ice-core samples from the Tibetan Plateau determined by reverse-phase high-performance liquid chromatography-mass spectrometry. J Glaciol 59:599–612. https://doi.org/10.3189/2013JoG12J157

Yasmeen F, Vermeylen R, Szmigielski R, et al (2010) Terpenylic acid and related compounds: Precursors for dimers in secondary organic aerosol from the ozonolysis of α-and β-pinene. Atmos Chem Phys 10:9383–9392. https://doi.org/10.5194/acp-10-9383-2010

Yee L, Isaacman-VanWertz G, Wernis R, et al (2018) Observations of sesquiterpenes and their oxidation products in central Amazonia during the wet and dry seasons. Atmos Chem Phys Discuss 1–31. https://doi.org/10.5194/acp-2018-191

You C, Song L, Xu B, Gao S (2016) Method for determination of levoglucosan in snow and ice at trace concentration levels using ultra-performance liquid chromatography coupled with triple quadrupole mass spectrometry. Talanta 148:534–538. https://doi.org/10.1016/j.talanta.2015.11.030

Zahardis J, Petrucci GA (2007) The oleic acid-ozone heterogeneous reaction system: Products, kinetics, secondary chemistry, and atmospheric implications of a model system - A review. Atmos Chem Phys 7:1237–1274. https://doi.org/10.5194/acp-7-1237-2007

Zakzeski J, Bruijnincx PCA, Jongerius AL, Weckhuysen BM (2010) The catalytic valorization of lignin for the production of renewable chemicals. Chem Rev 110:3552–3599. https://doi.org/10.1021/cr900354u

Zangrando R, Barbaro E, Vecchiato M, et al (2016) Levoglucosan and phenols in Antarctic marine, coastal and plateau aerosols. Sci Total Environ 544:606–616. https://doi.org/10.1016/j.scitotenv.2015.11.166

Zemankova K, Brechler J (2010) Emissions of biogenic VOC from forest ecosystems in central Europe: Estimation and comparison with anthropogenic emission inventory. Environ Pollut 158:462–469. https://doi.org/10.1016/j.envpol.2009.08.032

Zennaro P, Kehrwald N, McConnell JR, et al (2014) Fire in ice: Two millennia of boreal forest fire history from the Greenland NEEM ice core. Clim Past 10:1905–1924. https://doi.org/10.5194/cp-10-1905-2014

Zhang L, Wilcox LJ, Dunstone NJ, et al (2021) Future changes in Beijing haze events under different anthropogenic aerosol emission scenarios. Atmos Chem Phys 21:7499–7514. https://doi.org/10.5194/acp-21-7499-2021

Zhang R, Wang L, Khalizov AF, et al (2009) Formation of nanoparticles of blue haze enhanced by anthropogenic pollution. Proc Natl Acad Sci U S A 106:17650–17654. https://doi.org/10.1073/pnas.0910125106

Zhang X, Yang W, Dong C (2013) Levoglucosan formation mechanisms during cellulose pyrolysis. J Anal Appl Pyrolysis 104:19–27. https://doi.org/10.1016/j.jaap.2013.09.015

Zhang YY, Mueller L, Winterhalter R, et al (2010) Seasonal cycle and temperature dependence of pinene oxidation products, dicarboxylic acids and nitrophenols in fine and coarse air particulate matter. Atmos Chem Phys 10:7859–7873. https://doi.org/10.5194/acp-10-7859-2010

Zhao J, Levitt NP, Zhang R, Chen J (2006) Heterogeneous reactions of methylglyoxal in acidic media: Implications for secondary organic aerosol formation. Environ Sci Technol 40:7682–7687. https://doi.org/10.1021/es060610k

Zhao R, Aljawhary D, Lee AKY, Abbatt JPD (2017) Rapid Aqueous-Phase Photooxidation of Dimers in the α-Pinene Secondary Organic Aerosol. https://doi.org/10.1021/acs.estlett.7b00148

Zhao R, Mungall EL, Lee AKY, et al (2014) Aqueous-phase photooxidation of levoglucosan – A mechanistic study using aerosol time-of-flight chemical ionization mass spectrometry (Aerosol ToF-CIMS). Atmos Chem Phys 14:9695–9705. https://doi.org/10.5194/acp-14-9695-2014

Zhao W, Hopke PK (2006) Source identification for fine aerosols in Mammoth Cave National Park. Atmos Res 80:309–322. https://doi.org/10.1016/j.atmosres.2005.10.002

Zhao Z, Tolentino R, Lee J, et al (2019) Interfacial Dimerization by Organic Raical Reactions uring Heterogeneous Oxiative Aging of Oxygenate Organic Aerosols. J Phys Chem A 123:10782–10792. https://doi.org/10.1021/acs.jpca.9b10779

Zhu J, Penner JE (2020) Indirect Effects of Secondary Organic Aerosol on Cirrus Clouds. J Geophys Res Atmos 125:. https://doi.org/10.1029/2019JD032233

Ziemann PJ (2002) Evidence for low-volatility diacyl peroxides as a nucleating agent and major component of aerosol formed from reactions of O3 with cyclohexene and homologous compounds. J Phys Chem A 106:4390–4402. https://doi.org/10.1021/jp012925m

Zirbes M, Schmitt D, Beiser N, et al (2019) Anodic Degradation of Lignin at Active Transition Metal-based Alloys and Performance-enhanced Anodes. ChemElectroChem 6:155–161. https://doi.org/10.1002/celc.201801218

Zubarev RA, Makarov A (2013) Orbitrap mass spectrometry. Anal Chem 85:5288–5296. https://doi.org/10.1021/ac4001223

Zupan Hajna N (2003) Chemical Weathering of Limestones and Dolomites in A Cave Environment. Speleogenes Evol Karst Aquifers 3:1–6

Zuth C (2018) Organic Trace Analysis using High Resolution Mass Spectrometry for the Characterization of Ancient, Present and Simulated Atmospheric Systems. Johannes Gutenberg University Mainz

11. Appendix

11.1 Supplementary material chapter 5

Table S 1: Flowstone samples from Daves Cave with the respective depths in the flowstone (mm), measuring points (mm) and associated errors for age determination (kyrs BP), the sample weight (g) and weight of the remaining polymeric resin (g), re-calculated to the differential weight (g) representing the actual sample weight and the final volume (mL) of the dissolved flowstone sample.

Sample name	Depth (mm)	Measuring point (mm)	Error (mm)	Age (kyrs BP)	Error (kyrs BP)	Sample weight (g)	Resin weight (g)	Differential weight (g)	Volume HCl/H_2O [1:1] (mL)
DC15-3	18-26					6.31	2.76	3.55	30
DC15-4	26-35	29	1	1.614	0.052	9.64	4.12	5.52	24
DC15-5	35-46	34	1.5	5.816	0.067	8.97	3.89	5.08	24
DC15-6	46-58					11.47	5.20	6.27	28
DC15-7	58-70	63	1	6.244	0.047	11.21	5.22	5.99	24
DC15-8	70-81					11.39	5.15	6.24	28
DC15-9	81-92	83.5	4.5	6.553	0.051	9.37	4.56	4.81	24
DC15-10	92-103	92.5	1.5	8.994	0.08	10.21	5.05	5.16	24
DC15-11	103-111					7.61	3.76	3.85	20
DC15-12	111-121					10.10	4.96	5.14	24
DC15-13	121-131	126	1	10.667	0.119	9.04	4.39	4.65	24
DC15-14	131-141					8.12	3.63	4.49	20
DC15-15	141-151					9.47	4.14	5.33	24
DC15-16	151-161	157	3	12.125	0.094	9.44	4.05	5.39	24
DC15-17	161-170					9.03	4.03	5.00	24
DC15-18	170-180					9.27	4.41	4.86	24
DC15-19	180-190	180	2	15.046	0.123	9.29	4.53	4.76	24
DC15-20	190-200					9.60	4.70	4.90	24

Table S 2: Flowstone samples from Waipuna Cave with the respective depths in the flowstone (mm), measuring points (mm) and associated errors for age determination (kyrs BP), the sample weight (g) and weight of the remaining polymeric resin (g), re-calculated to the differential weight (g) representing the actual sample weight and the final volume (mL) of the dissolved flowstone sample.

Sample name	Depth (mm)	Measuring point (mm)	Error (mm)	Age (kyrs BP)	Error (kyrs BP)	Sample weight (g)	Resin weight (g)	Differential weight (g)	Volume HCl/H_2O [1:1] (mL)
WP15-1.1-3	20-30					9.27	5.04	4.23	24
WP15-1.1-4	30-40					9.98	5.55	4.43	24
WP15-1.1-5	40-50					10.96	6.25	4.71	24
WP15-1.1-6	50-60					10.12	5.42	4.70	24
WP15-1.1-7	60-70	62	3	7.082	0.420	9.00	4.63	4.37	24
WP15-1.1-8	70-80					10.68	5.69	4.99	24
WP15-1.1-9	80-90					9.86	5.42	4.44	24
WP15-1.1-10	90-100					9.39	5.45	3.94	20
WP15-1.1-11	100-110					8.83	5.19	3.64	20
WP15-1.1-12	110-120					10.43	5.99	4.44	24
WP15-1.1-13	120-130					10.21	5.73	4.48	22
WP15-1.1-14	130-140					9.16	5.01	4.15	20
WP15-1.1-15	140-150	144.5	3.5	10.71	0.382	9.99	5.43	4.56	26
WP15-1.1-16	150-160					9.34	5.20	4.14	26
WP15-1.1-17	160-170					9.38	5.30	4.08	26
WP15-1.1-18	210-220					9.59	5.55	4.04	26
WP15-1.1-19	260-270					8.06	4.52	3.54	26
WP15-1.2-20	310-320					11.20	4.80	6.40	30
WP15-1.2-21	320-330					11.73	5.16	6.57	30
WP15-1.2-22	330-340					12.87	5.79	7.08	40
WP15-1.2-23	380-390					10.99	4.62	6.37	30
WP15-1.2-24	430-440							7.08	30
WP15-1.2-25	440-450							6.91	30
WP15-1.2-26	450-460	453	3	17.317	0.191			6.53	30

11.2 Supplementary material chapter 6

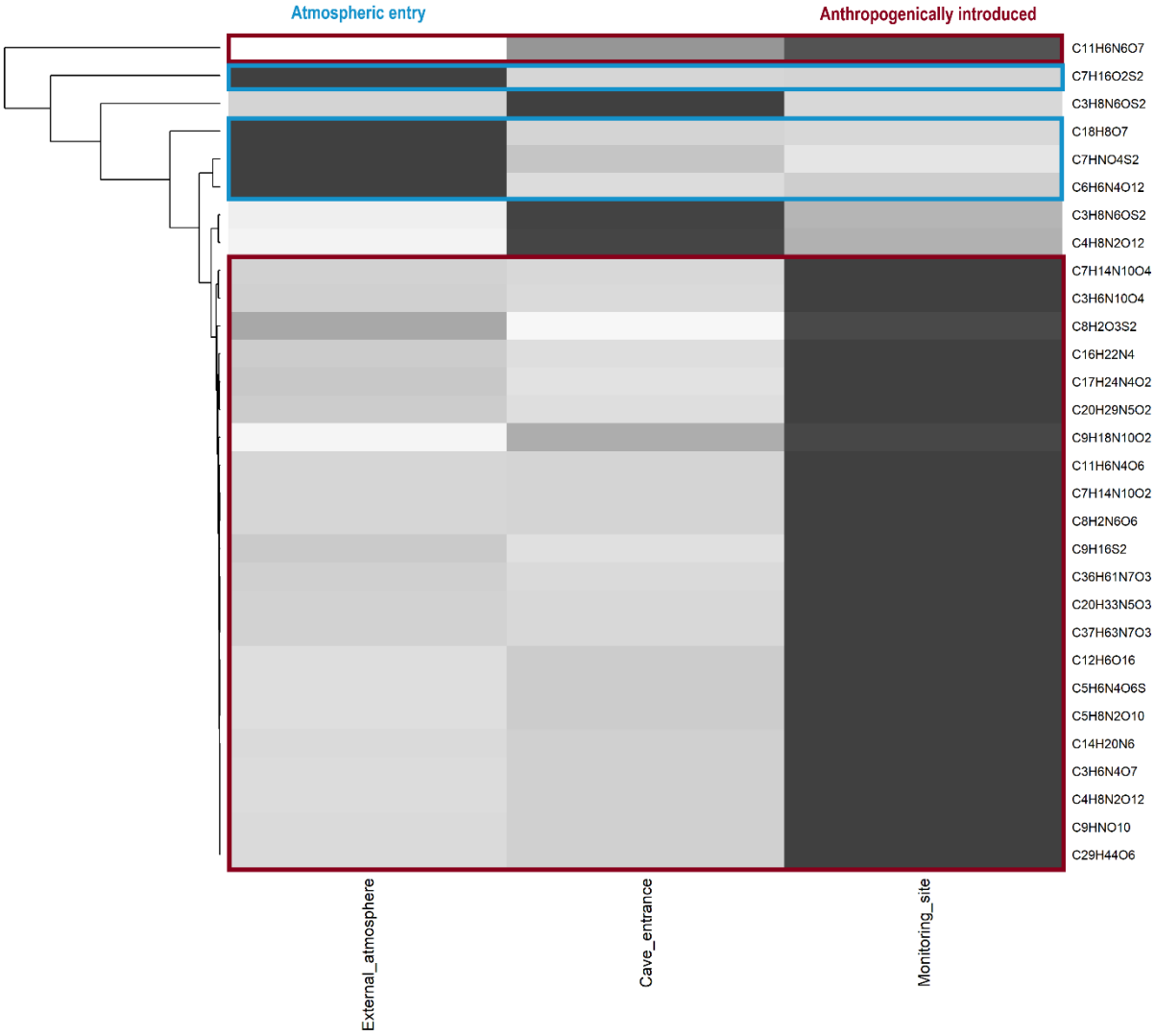

Figure S 1: Heatmap of signal intensities of the 50 most intense signals actively collected on filters at the different sampling sites. Rows were hierarchically clustered based on previous z-score normalization. Columns represent the different sampling sites. Distinct groups of the hierarchal clustering were assigned to compounds of atmospheric entry (blue) and human entry (red) based on their intensity distribution.

11.3 Supplementary material chapter 7

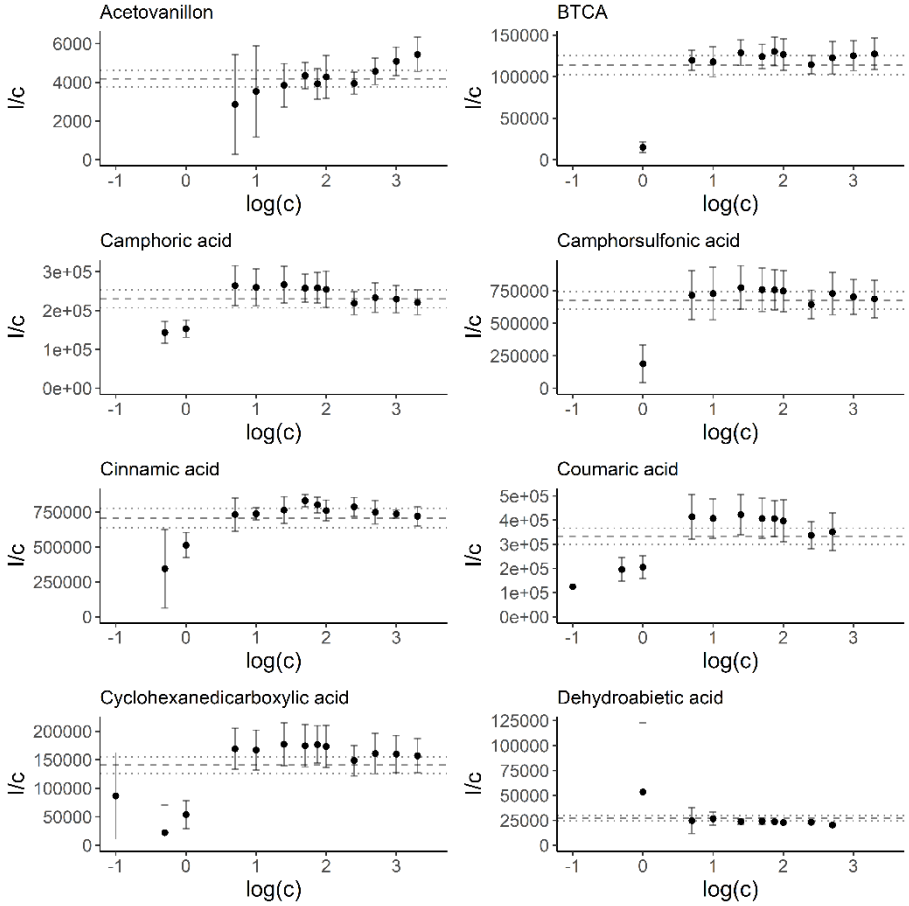

Figure S 2: Plots of intensity to concentration ratio (I/c) to the logarithm of concentration of a series of standard solutions with increasing concentrations for evaluation of linearity of the LC-MS methods on the PFP and HILIC column for selected compounds (Letters A-D).

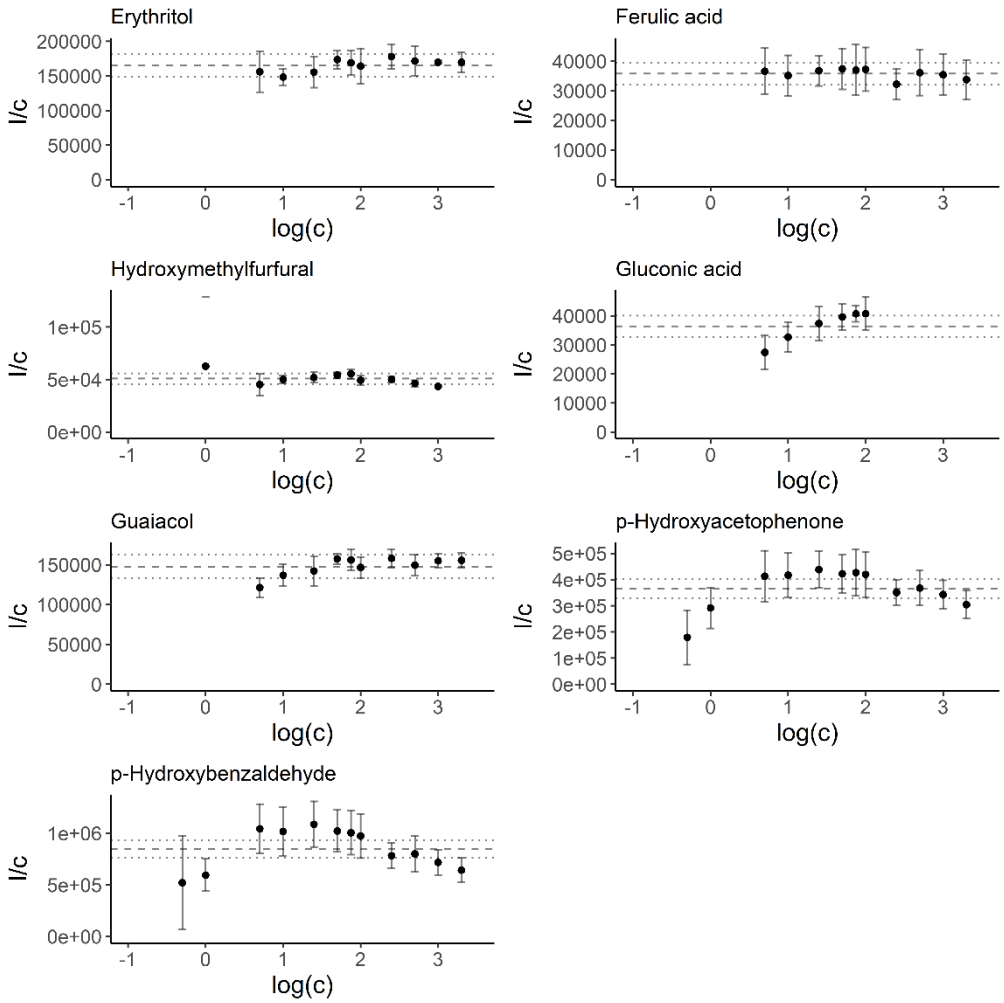

Figure S 3: Plots of intensity to concentration ratio (I/c) to the logarithm of concentration of a series of standard solutions with increasing concentrations for evaluation of linearity of the LC-MS methods on the PFP and HILIC column for selected compounds (Letters E-H).

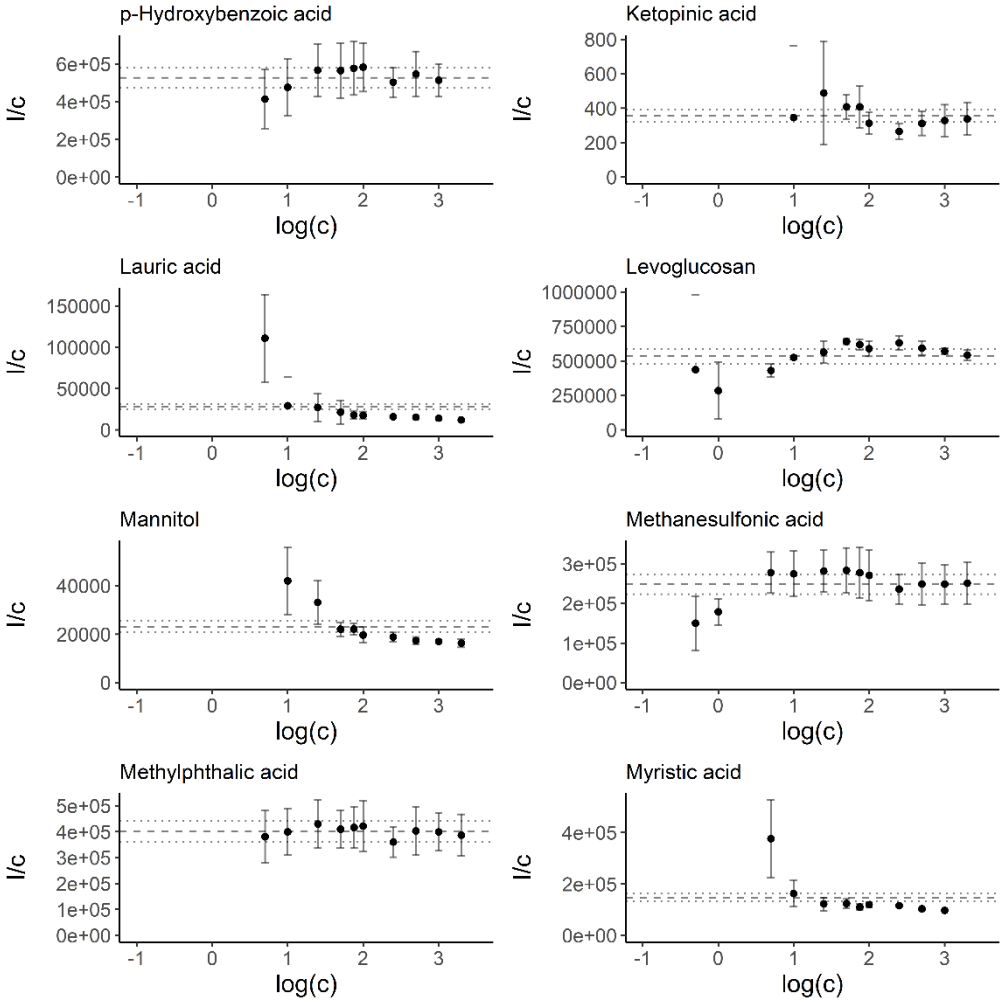

Figure S 4: Plots of intensity to concentration ratio (I/c) to the logarithm of concentration of a series of standard solutions with increasing concentrations for evaluation of linearity of the LC-MS methods on the PFP and HILIC column for selected compounds (Letters H-M).

Table S 3: LOD (ng/mL) and LOQ (ng/mL) of analytes measured either by HILIC or RP-MS, the working range (ng/mL) determined by the regression coefficient and linearity range determined by plotting of the signal intensity divided by the concentration to the logarithm of the concentration.

Analyte	**Method**	**LOD (ng/mL)**	**LOQ (ng/mL)**	**Working range (ng/mL)**	**Linearity (ng/mL)**
Cinnamic acid	HILIC	0.64	2.13	0.5-2000	5-2000
Xylitol	HILIC	0.65	2.16	0.5-500	5-500
Levoglucosan	HILIC	0.71	2.36	0.5-2000	10-2000
Erythritol	HILIC	0.73	2.44	1-2000	5-2000
Ketopinic acid	HILIC	0.74	2.46	1-2000	5-2000
p-Coumaric acid	HILIC	0.77	2.57	0.5-2000	5-2000
p-Hydroxybenzoic acid	HILIC	0.85	2.82	0.5-1000	5-1000
cis-Pinonic acid	HILIC	1.02	3.4	0.5-2000	5-2000
Camphorsulfonic acid	HILIC	1.20	4.01	0.5-2000	5-2000
Guaiacol	HILIC	1.92	6.4	1-2000	5-2000
Hydroxymethylfurfural	HILIC	3.84	12.8	1-1000	5-1000
Dehydroabietic acid	HILIC	4.21	14.04	0.1-500	1-500
Myristic acid	HILIC	23.22	77.41	0.1-1000	5-1000
Malic acid	HILIC	50	114.48	50-2000	75-1000
Mannitol	HILIC	37.27	124.25	5-2000	50-2000
Lauric acid	HILIC	70.22	234.07	0.5-2000	10-2000
Palmitic acid	HILIC	593.41	1978.02	10-1000	50-1000
Pimelic acid	PFP	0.5	0.82	0.5-2000	5-2000
trans-1,2-cyclohexanedicarboxylic acid	PFP	0.36	1.19	0.1-2000	5-2000
Pinic acid	PFP	0.5	1.2	0.5-2000	5-2000
MBTCA	PFP	0.5	1.51	0.5-2000	5-2000
BTCA	PFP	1	2.13	1-2000	5-2000
trans-Ferulic acid	PFP	0.66	2.2	0.5-2000	5-2000
Terebic acid	PFP	0.75	2.51	0.5-2000	5-2000
Methanesulfonic acid	PFP	0.81	2.71	0.5-2000	5-2000
Camphoric acid	PFP	0.83	2.76	0.5-2000	5-2000
Syringic acid	PFP	1.19	3.96	5-2000	10-2000
p-Hydroxyacetophenone	PFP	1.27	4.22	0.5-2000	5-100
Salicylic acid	PFP	1.52	5.07	1-2000	5-2000
Methylphthalic acid	PFP	1.66	5.52	5-2000	5-2000
p-Hydroxybenzaldehyde	PFP	1.66	5.54	0.5-500	5-100
Phthalic acid	PFP	2.64	8.79	1-2000	5-2000
Vanillin	PFP	2.82	9.39	1-2000	5-2000
Gluconic acid	PFP	5	13.47	5-100	5-100
Syringaldehyde	PFP	5	15.24	5-2000	10-1000
Acetovanillon	PFP	8.34	27.8	5-2000	25-250
Acetosyringone	PFP	15.82	52.72	10-2000	25-2000
Vanillic acid	PFP	17.47	58.24	1-2000	5-2000

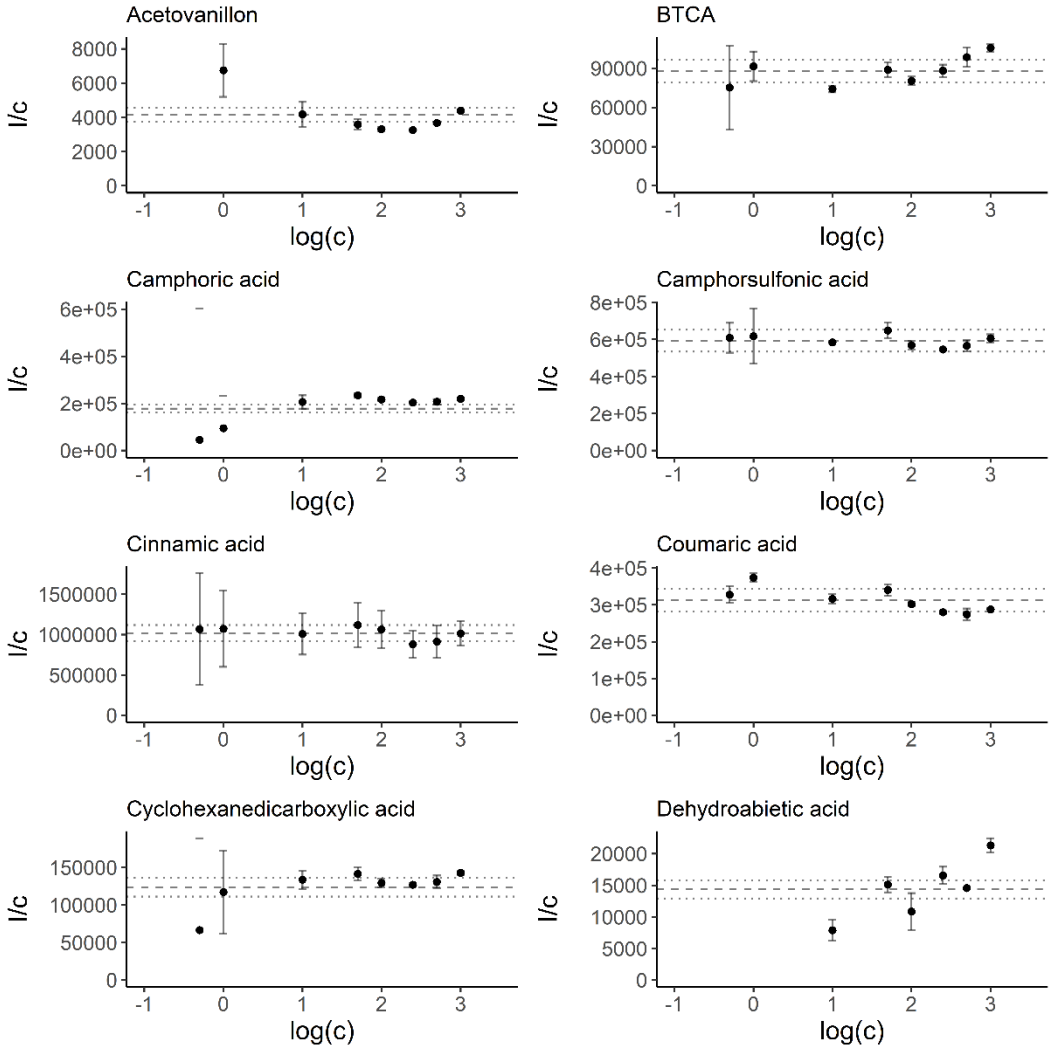

Figure S 5: Plots of intensity to concentration ratio (I/c) to the logarithm of concentration of a series of standard solutions with increasing concentrations for evaluation of linearity of the WAX-SPE method measured on the PFP and HILIC columns for selected compounds (Letters A-D).

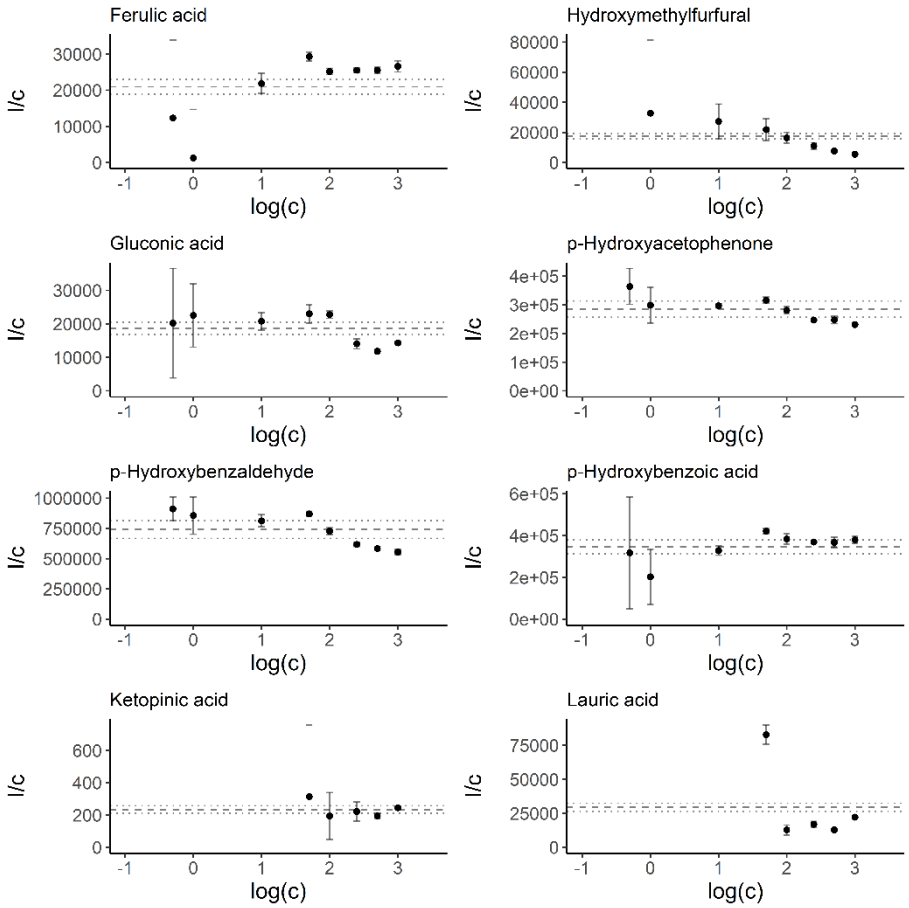

Figure S 6: Plots of intensity to concentration ratio (I/c) to the logarithm of concentration of a series of standard solutions with increasing concentrations for evaluation of linearity of the WAX-SPE method measured on the PFP and HILIC columns for selected compounds (Letters E-L).

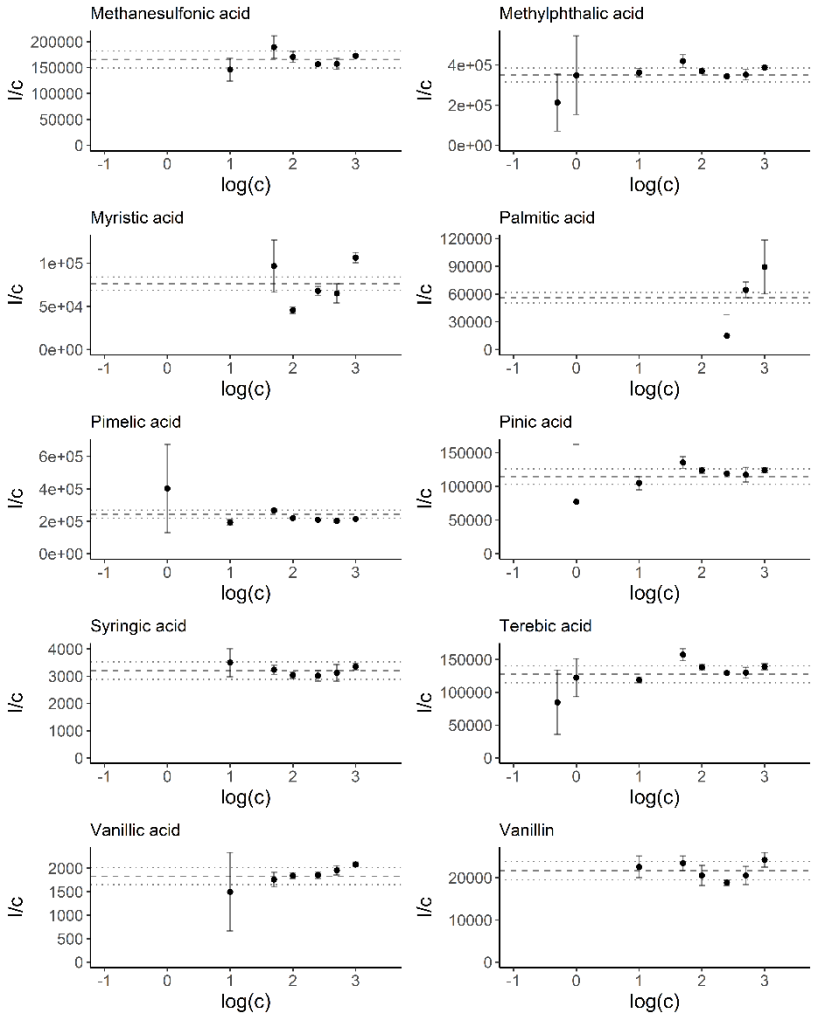

Figure S 7: Plots of intensity to concentration ratio (I/c) to the logarithm of concentration of a series of standard solutions with increasing concentrations for evaluation of linearity of the WAX-SPE method measured on the PFP and HILIC columns for selected compounds (Letters M-V).

Table S 4: Data on Colle Gnifetti samples including sample ID, date of extraction, weight of the respective empty and sample-filled vial, total volume of sample, middle depth of the ice core and the estimated calculated age.

Sample ID	Date of extraction	Weight empty vial (g)	Weight full vial (g)	Total volume (mL)	Mid depth (m)	Estimated age
CG25	05/10/2021	31.3875	61.2500	29.9	16.52	1995
CG26	05/10/2021	31.4909	62.5209	31.0	17.22	1993
CG27	05/10/2021	31.3712	64.3304	33.0	17.93	1992
CG28	26/10/2021	31.1380	64.6232	33.5	18.63	1990
CG29	26/10/2021	31.1580	62.5931	31.4	19.32	1988
CG30	26/10/2021	31.2656	61.8279	30.6	20.03	1985
CG31	27/10/2021	31.0735	61.5662	30.5	20.75	1984
CG32	27/10/2021	31.4798	61.6473	30.2	21.45	1982
CG33	27/10/2021	31.4880	62.2218	30.7	22.14	1981
CG34	16/11/2021	31.2927	63.5887	32.3	22.85	1979
CG35	16/11/2021	31.2600	64.1479	32.9	23.59	1977
CG36	16/11/2021	31.3790	63.6158	32.2	24.28	1976
CG37	17/11/2021	31.3835	62.0261	30.6	24.94	1974
CG38	24/11/2021	31.3835	62.3884	31.0	25.64	1972
CG39	24/11/2021	31.4488	63.2638	31.8	26.37	1969
CG40	30/11/2021	31.2637	61.9993	30.7	27.06	1966
CG41	30/11/2021	31.4366	63.8250	32.4	27.73	1964
CG42	30/11/2021	31.1847	63.5557	32.4	28.41	1961
CG43	01/12/2021	31.3042	63.2342	31.9	29.14	1958
CG44	01/12/2021	31.2191	63.7861	32.6	29.83	1954
CG45	01/12/2021	31.1615	60.7282	29.6	30.51	1952
CG46	07/12/2021	31.4531	62.8652	31.4	31.20	1948
CG47	07/12/2021	31.1274	63.7374	32.6	31.90	1944
CG48	07/12/2021	31.2797	62.1403	30.9	32.59	1941
CG49	08/12/2021	31.4016	64.3872	33.0	33.31	1937
CG50	08/12/2021	31.4140	63.9918	32.6	34.01	1932
CG51	08/12/2021	31.3152	63.5121	32.2	34.69	1929
CG52	14/12/2021	31.2148	64.4802	33.3	35.37	1927
CG53	14/12/2021	31.5770	64.3347	32.8	36.03	1924
CG66	14/12/2021	31.4586	64.6473	33.2	44.56	1860
CG67	15/12/2021	31.2936	64.4334	33.1	45.12	1855
CG68	15/12/2021	30.9747	64.2807	33.3	45.73	1851
CG69	15/12/2021	31.5120	63.5727	32.1	46.43	1844

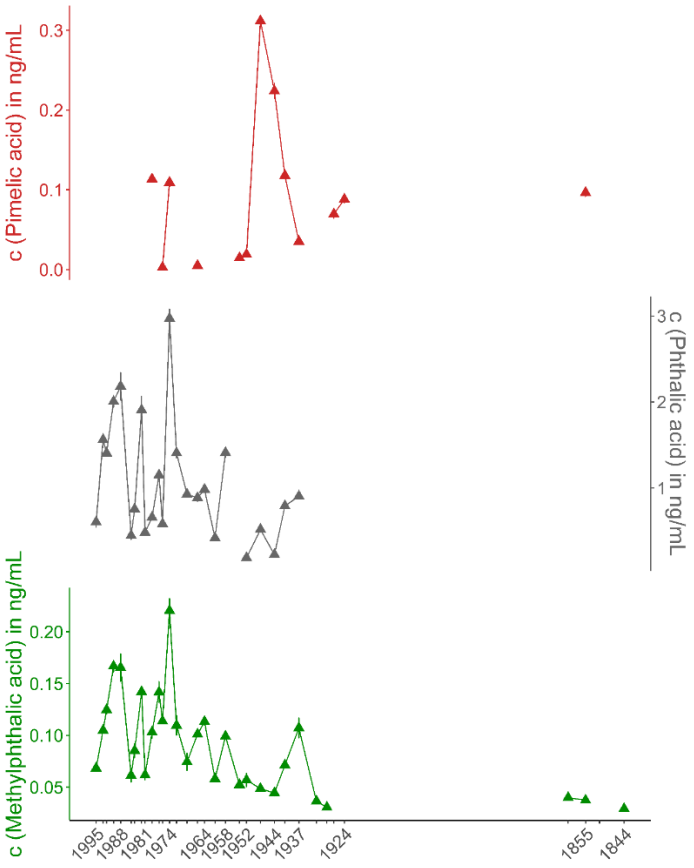

Figure S 8: Historic records of anthropogenic SOA marker compounds in ng/mL detected in Colle Gnifetti ice core samples from 1844 to 1995.

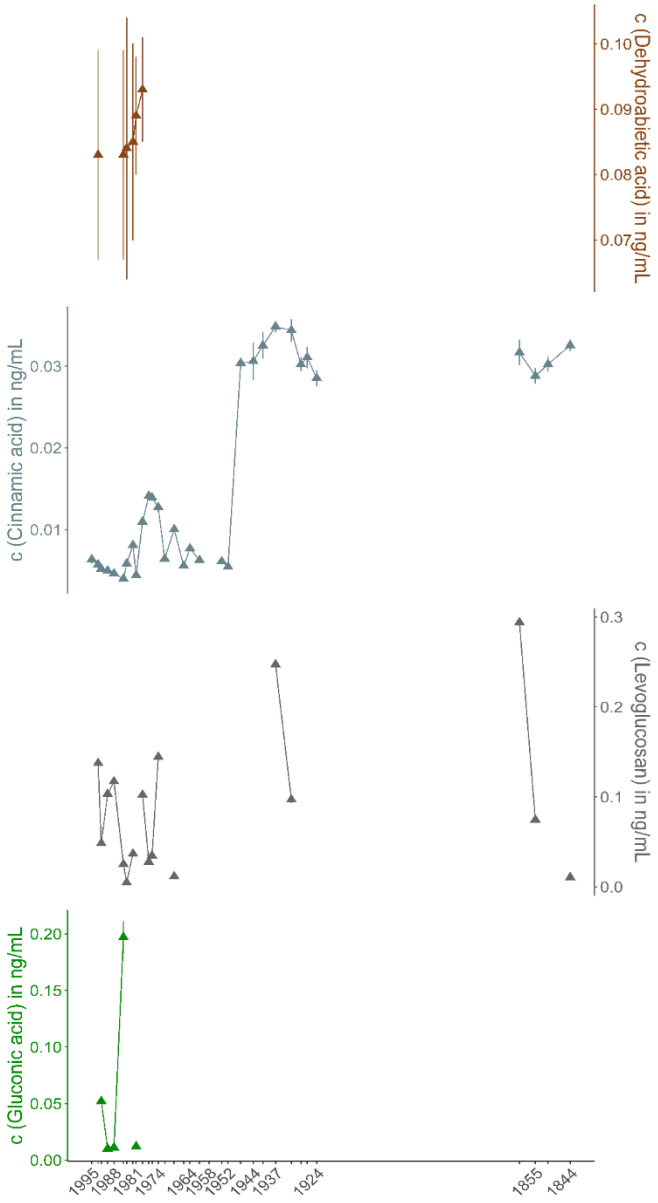

Figure S 9: Historic records of biomass burning markers from resin (dehydroabietic acid), lignin (cinnamic acid), and cellulose (levoglucosan and gluconic acid) in ng/mL detected in Colle Gnifetti ice core samples from 1844 to 1995.

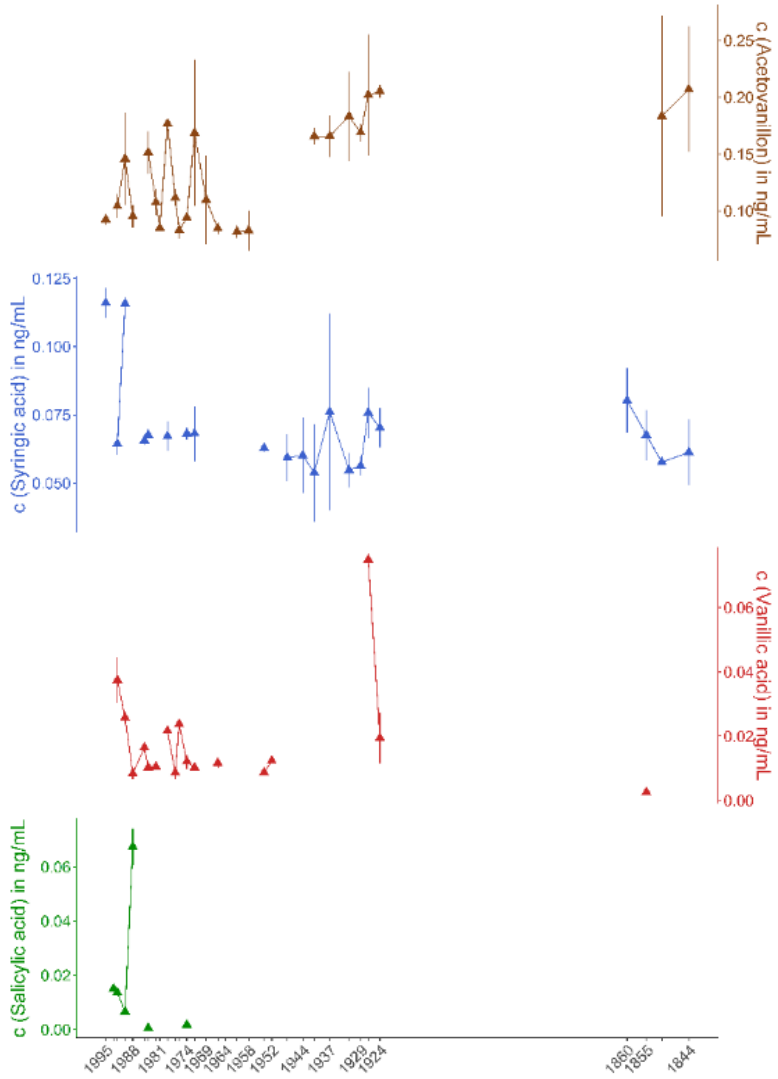

Figure S 10: Historic records of biomass burning markers from lignin (acetovanillon, syringic acid, vanillic acid, salicylic acid) in ng/mL detected in Colle Gnifetti ice core samples from 1844 to 1995.

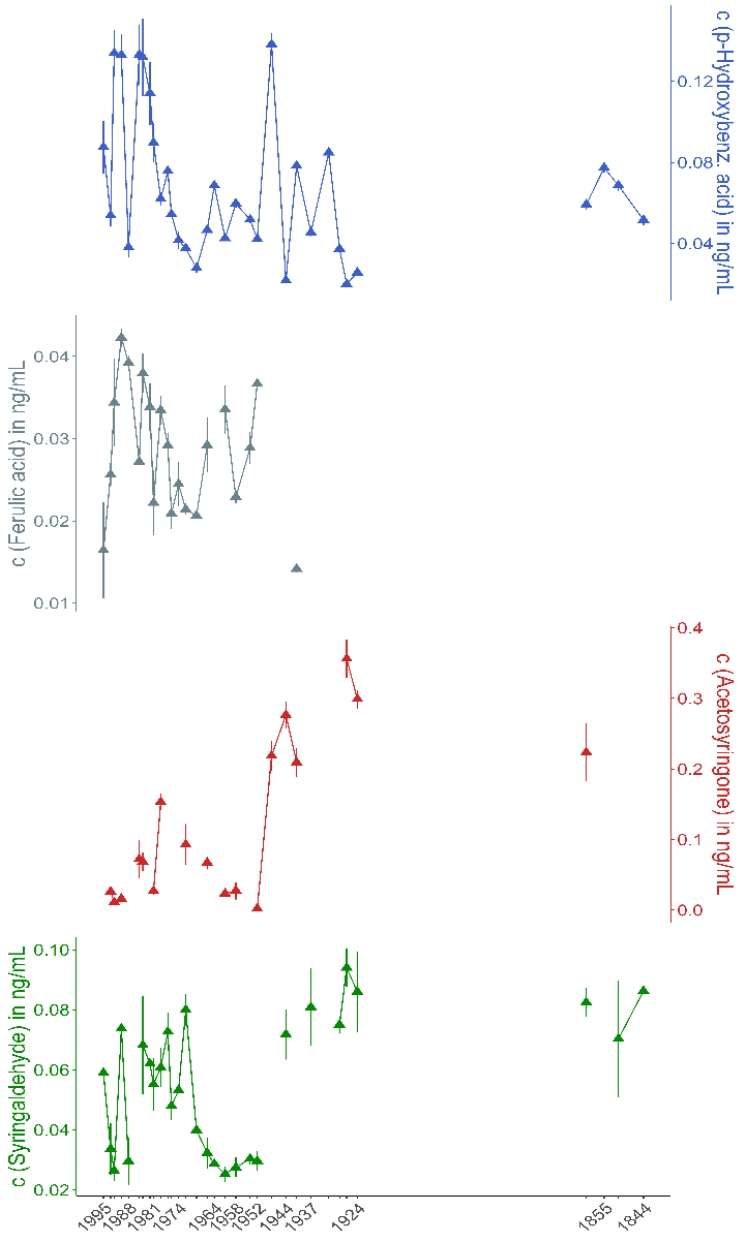

Figure S 11: Historic records of biomass burning markers from lignin (p-hydroxybenzoic acid, ferulic acid, acetosyringone, syringaldehyde) in ng/mL detected in Colle Gnifetti ice core samples from 1844 to 1995.

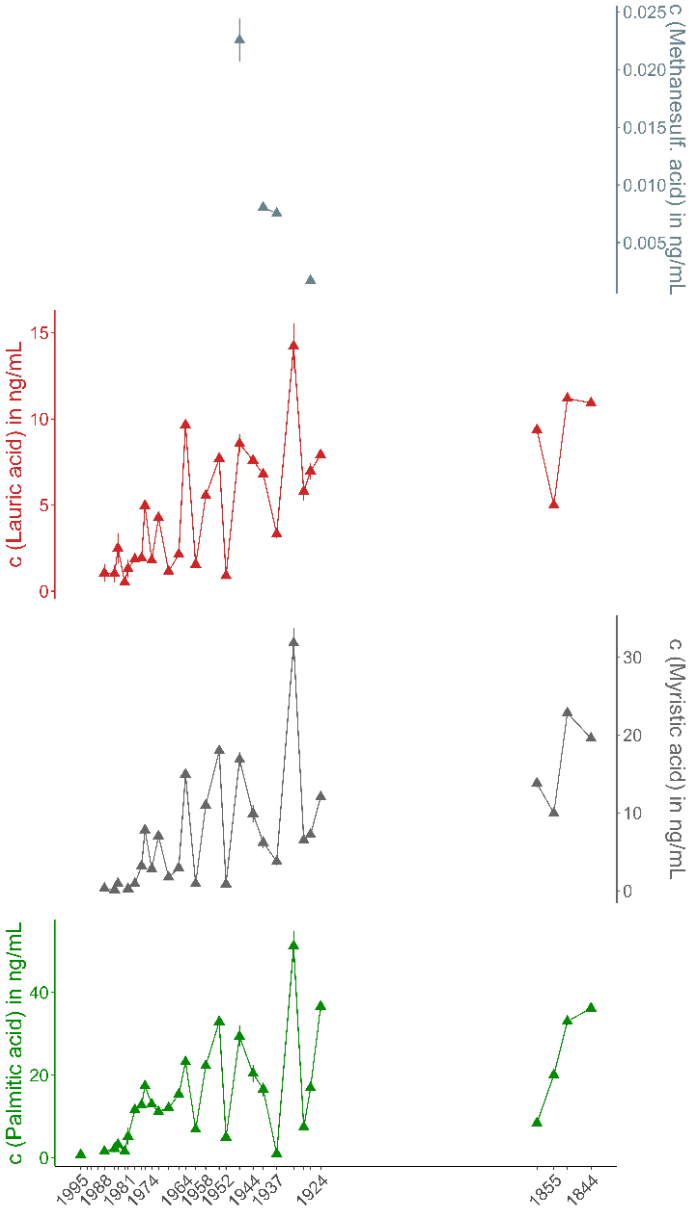

Figure S 12: Historic records of sea spray emission markers in ng/mL detected in Colle Gnifetti ice core samples from 1844 to 1995.

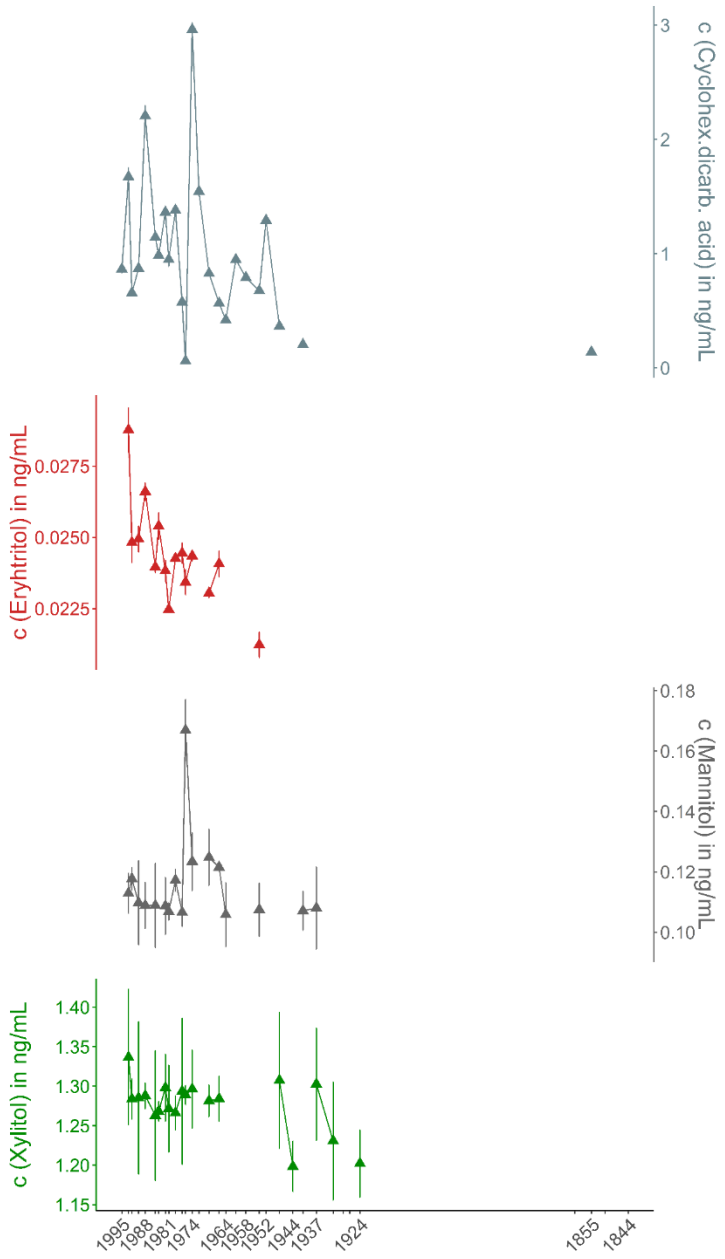

Figure S 13: Historic records of fungal spore emission markers (mannitol, xylitol), isoprene oxidation marker (erythritol), and biogenic SOA marker (*trans*-1,2-cyclohexanedicarboxylic acid) in ng/mL detected in Colle Gnifetti ice core samples from 1844 to 1995.

11.4 Supplementary material chapter 8

Table S 5: Tested conditions during *q*2D-LC method development using a 500 µL sample loop, including the sampled time window (min) and volume (µL), the starting ratio of H_2O/ACN on the RP column in the second dimension, used RP gradient [A=target gradient (see Table 1), B=linear gradient to end conditions of H_2O/ACN (1:99, v/v) within 5 minutes, C=isocratic], temperature (°C), injection flow (mL/min) and modulation volume in the sample loop (µL).

Time window (min)	**Sampled volume (µL)**	**Start ratio RP (H_2O/ACN)**	**Gradient RP**	**Temperature (°C)**	**Injection flow (mL/min)**	**Modulation vol. (µL)**
0.1-1.0	360	90:10	A	30		
0.5-1.5	400	90:10	A	30		
0.6-1.1	200	90:10	A	30		300
0.6-1.4	320	90:10	A	30		
0.6-1.4	320	90:10	A	30		200
0.7-1.5	320	90:10	A	30		
0.7-1.5	320	90:10	A	30		200
0.5-1.5	400	95:5	A	30		
0.5-1.5	400	90:10	B	30		
0.5-1.5	400	90:10	B	30	0.5	
0.5-1.5	400	99:1	B	30	0.5	
0.5-1.5	400	99:1	B	30		
0.5-1.5	400	90:10	B	35		
0.5-1.5	400	90:10	B	40		
0.5-1.5	400	99:1	B	40		
0.5-1.5	400	99:1	C	30		
0.5-1.5	400	99:1	C	40		
0.5-1.5	400	90:10	C	30		
0.5-1.5	400	90:10	C	40		
0.5-1.5	400	90:10	C	30	0.5	
0.5-1.5	400	90:10	C	30	0.6	
0.5-1.5	400	90:10	C	30	0.7	
0.5-1.5	400	90:10	C	30	0.7	100
0.5-1.5	400	90:10	C	30	0.7	50
0.5-1.5	400	95:5	C	30	0.7	
0.6-1.4	320	95:5	C	30	0.7	
0.7-1.3	**240**	**95:5**	**C**	**30**	**0.7**	
0.7-1.3	240	95:5	C	30	0.7	200
0.7-1.3	240	95:5	C	30	0.7	100
0.6-1.3	280	95:5	C	30	0.7	
0.6-1.3	280	95:5	C	30	0.7	50

Table S 6: Loadings of NTS compounds on PC1-PC5 (>|0.1|) used for prioritization.

	PC1	**PC2**	**PC3**	**PC4**	**PC5**
$C_9H_{16}O_3$	-0.14	0.66	0.17	0.34	-0.11
$C_9H_{18}O_3$	-0.12	0.41		0.24	0.06
$C_{13}H_{25}NO_3$	-0.12	0.43	-0.63	-0.60	
$C_5H_{10}O_7S$	-0.11	0.09	0.32	-0.28	0.21
$C_5H_8O_3$	-0.08	0.11	0.07		
$C_3H_4O_4$	-0.07	0.10	0.32	-0.24	0.09
$C_3H_6O_5S$	-0.07	-0.06	0.25	-0.38	0.09
$C_9H_{19}NO_4$	0.19		-0.03	0.07	
$C_{20}H_8N_2O_7$	0.24	0.09	0.07		0.09
$C_{19}H_6N_2O_7$	0.26	0.09	0.06		0.10
$C_{15}H_6O_2$	0.33	0.09	0.05		0.12
$C_6H_6N_2O_2$	0.34	0.08		-0.11	0.06
$C_5H_7NO_3$	0.68	0.18		-0.09	-0.12
$C_6H_{10}O_3$		0.04	0.09	-0.07	
$C_4H_{10}O_5S$			0.10	-0.14	
$C_8H_{16}O_3$		0.14		0.06	
$C_7H_{12}O_2$		0.12	0.05	0.09	
$C_5H_6O_4$		0.10	0.28	-0.19	
$C_5H_{12}O_7S$			0.21	-0.13	0.18

Table S 7: Suspect target list of dimers (Kristensen et al. 2014, 2016; Zhao et al. 2017)

m/z	**Molecular formula**	**Proposed identity**
197.0820	$C_{10}H_{14}O_4$	
213.0769	$C_{10}H_{14}O_5$	
229.0718	$C_{10}H_{14}O_6$	
183.1027	$C_{10}H_{16}O_3$	
199.0977	$C_{10}H_{16}O_4$	Hydroxy-pinonic acid
215.0926	$C_{10}H_{16}O_5$	
231.0875	$C_{10}H_{16}O_6$	Diaterpenylic acid acetate
315.1450	$C_{15}H_{24}O_7$	
331.1399	$C_{15}H_{24}O_8$	
347.1348	$C_{15}H_{24}O_9$	
301.1657	$C_{15}H_{26}O_6$	
325.1294	$C_{16}H_{22}O_7$	
311.1501	$C_{16}H_{24}O_6$	
327.1450	$C_{16}H_{24}O_7$	
343.1399	$C_{16}H_{24}O_8$	Pinyl-diaterbyl ester
377.1454	$C_{16}H_{26}O_{10}$	
313.1657	$C_{16}H_{26}O_6$	
329.1607	$C_{16}H_{26}O_7$	
345.1556	$C_{16}H_{26}O_8$	

m/z	**Molecular formula**	**Proposed identity**
361.1505	$C_{16}H_{26}O_9$	
325.1657	$C_{17}H_{26}O_6$	
341.1607	$C_{17}H_{26}O_7$	
357.1556	$C_{17}H_{26}O_8$	Pinyl-diaterpenyl ester
373.1505	$C_{17}H_{26}O_9$	
391.1611	$C_{17}H_{28}O_{10}$	
311.1865	$C_{17}H_{28}O_5$	
327.1814	$C_{17}H_{28}O_6$	
343.1763	$C_{17}H_{28}O_7$	
359.1712	$C_{17}H_{28}O_8$	
375.1661	$C_{17}H_{28}O_9$	
403.1611	$C_{18}H_{28}O_{10}$	
419.1560	$C_{18}H_{28}O_{11}$	
323.1865	$C_{18}H_{28}O_5$	
339.1814	$C_{18}H_{28}O_6$	
355.1763	$C_{18}H_{28}O_7$	
371.1712	$C_{18}H_{28}O_8$	
387.1661	$C_{18}H_{28}O_9$	
405.1767	$C_{18}H_{30}O_{10}$	
341.1970	$C_{18}H_{30}O_6$	
357.1920	$C_{18}H_{30}O_7$	
373.1869	$C_{18}H_{30}O_8$	
389.1818	$C_{18}H_{30}O_9$	
335.1865	$C_{19}H_{28}O_5$	
367.1763	$C_{19}H_{28}O_7$	Pinonyl-pinyl ester
383.1712	$C_{19}H_{28}O_8$	
399.1661	$C_{19}H_{28}O_9$	
417.1767	$C_{19}H_{30}O_{10}$	
337.2021	$C_{19}H_{30}O_5$	
353.1970	$C_{19}H_{30}O_6$	
369.1920	$C_{19}H_{30}O_7$	
385.1869	$C_{19}H_{30}O_8$	
401.1818	$C_{19}H_{30}O_9$	
189.0769	$C_8H_{14}O_5$	Diaterpenylic acid

Table S 8: Suspect target list of organosulfates

m/z	**Molecular formula**	**Proposed identity**
279.0545	$C_{10}H_{16}O_7S$	
342.0501	$C_{10}H_{17}NO_{10}S$	
294.0654	$C_{10}H_{17}NO_7S$	
326.0552	$C_{10}H_{17}NO_9S$	
373.0559	$C_{10}H_{18}N_2O_{11}S$	
249.0803	$C_{10}H_{18}O_5S$	Pinene/Limonene OS (Wang et al. 2017)
154.9657	$C_2H_4O_6S$	Glycolic acid sulfate (Olson et al. 2011)
168.9813	$C_3H_6O_6S$	Lactic acid sulfate (Olson et al. 2011)
304.9933	$C_5H_{10}N_2O_{11}S$	Dihydroxydinitrate sulfate ester (Darer et al. 2011)
213.0075	$C_5H_{10}O_7S$	
244.0133	$C_5H_{11}NO_8S$	Nitroxy diol sulfate ester (Darer et al. 2011)
260.0083	$C_5H_{11}NO_9S$	Trihydroxy nitrate sulfate ester (Darer et al. 2011)
215.0232	$C_5H_{12}O_7S$	2-Methyltetrol sulfate ester (Darer et al. 2011; Kristensen and Glasius 2011)
209.0854	$C_8H_{18}O_4S$	Octyl sulfate (Wang et al. 2017)
296.0446	$C_9H_{15}NO_8S$	
234.0568	$C_9H_{15}O_5S$	
251.0596	$C_9H_{16}O_6S$	Limonaketone OS (Wang et al. 2017)

Table S 9: Suspect list of sesquiterpene oxidation markers (Brüggemann et al. 2017)

m/z	**Molecular formula**	**Proposed identity**
253.1446	$C_{14}H_{22}O_4$	β-caryophyllinic acid
251.1653	$C_{15}H_{24}O_3$	β-nocaryophyllinic acid

11.5 List of abbreviations

2D-LC	two-dimensional liquid chromatography
ACN	acetonitrile
ADAP	automated data analysis pipeline
a.s.l	above sea level
BTCA	1,2,4-butanetricarboxylic acid
BVOC	biogenic volatile organic compound
CCN	cloud condensation nuclei
C-group	cinnamyl-group
COPRA	Constructing Proxy Records from Age Models
DC	Daves Cave
DCM	dichlormethane
DHBA	dihydroxybenzoic acid
ESI	electrospray ionization
FT-ICR	Fourier-transform ion cyclotrone resonance
Gal	galactosan
GC	gas chromatography
GCB	graphitized carbon black
HCD	higher-energy collisional dissociation
HCO	Holocene climate optimum
HESI	heated electrospray ionization
HETP	height equivalent to a theoretical plate
HILIC	hydrophilic interaction liquid chromatography
HLB	hydrophilic-lipophilic balanced
HPLC	high pressure liquid chromatography
HR-MS	high-resolution mass spectrometry
ICP	inductively coupled plasma
iLOQ	instrument limit of quantification
k’	capacity factor
KM_{CH2}	Kendrick mass
KMD	Kendrick mass defect
LC-LC	heart-cut two-dimensional liquid chromatography
LCxLC	comprehensive two-dimensional liquid chromatography
Lev	levoglucosan
LLE	liquid-liquid extraction
LMG	Lev/(Gal+Man)
LOPs	lignin oxidation products
Man	mannosan
MBTCA	3-methyl-1,2,3-butanetricarboxylic acid
MeOH	methanol
mLC-LC	multiple heart-cut two-dimensional liquid chromatography
mLOD	method limit of detection
mLOQ	method limit of quantification
MW	molecular weight
m/z	mass-to-charge ratio
NaOH	sodium hydroxide
NP	normal phase
NTS	non-target screening
OSc	average oxidation state
PAH	polycyclic aromatic hydrocarbons
PC	principal component
PCA	principal component analysis
PCF	post-column flow

PCP	prior calcite precipitation
PFP	pentafluoro-phenyl
PM	particulate matter
ppm	parts per million
*q*2D-LC	quasi-comprehensive two-dimensional liquid chromatography
RDBE	ring and double bond equivalent
RO	alkoxy radical
RO_2	alkyl peroxy radical
RP	reversed phase
SAX	strong anion-exchange
SCI	stabilized Criegee intermediate
S-group	syringyl-group
SOA	secondary organic aerosol
SPE	solid-phase extraction
STS	suspect target screening
TIC	total ion chromatogram
UHPLC	ultra high pressure liquid chromatography
V-group	vanillyl-group
VOC	volatile organic compound
WAX	weak anion-exchange
WP	Waipuna Cave
XIC	extracted ion chromatogram
yrs BP	years before present

11.6 List of related posters and publications

Publications

Beschnitt,A., Schwikowski, M., Hoffmann, T.: **Towards comprehensive non-target screening using heart-cut two-dimensional liquid chromatography for the analysis of organic atmospheric tracers in ice cores**, Journal of Chromatography A, 1661, (2022), https://doi.org/10.1016/j.chroma.2021.462706

Beschnitt, A., Hoffmann, T.: **Ein spurenanalytischer Blick in die Vergangenheit – Lignin Analyse in Speläothemen zur Rekonstruktion von Paläovegetation**, *GIT Labor-Fachzeitschrift*, 09/2020, p. 20-22, Wiley-VCH GmbH

Presentations

Beschnitt, A.: **Comprehensive non-target screening mittels heart-cut zweidimensionaler Flüssigchromatographie zur Analyse organischer Aerosolkomponenten in Eisbohrkernen**, *Doktorandenseminar FG Analytische Chemie AK Separation Science*, Hohenroda, Germany, January 2022

Beschnitt, A., Schäfer, J., Schwikowski, M., Hoffmann, T.: **Trace analysis of organic aerosol markers and lignin in samples from Alpine ice core Colle Gnifetti covering the 20th century using UHPLC-HRMS**, *European Geoscience Union, General Assembly*, Vienna, Austria, April 2022

Posters

Beschnitt, A., Hoffmann, T.: **Application of novel trace analysis methods for lignin and levoglucosan in flowstone samples from New Zealand during the Holocene**, *European Geoscience Union, General Assembly*, Vienna, Austria, May 2020 (online)

Homann, J., Beschnitt, A., Hoffmann, T.: **Trace analysis of levoglucosan and lignin-phenols in speleothems by HILIC-UHPLC-ESI-HRMS: A new method**, *European Geoscience Union, General Assembly*, Vienna, Austria, May 2020 (online)

Beschnitt, A., Hoffman, T.: **New methods for trace analysis of lignin and levoglucosan in speleothems from New Zealand by UHPLC-HRMS**, *Doktorandenseminar FG Analytische Chemie AK Separation Science*, Hohenroda, Germany, January 2020

Beschnitt, A., Heidke, I., Hoffmann, T.: **Trace analysis of lignin-phenols in speleothems by UHPLC-ESI-HRMS: Comparison of two lignin degradation methods**, *European Geosciences Union, General Assembly*, Vienna, Austria, April 2019

Beschnitt, A., Heidke, I., Hoffmann, T.: **Spurenanalyse von Lignin-Phenolen in Tropfsteinen mittels UHPLC-ESI-HRMS: Vergleich zweier Aufschlussmethoden zur Aufspaltung Lignin**, *ANAKON*, Münster, Germany, March 2019

11.7 Acknowledgments

I would like to thank my supervisor for the opportunity to work in his research group and to explore two exciting research fields of ice cores and speleothems. I am thankful for the discussions, support, and trust in my ideas. I am especially grateful for the participation in research campaigns, which made my PhD truly adventurous, conferences and seminars.

Thanks to, and from the Paul-Scherrer Institute in Switzerland for providing me with ice core samples and the successful collaboration. Further I would like to thank the group from the High Altitude Research Stations Jungfraujoch & Gornergrat for the stay at Jungfraujoch and the opportunity to collect snow samples at an altitude over 3000 m.

I would also like to thank and from the University of Waikato in New Zealand for providing me with speleothem samples and the entire team from the QUEST project for the amazing workshop in New Zealand and the visit of Waipuna Cave. A special thank you goes to for all his support and discussions and for introducing me in the field of speleothem research.

Furthermore, I would like to thank all current and former members of the working group for the productive work environment and helpful discussions. Thank you for all the fun game nights, group excursions, and the trip to Mar Lodge. Special thanks go to the bachelor and master students who supported my project.

Finally, I would like to thank my parents and my sister for their never-ending love and support, my friends who I could always turn to and last but not least I deeply thank my boyfriend for his patience, support, encouragement, and love.

11.8 Curriculum Vitae

Personal information

Name	Anja Beschnitt
Date of birth	18.11.1994
Place of birth	Bad Schwalbach, Germany

Professional Experience

Since 03/2022	Scientist Instrumental RNA Analytics BioNTech SE, Mainz, Germany

Education

11/2018-02/2022	**PhD studies** Department of Chemistry Johannes Gutenberg-University, Mainz, Germany Workgroup of Prof. Dr. Thorsten Hoffmann
02/2018-10/2018	**Master-thesis** "Organic trace analysis of atmospheric marker species in ice cores by high-resolution mass spectrometry" Johannes Gutenberg-University, Mainz, Germany
09/2017-10/2018	**Master studies** Bio- and Pharmaceutical Analysis University of Applied Sciences Fresenius, Idstein, Germany
02/2017-07/2017	**Bachelor-thesis** "Characterization of IgG N-glycosylation in human sera by MALDI-TOF MS" Experimental Ophthalmology, University Medicine eye and polyclinic, Mainz, Germany
09/2013-07/2017	**Bachelor studies** Applied Chemistry University of Applied Sciences Fresenius, Idstein, Germany
06/2013	**Abitur** Nikolaus-August-Otto School, Bad Schwalbach, Germany

Mainz, 29.03.2022